1-1-2012

Investigation and improvment of noise, vibration and harshness(nvh) properties of automotive panels

Mohammad Al zubi
Wayne State University,

INVESTIGATION AND IMPROVEMENT OF NOISE, VIBRATION AND HARSHNESS (NVH) PROPERTIES OF AUTOMOTIVE PANELS

by

MOHAMMAD AL-ZUBI

DISSERTATION

Submitted to the Graduate School

of Wayne State University,

Detroit, Michigan

in partial fulfillment of the requirements

for the degree of

DOCTOR OF PHILOSOPHY

2012

MAJOR: MECHANICAL ENGINEERING

Approved by:

_____ . _____ .
Advisor Date

_____ . _____ .

_____ . _____ .

_____ . _____ .

DEDICATION

To my parents who had me in all their prayers.
To my beloved wife, I could not have done this without her support
To my daughter Lina, and son Abdullah. They saw little of their father
in the last couple of months.

ACKNOWLEDGEMENT

I would like to start by thanking the almighty Allah for granting me the will and patience to do this work.

I am sincerely and heartily grateful to my advisor, Dr. E.O. Ayorinde, for the support and guidance he showed me throughout the period I spent under his supervision and through my dissertation writing. I am sure it would have not been possible without his help and support. I would like to thank my committee members Dr. Trilochan Singh, Dr. Golam Newaz and Dr Hwai-Chung Wu. I benefited greatly from the advice of every single one of them.

Besides I would like to thank my colleagues, Mehmet Akif Dundar , and Manjinder Singh for their cooperation and support during this work.

TABLE OF CONTENTS

LIST OF FIGURES

LIST OF TABLES

CHAPTER 1
BACKGROUND AND INTRODUCTION

Vehicle manufacturers initially relied on horsepower and speed performances as "standout qualities" to sell their products, but as time progressed, it became increasingly clear that customers were very much concerned about their comfort as they drove the vehicles. In the late seventies, requirements for driver and passenger comfort were increased significantly. Since then, a large amount of effort has been invested into the improvement of the technology of noise and vibration reduction and containment. It became no longer adequate to simply cram as much insulation as possible into the panels (door, roof, floor, etc.,) to abate rattling movements and achieve quiet. Saha (in Anon [1]) recalled that the earlier power trains were so noisy that one could not even hear the wind noise at all within the vehicle. When success was achieved in quietening down the power train, the wind noise then became the major challenge. He remarked that historical data shows that the persistent drive towards ever-increasing noise and vibration performance has in fact been driven mainly by customer demand rather than legal and regulatory requirements and standards. Kropp (in Anon [1]) summarized that "noise and vibration have become a statement of car quality". He further explained that people buy cars to get from one point to another – reliably and comfortably, but that they also want a quiet ride for their money, and for example want to listen to the radio without being disturbed by a lot of noise.

A novel vibro-acoustic containment method [2] builds on the discovery that plate flexural vibrations can be effectively stopped from reflecting back by terminating the plate with a small layer or wedge of damping material, thus effectively ending the life of such a propagating wave. Accordingly, acoustic effects emanating from the vibration of such a plate are also practically terminated. This approach is in its infancy, and is not covered in the work of this dissertation.

Yet another novel approach is the use of micro honeycomb constructions [3], whereby the honeycomb comprises micrometer size cylinders through which sound can travel and interact with the material in shear, and thus get practically dully dissipated before or by the time that it arrives at the end of the protrusion. The energy destruction mechanism is through shearing rather than absorption.

This work concentrates on the automotive panel for good reason. The automotive panel is of significant importance, as there are several kinds [4] in a typical vehicle. Which combination of panels are used in a particular application would depend on the geometry of the vehicle – whether salon, truck, cab-style, station wagon, convertible, or some other. These panels accordingly include the full floor panel, cab floor panel, front side panel, car rocker panels, front floor panels, pan panels, lower front door skins, lower rear quarter panels, under-seat floor pan panel, roof panel, etc.

According to the importance that automotive vibro-acoustics has commanded, several institutions in many parts of the world [1] have evolved formal study courses and vigorous research programs in academic disciplines designed to abate noise and vibration in the automotive environment. Examples of colleges with these programs include the Institute of Sound and Vibration Research in the UK, Chalmers Institution of Technology in Sweden, and the Technical University of Denmark.

The reduction of vibration and noise in and across several components and modules of the automotive, such as the panels, doors, engine covers, seats, and others, is of primary importance. The NVH performance may be a crucial factor in the purchase decisions of numerous buyers. In this work, experimental and other investigations are made on monolayer, composite and periodic

material constructions to assess their suitability for minimal transmission of noise and vibration. With respect to the materials and constructions that are suitable for noise and vibration containment, some are more suitable for noise control, and some for vibration control and some may be good in both areas. A major goal of this work is to investigate sample materials and architectures that are more applicable in the industry and are being examined for possible utilization, or that may be recommended for NVH amelioration.

Vehicle interior noise perceived in the passenger cabin of an automobile is one of the most important factors in a customer's determination of the quality and durability of the vehicle. Thus, the reduction of interior noise is a major concern for automobile manufacturers trying to achieve customer satisfaction and a market leadership position in the highly competitive automotive market.

Automotive interior noise is generated by various elements such as the engine, transmission, and climate-control system [5]. However, due to technological advancement in the sound and vibration engineering of vehicles, the overall noise level from vehicles has been continuously reduced, which has resulted in drawing the occupant's attention to intermittent noise such as buzz, squeak, and rattle (BSR) [6] [7] . A market survey reported BSR as the third most important customer concern in cars after 3 months of ownership [8]. Thus, BSR noise is increasingly seen as a direct indicator of vehicle quality and reliability.

The sound wave emanating from the vibrating structure alone is called "buzz". "Squeak" is noise originating from frictional movement between two parts, and "rattle" is noise due to the impact of one part on another [9]. Squeak is caused by the elastic deformation of the contact surfaces storing energy, which is released when the static friction exceeds the kinetic friction and rattle is generated by loose or very flexible elements under forced excitation. For both squeak and rattle

noises, the exciting force is due mainly to the road surface, which forces components to vibrate vertically. The main causes of BSR noise can be categorized as structural deficiencies, non-matching material pairs, and bad geometrical alignment [8] and [9]. The basic cause of BSR noise is the relative motion of structural components exceeding a threshold value.

Since BSR is noticed by customers, manufacturers have worked out many specifications for assemblies and components. The physics of the phenomena have been reported earlier, but direct applications relating to the BSR problem have only been published recently [10].

. The main issues in BSR are the lack of real test standards and nebulous acceptance criteria written into existing specifications [11]. Traditionally, vehicle product evaluation from the BSR perspective depends heavily on physical testing and engineering experience.

Most vehicle manufacturers detect and fix BSR problems with the road test as a result of various excitation sources, complex generation mechanisms, and responses of human subjects. To improve the situation, it has been suggested [9] that (1) find and fix BSR problems for modules instead of a full vehicle to address the problems in the early stage; (2) design vibration exciters to perfectly reproduce input signals to the vehicle from the road; (3) develop techniques to automatically localize the source region of BSR in spite of various potential noise sources; and (4) to establish a sound quality evaluation system allowing for subjective responses to BSR. In a study [7] a BSR evaluation system and procedures were developed for automotive interior modules that consist of an excitation shaker and vibration jigs for the modules, acoustic-field visualization techniques, and the evaluation of sound quality. Instrument panels, seats, and doors are considered to be responsible for over 50% of the total BSR vehicle interior noise problems, with the instrument panel (IP) module being the main source [8].

CHAPTER 2

LITERATURE SURVEY

Poisson [12] first examined the vibrations of circular plates investigating the three cases of fixed, simply supported and free edges. He analyzed theoretically some of the symmetrical modes of vibrations and calculated the ratios of the radii of the nodal circles to the radius of the plate when the vibrating plate had no nodal diameter or one or two nodal circles. The full theory of the vibration of a free circular plate was later developed by the Kirchhoff [13]. Kirchhoff extended the Poisson's results for the vibration of free plate by calculating six ratios of the radii with one, two or three nodal diameters. Lord Rayleigh [14] developed a general theory of these vibrations and highlighted the low frequencies of thin plates; while Lamb [15] gave a summary of the theoretical work to date. The general Rayleigh method is based on the energy principle, while a latter modification by Ritz uses a sum of functions to represent the vibratory deflection, while the method by Bolotin utilizes asymptotic approximations to the eigen functions.

Airey [16] studied the vibrations of circular plates and, like Rayleigh, also explored their treatment with Bessel functions, and generated a method of solving the plate equations to yield the characteristic equation roots, and the radii of the nodal circles for any vibration mode. Timoshenko [17] analyzed the transverse vibration of rectangular and circular isotropic plates under different boundary conditions, obtaining natural frequency formulas. Wood [18] experimentally investigated the free transverse vibration of circular plates having significant thickness. These plates have high transverse vibration natural frequencies that may even be beyond the human hearing.

Iguchi [19] explored the vibrations variously constrained plate, focusing in a latter work [20] on the completely free boundary condition, and employing the summation of symmetric and asymmetric Levy expansions to obtain exact solutions for the Eigen functions. Warburton [21] utilized characteristic beam vibration functions in Rayleigh's method to evolve simple approximate expressions for natural frequencies of thin, isotropic rectangular plates under different boundary conditions and various ratios of the plate side lengths. This method saves significantly on the time and computer resources normally utilized by many other methods such as the Ritz, Bolotin's, series solutions, finite difference and finite element method. An extensive work, embracing many boundary conditions and anisotropic material behavior, was presented by Lekhnitskii, Tsai and Cheron [22] for mode shapes and natural frequencies. A comprehensive work on the vibration of plates, commissioned by NASA, was published by Leissa [23]. Zelenov and Elektrova [24] utilized experimental vibration results and analysis to estimate the elastic constants of an isotropic circular plate having different boundary conditions. Gorman et al. [25][26][27] analyzed the free vibration of rectangular plates, utilizing symmetries and simplified functions. Dickinson et al. [28] advanced Warburton's approach to especially orthotropic plates and also inclusion of the effect of uniform, direct-in-plane force in generating approximate formulas for natural frequencies of flexural vibration. An early example of the finite element application may be found in the work of Dinis and Owen [29], analyzing elasto-viscoplastic plates.

A utilitarian handbook of principles and formulas of the vibration of structural and fluid systems was published by Blevins in 1979 [30] to facilitate finding the frequencies and mode shapes of a wide range structures. A finite element method for the vibration analysis of sandwich structures was presented by Connor in 1987 [31], including the effect of transverse

normal deformation of core. Ewins [32] published an analytical and practical work on modal testing technology, with a mathematical model expressing the vibration properties of a structure based on test data.

Deobald and Gibson [33] matched vibration analysis calculations with experimental data to extract elastic constants of specimens. Bardell [34] determined the natural frequencies and modes of a flat rectangular plate with the finite element method, utilizing boundary conditions and presented several parameters (including the variation of frequency with the aspect ratio and the Poisson's ratio. Lai and Lau [35] extended the method of Deobald and Gibson [33] to examine the full modal testing of a plate with free edges, and calculated elastic constants. Lee and Fan [36] explored the finite element analysis of composite sandwich plates, utilizing Mindlin's plate theory (which assumes that shear deformation takes place, and the plate section is deformed into the shape of a parallelepiped), and investigating the effect of the transverse normal deformation of the core. They concluded that cores that are flexible in the transverse normal direction tend to decrease natural frequencies without significant alteration of mode shapes.

Galerkin's work on damped sandwich beams was extended to the plates domain by Zhang and Sainsbury [37], while further finite element applications may be found in the works of Klosowski et al [38]. Klosowski [39] studied the vibrations of circular plates subjected to shock-wave impulses. They utilized finite element analysis and compared to experimental data, with good correlation.

Hoshino, Takura and Takahashi [40] simulated and analyzed the vibration containment of heavy duty truck cabins with a load transfer path theory. The load paths identify load transfer

and warn the designer of the creation of bending moments and the location of features such as holes on the load path. The algorithm of the theory provides insight into the way a structure is carrying loads by identifying the material most effective in performing the load transfer. They concluded that the floor panel is closely related to the stiffness of the front cross-member of the floor structure,, and that discontinuities and non-uniformities in the load paths reduces the front cross-member stiffness. Sun et al. [41] applied Statistical Energy Analysis (SEA) to the design of car interior trims and concluded that proper design of such trims may be guided by such analyses. Car interior pressures before and after applications of various trims confirmed the improvements achieved. Pappada et al. [42] investigated the upgrade of damping in laminated composite plates by embedding shape memory alloy (i.e. those which manifest this behavior recover their pre-deformation shapes when load is removed or temperature is altered.) composite wires in them. They found that damping always improved by this method, but found that curved and patterned wires were more effective than straight wires. Shin and Cheong [43] experimentally characterized buzz, squeak and rattle (BSR) noise in stationary automobiles and stated from their results that their procedure offers a reliable method to systematically obtain BSR data for various automotive component sources.

Earlier on, study of wall transmission loss was limited by because only the wall mass was considered, and consequently; the results obtained only gave a basic approximation and did not explain all the observed phenomena (e.g., critical frequency).

Elasticity was introduced in to the problem for an infinite plate by Cremer [44], revealing the important phenomenon of critical frequency, when the wave propagation speeds of the plate and of the fluid are equal. London [45] used the hypothesis of the infinite plate, and also contributed how to find transmission loss in a diffuse field of a simple wall and for double wall.

In their treatise on sound absorbing materials, Zwikker and Kosten [46] gave an extensive literature review with substantial data and tables on the sound absorption coefficients of several materials. They supplied useful insight into the acoustic roles of physical features of the materials (thickness, porosity, diameter, stiffness), thus guiding the adequate design of sound abatement materials. Their models and theories were practical but proved unable to highlight detailed phenomena, especially at low frequency. The work of Vogels [47] on finite plates was equivalent to a foundation effort in modal analysis, which permitted the establishment of detailed laws and a clearer understanding of these phenomena. Interest was stimulated in the study of wall radiation (i.e. due to the vibration of a flexible wall), and of the influence of internal damping of the plate. Hickman [48], who studied the infinite model of the complex plate (sandwich), only considered the flexure and extension of the wall. Kurtze [49] enunciated a principle of wave propagation and Watters [50] studied a basic model of sandwich behavior, where the core acts as a spacer that has mass and transmits shear, while the skins behave as ordinary bent plates. He obtained the impedance for such a composite plate from an equivalent circuit analog, and the imposition of a null value on that impedance led to a bi-cubic equation for admissible wave speeds of bending and shears waves in the plate. Maidanik [51] evaluated impedance radiation values for the cases of single-mode excitation of the plate, or when the plate is loaded by a diffuse field.

Free vibration analysis of a basic sandwich model was provided by Ford, Lord, and Walker [52] with observation of a relation between dips in experimental transmission loss curves and the resonance frequencies in both bending and dilatational modes. Sharp and Beauchamp [53] utilized Hickman's hypothesis to generalize the results for the case of n layers. Using the double Fourier transform, Spronck [54] obtained an expression for the radiation impedance for a

general case. He mentioned non-diagonal terms in the radiation impedance matrix, which signified an interaction of one mode with another, on account of the fluid spaces. The radiation impedance was not obtained for the general case, but was assumed to be negligible after the earlier observation of Sewell [55]. Incidentally, this was proved by later workers to be incorrect.

The energy expression by Ford, Lord, and Walker was corrected by Smolenski and Krokosky [56], who compared resonance data from their further experimental work with analytical results. They also highlighted a coincidence effect beyond the bending coincidence. Analytic expressions for impedance and transmission loss of a sandwich panel were obtained by Dym and Lang [57] thus facilitating comparisons with experimental data thenceforth. Guyader and Lesueur [58] derived an analytic expression for the infinite plate transmission for the three-layered sandwich plate, and extended it to multi-layered plates.

Many aspects of low-frequency range sound transmission were studied in detail by Woodcock and Nicolas [59], with emphasis on the finite-size panel, its orthotropic properties and the boundary conditions, apparently for the first time. The intermodal interaction was well highlighted. Pates, Mei and Shirahatti [60] compared coupled BEM/FEM analysis with existing classical modal approximation, and experimental solutions for isotropic panels were found to be accurate and reliable solutions to complex problems. Transmission loss data for isotropic and composite panels were analyzed and compared. Lamination study was also done to illustrate the effect of orientation angle on overall transmission loss.

In a model based on the compilation of the impedances encountered by an acoustic wave as it propagates through the wall, Fringuellino and Guglielmone [61] proposed a formula for the

transmission loss of multilayered walls. The characteristic impedance and the propagation constant of each layer are utilized as input parameters.

Lim [62] studied the radiated noise contributions of automotive body panels to the interior sound pressure levels, with an approximate spectral formulation model, and also applying it to a real car. The results showed structural panels that contributed most significantly to the interior noise spectra, and thus which should be prime candidates for design modifications to reduce the interior noise levels.

Hills, Mace and Ferguson [63] investigated the statistical variability of noise response in automotive interiors. They suggested reasonable assumptions, and concluded that changes in specification such as trim, minor body modifications and, in particular, tire and rim type might cause significant variability from one specification to another, thus providing a challenge to the engineer's effort to produce robust, low noise products.

Binxing et al. [64] combined various numerical calculation methods to model and analyze the acoustic characteristics of a heavy truck cab. They concluded that various numerical calculation methods, such as FEM, BEM and SEA, can be rigorously combined to model and analyze the acoustic characteristics of vehicles. They also concluded that the sound quality of the cab can be improved after acoustic topology optimization. The interior noise level was reduced by a few decibels.

CHAPTER 3

OBJECTIVES AND THEORY

The traditional method for constructing the automotive panel structure has been typically to layer a metal panel outer member with a visco-elastic damping layer, then a porous layer, and then a rubber/plastic layer in order to affect improved vibro-acoustic performance. More recently [65], efforts have been directed in the industry towards improving the nature and/or architecture of the panel material itself, such that extra costs associated with added materials and the fabrication and assembly labor costs that are involved are saved as much as possible, and yet such panels have good vibration and acoustics performances.

From the existing literature, it is obvious that newer vibro-acoustic materials have not been tested yet. They have not been modeled, and have not been studied to observe factors in their properties or configurations that promote or retard acoustic absorption, or, their vibratory amplitudes and natural frequency distributions. Comparisons of their performances across materials and across methods of experiment, analysis and numerical approximations have not been made. The issue of compounding better materials from those tested, and also the exploration of the principles of tailoring such better materials from tested ones has not been addressed.

3.1 OBJECTIVES OF THE RESEARCH

Accordingly, the objectives of the work are to:-

i. Investigate by experimental, analytical and numerical methods the vibration and acoustic performances of trial panel materials

ii. investigate and establish what physical and material properties and architectural constructions yield better vibration and acoustic performances, and thus advance towards the development of better and newer automotive panels with good NVH performances

iii. investigate the acoustic and vibration responses of periodic cellular material structures (PCMS) samples

iv. Do some parametric studies to understand the behavior of samples of different materials and geometries which enable us to avoid costly numerous experimental trails.

v. supply some design guidance in selecting or designing automotive panels for good NVH (noise, vibration and harshness) performances

3.2. INTRODUCTION TO VIBRATION OF CIRCULAR PLATES

Although vibration tests are carried out on the samples mainly in the frequency range 50 Hz to 6.4 kHz, the PULSE system, is technically able to extend this range to 25.6 kHz. However, resolution accuracy falls off with the wider frequency spans. The first three natural frequencies, which are usually the most practically significant, are very often within this range

The circular plate is the appropriate structure to consider because the impedance tube which is used to test acoustic properties of material samples, dictates that two samples of each material, respectively of diameters 100mm and 29 mm, be procured to match the acoustic impedance tube internal diameters in order to obtain results covering up to 6.4 kHz frequency. It has therefore been widely found convenient to test the same sample for both acoustics and vibration.

All structures are three-dimensional, and the exact analysis of stresses in them presents much difficulties. However, such precision is seldom needed, nor indeed justified, for the magnitude and distribution of the applied loading and the strength and stiffness of the structural

material are not known accurately. For this reason it is adequate to analyze certain structures as if they are one- or two-dimensional. Thus the engineer's theory of beams is one-dimensional: the distribution of normal and shearing stresses across any section is assumed to depend only on the moment and shear at that section. By the same token, a plate, which is characterized by the fact that its thickness is small compared with its other linear dimensions, may be analyzed in a two-dimensional manner. The simplest and most widely used plate theory is the *classical small-deflection theory* which we will now consider. The classical small-deflection theory of plates, developed by Lagrange [66], is based on the following assumptions:

(i) Points which lie on a normal to the mid-plane of the undeflected plate lie on a normal to the mid-plane of the deflected plate.

(ii) The stresses normal to the mid-plane of the plate, arising from the applied loading, are negligible in comparison with the stresses in the plane of the plate.

(iii) The slope of the deflected plate in any direction is small so that its square may be neglected in comparison with unity.

(iv) The mid-plane of the plate is a 'neutral plane', that is, any mid-plane stresses arising from the deflection of the plate into a non-developable surface may be ignored.

These assumptions have their counterparts in the engineer's theory of beams; assumption (i), for example, corresponds to the dual assumptions in beam theory that 'plane sections remain plane' and 'deflections due to shear may be neglected'. Possible sources of error arising from these assumptions are discussed.

3.3 GENERAL PLATE VIBRATION

The subject of plate vibrations is treated to various levels of detail in many texts and papers, e.g. Timoshenko [17]. Following Timoshenko, Consider an element of a vibrating plate as shown in Figure 3.1.

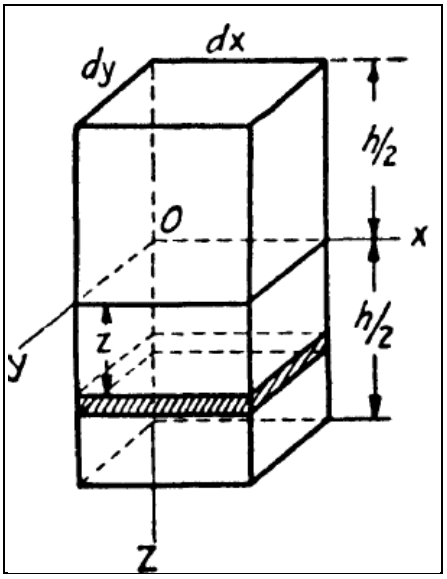

Figure3.1: Element of vibrating plate [17]

The plate consists of a perfectly elastic, homogeneous, isotropic material that has a uniform thickness *h* which is small in comparison with its other dimensions. We take the x*y* plane as the middle plane of the plate and assume that with small deflections the lateral sides of an element, cut out from the plate by planes parallel to the *zx* and *zy* planes (see Fig. 3.1) remain plane, and rotate so as to be normal to the deflected middle surface of the plate. Then the strain in a thin layer of this element, indicated by the shaded area and distance *z* from the middle plane can be obtained from a simple geometrical consideration and will be represented by the following equation:

$$\gamma_{xy} = -2z\frac{\partial^2 w}{\partial x \partial y} \tag{3.1}$$

It is assumed that the deflections are small in comparison to the thickness of the plate, and the middle plane is considered to be unstretched.

Thus:

$$\varepsilon_y = -z\frac{\partial^2 w}{\partial y^2} \tag{3.2}$$

$$\varepsilon_x = -z\frac{\partial^2 w}{\partial x^2} \tag{3.3}$$

In which:

ε_x, ε_y are unit elongations in the x and y directions,
γ_{xy} is shear deformation in the xy plane,
w is deflection of the plate,
h is the thickness of the plate.
z is the distance from the shaded area to the middle surface

The corresponding stresses will therefore be obtained from the well-established equations:

$$\begin{aligned}
\sigma_x &= -\frac{Ez}{1-\nu^2}\left(\frac{\partial^2 w}{\partial x^2} + \nu\frac{\partial^2 w}{\partial y^2}\right) \\
\sigma_y &= -\frac{Ez}{1-\nu^2}\left(\frac{\partial^2 w}{\partial y^2} + \nu\frac{\partial^2 w}{\partial x^2}\right) \\
\tau_{xy} &= -\frac{Ez}{1+\nu}\left(\frac{\partial^2 w}{\partial x \partial y}\right),
\end{aligned} \tag{3.4}$$

In which ν represents the Poisson's ratio.

The potential energy stored in the shaded part of the element in the diagram during deformation will be:

$$dU = \left(\frac{\varepsilon_x \sigma_x}{2} + \frac{\varepsilon_y \sigma_y}{2} + \frac{\gamma_{xy}\tau_{xy}}{2}\right) dx\, dy\, dz \tag{3.5}$$

When the above equations (3.1-3.4) for unit elongations, shear deformations, and stresses are applied, we have:

$$dU = \frac{Ez^2}{2\left(1-\nu^2\right)}\left\{\left(\frac{\partial^2 w}{\partial x^2}\right)^2 + \left(\frac{\partial^2 w}{\partial y^2}\right)^2 + 2\nu\frac{\partial^2 w}{\partial x^2}\frac{\partial^2 w}{\partial y^2} + 2\left(1-\nu\right)\left(\frac{\partial^2 w}{\partial x \partial y}\right)^2\right\} dx\, dy\, dz, \tag{3.6}$$

From this, upon integration, we get the potential energy of bending of the plate as:

$$U = \frac{D}{2}\iint\left\{\left(\frac{\partial^2 w}{\partial x^2}\right)^2 + \left(\frac{\partial^2 w}{\partial y^2}\right)^2 + 2\nu\frac{\partial^2 w}{\partial x^2}\frac{\partial^2 w}{\partial y^2} + 2\left(1-\nu\right)\left(\frac{\partial^2 w}{\partial x \partial y}\right)^2\right\} dx\, dy \tag{3.7}$$

Where the flexural (i.e. bending) rigidity of the plate has been denoted by (D), and is given by:

$$D = \frac{E\,h^3}{12\left(1-\nu^2\right)} \tag{3.8}$$

Where, E is Young's modulus, h is plate thickness, and ν is Poisson's ratio.

Similarly, the kinetic energy (T) of the vibrating plate may be written as:

$$T = \frac{\rho h}{2}\iint \dot{w}^2 dxdy \tag{3.9}$$

Where ρh is the mass per unit area of the plate, and $\dot{w}$ is the first derivative of displacement.

From the expressions for potential and kinetic energies, different suitable methods, such as the energy conservation principle, may be utilized to obtain the natural frequencies

Lord Rayleigh's method of deducing natural frequencies of vibrating structures consisted in equating the maximum kinetic energy, T_{max} (occurring in the mean position where deflection is nil but velocity is maximum) to the maximum potential energy, U_{max} (which occurs in the

extreme position where deflection is maximum but the velocity is zero). Ritz introduced the use of functions to approximate the deflection.

For example, when Ritz studied the vibration of a completely free square plate, he took the deflection function as:

$$w = Zcos(\omega t - \alpha) \tag{3.10}$$

Where Z is a function of x and y and it determines the mode of vibration, if we take Z in a series form, we get:

$$Z = a_1\varphi_1(x,y) + a_2\varphi_2(x,y) + a_3\varphi_3(x,y) + \cdots \tag{3.11}$$

Or, in separable form:

$$Z = \sum_m \sum_n a_{mn} X_m(x) Y_n(y) \tag{3.12}$$

where $X_m(x)$ and $Y_n(y)$ are the normal functions of the vibration of a prismatic bar with free ends. Substituting equation (3.10) into equations (3.7) and (3.9), we get the following expression for maximum potential energy:

$$U = \frac{D}{2}\int\int\left\{\left(\frac{\partial^2 Z}{\partial x^2}\right)^2 + \left(\frac{\partial^2 Z}{\partial y^2}\right)^2 + 2\nu\frac{\partial^2 Z}{\partial x^2}\frac{\partial^2 Z}{\partial y^2} + 2(1-\nu)\left(\frac{\partial^2 Z}{\partial x \partial y}\right)^2\right\} dx\,dy \tag{3.13}$$

The kinetic energy for the plate is given by:

$$T_{\max} = \frac{\rho h}{2}\omega^2 \int\int Z^2 dx\,dy \tag{3.14}$$

Where ω, is the natural frequency in Hz.

By equating the maximum potential and kinetic energies, we obtain the eigenvalues (squares of frequency) of the system

$$\omega^2 = \frac{2}{\rho h} \frac{U_{\max}}{\int\int Z^2 dx\, dy} \tag{3.15}$$

The frequencies of vibration are then determined by the equation

$$\omega = \frac{\alpha}{a^2} \sqrt{\frac{D}{\rho h}} \tag{3.16}$$

Where α is a constant depending on the vibration mode, ρ is the density, a is the length of the square rib, and h is the plate thickness. The values for α [17] are (14.1, 20.56, and 23.91) for the first three modes respectively.

From this equation, some general conclusions can be drawn which hold also in other cases of vibration of plates, namely,

(a) The period of the vibration of any natural mode varies with the square of the linear dimensions, provided the thickness remains the same;

(b) If all the dimensions of a plate, including the thickness, are increased in the same proportion, the period increases with the linear dimensions;

(c) The period varies inversely with the square root of the modulus of elasticity and directly as the square root of the density of material.

3.4 VIBRATION OF A CIRCULAR PLATE

The above general procedure and results can be easily adapted for circular plates. Kirchhoff [13] solved the problem of the vibration of a circular plate and calculated the frequencies of several modes of vibration for a plate with free boundary. The exact solution of this problem involves the use of Bessel functions. In the following, an approximate solution using the Rayleigh-Ritz method is used. The Rayleigh-Ritz approach usually gives results of

sufficient accuracy for practical applications, when sufficient numbers of terms are retained in the representing deflection expression. For circular and cylindrical geometries, it is necessary to transform the energy expressions to polar coordinates.

The basics of this transformation can be seen in figure 3.2. From the elemental triangle *mns* it may be seen that a small increase *dx* would lead to small increases

$$dr = dx\cos\theta\,;\, d\theta = -\frac{dx\sin\theta}{r} \tag{3.17}$$

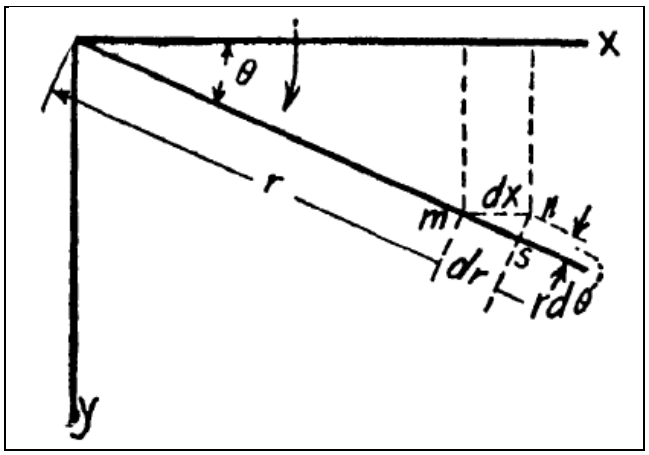

Figure 3.2: Model of deformed coordinates in plate vibration [17]

By considering the deflection *v* as a function of r and Θ we obtain:

$$\frac{\partial w}{\partial x} = \frac{\partial w}{\partial r}\frac{\partial r}{\partial x} + \frac{\partial w}{\partial \theta}\frac{\partial \theta}{\partial x} = \frac{\partial w}{\partial r}\cos\theta - \frac{\partial w}{\partial \theta}\frac{\sin\theta}{r} \tag{3.18}$$

Similarly we will find:

$$\frac{\partial w}{\partial y} = \frac{\partial w}{\partial r}\sin\theta + \frac{\partial w}{\partial \theta}\frac{\cos\theta}{r} \tag{3.19}$$

Differentiating (3.18) and (3.19) once more we get:

$$\frac{\partial^2 w}{\partial x^2} = \left(\frac{\partial}{\partial r}\cos\theta - \frac{\partial}{\partial \theta}\frac{\sin\theta}{r}\right)\left(\frac{\partial w}{\partial r}\cos\theta - \frac{\partial w}{\partial \theta}\frac{\sin\theta}{r}\right) \tag{3.20}$$

$$= \frac{\partial^2 w}{\partial r^2}\cos^2\theta - 2\frac{\partial^2 w}{\partial r \partial \theta}\frac{\sin\theta\cos\theta}{r} + \frac{\partial w}{\partial r}\frac{\sin^2\theta}{r} + 2\frac{\partial w}{\partial \theta}\frac{\sin\theta\cos\theta}{r^2} + \frac{\partial^2 w}{\partial \theta^2}\frac{\sin^2\theta}{r^2} \tag{3.21}$$

and

$$\frac{\partial^2 w}{\partial y^2} = \frac{\partial^2 w}{\partial r^2}\sin^2\theta + 2\frac{\partial^2 w}{\partial r \partial \theta}\frac{\sin\theta\cos\theta}{r} + \frac{\partial w}{\partial r}\frac{\cos^2\theta}{r} - 2\frac{\partial w}{\partial \theta}\frac{\sin\theta\cos\theta}{r^2} + \frac{\partial^2 w}{\partial \theta^2}\frac{\cos^2\theta}{r^2} \tag{3.22}$$

$$\frac{\partial^2 w}{\partial x \partial y} = \frac{\partial^2 w}{\partial r^2}\sin\theta\cos\theta + \frac{\partial^2 w}{\partial r \partial \theta}\frac{\cos 2\theta}{r} - \frac{\partial w}{\partial \theta}\frac{\cos 2\theta}{r^2} - \frac{\partial w}{\partial r}\frac{\sin\theta\cos\theta}{r} - \frac{\partial^2 w}{\partial \theta^2}\frac{\sin\theta\cos\theta}{r^2} \tag{3.23}$$

These lead to:

$$\frac{\partial^2 w}{\partial x^2} + \frac{\partial^2 w}{\partial y^2} = \frac{\partial^2 w}{\partial r^2} + \frac{1}{r}\frac{\partial w}{\partial r} + \frac{1}{r^2}\frac{\partial^2 w}{\partial \theta^2} \tag{3.24}$$

and:

$$\frac{\partial^2 w}{\partial x^2}\frac{\partial^2 w}{\partial y^2} - \left(\frac{\partial^2 w}{\partial x \partial y}\right)^2 = \frac{\partial^2 w}{\partial r^2}\left(\frac{1}{r}\frac{\partial w}{\partial r} + \frac{1}{r^2}\frac{\partial^2 w}{\partial \theta^2}\right) - \left\{\frac{\partial}{\partial r}\left(\frac{1}{r}\frac{\partial w}{\partial \theta}\right)\right\}^2 \tag{3.25}$$

Substituting (3.24) and (3.25) in equation (3.7) and referencing the plate center as origin then yields:

$$U = \frac{D}{2}\int_0^{2\pi}\int_0^{R}\left\{\left(\frac{\partial^2 w}{\partial r^2} + \frac{1}{r}\frac{\partial w}{\partial r} + \frac{1}{r^2}\frac{\partial^2 w}{\partial \theta^2}\right)^2 - 2(1-\nu)\frac{\partial^2 w}{\partial r^2}\left(\frac{1}{r}\frac{\partial w}{\partial r} + \frac{1}{r^2}\frac{\partial^2 w}{\partial \theta^2}\right) + 2(1-\nu)\left\{\frac{\partial}{\partial r}\left(\frac{1}{r}\frac{\partial w}{\partial \theta}\right)^2\right\}\right\} r\,d\theta\,dr, \tag{3.26}$$

Where *R* represents the radius of the plate.

If the plate deflection is symmetrical about the center, *w* will be a function of r only, and the last equation simplifies to:

$$U = \pi D \int_0^r \left\{ \left(\frac{d^2w}{dr^2} + \frac{1}{r}\frac{dw}{dr} \right)^2 - 2(1-\nu)\frac{d^2w}{dr^2}\frac{1}{r}\frac{dw}{dr} \right\} r\,dr \tag{3.27}$$

The kinetic energy in polar coordinates is given by:

$$T = \frac{\rho h}{2} \int_0^{2\pi} \int_0^R \dot{w}^2 r\,dr\,d\theta \tag{3.28}$$

and for symmetrical cases,

$$T = \pi \rho h \int_0^R \dot{w}^2 r\,dr \tag{3.29}$$

When these expressions are utilized for the potential and kinetic energies, the frequencies and natural modes of vibration of circular plates for various particular boundary conditions may be obtained. In the application of the Rayleigh-Ritz method here we may assume that the solution takes the form of equation (3.10), however, when Z is expressed as a function of both *r* and θ. For vibration which is symmetric about the center, Z will be a function of *r* only, and can be expressed as:

$$Z = a_1 \left(1 - \frac{r^2}{R^2} \right)^2 + a_2 \left(1 - \frac{r^2}{R^2} \right)^3 + \cdots \tag{3.30}$$

To get an approximation to the first mode one uses the first term in the representative expansion. The first two terms are utilized to solve for the second mode, etc. The vibration frequency in all cases can be determined by the equation shown below [17]:

$$\omega = \frac{\alpha}{R^2}\sqrt{\frac{D}{\rho h}} \tag{3.31}$$

Where R is the radius of the plate, ρ is the density, h is the plate thickness, α is called modal constant, and D is the modulus of rigidity. For a free circular plate with n nodal diameters and s nodal circles, the values of α are given for various modes in the following table [17].

Table 3.1: Alpha values for different nodal lines and circles

s	n			
	0	1	2	3
0	…….	……	5.251	12.23
1	9.076	20.52	35.24	52.91
2	38.52	59.86	……..	……..

3.5 ACOUSTICS THEORY

The acoustics theory of waves incident on plates has also been treated by many authors in books and technical papers; we have followed the development by Zwikker and Kosten [46], Biot [67] and Allard [68].

3.5.1 DYNAMICS OF ACOUSTIC PLANE WAVES

In one-dimensional flow, the instantaneous pressure of a sound wave at a point traveling in the positive coordinate direction may be expressed in terms of frequency, sound speed, coordinate and time as:

$$p(x) = A \exp\left\{ j\omega\left(t - \frac{x}{c} \right) - \alpha x \right\} \qquad (3.32)$$

Here, j^2 is -1, ω is radian frequency equal 2 π . Hertzian frequency in cycles/sec, and A is a constant. At the starting point $x = 0$, $p(0) = A \exp j\omega t$.

If we use the representations β for ω/c, and γ for α + jβ, then:

$$p(x) = p(0)\exp(-\gamma x). \qquad (3.33)$$

Where γ, called the propagation constant, is a characteristic of the medium. The real and imaginary parts of this quantity, respectively α and β, are called the attenuation constant and phase constant. The velocity at a coordinate point can also be written as

$$v(x) = v(0)\exp(-\gamma x). \qquad (3.34)$$

The ratio, at a point, of acoustic pressure to acoustic velocity, *p(x)/v(x)*, is called the specific acoustic impedance, *z(x)*.

In an infinite medium, this impedance depends only on the material of the medium, hence it is often known as the wave impedance in the medium, *W*. For an inlet pressure *p(0)* applied at *x = 0* to an infinite medium, instantaneous pressure and velocity at any coordinate may be obtained from *W* and *γ*, which thus completely characterize the acoustic response of such a medium.

3.5.2 ACOUSTIC TRANSMISSION IN THICK FINITE MEDIUM

Let the impedance of a plate having thickness *l* be z_1 *at x = 0* and z_2 at *x = l*. Since some of the sound signal will be reflected back at the termination point *x = l*, then pressure *p* at any coordinate *x* between inlet and end must be a superposition of both the forward-traveling (positive) and reflected (negative-traveling) signals:

$$p(x) = p_i \exp\{\gamma(l-x)\} + p_r \exp\{-\gamma(l-x)\} \qquad (3.35)$$

and velocity,

$$v(x) = \left(\frac{p_i}{W}\right)\exp\{\gamma(l-x)\} - \left(\frac{p_r}{W}\right)\exp\{-\gamma(l-x)\} \qquad (3.36)$$

Where p_i and p_r stand for inward and reflected pressure. The negative sign is necessary for the velocity of the reflected signal (velocity is a vector) . Using boundary conditions at l as $p(l)/v(l) = z_2$ in Equation (3.36), we get:

$$\frac{p_r}{p_i} = \frac{(z_2 - W)}{(z_2 + W)} \tag{3.37}$$

Equation (3.37) and its predecessor taken together yield the impedance z_1 at x = 0 as

$$z_1 = W \frac{z_2 \cosh \gamma l + W \sinh \gamma l}{z_2 \sinh \gamma l + W \cosh \gamma l} \tag{3.38}$$

A particular instance of this relationship occurs when the absorbent is backed by a rigid termination, thus making the impedance z_2 to become infinite, and then

$$z_1 = W \coth \gamma l. \tag{3.39}$$

3.5.3. ANALYSIS FOR AIR PROPAGATION CONSTANT, γ, AND WAVE IMPEDANCE, W.

Newton's second law, or the motion Equation for a layer of air having thickness dx, becomes

$$-\frac{\partial p}{\partial x} = \rho_0 \frac{\partial v}{\partial t} \tag{3.40}$$

Where ρ_o represents air density. The continuity may be stated as

$$-\frac{\partial v}{\partial x} = \frac{1}{\rho_0}\frac{\partial \rho}{\partial t} = \frac{1}{\rho_0}\frac{d\rho}{dp}\frac{\partial p}{\partial t} \tag{3.41}$$

Let the air bulk modulus, which equals volumetric stress divided by volumetric strain, be represented by $K_0 = dp/((d\rho/\rho_0))$. Eliminating *v* by equating the signed differentials of equation (3.40) with respect to *x* and equation (3.41) with respect to *t* respectively leads to:

$$\frac{\partial^2 p}{\partial x^2} = \frac{\rho_0}{K_0}\frac{\partial^2 p}{\partial t^2}. \tag{3.42}$$

But pressure p along coordinate x can be defined in terms of frequency, time, and propagation constant as:

$$p = A\exp(j\omega t)\exp(-\gamma_0 x) \tag{3.43}$$

Equation (3.43) may be substituted into (3.42) to obtain:

$$\gamma_0^2 = -\frac{\rho_0}{K_0}\omega^2 \tag{3.44}$$

Then:

$$\gamma_0 = \pm j\omega\sqrt{\frac{\rho_0}{K_0}} \tag{3.45}$$

A comparison of equations (3.32) and (3.45) leads to the physical meaning of $\sqrt{(\rho_0/K_0)}$ as the velocity, c_o of sound propagation in air. When equation (3.45) and the velocity expression

$$v = B\exp(j\omega t)\exp(-\gamma_0 x) \tag{3.46}$$

Are substituted into the wave impedance equations (3.40) and (3.41), we obtain

$$\frac{p}{v} = W_0 = \sqrt{K_0\rho_0} = \rho_0 c_0 \tag{3.47}$$

3.5.4 DEDUCTION OF ABSORPTION AND REFLECTION COEFFICIENTS

Consider the plane waves through the air to be incident at a wall of specific impedance z. The reflection coefficient, r, thus becomes:

$$r = \frac{p_r}{p_i} = \frac{z - W_0}{z + W_0} \tag{3.48}$$

This is based on pressure. Hence, based on energy, which is proportional to (pressure) ^{2}, R = $|r|^2$, where R is the energy-based reflection coefficient. Assuming that the sound is only either absorbed or reflected, α + R add up to unity, where α is the energy-based absorption coefficient, thus:

$$\alpha_0 = 1 - \left|\frac{p_r}{p_i}\right|^2 = 1 - \left|\frac{z - W_0}{z + W_0}\right|^2 \tag{3.49}$$

Here, according to equation (3.49), W_o can be replaced by $\rho_o c_o$, the product of air density and sound velocity in air. Equation (3.49) can then be rendered as:

$$\alpha_0 = 1 - \left|\frac{\frac{z}{\rho_0 c_0} - 1}{\frac{z}{\rho_0 c_0} + 1}\right|^2 \tag{3.50}$$

Recalling that $z/\rho_o c_o$ is a complex quantity with a real and an imaginary part, then:

$$\alpha_0 = \frac{4\,\mathrm{Re}\left(\frac{z}{\rho_0 c_0}\right)}{\left(\mathrm{Re}\left(\frac{z}{\rho_0 c_0}\right) + 1\right)^2 + \left(\mathrm{Im}\left(\frac{z}{\rho_0 c_0}\right)\right)^2} \tag{3.51}$$

3.5.5 ACOUSTIC ANALYSIS OF RIGID POROUS MATERIALS

Acoustic absorption is normally attributed to heat generation and dissipation, and also dissipative viscous friction. Increased surface area from surface extension, roughness, pores and more tortuous paths enhance these effects. The Rayleigh model of acoustic propagation is one that simplifies the rigid porous medium as comprising multiple parallel air channels within a similar rigid frame. Using a low-frequency approximation that ignores air inertia and focusing on one cell. Flow resistance (R), defined per unit length of this cell, as pressure gradient divided by average velocity, is given by

$$R = -\frac{1}{\tilde{v}}\frac{\partial p}{\partial x} \tag{3.52}$$

Where v is average velocity. In a medium of viscosity η and a narrow channel of width b,

$$R = \frac{12\eta}{b^2} \tag{3.53}$$

But for a circular section cell of radius a,

$$R = \frac{8\eta}{d * a^2} \tag{3.54}$$

Where d is the material thickness.The flow per unit cross section area per unit time is defined as the Rayl, and the unit of the specific flow resistance is Rayl per cm of cell length traversed. For an element length dx, equating the internal motive force (Mass. acceleration) in the positive direction to the sum of external forces, i.e. net pressure force and flow resistance in the same direction yields $\rho_o$dxda. $\partial\tilde{v}/\partial t = -\partial p/\partial x$. dxda – R $\tilde{v}$ dxda, where cross section area is a, gives

$$\rho_0 \frac{\partial \tilde{v}}{\partial x} = -\frac{\partial \rho}{\partial t} = -\frac{1}{c^2}\frac{\partial p}{\partial t} \tag{3.55}$$

When some flow channel areas are unparallel to sound-impacted material surface a constant called the structure factor, K_s, is introduced. It is defined as the ratio of the unparallel plus parallel channel area to the parallel, and may be used to multiply the medium density to yield an effective density ρ_s. If porosity, Ω, defined as the ratio of total void area to overall area. The motion and continuity equations become

$$-\frac{\partial P}{\partial x} = \rho_0 \frac{\partial \tilde{v}}{\partial t} + R\tilde{v} \tag{3.56}$$

$$-\frac{\Omega}{\rho_0 c^2}\frac{\partial p}{\partial t} = \frac{\partial v}{\partial x} \tag{3.57}$$

The pressure and velocity equations in the case of a harmonic plane wave then become

$$P = \hat{P}\exp\{j(\omega t - \gamma x)\} \quad , \quad v = \hat{v}\exp\{j(\omega t - \gamma x)\} \tag{3.58}$$

Merging the last equations set into the preceding equation gives the equations

$$j\gamma\hat{P} - (j\omega\rho_0 + R)\hat{v} = 0 \quad , \quad -\left(\frac{j\omega\Omega}{\rho_0 c_0^2}\right)\hat{P} + j\gamma\hat{v} = 0 \tag{3.59}$$

Or, setting the coefficients of the amplitude expressions P^ and V^ to null,

$$\begin{vmatrix} j\gamma & -(j\omega\rho_0 + R) \\ -\frac{j\omega\Omega}{\rho_0 c_0^2} & j\gamma \end{vmatrix} = 0 \tag{3.60}$$

$$\gamma = \left(\frac{\omega}{c_0^2}\right)\Omega^{\frac{1}{2}}\left(K_s - i\frac{R}{\rho_0\omega}\right)^{\frac{1}{2}} \tag{3.61}$$

From the earlier definition, the wave impedance becomes

$$W = \frac{p}{v} = \left(\frac{\rho_0 c_0}{\Omega^{\frac{1}{2}}} \right) \left(K_s - i \frac{R}{\rho_0 \omega} \right)^{\frac{1}{2}} \qquad (3.62)$$

The two equations (3.61) and (3.62) may be applied with the appropriate boundary conditions for the solution to many propagation problems. An example is when the medium is a rigid porous material, and the boundary is a rigid wall termination, in which the surface impedance z is now obtained from these two equations substituted back into (3.38) as

$$z = \left(\frac{\rho_0 c_0}{\Omega^{\frac{1}{2}}} \right) \left(K_s - i \frac{R}{\rho_0 \omega} \right)^{\frac{1}{2}} \coth j \left[\left(\frac{\omega}{c_0} \right) \Omega^{\frac{1}{2}} \left\{ K_s - j \left(\frac{R}{\rho \omega} \right) \right\}^{\frac{1}{2}} \right] d \qquad (3.63)$$

Where d is the material thickness, and the acoustic absorption coefficient α can then be obtained by inserting the last equation (3.63) into (3.49).

CHAPTER 4

EXPERIMENTAL WORK

4.1. MATERIALS

In such a work as this, it is although experiments will be augmented by parametric studies, it is essential that a reasonable number of types of materials be tested, so that results pertaining to a broad class of materials may be obtained for better generality of conclusions. For this purpose, a variety of materials, both traditional (for comparisons) and novel, are classifiable into six groups, were tested. They include fabric materials, foam materials, honeycomb materials, monolithic and sandwich materials, periodic cellular material structures, and generally periodic materials. The materials have been chosen, either for their economic importance in the vibro-acoustic industry or for their novelty and promise in the area. Tested fabric materials included basalt, resonated cotton, two types of fiberglass, and polyethylene terephthalate (PET) fiber mass. Two foam materials under development for acoustic containment were supplied by the Kathawate Inc. Company, and respectively named Kathawate magic foam orange, and Kathawate magic foam white. These were expanded in our laboratory oven at 150 degree Celsius from plastic feedstock. In addition polyurethane foam from the Bruel & Kjaer Company was also tested. Seven honeycomb materials of different material or structural characteristics were tested. These were the all-aluminum honeycomb, fiberglass/Nomex honeycomb; cold rolled steel (CRS)/Nomex honeycomb, glass-epoxy/aluminum honeycomb, glass-epoxy/polypropylene (PP) honeycomb.AA5.2-95, epoxy-primed aluminum/aluminum honeycomb.AA3.6-80, and phenolic coated polyester/Aramid (Nomex) core honeycomb. The class of monolithic and sandwich constructions included the Lexan, and cold-rolled steel monolithic as well as CRS//hard foam

and steel/polypropylene (USIL Light) sandwiches. Three periodic cellular material structure (PCMS) materials from Cellular Materials International (CMI) Inc. were also tested. The rationale for choosing this group of materials is that they are novel, multifunctional, and have not been tested for vibro-acoustic applications yet. Applications to heat transfer, conduit, structural, and other applications have been explored and adopted. The materials are the aluminum prismatic Microtruss, the aluminum pyramidal Microtruss, and the stainless steel triangular honeycomb PCMS. The general periodic materials tested were the single row Micropillars with resonators, the double row, in-line Micropillars, and the double row, staggered Micropillars.

4.1.1 FABRIC MATERIALS

Five different materials from this category were selected, figure 4.1 below shows pictures of those materials.

Figure 4.1: Tested fabric materials

Basalt is a hard, black volcanic rock with about 52% silica (SiO_2) basalt fiber by weight. Basalt rock is a fine-grained mixture of minerals with slight different chemical compositions. Basalt commonly contains olivine, pyroxene, plagioclase and some trace minerals. Resinated cotton is

bonded acoustical cotton, with panels normally available in 3 lb. or 6 lb. per cubic foot densities, and various area sizes. They are both flame and noise resistant. Fiberglass is used as for acoustic absorption, considered effective, especially at high densities and thicknesses from 2 inches upward. The geometrical properties of the samples tested are shown in table4.1 below, taking into account that all the samples are 100mm diameter. Polyethylene terephthalate plastic fibers have been found to be one of the better plastic materials to deploy in automotive acoustic abatement.

Table 4.1: Fabric materials properties

Material	Weight(gram)	Thickness(mm)	Density(kg/m^3)
Basalt	15.7	12.7	157
Resinated cotton	24.68	17	184.84
Fiberglass	4.05	9.5	54.36
B&K Fiberglass	22.35	27	105.4
B&K PET	3.91	18	27.65

4.1.2 FOAM MATERIALS

The foam material, by its unevenness and porosity, naturally yields much larger effective areas (some products claim about 400% and upwards) for sound mitigation than plain, smooth surfaces, and also permits sound signals to sink to various depths. Soft polyurethane is well known to generally control noise propagation. The two proprietary foams tested came from the G. R. Kathawate Inc. company, and are being developed for sound control, based, according to them, on the construction of the surface properties of the materials, figure 4.2 and table 4.2 below shows pictures and geometrical properties of the samples tested respectively.

Figure 4.2: Tested foam materials

Table 4.2: Foam materials properties

Material	Weight(gram)	Thickness(mm)	Density(kg/m3)
B&K Polyurethane foam	7.35	32	29.24
Orange magic foam	11.47	7.5	194.72
White magic foam	24.64	11	285.20

4.1.3 HONEYCOMB MATERIALS

Seven honeycomb structures were tested as shown in figure 4.3 below. The honeycomb construction is a good candidate for sound reduction because it greatly multiplies the contact area. The constituent materials of skins and core are of metal, plastic and specialized paper like aramid in the tests performed.

Figure 4.3 Tested honeycomb materials

Table 4.3 below shows the properties of honeycomb materials, the Young's modulus, and Poisson's ratio have been gotten through curve fit approach, the values showed good match between experimental and finite element simulation. For those cases where no property value was available, the curve fit approach consisted in interpolating trail values until a mach with experiment was achieved. This was done using the finite element method. We resorted to this approach after failing to obtain these values from exhaustive literature search, coupled with persistent and diligent inquires from several companies.

Table 4.3: Properties for Honey comb Materials

#	Panel ID	Skin	Core	Cell Size(inch)	Weight (gram)	Total Density (kg/m3)	Young's Modulus (Mpa)	Poisson's ratio
1	AA5.2-95 (A)	Glass epoxy t=0.018"	Aluminum Honeycomb ρ=5.2pcf	1/4	28.34	48	2438	0.4
2	PP5.0-90 (B)	Glass epoxy w/peel ply t=0.014"	Polypropylene Honeycomb, ρ=5 pcf	1/4	29.5	47	1100	0.28
3	AA3.6-80 (C)	Aluminum epoxy primer finish(t=0.02")	Aluminum Honeycomb, ρ=3.6pcf	3/8	26.1	140	2100	0.35
4	PN1-1/8-3.0 (D)	Polyester	Aramid Nomex	1/8	17.5	89.5	2250	0.25
5		Aluminum (0.032",0.02")	Aluminum	3/8	40.8	130.65	2000	0.4
6	303	Fiberglass (0.01")	Nomex Honeycomb	1/4	21	52.86	1800	0.37
7*	-	CRS(0.024")	Nomex Honeycomb	-	79.25	179.76	-	-

*: this material was not simulated using Finite element according to the thickness of the core.

4.1.4 MONOLITHIC AND SANDWICH MATERIALS

This group encompasses the cold rolled steel (CRS), Lexan (a polycarbonate plastic) as monolithic materials, where, CRS with LE5208 foam, and USIL light (trade name) which is a steel skins and thin polypropylene core are the sandwich materials (figure 4.4).

The Lexan material was tested in many structural forms, including simple solid, multi-layer solids, disks with holes of different sizes, and layered structures of some combinations of these.

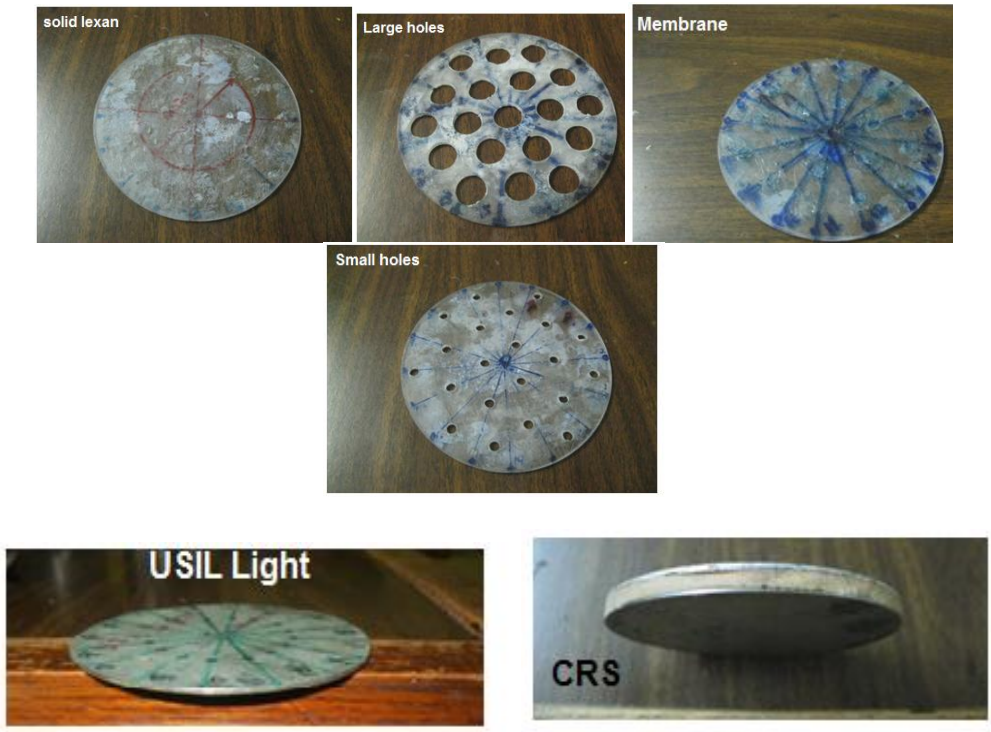

Figure 4.4: Tested monolithic and sandwich materials

Table 4.4 shows the properties of those materials.

Table 4.4: Properties of sandwich and monolithic materials

Material	Density (kg/m^3)		Young's Modulus(Pa)		Poisson's ratio		Thickness (mm)		Mass(gram)
	Skin	core	Skin	core	Skin	core	Skin	core	
CRS w/LE5208	7870	800	205e9	1.35e9	0.29	0.27	0.75	5	128
USIL Light	7870	1990	205e9	12.85e9	0.29	0.26	0.375	0.75	38.2
Lexan	1200		2350e9		0.375		2.2		21

4.1.5 PERIODIC CELLULAR MATERIAL STRUCTURES (PCMS) MATERIALS

PCMS are multifunctional materials often used as cores of general honeycomb structures. They are usually made of struts (tetrahedral, pyramidal, etc), prismatic (triangular, square, hexagonal, etc.), and shell (egg-case, etc.) types of elements. The three types tested are shown in Figure .they have great functional and economic importance and have started to be utilized by the military (ONR/US Navy) and industrial interests. Their multi functional uses have been applied for heat exchanger constructions [69][70]. Figure 4.5, and table 4.5 below shows those materials and their properties respectively.

Figure 4.5: Tested periodic cellular material structures (PCMS) materials

Table 4.5: Properties of PCMS materials

Material	Density(kg/m^3)	Young's Modulus(Pa)	Poisson's ratio
PCMS Aluminum	2700	68.9e9	0.33
PCMS Stainless Steel	800	200e9	0.29

4.1.6 GENERAL PERIODIC MATERIALS

There is an almost infinite number of ways to construct these structures, which basically manifest regular periodicity in their arrangement. This confers on them some response behaviors in case of mechanical, acoustic, and various other types of excitations. We tested three micro-

pillars structures in this category, and they are shown in figure 4.6 below. Although this research doesn't include analysis of the vibroacoustics of meta materials ,this work gives experimental results for these constructions which constitute candidate meta materials .If we can tune the masses and springs appropertly we should get the negative effective mass , effective stiffness and band gaps which normally characterize meta materials ,this aspect is being reserved for a future research. The micropillars are made of nylon 66 cylinders, and the metal parts are of mild steel, including the masses (nuts) of the internal mechanical resonators in the first case. The properties of these materials are shown in table 4.6 below.

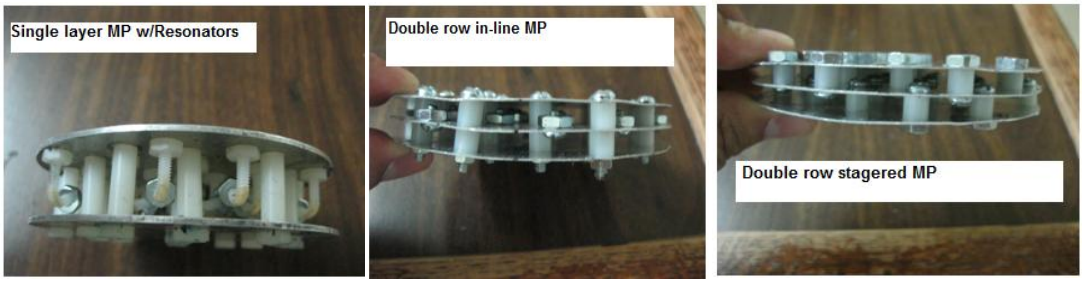

Figure 4.6: Tested general periodic material structures

Table 4.6: Properties of general periodic material structures

Material	Young's Modulus(Mpa)	Density(kg/m$^{3)}$	Thickness of skin(mm)	Poisson's Ratio
Nylon 66	811	645	Dia(2.5)	0.4
Mild Steel	210000	7880	Dia(4)	0.3
Aluminum 6061T	68900	2700	1.54(sample1) 0.43(sample 2 and 3)	0.33

4.2 APPARATUS

In both cases of vibration and acoustics testing, the core of the system was the computerized "PULSE" vibration and acoustics hardware and software system, made by Bruel &

Kjaer Company [71]. It's most recent software PULSE 16.0 was utilized. Later the PULSE Reflex 16.1 was adopted as it became available from B&K.

4.2.1 VIBRATION TEST APPARATUS

The vibration test apparatus consists of the PULSE front end which contains the channels that connect the cables for both the force and acceleration transducers, the accelerometers and hammers used in the experiments were from Bruel& Kjear Inc., and PCB Piezotronics Inc, the range of those accelerometers is from 0 up to 50 kHz to cover complex structures that have high natural frequencies, those accelerometers were calibrated according to the manufacturer recommendations, the front end is connected to the computer through an ether net cable and it has its own IP address, the PULSE software was installed on the computer for post processing the data collected from each experiment. All these components are shown in figure 4.7 below

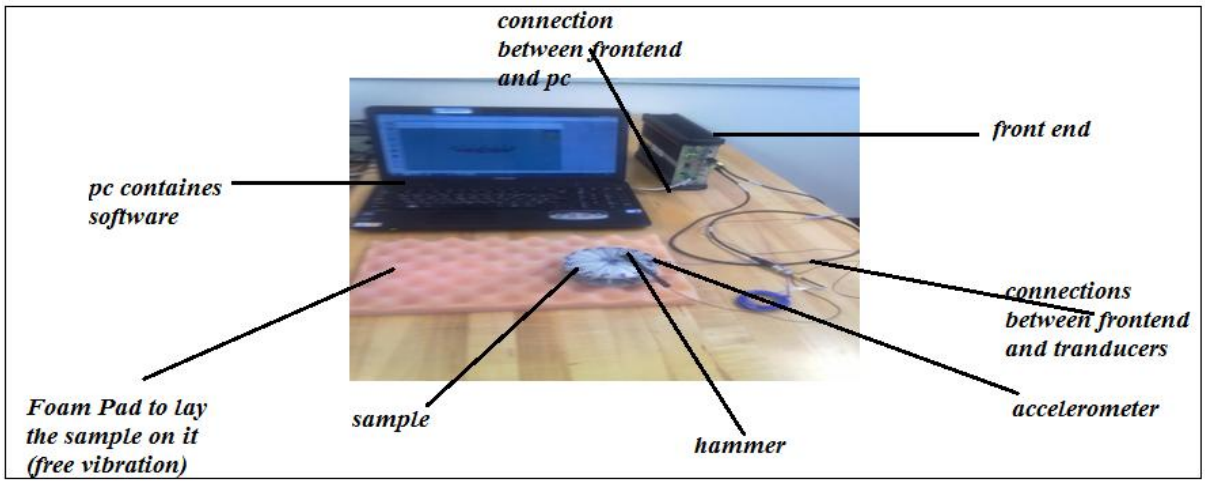

Figure 4.7: Vibration test apparatus with its components

A sketch is shown in figure 4.8 below to demonstrate the different components and how they are connected together, the geometry which we draw inside the software to indicate a circular disk with the transducers on it is shown in figure 4.9 below, the hammer is shown at each point to

indicate that the experiment was done with a roving hammer at each point while the accelerometer is fixed at a specific point.

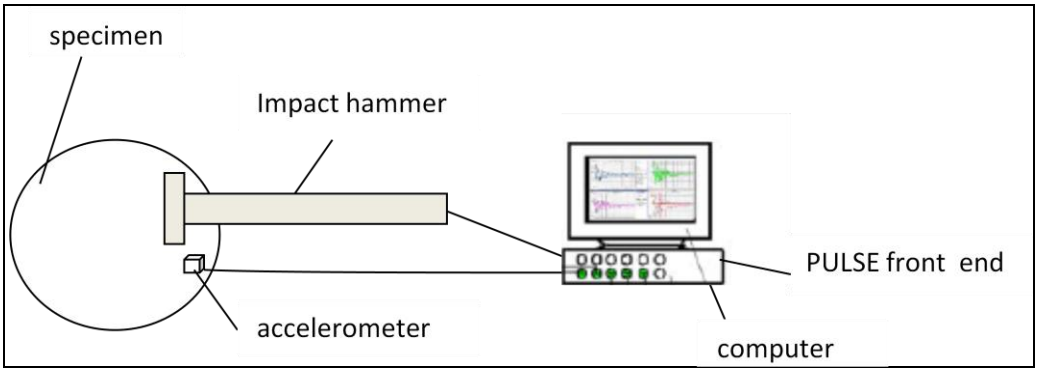

Figure 4.8: A sketch for the vibration apparatus

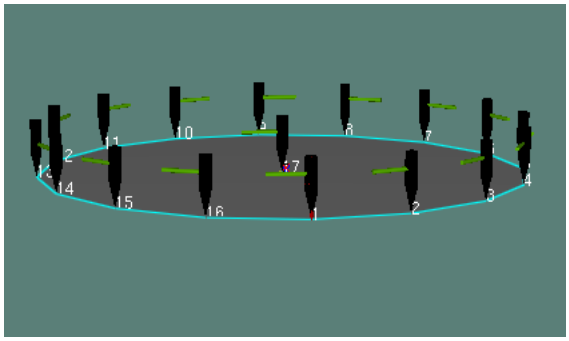

Figure 4.9: Geometry drawn inside PULSE, the hammer is roving, while accelerometer is fixed at point1.

4.2.2 ACOUSTICS TEST APPARATUS

The acoustics apparatus contains the PULSE front end and the computer for the data processing, as mentioned before for the vibration apparatus, however the acoustics one includes the impedance tube in which the sample is fixed inside ,this tube has two types, the large one which is shown in figure 4.10 below, this is 100mm diameter and is used to calculate the sound absorption in the low frequency range(0-1.6 kHz), the other part is the small tube which is used

to measure the sound absorption in the high frequency range(500 Hz-6.4 kHz), the other part of this apparatus is the power amplifier which is used to generate a sound signal inside the tube ,also it contains knobs to calibrate the gain and the current levels .

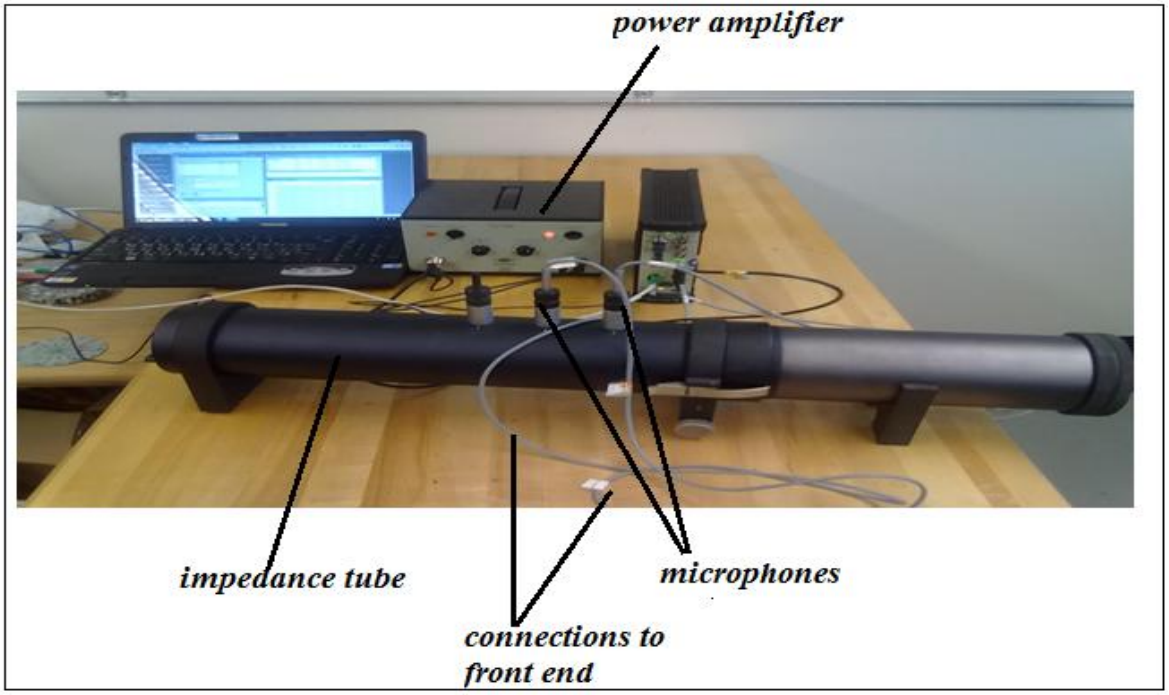

Figure 4.10: Acoustic test apparatus

To demonstrate the impedance tube from inside, figure 4.11 shows a cutaway of this tube, it is clear that there is an incident acoustic wave and a reflected acoustic wave, the software is capable of calculating the sound absorption coefficient according to these values as it will be shown later.

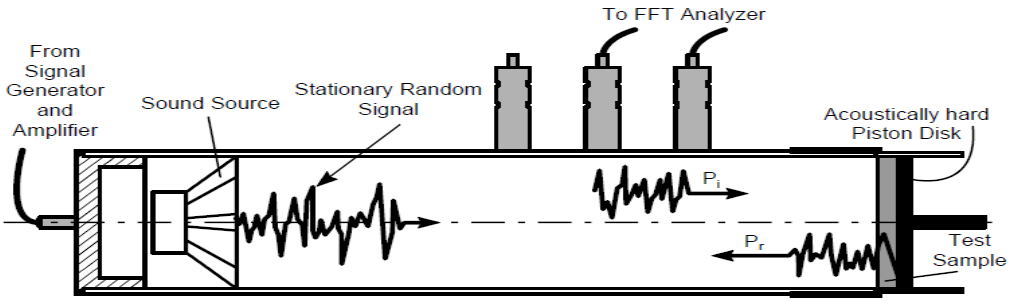

Figure 4.11: Cut-away diagram of the impedance measurement tube, showing the incident and reflected components of the stationary-random signal

The "PULSE" 16.0 vibro-acoustic instrumentation and software platform was utilized in our experiments, along with the impedance tube, from Bruel &Kjaer, Inc. The tube utilized was the B&K Two-Microphone Impedance Measurement Tube Type 4206, fitted with two specially designed ¼-inch Microphones Type 4187 with preamplifiers [72]. Specimens of diameters 100mm and 29 mm were cut from each material for acoustic absorption tests, and the larger samples were also subjected to impact response vibration tests. Results were obtained from experimental, analytical and numerical approaches. Figure 4.3 shows the essential parts of the experimental setup.

4.3 EXPERIMENTAL TEST PROCEDURES

4.3.1 VIBRATION TEST PROCEDURE

Although, PULSE comes with numerous built-in setups for measuring various situations, for example modal test consultant [73] is a powerful template performing modal analysis. It is important to understand how to setup these templates, so that the user can understand how to modify these pre-set configuration if necessary, or how to set up templates that are not provided.

The test procedure is as follows [74]:

1. Go to the start menu and select programs, PULSE, applications, modal analysis and MTC hammer as shown in figure 4.12.

Figure 4.12: the first step in opening modal analysis application from PULSE

2. The following screen(figure 4.13) will open in which , the roving hammer option is selected

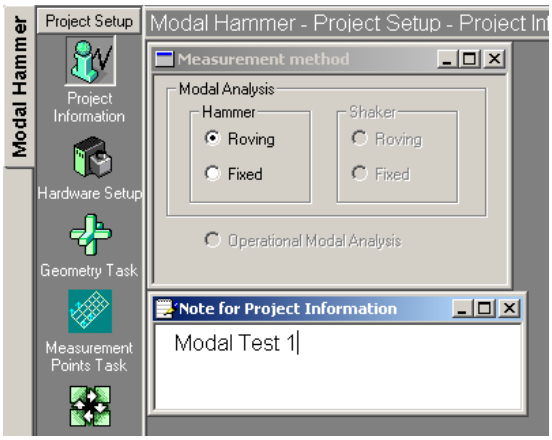

Figure 4.13: Selection of roving hammer test

Either the hammer or response accelerometer(s) can be ‘roved’ from location to location. The most common setup is a roving hammer test where the accelerometer(s) stays in one fixed location and the hammer is roved.

3. PULSE automatically detects whether or not the connected data acquisition equipment matches the saved configuration. If the hardware is different, PULSE prompts the user to reconfigure.

4. When you click the hardware setup window, detect TEDS (transducer electronic data base) appears, as shown in figure 4.14, which checks for and automatically configures TEDS transducers on all channels but keeps the existing setup for channels with non-TEDS transducers. It is important to mention here that most force sensors and impact hammers do not have TEDS; in this case any non-TEDS channels are cleared and must be manually reconfigured. To do this, in the configuration tab, we add any non-TED transducer to the system by inputting the data related to this transducer like sensitivity, weight, serial number, and then saving it in the database.

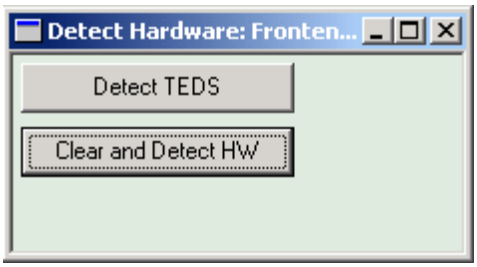

Figure 4.14: Detection of Transducer electronic database

5. In the geometry window we insert the dimensions of the geometry we want to test, then insert the number of points we want to hit, in our case we plot a circle with 17 points, then we should assign a transducer for each point, In this case each point gets one hammer hit, The transducer (accelerometer) is located at point 1.

6. In the measurement sequence task, a complete measurement plan is found. For each measurement, both excitation and response point and direction are indicated. The sequence is editable by the changing point numbers for a measurement, as was shown in figure 4.9 before.

7. In the analyzer setup task, select the number of impacts that will be made at each location by setting the number of averages in the modal FFT (fast Fourier transform) analyzer window. Set the averaging mode to linear.

8. In the hammer setup task, choose the trigger level setup in the hammer view as shown in figure 4.15. Press the **activate** button, and wait for the system to activate.

Figure 4.15: Trigger level setup selection

Then, press the **start** button, to start the hammer recorder. Impact the structure several times with the same force level to be used during the test as shown below. The trigger level can be graphically set by moving the blue line up or down as shown in figure 4.16 below.

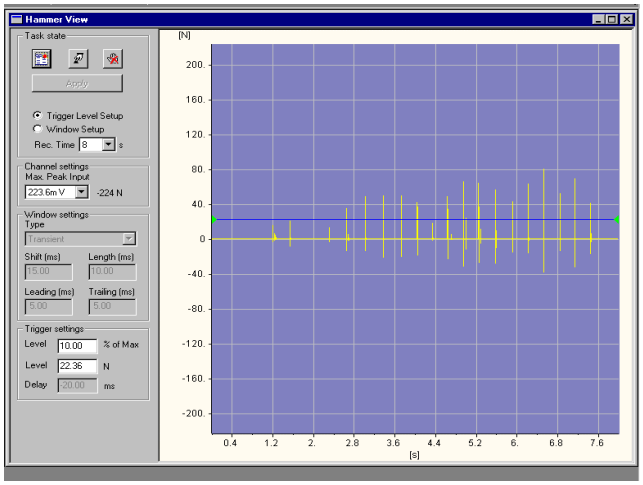

Figure 4.16: Setting the trigger level manually

9. In the response setup task, press the **activate** button, and wait for the system to activate. Press the **start** button. Impact the structure with the same force level to be used during the test. The response window can be graphically set in the response view. A uniform window is the preference for impact testing since it does not affect damping like an exponential window, as shown in figure 4.17.

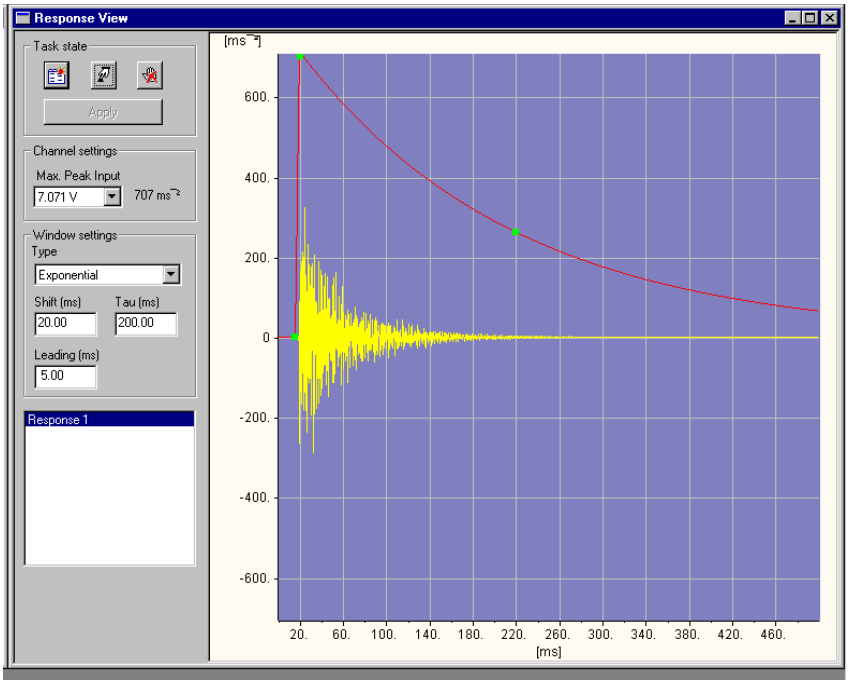

Figure 4.17: Response window shows the signal decay with time

10. In the measurement task, press the activate button, and wait for the system to activate. When a measurement is selected in the measurement control window, the geometry window shows where to place the accelerometer(s) for that measurement. Press the start button, to start the generator and analyzer. The average monitor indicates the number of averages during the measurement. When the measurement is finished, press the Save button to proceed to the next measurement. Click on the measurement number in the measurement to view results from

different measurement. Measurement can be taken by selecting the measurement tab, pressing start and then save.

4.3.2 PULSE REFLEX™ MODAL ANALYSIS

PULSE Reflex is the latest addition to the PULSE platform of software products by Brüel&Kjær [75]. It provides post-processing in a modern, intuitive GUI (graphical user interface) environment and it resolves the most important issues when analyzing sound and vibration data.

PULSE reflex modal analysis is an efficient workflow with just a few steps to perform a complete

Modal analysis, i.e., modal analysis based on hammer and shaker testing. It allows the user to observe, analyze and document the dynamic behavior of structures and provides accurate and reliable results.

It is an easy-to-use post-processing application that enables the user to perform Classical Modal Analysis even in the most demanding situations by using a set of best-in-class mode indicator functions, curve-fitters and validation tools. Accurate results are quickly obtained by following an intuitive and flexible workflow process that guides the user efficiently through measurement validation, parameter estimation setup, mode selection, analysis validation and reporting.

The steps included in PULSE Reflex Modal Analysis are [75]:

1. Geometry creation and import

Geometry can be imported in standard data formats like UFF, DXF and CSV from PULSE hammer test; alternatively, geometries can be created from scratch using the embedded drawing tools. The measurement DOFs (degrees of freedom) contained in the imported measurement files

are automatically added to and shown on the geometry in the subsequent tasks as shown in figure 4.18.

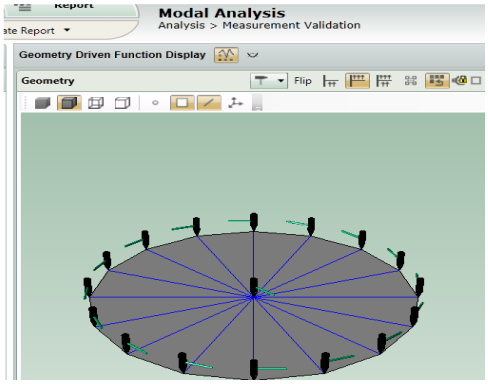

Figure 4:18: Geometry imported from PULSE to Reflex

2. Measurement validation

The Measurement validation task is used to check the quality of the measurement data prior to performing the modal parameter extraction. Functions like Coherence, FRF (frequency response function), from selected references can easily be shown by simply dragging the functions from the Project Browser.

The Geometry Driven Function Display provides a graphical tool that allows the user to select on the geometry the DOFs that are to be used for the displayed function types. Figure 4.19 shows the measurement validation step

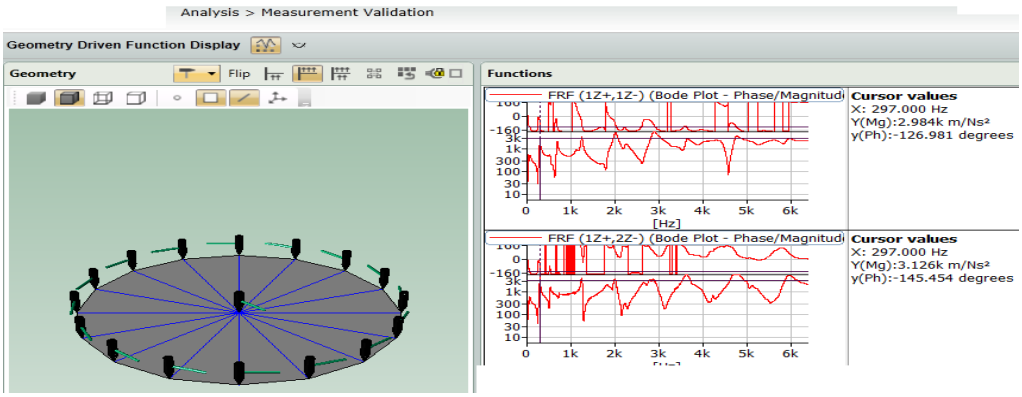

Figure 4.19: Measurement validation step in Reflex

3. Parameter estimation setup

The parameter estimation setup task is the step where the preparation and execution of the curve-fitting occurred. FRF data to be included in the analysis are easily filtered, sorted and then selected. In the same screen layout, the geometry with DOF information is shown together with a graph area for investigating potential modes using different Mode Indicator Functions. Various SDOF (single degree of freedom system) and MDOF (multi degree of freedom system) curve fitters can be selected and the frequency range of interest can be set. The unique enhanced mode solution algorithm provides very clear stability diagrams, making it easy to discriminate true physical modes from non-physical modes. Figure 4.20 shows this step.

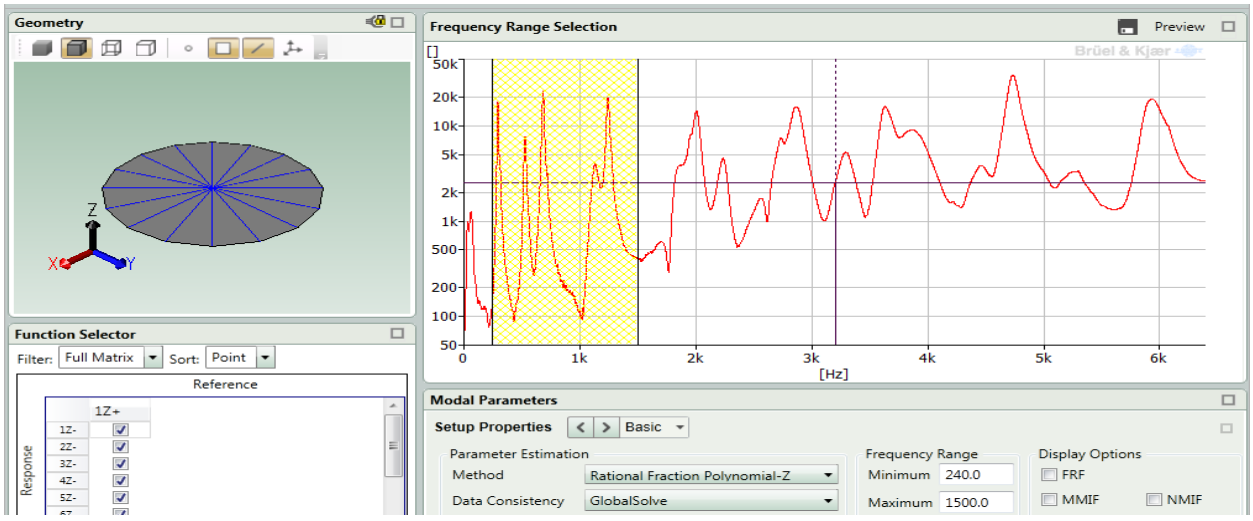

Figure 4.20: Parameter estimation setup in Reflex (auto selection of frequency range)

4. Mode Selection

In the mode Selection task, includes the modal results shown in terms of natural frequency, damping ratio, and mode shape animation (figure 4.21). Once a mode is selected, it will immediately show up in the Mode Table, the mode will be animated and the synthesized FRF's (frequency response function) will be compared to the measured ones. Automated mode

selection is supported for fast preliminary investigations of unknown structures or when conducting repetitive testing. It also eliminates the potential risk of user-dependent results. Automated mode selection works for all MDOF curve-fitters by indicating the modes in the stability diagrams, populating the mode table, animating the first mode and showing the synthesis functions. The Mode Selection task provides full flexibility for selection and comparison of modes from different curve fitting.

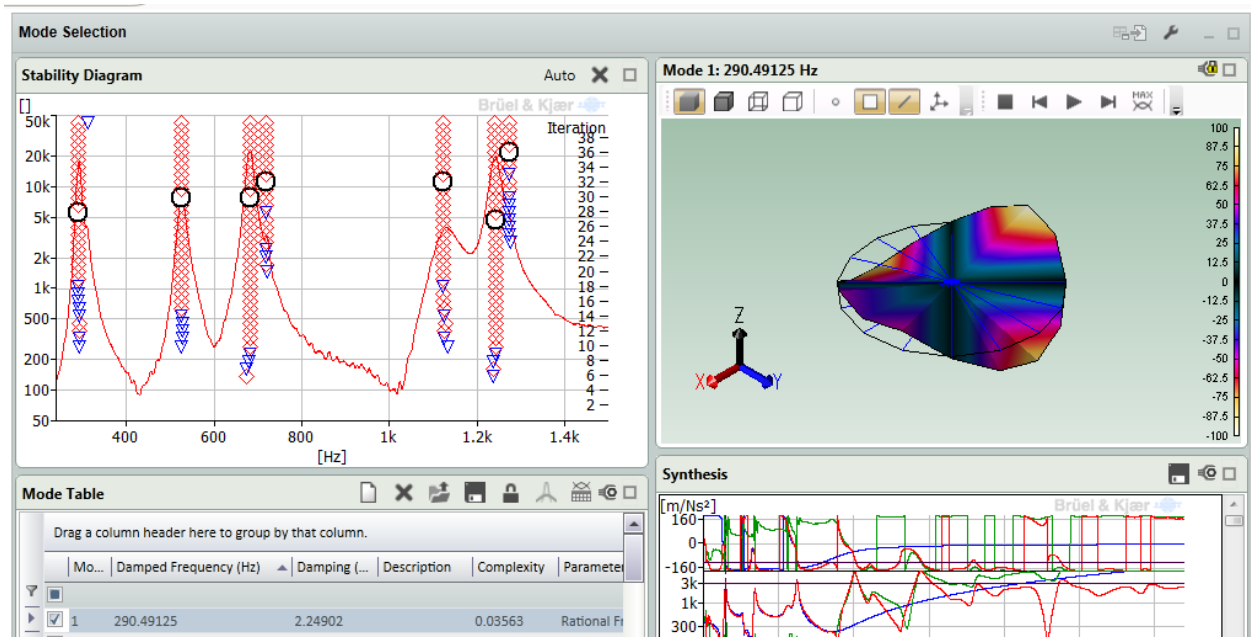

Figure 4.21: Mode selection in Reflex (natural frequencies and mode shapes)

5. Analysis validation

The analysis validation task (figure 4.22) supplies the user with a number of tools for further investigation of the obtained modal results for maximum confidence in the obtained modal model like Mode Shapes Animation, and AutoMAC (modal assurance criterion) tables.

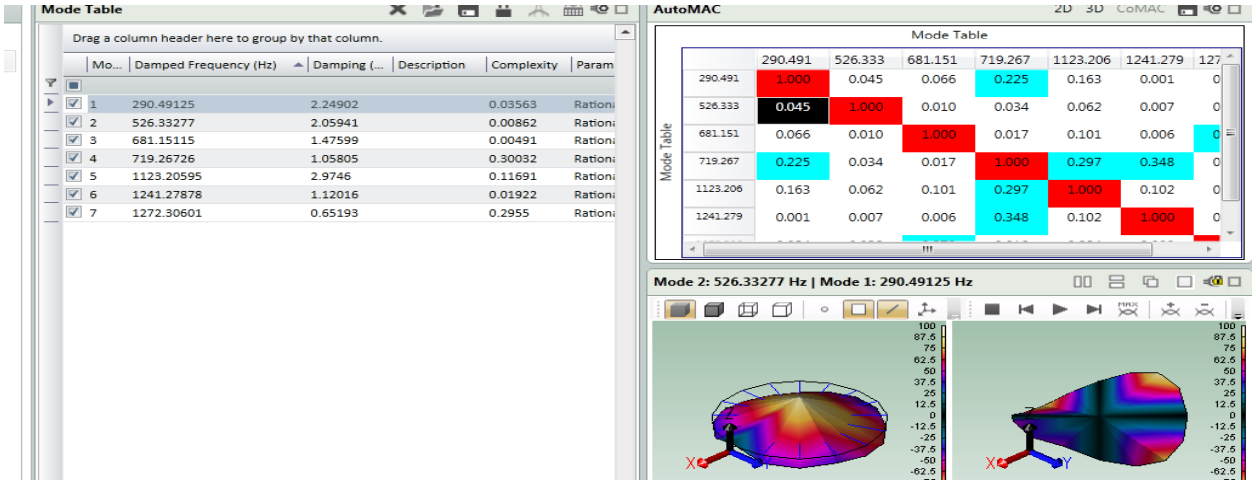

Figure 4.22: Analysis validation includes the first two modes.

6. Reporting

The report task enables reports to be prepared in parallel with the analysis process, linking important results as they are produced. Store geometries, displays, tables and text in the project browser as report elements so when you are ready, you only need to generate and save the report. Reports are easily created directly in Microsoft word, Excel or PowerPoint.

.

4.3.3 ACOUSTICS TEST PROCEDURE

The two-microphone acoustic impedance measurement tube type 4206[72] is used in measuring the acoustic absorption coefficient, acoustic reflection coefficient and normalized impedance there are many others but we are mainly interested in the acoustic absorption coefficient although the resolution gets poor with the higher frequencies and frequency bandwidths. It takes quick measurements over a large frequency range. It is software-controlled and the data is easily manageable. It is used to measure complex or composite materials, laminates, alloy materials and etc. It can be also used to measure the acoustic properties of the material that are sensitive to orientations.

The two-microphone impedance tube uses two specially designed ¼ inch microphones with preamplifiers. It has a Bruel and Kjaer dual channel signal analyzer embedded in PULSE. There are three types of tubes available in two-microphone impedance measurements tube of type 4206. We use two, one is a large tube, which is also called low-frequency measurement tube as it measure frequency ranging from 50 Hz to 1.6 kHz. It has three couplers for mounting microphones flush with the inside of the tube. The second is a small tube also called high frequency measurement tube and its frequency range varies from 500 Hz to 6.4 kHz. It has two microphone couplers which are mounted directly on to the open end of the large measurement tube. There is a large and a small sample holder and both have an acoustically hard back-plate, which is connected to a sliding piston. The types of frequency weighting unit are according to the type of tube (large/small) used and the accuracy needed for the measurement of the parameter. They are high-pass, low-pass and the linear pass. High pass is used with small tube and for high frequency measurements. The linear is used with large tube for low frequency measurements and for the extra measurement accuracy below 100 Hz the low pass is recommended.

The sequence for preparation is:

i. Connect amplifier to impedance tube filter using 2 banana plugs

ii. Set noise generator, amplifier, and filter characteristics to specifications desired

iii. Screw microphones onto impedance tube

iv. Connect the microphones to the front end and choose channel 3 to microphone 2 and channel 4 for microphone 3.

v. Open the PULSE software and choose from applications the acoustic material testing in tube, then choose the normal incidence absorption.

vi. Go to project setup in the PULSE window and choose “connect signals” to insure that the microphones are connected adequately to the front end.

Procedure followed for the measurement in both large and small tube:

1. Once the setups are done the test is run on the calibration sample and the sensors are calibrated. At this time we have already got calibration curve for use with both the large and small tubes and this can be saved in directory and then it can be directly utilized in future whenever we want to take test on other material samples instead of calibrating the instrument again.

2. Now place the test sample inside the tube and make sure it is exactly aligned with the inside of the tube with no air gap between rigid backup plate and the sample holder. If there is an air gap, remove it by adjusting piston position to and fro.

3. Start the measurement.

4. The analyzer generates a random signal, which is then amplified by power amplifier and frequency weighted by frequency weighting unit in the tube and then applied to the sound source. The analyzer then measures the frequency response of the two microphones channels and calculates H_1 frequency response function. From the incident and reflected components of the sound pressure at the two microphone positions, PULSE calculates the H_1 frequency response functions, H_i frequency response functions associated with incident component and H_r frequency response functions associated with the reflected component.

5. Read off or save the results.

The PULSE system is able to obtain several parameters including the reflection coefficient, the absorption coefficient, normalized impedance, frequency response function, and calibration data each with magnitude, phase, real and imaginary part etc. The post-processing facilities of

the PULSE may then be requested to present the results for any of the parameters in various graphical, data or tabular forms. Data export to Excel may also be utilized to plot results in several ways.

For example, using frequency response functions, the reflection coefficient R, is calculated internally in PULSE from the expression.

$$R = \left(\frac{H_{12} - H_i}{H_r - H_{12}} \right) e^{j2k(l+s)} \qquad (4.1)$$

Where k is wave number, s is distance between two microphones and *l* is distance between the first microphone and the material sample.

Using value of reflection coefficient, the normalized impedance and acoustic absorption is also found from the expressions

$$\frac{z}{\rho c} = \frac{1+R}{1-R} \qquad (4.2)$$

$$\alpha = 1 - |R|^2 \qquad (4.3)$$

The two-microphone theory assumes plane-wave propagation, no mean flow and no losses due to absorption at tube wall. For the accuracy of the measurement we can rotate the sample by 90 degree every time and take four different measurement for circular sample and then using the post processing tools to find the mean curve of all the four curves and the resultant mean curve will be the most accurate curve of the parameter being measured.

The PULSE software has excellent post processing features like combination of measurement data in overlapping frequency ranges, simultaneous graphical display of several

sets of measurement data, averaging of up to ten sets of measurement data and data file management on hard or floppy disk and hard copy facilities in tabular or graphical format.

CHAPTER 5

NUMERICAL WORK

5.1 CALCULATION

The formula derived for the natural frequency of the vibrating circular plate is applied, using the tabulated values for the constant α as given in equation 3.33. The frequencies for different modes are obtained by choosing the value of this constant that corresponds to each mode desired, which is itself identified by the numbers of modal diameters and nodal circles respectively. The lowest value of alpha applies to the first resonance mode, the next one to the following mode, etc. The following example for single layer solid Lexan illustrates these points, the value for each parameter is shown on the left of the specific parameter, the equation used in these calculations is:

$$\omega = \frac{\alpha}{R^2}\sqrt{\frac{D}{\rho h}} \qquad (3.31)$$

where:

ω: Angular frequency (rad/sec)=$2\pi f$ (f in Hz)

α : Modal vibration constant

R: plate radius in (meter). 0.05 m

D: Flexural rigidity in (N.m), 1.823 N.m

E: Young's modulus of elasticity (in Pa), 2.35e9 Pa

h: Plate thickness in (meter) ,2.2e-3 m

ν :Poisson's ratio, 0.375

ρ: Material density (kg/m^3), 1200 kg/m^3

Table 5.1 shows the first three natural frequencies for single layer solid Lexan.

Table 5.1 Calculated Natural frequencies for Solid Lexan

Mode #	α value	# of nodal diameters	# of nodal circles	Natural frequencies(Hz)
Mode1	5.252	2	0	$f_1=320$
Mode 2	9.076	0	1	$f_2=553$
Mode 3	12.25	3	0	$f_3=746$

5.2 FINITE ELEMENT

Finite Element Analysis (FEA) is considered as a numerical method to provide solutions to many engineering problems that couldn't be solved manually. In 1943 R.Courant used Ritz method to obtain an approximate solution for some vibration problems [76].

FEA consists of a mathematical model of a material or design that is analyzed for specific results, in this application the results are the natural frequencies, and mode shape. In finite element method the structure under study is divided into very tiny elements connected together by nodes .The preprocessor and post processor were Hypermesh version 10 from Altair Engineering Inc, the solver used was Abaqus standard 3D. The algorithm used in this solver was Lancsoz Eigensolver Method to calculate the fundamental frequencies and the corresponding mode shapes related to each frequency as this method is considered a powerful tool for extraction of the extreme eigenvalues and the corresponding eigenvectors of vibration problems in engineering [77]. It uses interpolation methods to extract mode shapes and natural frequencies for mechanical structures with complex geometries.

The samples are considered as solid. According to the complexity of some structures like PCMS and Honeycomb, the Unigraphics software was used to draw these geometries, and we then

imported them to hypermesh in which the geometry was meshed and the material properties were plugged inside the software .The element type is really significant in ABAQUS software to obtain accurate results and it depends upon the mesh style used for each case. The element types for each case will be shown later on, as an example the C3D20R quadric element type, which is the second order of the C3D8R quadric element type, is used in some of the simulations. This element type allows us to increase the integration points on each element and to obtain more accurate results. The boundary condition which we consider in this simulation is the completely free boundary conditions. Hypermesh post-processor is used to show the natural frequencies, displacements, and mode shapes. The results showed a very good agreement between the experimental results from PULSE Reflex and Abaqus finite element analysis as we will see later. It should be mentioned here that the license which we have at Wayne State University is limited to 100000 nodes. On the other hand the thickness of some structures like Nomex was so thin that the software was not able to mesh it. The second finite element analysis solver used was Radioss in which the frequency response function was calculated using the fast Fourier transform, the most important point in this simulation is the capacity of the processor (CPU) of the computers which we have in our lab, the accuracy of results in this solver depends strongly on the frequency step length used, the lesser the better. Also the number of nodes selected to show FRF is important - in this case the more the better. We got some good results that show a match between experiment and simulation for some materials. However the simulation took around 2 weeks in some cases where the geometry is heavy.

The selected frequency range was different from case to case depending upon the experimental results. The maximum value selected was 24 kHz for PCMS materials, and the number of elements (type PSOLID) used exceeded 450000 in some cases. The material properties, Young’s

modulus (E), Poisson's ratio (ν) and mass density (ρ) were inserted and the geometry with no constraints (representing completely free boundary conditions in the vibration) were input. The work was saved, and the solver was then accessed to compile the work and obtain the results. It should be emphasized here that the material properties for honeycomb samples were difficult to get either from the company or the literature, so the curve fit approach was used to get approximate values for these properties. After an interpolation and extrapolation, we succeeded to get values that showed a reasonable match between experimental and simulation results for these materials. This approach of reverse engineering may be modified in the future to get even more accurate results.

The particulars and procedure to calculate vibrations parameters for the plate are summarized below to calculate the eigenvalues (natural frequencies) and eigenvectors (mode shapes) for circular plates is:

- Pre- and Post-Processor: Hypermesh (Version 10 from Altair Engineering Inc.)
- Solver: Abaqus standard 3D, and RADIOSS
- Selected frequency range: 0 to 24 kHz
- Elements Type: PSOLID
- Number of elements: 10000-470000
- Mesh Style: It depends upon structure
- Solver: Lanczos Eigen Solver (for normal modes)
- Procedure:

For the RADIOSS solver[78] which was used to extract the frequency response function (FRF), for a specific material, again in the preprocessing stage, the geometry was constructed, then the material properties were assigned for the geometry, the frequency range of interest was chosen, a specific dynamic load was put on the structure at a specific node and direction. The frequency resolution (df) is inserted for the purpose of fast Fourier transform (FFT) calculations. It proved

difficult to use very small values of this variable because of limited CPU (central processing unit) capacity. On the other hand a small number of nodes were selected in order to see the FRF of the structure through them. Increasing the number of selected nodes will show better results as one or more of these nodes my lie on a nodal line or circle, but there was no ability to increase this number due to limited processor capabilities. However the results obtained were acceptable.

5.3 MATLAB

The Matlab simulation system was also used to solve the vibration problem, in order to have assurance of accuracy among several methods. The vibration toolbox was used to insert the values of the plate radius, thickness, Young's modulus, and Poisson's ration. The functions "Plate_Pars", and "cirplate" from the command window were used to calculate the plate frequencies. The function "plotmsh4(m,n) , where m represents the number of nodal diameters and n the number of nodal diameters and n the number of nodal circles, was used to plot the mode shape of any specific mode. The function ANIMODE4(m,n) was used to animate any mode shape desired, The completely free boundary condition was realized by setting " BC_Spec" (an integer specifying the boundary condition) to zero..

The Handbook "Stress, strain and structural dynamics" [79] was utilized in writing the Matlab computer program to calculate the natural frequencies of the circular plates and animate their mode shapes. Appendix B contains the code for calculating these modal values for solid Lexan. A stepwise procedure is:

- Vibration toolbox: used to insert the values of the plate radius, thickness, Young's modulus, and Poisson's ration).

- Functions: “plate_pars”, & “cirplate”: used from the command window to calculate the plate frequencies, while, “plotmsh4 (m,n)” , (where m represents the number of nodal diameters and n the number of nodal diameters and n the number of nodal circles): is used to plot the mode shape of any specific mode. The function“animode4(m,n)” is used to animate any mode shape desired, the completely free boundary condition was realized by setting m and n. Finally the function “bc_spec” (an integer specifying the boundary condition) is set to zero to describe free boundary conditions.

CHAPTER 6

RESULTS AND DISCUSSION

6.1 INTRODUCTION

The results of both acoustic and vibration tests on the tested samples are now given. The samples may be categorized into (a) Fabric materials, (b) Foam materials, (c) Honeycomb materials, (d) Monolithic and Sandwich materials, (e) Periodic cellular material structures (PCMS) materials, and (f) General periodic materials.

6.2 ACOUSTICS RESULTS

There are two models for acoustic absorption [80], i.e., the equivalent fluid model and the sophisticated or the Biot theory. The former assumes that the sound absorption material is isotropic in mixed flow and the sound propagation is determined by two complex quantities - characteristic impedance (W_0 for air flow), and wave number ($k=\omega/c$, where ω is the frequency and c is the speed of sound in the medium). In the later, the absorption material is assumed to be a linear elastic solid frame with numerous randomly distributed, small, inter-connected, pores and the fluid is assumed to be Newtonian, viscous, and incompressible. The fluid inertia and friction are characterized with density, viscosity, and pore dimension. The issue of absorption coefficient dependence on sample thickness, geometry, and the fluid speed has been treated by many researchers, e.g. [81].

It should also be remarked that at frequencies coinciding with internal resonances of the system there will be enhanced motion. These correspondingly increase pressure at such frequencies, thus increasing absorption as the sound-bearing air flow is impinging more forcefully against the

absorbent medium. The thermal losses are also increasing by increased flexing of the material, thus also increasing the absorption.

In order to be effective, the thickness of absorbent material must be comparable to the wave length of the sound. Thus thick absorbent layers will absorb low frequency sound, but thin layers will suffice to absorb high frequency sound.

6.2.1. FABRIC MATERIALS

Fabric materials are widely used to control noise. Applications include the use of drapes, curtains, ceiling covers and uses in automotive,aircraft and marine craft.The following section examines the acoustic performance of representative samples of this class of materials.

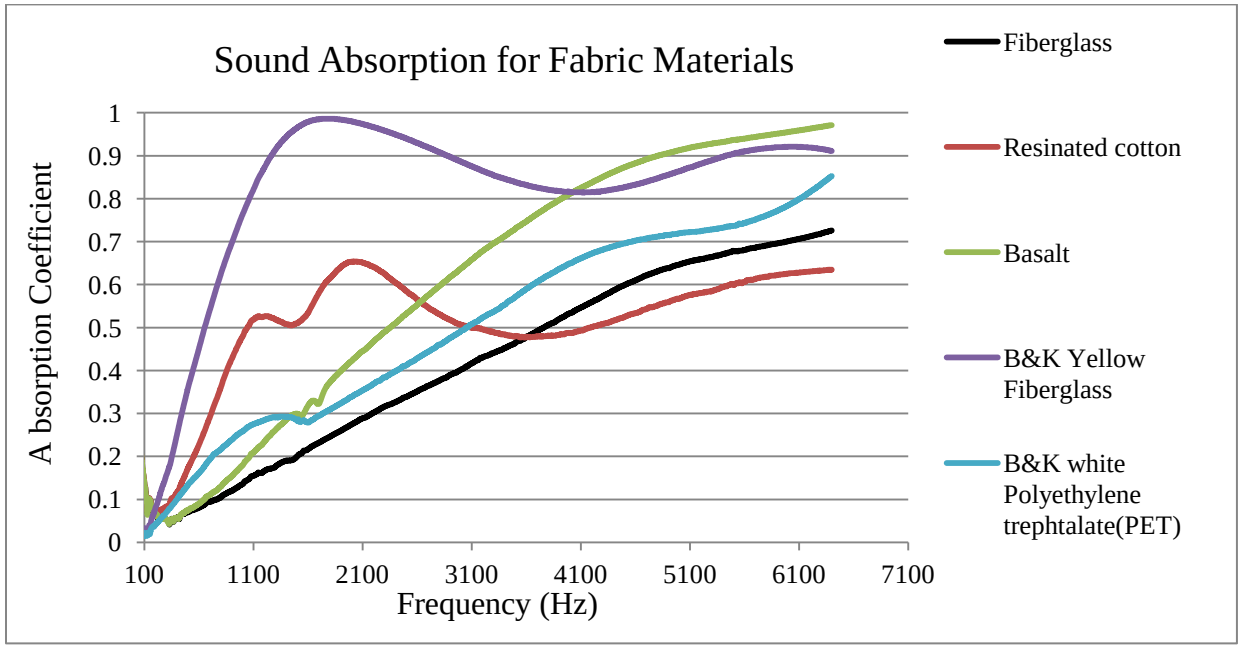

Figure 6.1: Absorption coefficient versus frequency for fabric materials

Resinated cotton, basalt, fiber glass and polyethylene terephthalate (PET) are fabric materials, which are limp in vibration but capable of acoustic absorption. Figure 6.1 shows that their acoustic absorption is higher than 0.5 generally, from about 2000Hz. The yellow fiberglass

and the resonated cotton actually cross the 0.5 absorption coefficient threshold at much earlier frequency values. The effect of higher density and wider thickness is to considerably increase acoustic absorption in the low frequency range and slightly decrease this parameter in the higher frequency range. This may be observed from the table of properties for these materials where the density and thickness of the yellow fiber glass (B&K) are much higher than those for the other fiberglass material, and accordingly figure 6.1 shows a marked increase in the absorption coefficient values. The absorption coefficient in general also increases monotonically with frequency. It may be concluded that clearly, basalt, fiberglass, and PET show good absorption at high frequency values. This suggests that judicious combinations of materials may be made to most economically target any frequency range where acoustic absorption increase is desired. Fabric materials generally have high absorption coefficient at high frequencies and can effectively reduce high-frequency noise components. Some of them, for example the yellow fiberglass (which appears to be useful down to about 100Hz), resonated cotton, and basalt, may in fact be applied to combat lower frequency noise. They are also useful as fillers/additions in synthesized panel materials to improve acoustics.

The thickness effect is well illustrated in the results of figure 6.1. The thicker B&K fiberglass shows a much improved absorption over the thinner (9.5mm compared to 27 mm, in table 4.1). It should be mentioned here that increase of thickness is only beneficial up to a point. The reason is because sound pressure dies out with distance according to an exponential decrement low. The maximum useful thickness is often called the critical thickness [82] .In practice, a thickness of 40 cm's is considered to be the maximum. Resinated cotton shows better performance than all other materials in the low frequency range (for similar thickness) because

of its better ability to be set in motion by incident sound pressure than most other materials. This why it has historically been widely applied for noise control.

6.2.2 FOAM MATERIALS

Foam materials are also widely applied for acoustic abatement on account of their lightness and efficiency in controlling sound of various frequencies. An in-depth look at three such materials follows in the next section.

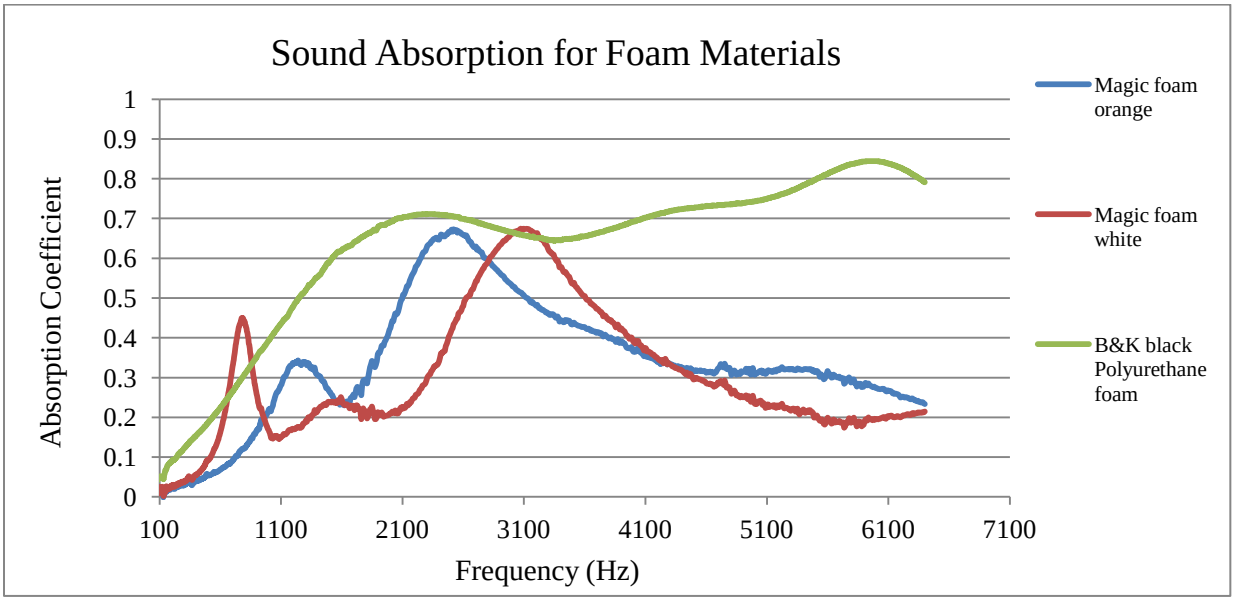

Figure 6.2: Absorption coefficient versus frequency for foam materials

The absorption coefficient shows a number of peaks (max and min) related to the thickness of the material. This max-min profile is undesirable because of unsteadiness of the acoustic absorption value. In order to smooth out the absorption curve, wedge-shaped specimens do a much better job. Acoustic response is very dependent on foam cell behavior because the phenomena experienced with solid visco-elastic materials are also observed with porous materials that have been expanded from polymer stock. These foams have trapped gases in their

cell walls. Thus, they are also subject to creep (strain increasing with time, for maintained stress), relaxation (stress decreasing with time for maintained strain), hysteresis (energy loss over each cycle, for cyclic loading), and strain-rate dependence of effective stiffness/Young's modulus. The propagation of both sound and vibration waves will be affected by the gas phase behavior - gas properties and entrapment pressure.

The overall acoustical behavior of the foam comes from the collection of the micro-structural characteristics of the local cells which themselves come from the frequency–dependent viscous and thermal parameters. The two key parameters are porosity and permeability. At low frequencies the viscous effect is dominant and at higher frequencies the viscous boundary layer becomes negligible and thermal effects dominate (the fluid moves as if it has no viscosity except at the boundary layer). Vibration induces pressure fluctuation in the fluid, which in turn induces temperature variation in fluid-structure interface.

The sound absorption coefficient depends on frequency because the dynamic viscous permeability, dynamic thermal permeability and viscosity are all frequency dependent.

Sound resistance may be by sound absorption or sound insulation, which is also called sound reflection or shock absorption. Smaller cell sizes normally occur with thicker cell wall sizes, higher cell pressures and higher wave velocities, which all increase sound absorption.

Foam materials (figure 6.2) appear to be not as good as fabric ones in containing sound. The polyurethane foam, which seems to perform best in the group tested mainly has about 0.7 absorption, although this spikes to about 0.85 at about 6200 Hz. The magic foams show resonance-type, rather than broad-band behavior in their acoustic performances. They only peak at multiple frequencies, and manifest peaks that are for the major part, below the polyurethane

level. It would seem that some re-formulation is required before they can give better acoustic response. It should be noted that the magic foam materials may actually be acoustically better than the experimental results show. This may be due to manufacturing problems in the oven expansion of the raw stock and inability to machine the test samples with exact fit in the impedance tubes. This latter reason accounts for gaps around the edge of the samples in those tubes. Even though Vaseline jelly was used as a sealant in such gaps, the results could not be guaranteed to be accurate.

6.2.3 HONEYCOMB MATERIALS

Honeycomb materials are used to combat excessive noise as they are light and contain ample air volumes that are useful in attenuating sound. Since they can be made to different geometries, a number of representative samples were examined to their acoustic behavior.

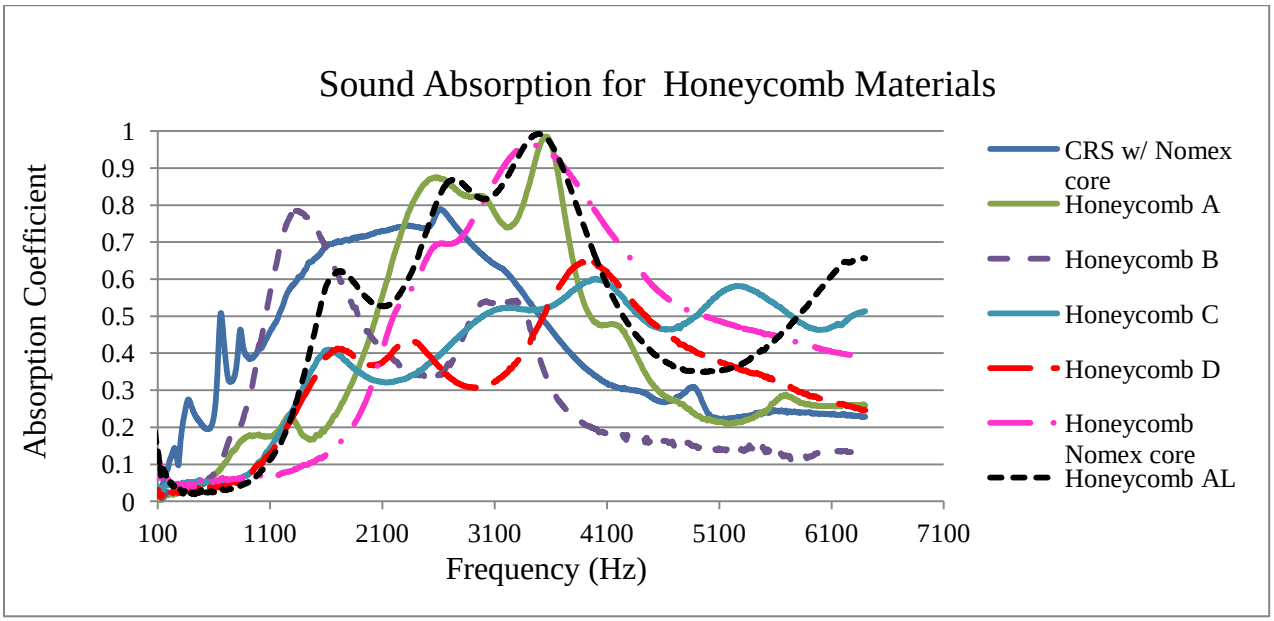

Figure 6.3: Absorption coefficient versus frequency for honeycomb materials

The honeycomb structure is a typically complex one by virtue of the multiple units that are duplicated all over to make it up. Thus the occurrences of many internal resonances make its response to manifest several peaks, at varying frequencies. The acoustic responses of seven such structures are shown in figure. 6.3. There is none of the materials that is a clearly better one over all the frequencies. In fact, it appears that they show incremental goodness from the low frequencies to the high zone. As mentioned before for foam materials, surface material placed on a porous or absorptive material acts in part as a spring-mass structure which tends to increase low-frequency absorption and decrease high-frequency absorption. Increasing thickness tends to have this effect as well in both porous and absorbent materials.

Acoustically, when a honeycomb structure is placed behind a porous absorbent layer it improves the absorption especially at low frequencies and can in fact broaden the frequency range of effectiveness. A very important property of the honeycomb is that its compartmental box structure forces the sound wave that intrudes into the honeycomb to propagate normal to the absorbing surface.

The honeycomb structure has many resonant modes because of its box structure in which very many compartments may resonate locally. Hence, the acoustic absorption and FRF curves may show multiple peaks.

6.2.4 MONOLITHIC AND SANDWICH MATERIALS

A material of one nature acting alone is here referred to as monolithic. The idea here is briefly look at such materials as may be used as skins for sandwiches, partition materials, etc. Naturally these tend to be metallic or other relatively acoustically hard materials. Generally, the rate at which a flexible panel absorbs acoustic energy is proportional to the product of the amplitude

and frequency of vibration , internal damping, and to frictional losses at its mounting edges. The two representative materials examined here are Lexan and cold rolled steel (CRS). On the other hand, two sandwich materials (cold rolled steel with a hard rubbery core LE5208 in between steel skins of L&L proprietary material), and the USIL light with steel skins and thin polypropylene core.

Figure 6.4 shows low acoustic absorption over a wide frequency range for sandwich materials as well. However, over a small frequency band, there is an improved, but still modest absorption. Such materials might be used for their vibration properties, but contribute relatively little to acoustic performance.

The absorption of the CRS material is very small because the constituent materials are not very absorbed but acoustically hard. The LE5208 is hard, closed-cell foam that doesn't permit sound-bearing air to effectively intrude into it. The USIL light is much thinner than the CRS sandwich (1.5mm to 6.5 mm total thickness) and is therefore more vibrated by sinusoidal pressure than the CRS sandwich. The peak around 1100 Hz corresponds to resonance effect vibration of the material. Such materials can be used as barriers both within and outside the material.

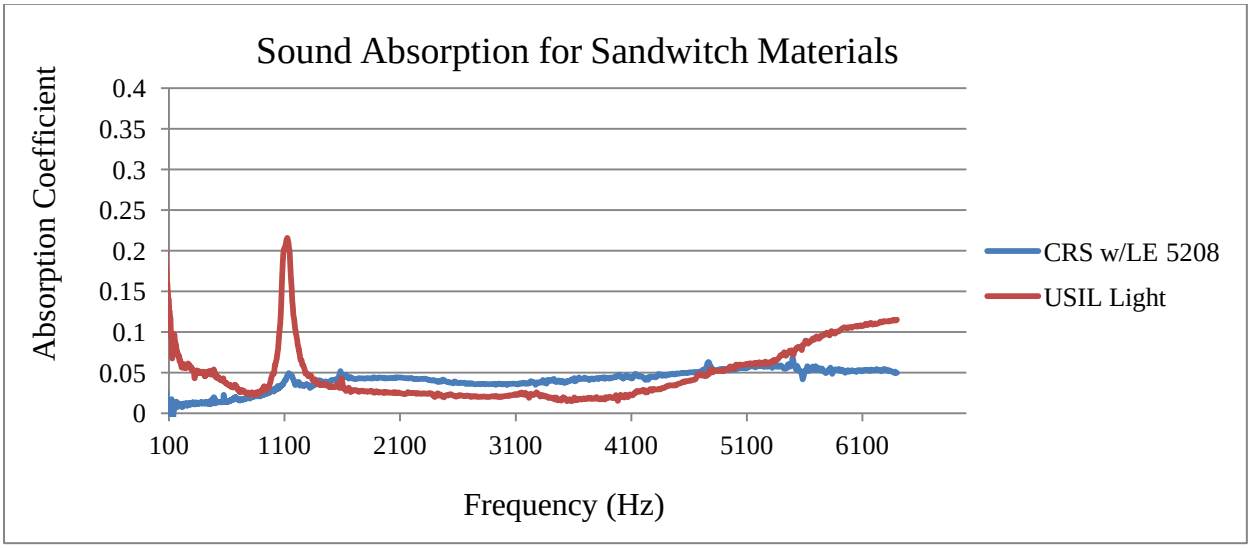

Figure 6.4: Absorption coefficient versus frequency for sandwich materials

For monolithic materials, Lexan with different configurations has been tested. Figure 6.5 shows the acoustic performances of two Lexan arrangements. The curves show that replacing some of the solid material with membrane or more flexible material will increase absorption coefficient. It seems that partial replacement of solid material with membrane or more flexible material significantly increases α, the absorption coefficient, at a lower peak-α frequency, and at more frequency bands. More flexibility in the more intricate pattern promotes more resonance effect.

The solid Lexan and single layer membrane covered Lexan also have low absorption coefficient except at a couple of frequencies. These frequencies correspond to the resonances of the two material systems, the Lexan plate with holes covered by 0.2 mm membrane is defiantly more flexible than the solid Lexan, and hence, its lowest resonance frequency is also less. Being more flexible, its vibration amplitude and hence acoustic pressure amplitude is also higher. Thus the acoustic absorption is higher.

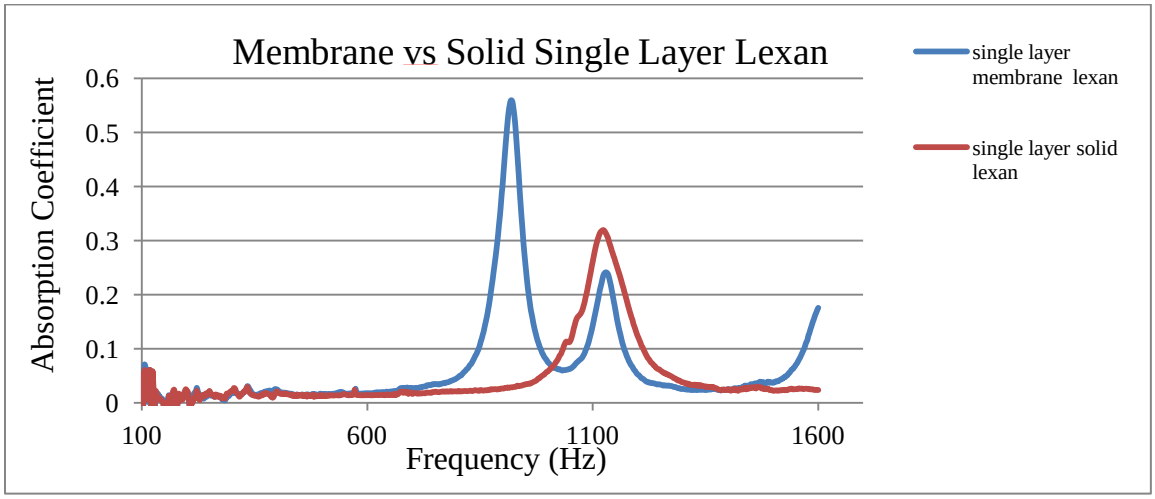

Figure 6.5: Sound absorption of two different Lexan configurations

The effect of thickness on acoustic absorption, in one instance, is illustrated in figure 6.6. Whereas in general, thickness increase tends to increase the lower frequency absorption and depreciate the high frequency values to some extent, yet the effect depends on the actual thickness and its relation to the geometry of the acoustic path of the structure because the wave motion depends on this. Thus, where the peak acoustic absorption occurs and its extent are variable, depending on this relationship. Here thickness increase of acoustically hard material deteriorates acoustic absorption, and lowers the peak-frequency.

The samples again show bad absorption except at two narrow frequency bands. The effect noticed, as explained earlier come from resonance magnification. The two layer solid Lexan shows a first peak that is lower than that of the one-layer solid Lexan. The reason due to the bonding imperfection between the two Lexan layers. It was difficult to make the bond of the "superglue" used uniform, and since it was found necessary to dismantle and re-bond the layers, the structure acted like a sandwich with weak adhesive bonds, hence the assembly was effectively more flexible than the single layer.

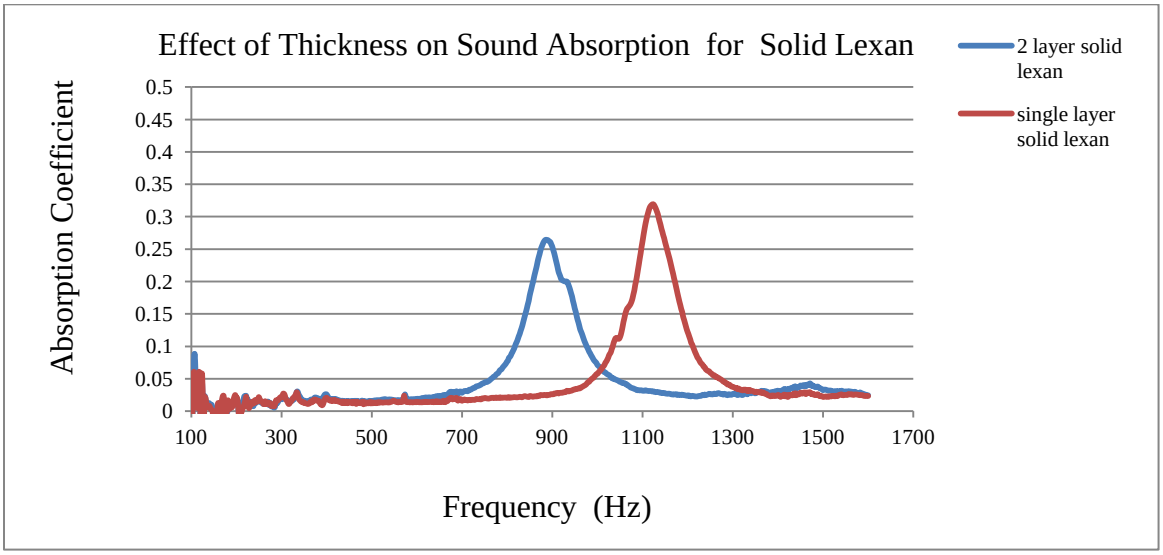

Figure 6.6: Absorption coefficient for 2-layer solid Lexan versus single-Layer one

As seen in figure 6.7, there are notable effects from increasing the hole size in the sample. Increasing confined air volume (such as by increasing hole size for the same thickness) significantly increases absorption. Air volume increase facilitates increase in destructive internal reflections of the sound signal. Increasing confined air volume yields multiple frequency bands of high absorption, thus, this is one way of increasing absorption in more frequency ranges. The presence of holes as compare to the solid material shows a significant increase in absorption because the holes, which bear against the solid end piece in the tube, then act as Helmholtz resonators that promote the destruction (i.e. as viscous and thermal losses) of the incident acoustic waves. The volumes of air in both cases are 3.29e-6 m^3 and 2.01e-5 m^3 for small holes and large holes respectively.

Figure 6.7 shows even more clearly the effect of stiffness because of thickness equality, the materials are both reflective panels except that one has being drilled with larger holes (13mm ϕ) than the other (5mm, ϕ). The sample with larger drilled holes has more material removed from it and is therefore less stiff, making its first absorption peak to occur at a lower frequency than for the second material. Its deflection amplitudes are also larger and therefore the pressure values are larger and the absorption is more.

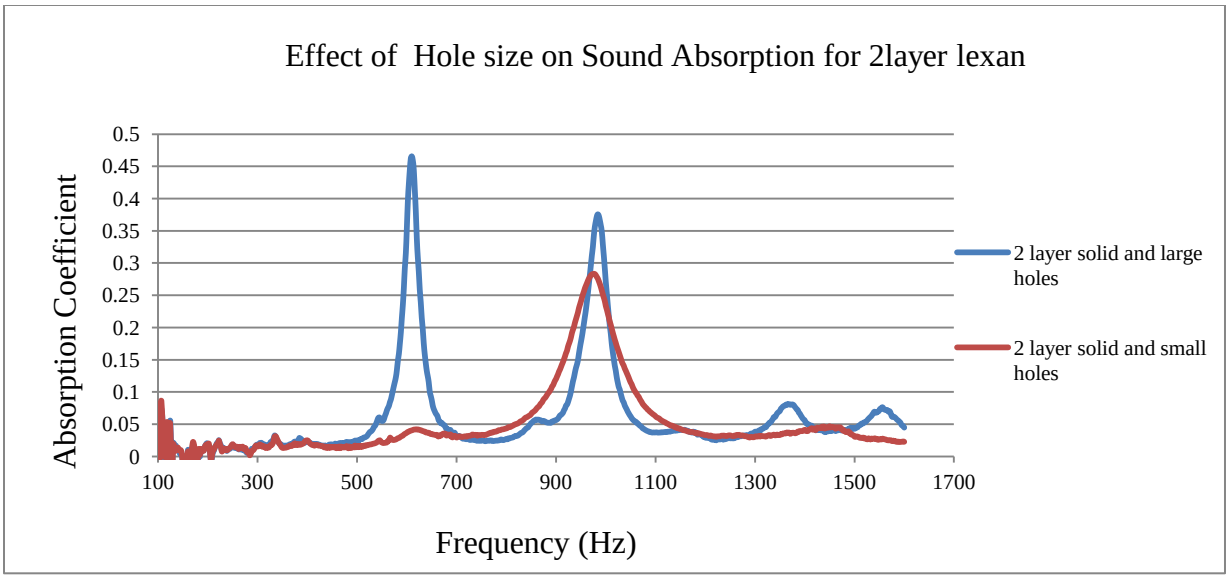

Figure 6.7 Absorption coefficient for sold 2-layer Lexan with small holes

Versus one with large holes

In figure 6.8, the effect of air gap as a "layer" in the sample is observed. Introducing air gaps greatly increases α, but at much lower frequencies and across narrower frequency bands. In general, the effect of an air-gap is to increase absorption at the lower frequencies and somewhat depress it at the higher frequencies. The extent of these adjustments depends on the size of the air-gap. Moreover the air-gap effect is not strictly monotonic, but is tied to the resonance effect of the wave motion in the structure. Analysis of wave motion shows that the absorption peaks would occur at air gaps equal to about 1 quarter (or odd multiples of these) of the wavelength of the sound, while the minimal would occur at about half the wavelength and its even harmonics[83]

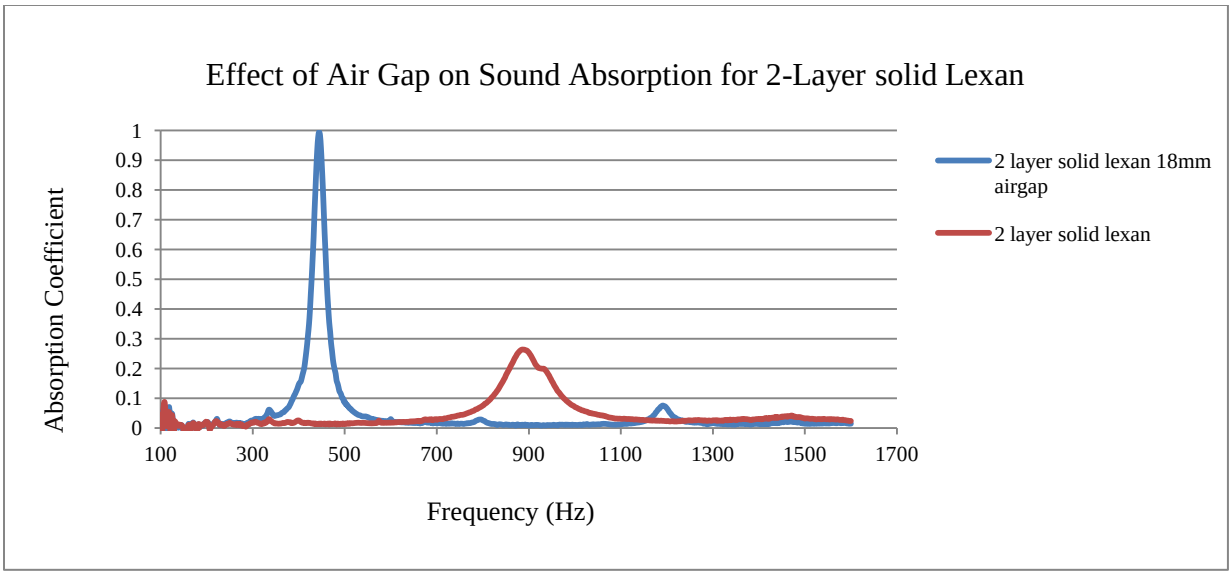

Figure 6.8: Absorption coefficient for 2-layer solid Lexan versus one with An air-gap of 18mm

Overall, Lexan itself, although light, appears to be a bad acoustic absorber and is best used in thicker dimensions, or with supplementary layers of better absorbing materials. It serves as a good acoustic barrier in thick form.

6.2.5 PERIODIC CELLULAR MATERIAL STRUCTURES (PCMS) MATERIALS

Figure 6.9 shows the sound absorption of PCMS materials.

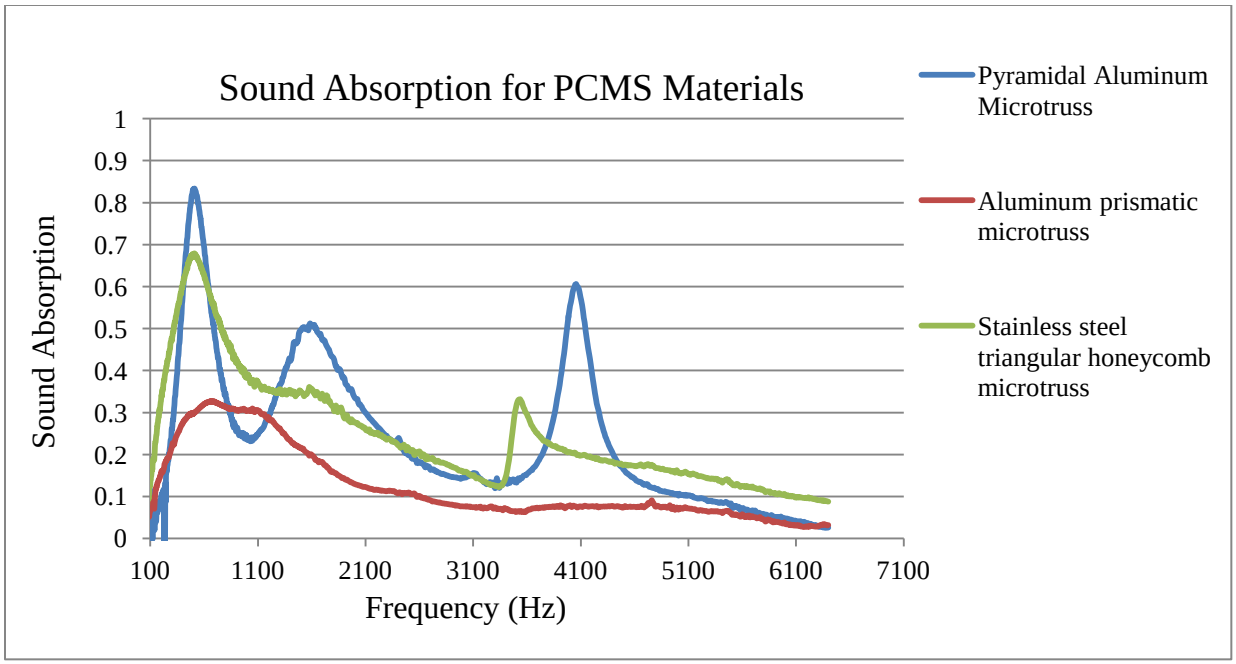

Figure 6.9: Sound absorption for PCMS Materials

Although the economic significance of PCMS structures is high, as discussed earlier, their acoustic and vibration properties have not been significantly explored. The acoustic response of three such materials is shown in figure 6.9. The response patterns appear to be quite logical. The pyramidal aluminum Microtruss seems to perform best in this group, as it has the most air cushion between its skins, and the response shows the typical structural resonance peaks. Its response appears to be more strongly frequency-dependent. The stainless steel triangular honeycomb structure behaves to a lesser extent like the previous sample for similar reasons, except that the absorption is less, as is the frequency dependence. Less air is confined mid-structure, and the geometry is less solid than for the pyramidal Microtruss. The aluminum triangular channel PCMS is much more solid than the previous two and has much less enclosed air volume. The absorption is thus much less. This sample is not likely to be deployed for the sake of its acoustic absorption capability. However, this group of materials being highly

multifunctional is very useful and if there results have any deficiency in a particular property, it would be remedied, by augmentation with a compensatory material, or else by appropriate re-design of the necessary section

The aluminum prismatic Microtruss is a heavy block structure with thicker dimensions of sections inside it than the other PCMS materials. Hence, its absorption is generally low since it can not be easily set into motion by air pressure vibration, and is only slightly more absorptive at the lower frequencies than at the higher frequencies.

6.2.6 GENERAL PERIODIC MATERIALS

Materials with periodic arrangement, which do not belong in the class of PCMS structures, are general periodic materials. These ones examined here are only typical, as the possibility is infinite. When such structures are constructed with internal resonances, the possibility of obtaining meta-materials with some negative mechanical indices (effective mass and effective stiffness) exists. The subject of meta-materials is excluded from the coverage of this dissertation as it is a huge topic on its own. However, the overall acoustic response of three general periodic materials are examined

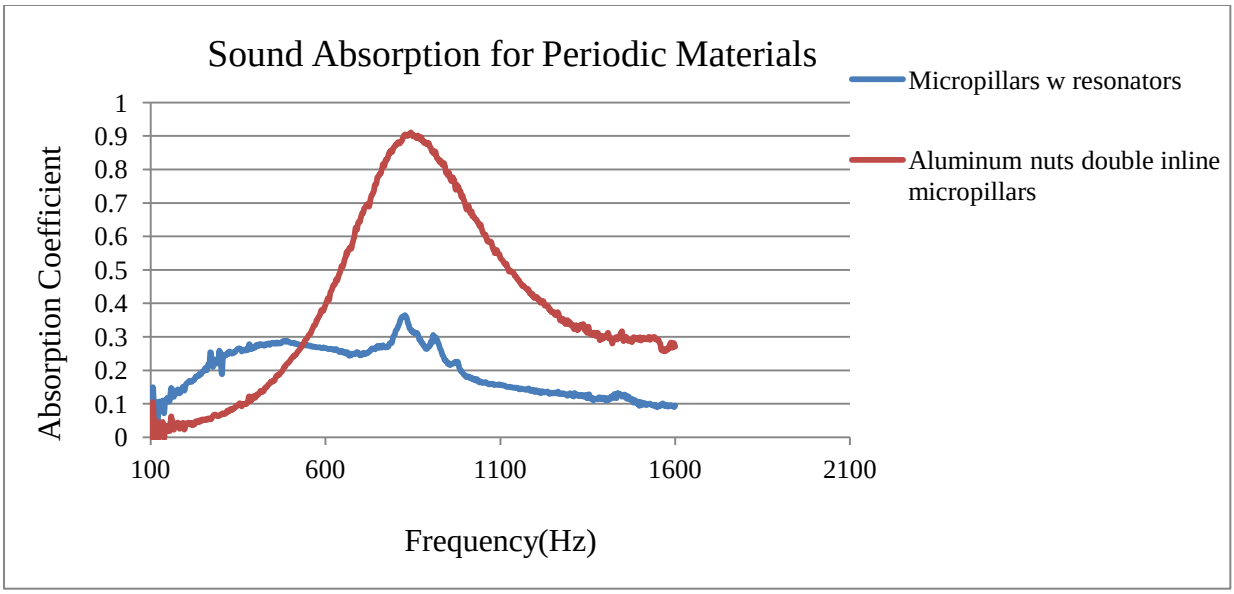

Figure 6.10: sound absorption for two periodic materials (large size only)

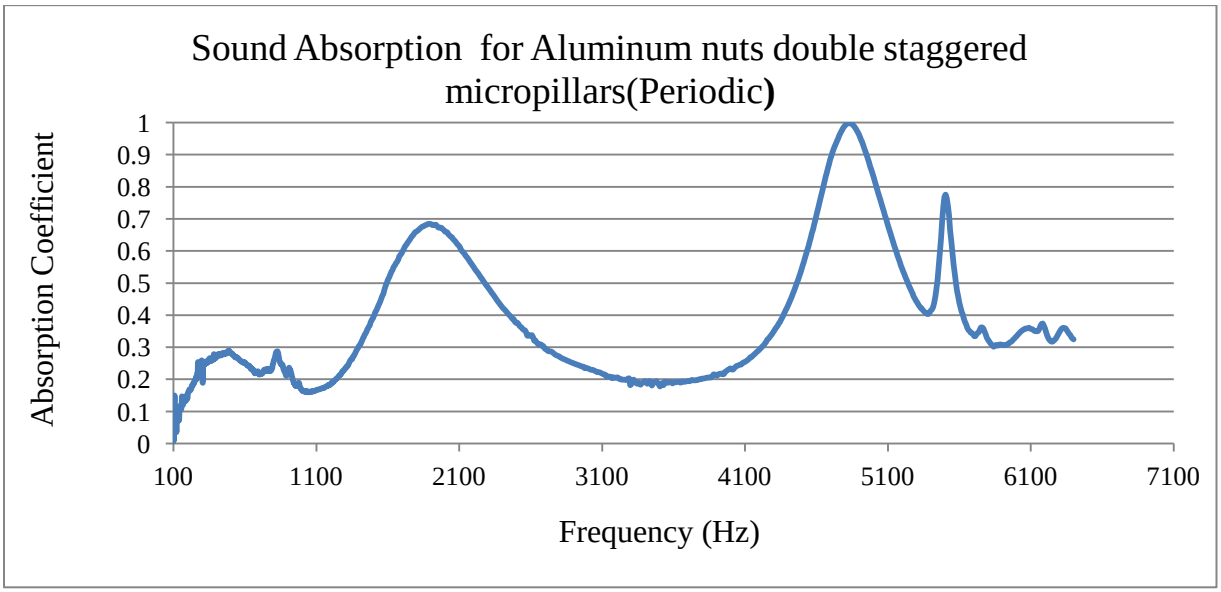

Figure 6.11: Absorption coefficient versus frequency for Aluminum nuts double staggered micropillars

Figures 6.10 shows the sound absorption of two general periodic materials, and figure 6.11 that of the third one. The first two had just the large samples (100 mm diameter, which can only measure up to 1.6 kHz), because of their structure so they were tested for the low frequency

range, the absorption for the double in-line micropillars is strongly resonant. Its absorption exceeds 0.5 only between 600 and 1200 Hz, in the low-to-medium frequency range. The double staggered micropillars also manifests resonance behavior and shows absorption above 0.5 for the frequency ranges 1600-2500 Hz and 4500-5200Hz. It seems clear that specific design of the component parts in terms of mass and stiffness distributions may be used to tailor the frequency ranges where high absorptions may be attained. The structure with internal resonators does not show good absorption anywhere in the 0-1600 Hz range and its use will probably be in connection with vibration rather than acoustics. The presence of many local component systems in the last two structures leads to many internal resonances and absorption peaks.

The micropillar constructions show very high absorptions ant frequency bands where their particular constructions allow them to resonate with relatively large amplitudes, but as non-absorbers ,they have weak absorption at other frequencies

6.3 VIBRATION RESULTS

On account of the modal effect of distributed mass structures, even a simple, isotropic panel will have an infinite number of vibration modes. In addition, when internal components exist which may also vibrate locally, the responses become even more. This effect is seen in all the vibration results.

In these results we will show only one complete set of results for one sample in each group due to the large amount of results. However the complete results for the remaining samples will be shown in tables. On the other hand one more complete set of results for another sample from each group will be shown in appendix D at the end of this dissertation, a comparison between

results for the whole set of each group will be shown after the results of the selected material of each group has finished.

The results will be in the following sequence:

1. Stability diagram which shows the exact natural frequencies for the structure using PULSE Reflex.
2. FRF, Phase and Coherence.
3. FRF from RADIOSS for samples computed.
4. Finite element results from Abaqus including the 1^{st} three mode shapes
5. Matlab results for samples computed
6. Diagrams for the following
    - 6.1 Maximum deflections for the 1^{st} three modes
    - 6.2 Damping ratios for the 1^{st} three modes
    - 6.3 Compatibility between results (experimental and numerical)
    - 6.4 Comparisons between the results for the whole set of samples for each group
7. Tables to show the results for the whole group

6.3.1 HONEYCOMB MATERIALS

The honeycomb materials were tested for vibration behavior using PULSE 16.1. To verify the experimental results, finite element simulation was used to get the natural frequencies, and mode shapes for each of the samples. The analysis of the vibration and acoustics of honeycomb materials involves at least four key stiffness and strength properties in each direction-longitudinal and transverse. These properties are Young's modulus, shear modulus tensile strength, and compressive strength. The failure modes of the honeycomb are usually local

crushing; bending fracture, compression fracture, global buckling, face wrinkling with debonding, face wrinkling with core-crushing, and shear crimping. However the CRS with Nomex was not simulated due to the very thin cell size which prevents the mesh of the structure. The sample selected for honeycomb group was Nomex Honeycomb. Figures 6.12-6.17 shows the following results for Nomex honeycomb:

Figure 6.12: The stability diagram which indicates the first three natural frequencies.

Figure 6.13: FRF, Coherence and phase.

Figure 6.14: 1st three mode shapes (displacement contour).

Figure 6.15: Maximum deflection for the 1st three modes.

Figure 6.16: Damping ratio for the 1st three modes.

Figure 6.17: Compatibility between experiment and FEM results.

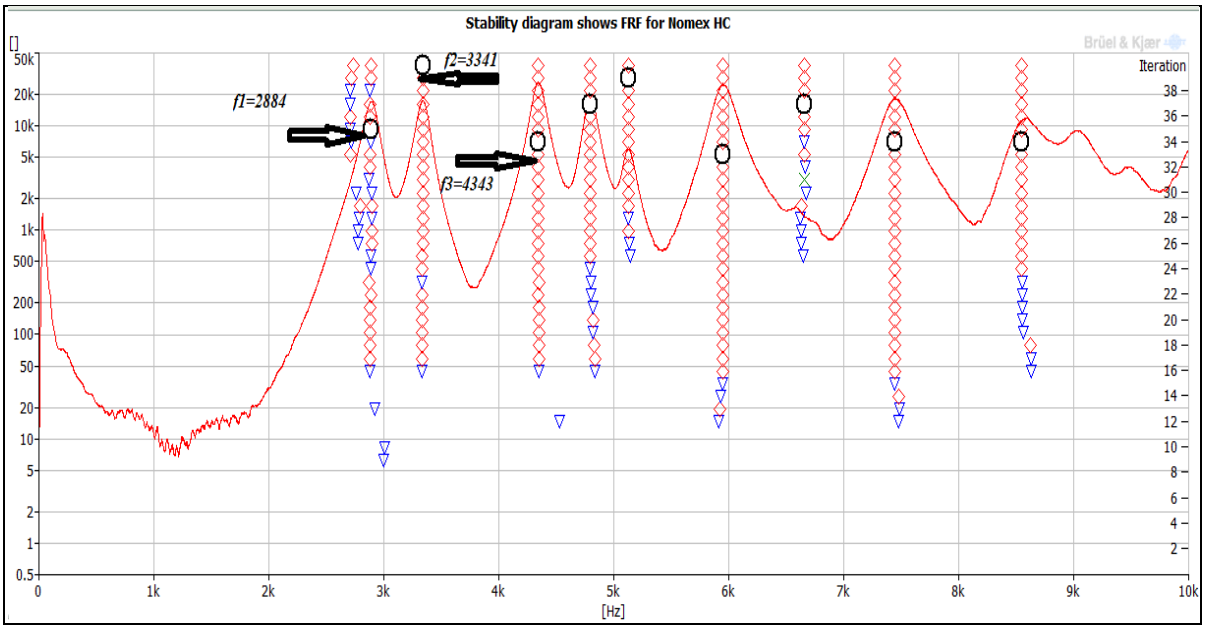

Figure 6.12: Stability diagram shows the 1st three natural frequencies (Nomex HC).

Figure 6.12 shows the true natural frequencies as picked out by the PULSE Reflex 16.1 program by Bruel and Kjear Inc. the program uses about half a dozen algorithms to determine the most

accurate locations of the resonance frequencies, taking a host of parameters into account. Thus, even if some of the peaks indicated don't appear to be obvious yet they would still be the best ones from these detailed computations. However in this figure the peaks are all clear. The FRF is multi-peaked because of multiple resonances of the vibration of these complex structures.

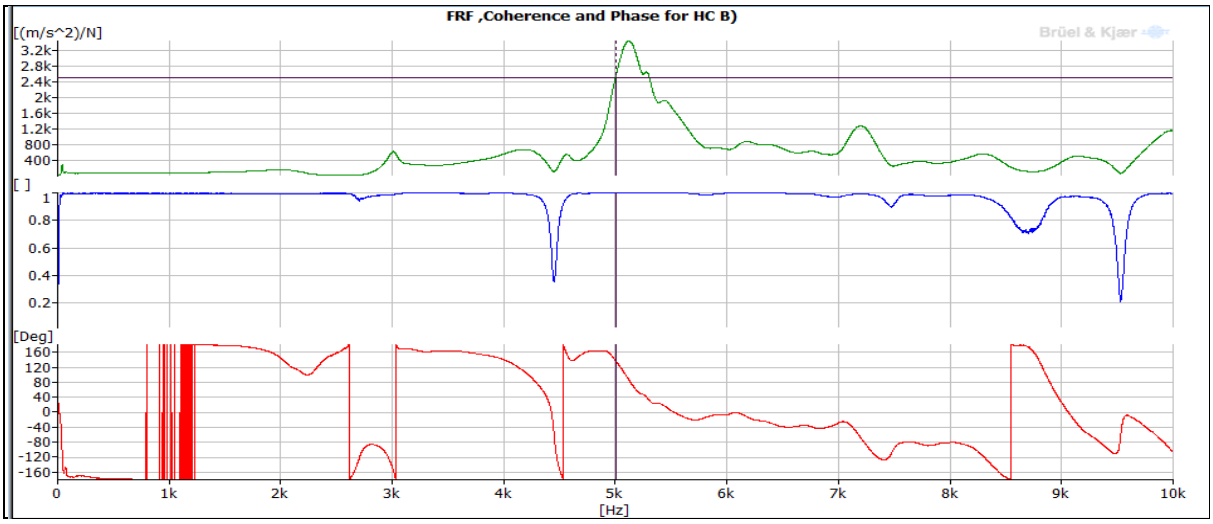

Figure 6.13: FRF, Coherence and phase (Nomex HC)

The coherence values are virtually at the maximum level (unity value) throughout the frequency range, thus indicating the accuracy of the results.

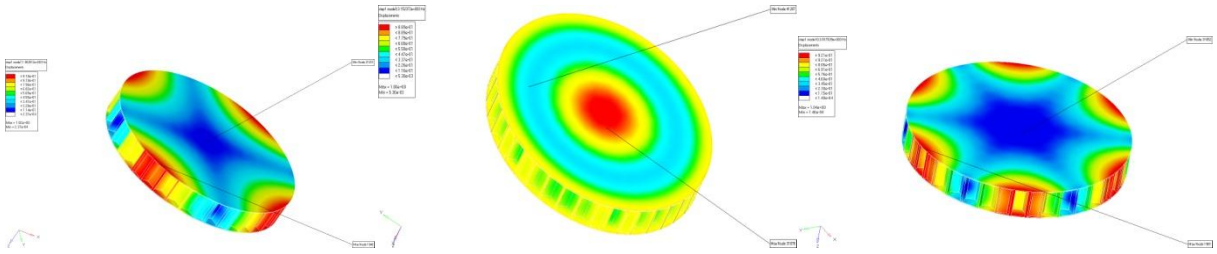

(Displacement contour) Mode1 Mode 2 Mode3

Figure 6.14: 1st three mode shapes (displacement contour, Nomex HC)

The first three mode shapes as can be seen in figure 6.14 conform to the pattern observed for a circular plate in bending vibration, showing the two diametral nodes for the first mode, one circular node for the second mode and three diametral nodes for the third mode. The contour

plots also show the regions of maximum displacements where the maximum stresses are also experienced. This pattern was found to be repeated in all cases except for the PCMS materials.

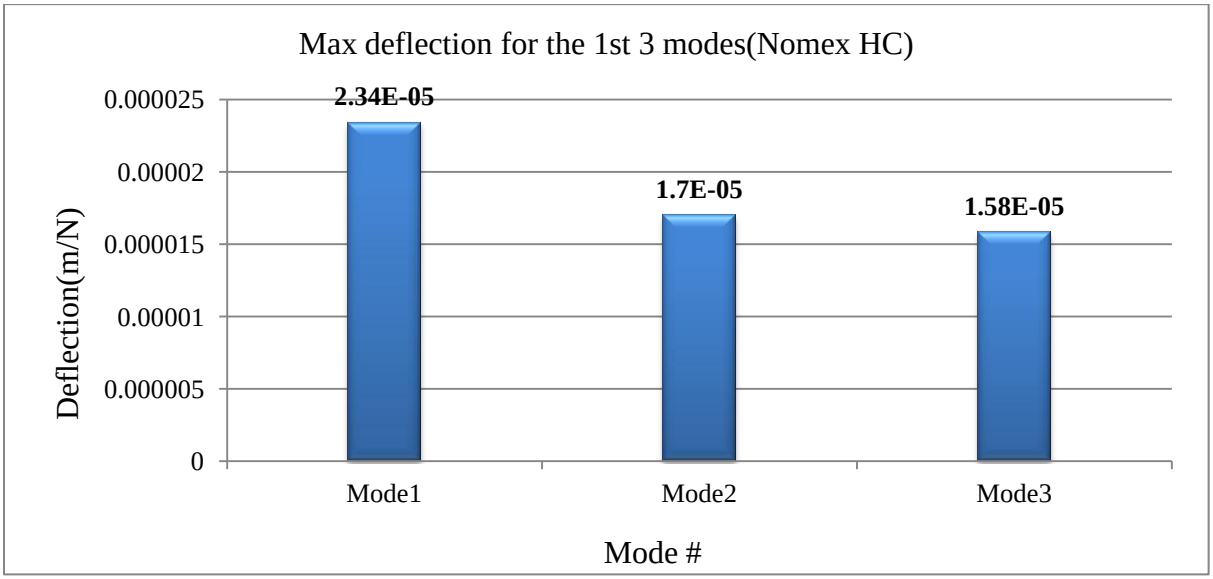

Figure 6.15: Maximum deflection for the 1st three modes (Nomex HC)

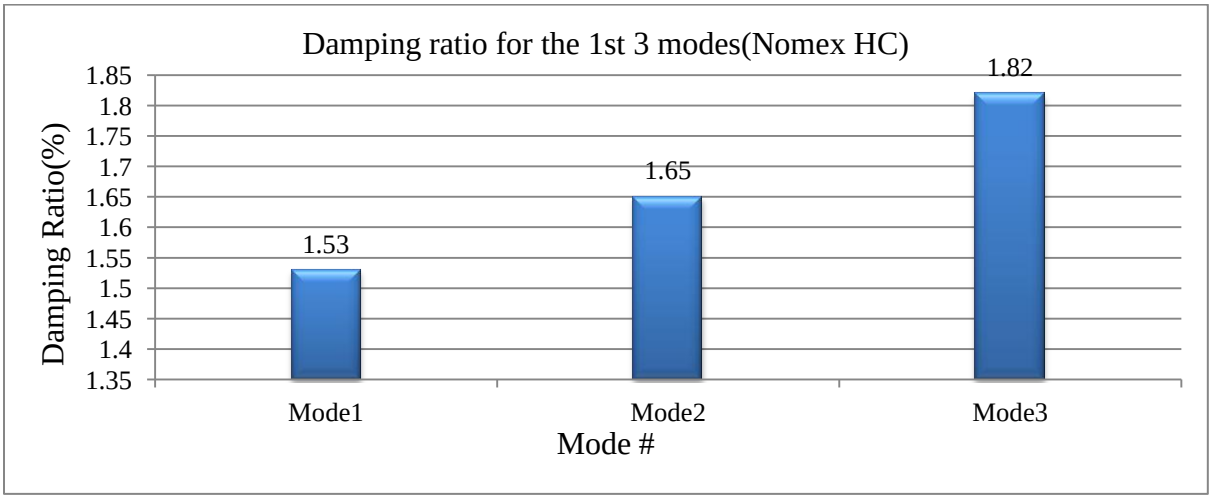

Figure 6.16: Damping ratio for the 1st three modes (Nomex HC)

The first mode has the largest maximum deflection and the minimum modal damping ratio as expected among the first three modes shown in figures 6.15 and 6.16.

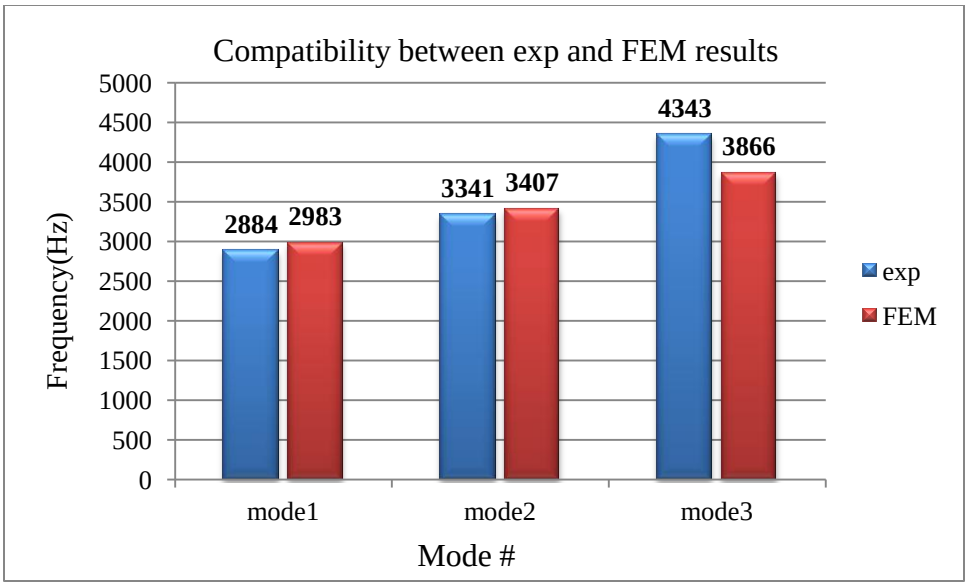

Figure 6.17: Compatibility between experiment and FEM results (Nomex HC)

For the first two modes(figure 6.17), the maximum deviation of the computed resonance frequency from the experimental is less than 4%, and even for the third mode the difference is less than 11%. These again attests to the accuracy of the experimental work and to the appropriateness of using the curve fit approach for the few property values that could not otherwise be obtained.

Table 6.1 compares the number of elements, number of nodes and element type from finite element simulations for the honeycomb group; on the other hand the number of peaks from experimental results is shown to indicate modal densities of these samples over a specified frequency range.

Table 6.1: Comparison between honey comb samples according to number of nodes, elements and element type, with the modal densities

Material	#of nodes	#of elements	Element type	# of peaks in the frequency range(0-6.4 kHz)
AL HC	89762	294252	C3D4	3
HC A	98676	199812	S3	5
HC B	77390	249818	C3D4	7
HC C	57862	188487	C3D4	4
HC D	31123	65838	S3	9
Nomex HC	89412	179810	S3	6
CRS w/Nomex*				4

*: the software was not able to mesh it because the cell thickness was too small

Table 6.2 compares the vibration results for the honeycomb group, and then these results are shown in a graphical representation in order to give a better understanding about the behavior of these structures.

Table 6.2: Vibration results for Honeycomb structures

Material	Mode#	Damping ratio(η)%	Natural frequency(Hz)		Max deflection(m/N)
			Experimental	Finite Element	
AL HC	1	1.86	3547	3291(7%)*	0.00000541
	2	3.39	5570	5262(5.5%)	0.00000176
	3	2.14	6209	5908(4.8%)	0.0000027
HC A	1	0.79	4888	5000(2.2%)	0.00000565
	2	2.48	6458	6074(6%)	0.000000855
	3	1.81	9284	8557(7.8%)	0.00000324
HC B	1	4.5	2154	1863(13%)	0.0000318
	2	7.6	2907	3152(8%)	0.0000262
	3	4.7	3476	3817(9.8%)	0.0000272
HC C	1	0.96	1871	2022(8%)	0.000113
	2	1.46	3288	3468(5%)	0.0000287
	3	1.69	4599	4040(12%)	0.0000167
HC D	1	1.15	1875	1856(1%)	0.000113
	2	3.63	2061	2265(9.8%)	0.0000177
	3	4.56	2356	2359(0.1%)	0.00000572
Nomex Hc	1	1.53	2884	2983(3.4%)	0.0000234
	2	1.65	3341	3407(1.9%)	0.000017
	3	1.82	4343	3866(10.9%)	0.0000158
CRS w/Nomex**	1	0.86	878	-	0.000158
	2	1.51	1483	-	0.0000849
	3	1.9	2892	-	0.0000116

* : (%) Percentage error between experimental and finite element results

**: The material couldn't be simulated in FEM because of very thin core thickness

Figures 6.18-6.22 show the comparisons between the different samples of the honeycomb materials as follows:

Figure 6.18: Comparison between numbers of elements

Figure 6.19: Comparison between natural frequencies for the 1st three modes

Figure 6.20: Comparison between maximum deflections for the 1st three modes

Figure 6.22: Comparison between damping ratios for the 1st three modes

Figure 6.23: Comparison between modal densities

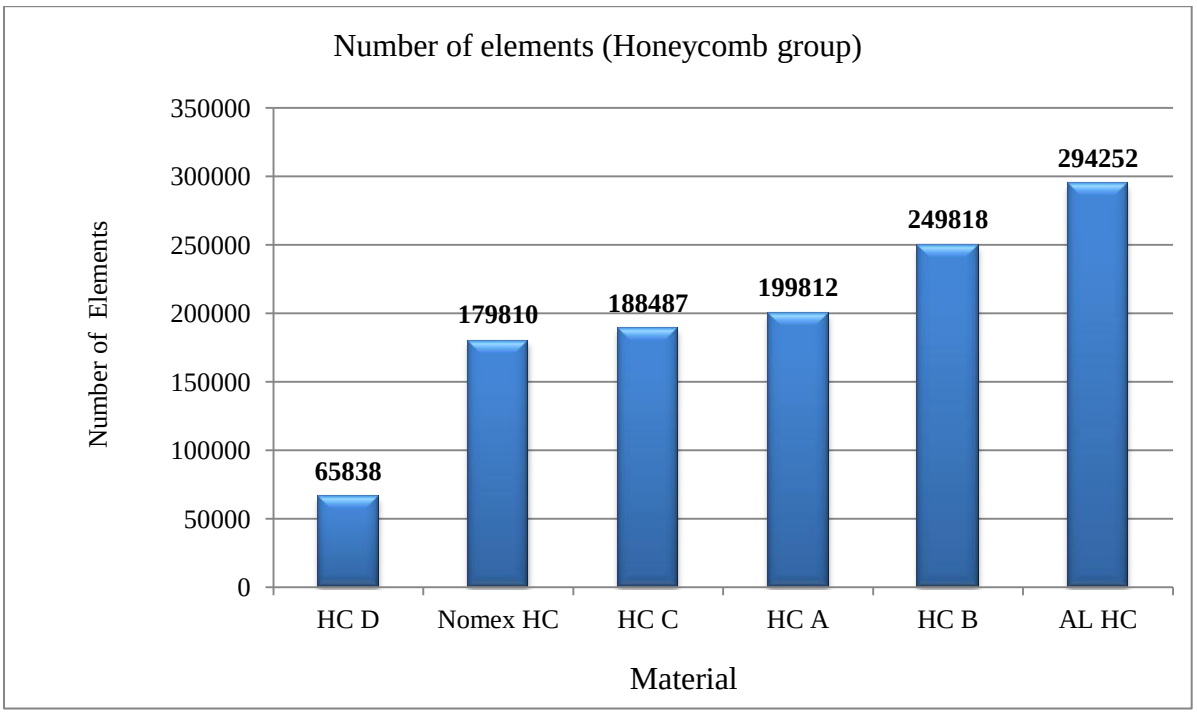

Figure 6.18: Comparison between numbers of elements (Honeycomb group)

Figure 6.18 shows the various numbers of elements that were used to simulate the different samples on account of the relative complexities of their structures, and the available computing resources. These numbers vary between almost 66,000 to almost 300,000, showing that these structures are quite complex to model if reasonable results are desired.

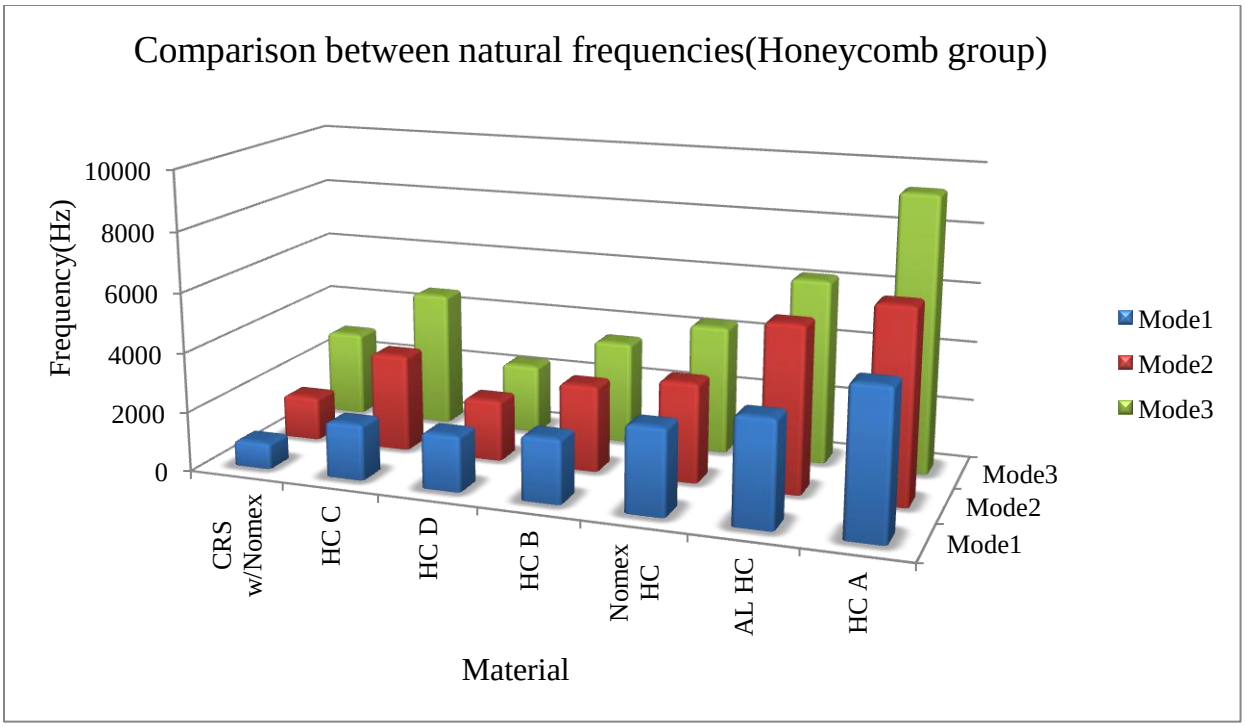

Figure 6.19: Comparison between 1st three natural frequencies (Honeycomb group)

The natural frequency is an approximate expression of the stiffness distribution relative to mass distribution in the structure. The comparison of this parameter for the honeycomb structures is shown in figure 6.19, here a monotonic arrangement for mode 1 (the fundamental, and usually most important for vibration consideration) is constructed. All other things being equal, this ratio is often loosely correlated with stiffness. Thus, the CRS/Nomex honeycomb is the "softest" structure in the group, while the honeycomb A (glass-epoxy skins and aluminum honeycomb core) is the "stiffest". The differences in construction give us possible design latitude in tailoring our desired natural frequencies. It must also be remembered that the skins are normally bonded to honeycomb cores with adhesives. The strength of such adhesives and the quality of bonding both affect the relative softness or stiffness

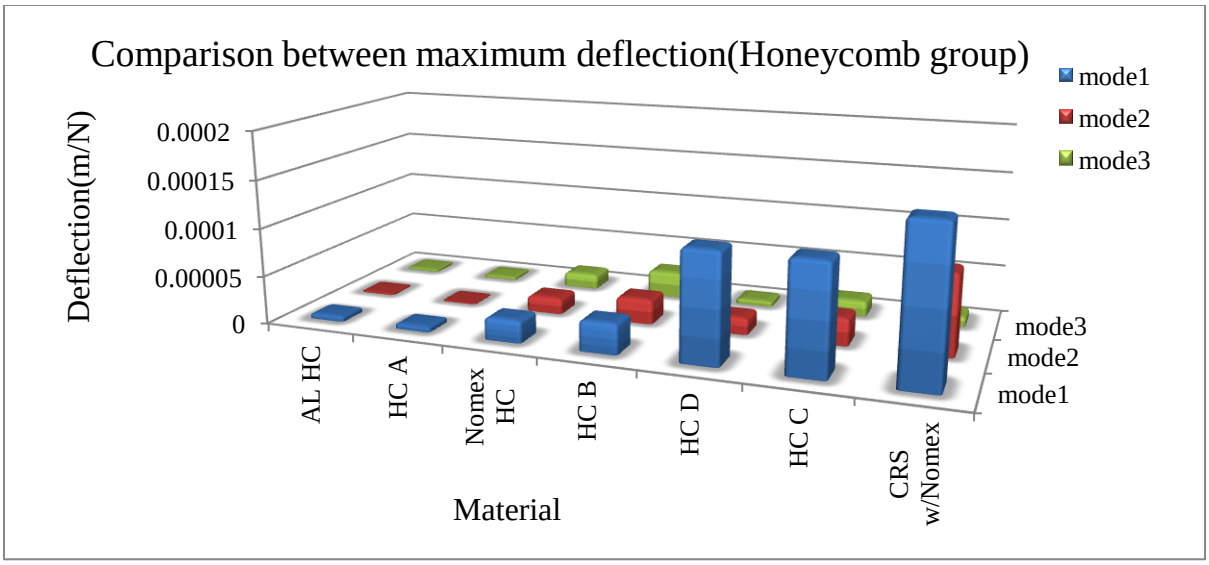

Figure 6.20: Comparison between maximum deflections for the 1st three modes(Honeycomb group)

As it can seen from figure 6.20, mode one for all the samples is the dominant mode where the maximum deflection is largest. Since stress is proportional to deflection at a point, this also indicates that the maximum stresses are experienced in the mode 1 of vibration resonance. Hence if steps are taken to ameliorate mode 1 effects, then it would not be necessary to worry about the immediate higher modes, from the point of view of damage.

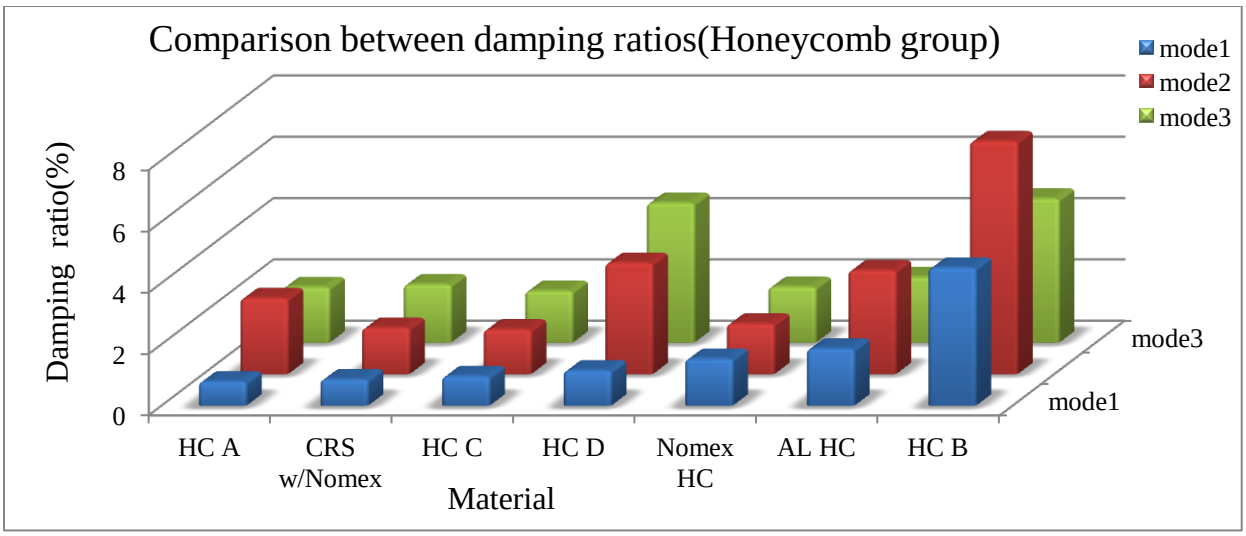

Figure 6.21: Comparison between damping ratios for the 1st three modes(Honeycomb group)

The modal damping ratio (figure 6.21) is least for mode 1 for all the honeycomb materials. The modal damping effectively contributes to the restraint of motion. For each material the results for maximum deflection and damping ratio are consistent in the sense that relatively high deflections are generally associated with relatively low damping ratios.

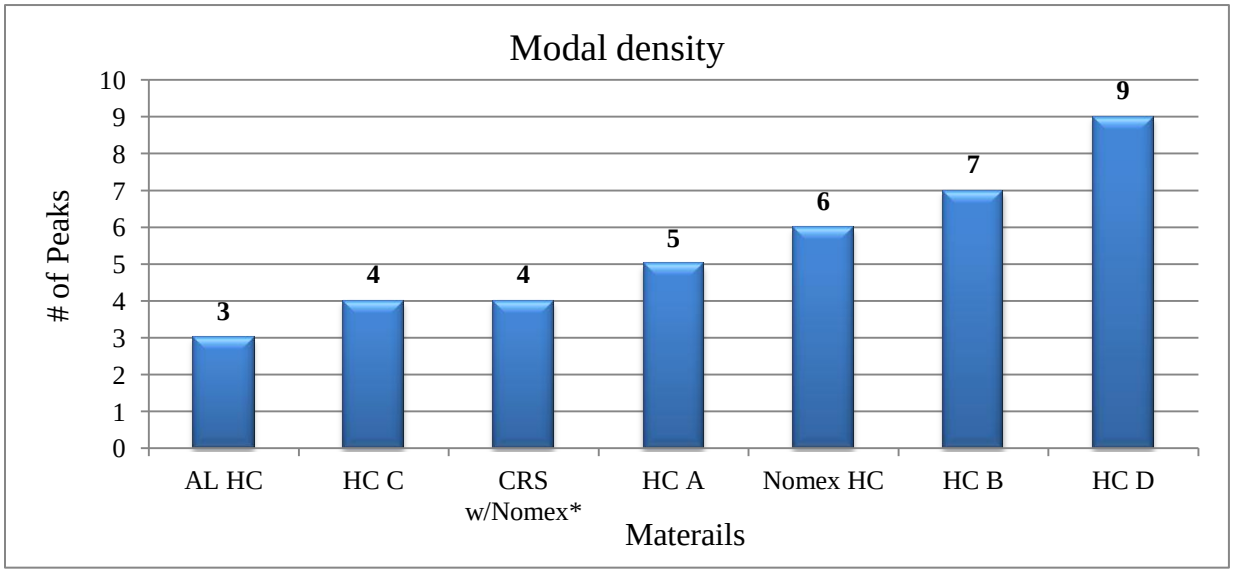

Figure 6.22: Comparison between modal densities (Honeycomb group)

Figure 6.22 shows the modal density, which is a measure of the complexity of the structure, it is effectively indicated here by the number of resonant peaks in a given frequency band. Arranged monotonically, it is seen that the aluminum honeycomb seems to be the least complex while honeycomb D (polyester skins and aramid core), appears to be the most complex. Complexity is a cost in terms of material, labor and delay time charges, and this would normally go into decision making before particular structures are deployed.

6.3.2 MONOLITHIC AND SANDWICH MATERIALS

The monolithic and sandwich materials were tested for vibration behavior using PULSE 16.1. To verify the experimental results, finite element simulation was used to get the natural frequencies, and mode shapes, for each of the samples. The sample selected for monolithic group was single layer Lexan with large holes while USIL light was selected as a sandwich sample. Figures 6.23 to 6.29 show the following results for single layer Lexan with large holes:

Figure 6.23: The stability diagram which indicates the first three natural frequencies

Figure 6.24: FRF, Coherence and phase

Figure 6.25: FRF results from RADIOSS

Figure 6.26: 1st three mode shapes (displacement contour)

Figure 6.27: Maximum deflection for the 1st three modes

Figure 6.28: Damping ratio for the 1st three modes

Figure 6.29: Compatibility between experiment and FEM results

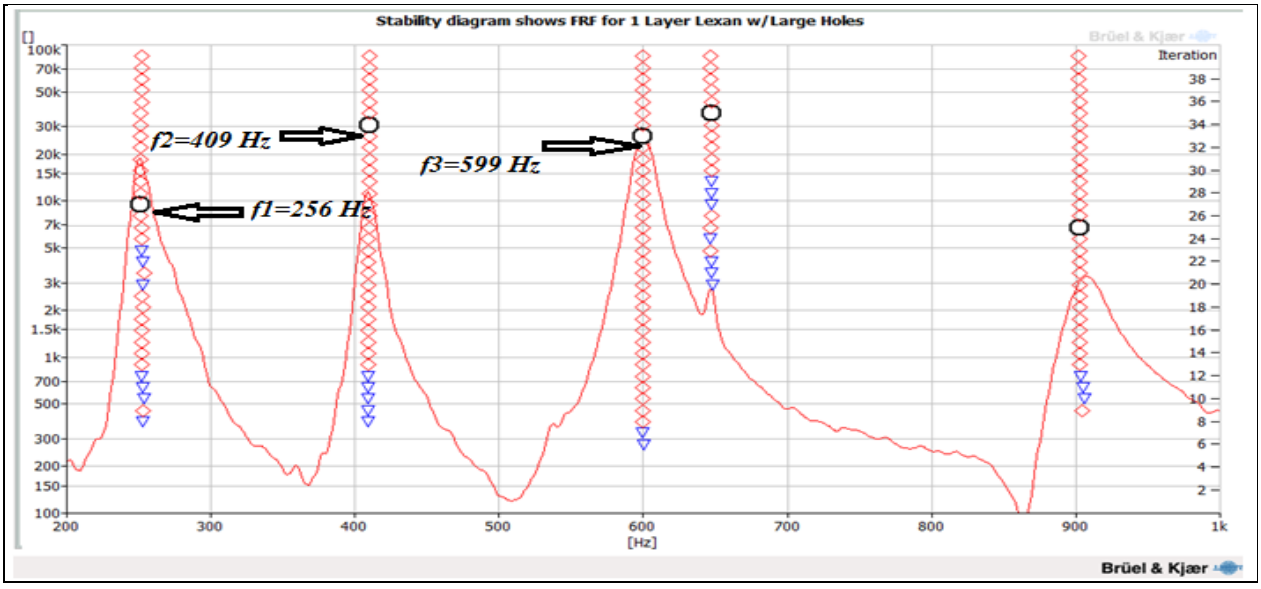

Figure 6.23: The stability diagram shows the first three natural frequencies (1 Layer Lexan with large holes)

The peaks in the stability diagram as shown in figure 6.23 are distinct and more than in the comparable solid sample (3 peaks) as can seen in appendix D, the amplitudes at the peaks for this sample are higher than for the solid one. This is as expected because this sample has been rendered more flexible and softer by the punching of holes in it.

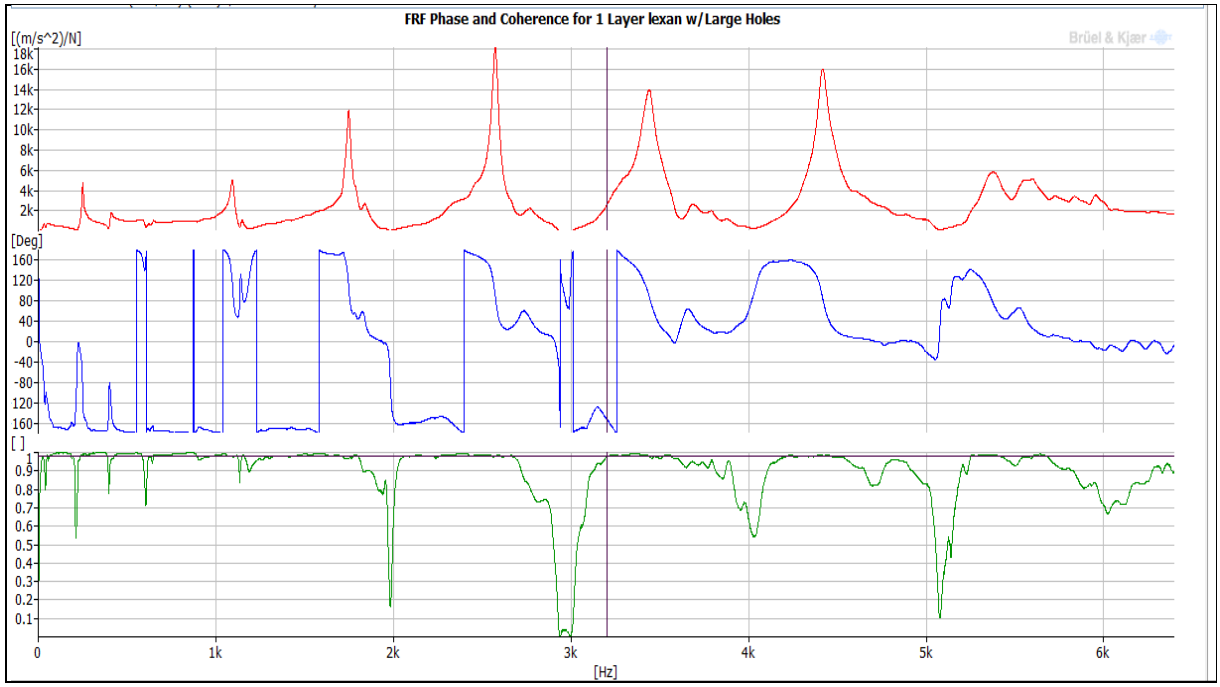

Figure 6.24: FRF, Coherence and phase (1 Layer Lexan w/large holes).

Figure 6.24 shows a good coherence values (unity) over the frequency band, in addition to this, the phase tends to be around 90^0 at resonance frequencies which is again an indication of the accuracy of the experimental work. The top diagram of figure 6.24, which is the FRF is only a more diffuse image of the stability diagram of figure 6.23, which has been discussed.

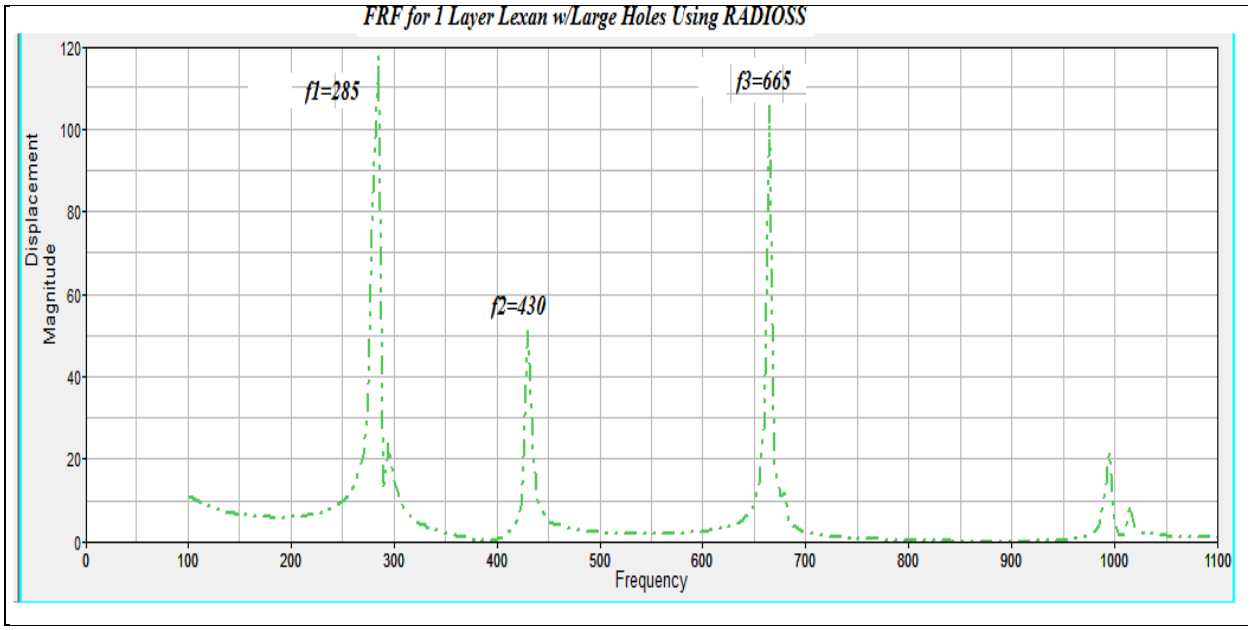

Figure 6.25: FRF results from RADIOSS (1 Layer Lexan w/large holes).

The finite element results (Radioss and Abaqus) agree very well with the experimental results(less than 5% for the first mode) as it can be seen from figures 6.24 and 6.25, this signifies that the experiments were carried out in sufficient accuracy.

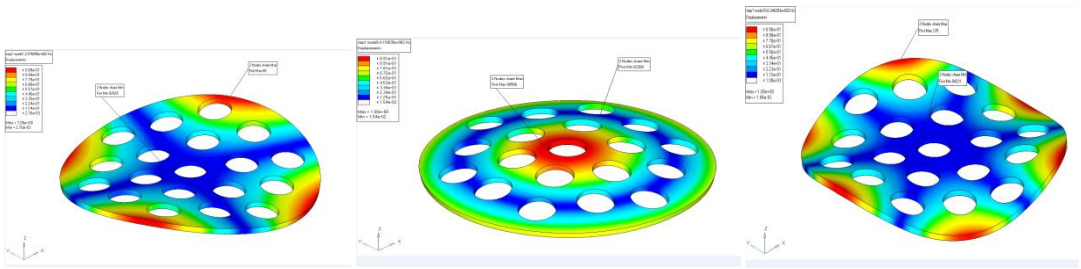

(Displacement Contour) Mode1 Mode2 Mode3

Figure 6.26: 1st three mode shapes (displacement contour, 1 Layer Lexan w/large holes).

The first three mode shapes (figure 6.26) conform to the pattern observed for a circular plate in bending vibration, showing the two diametral nodes for the first mode, one circular node for the

second mode and three diametral nodes for the third mode. The contour plots also show the regions of maximum displacements where the maximum stresses are also experienced.

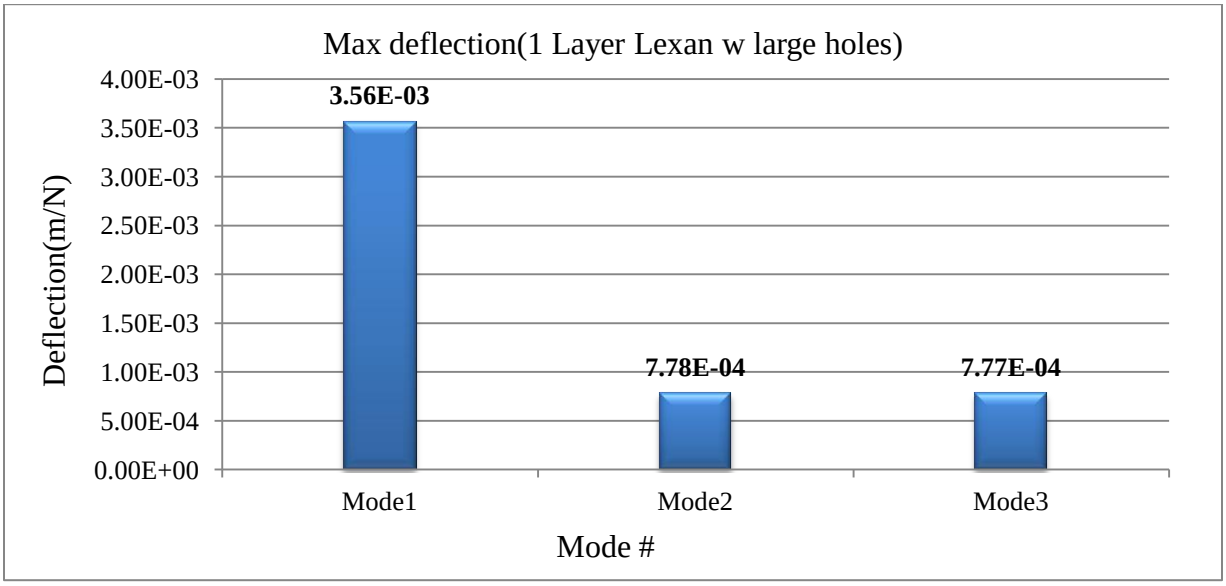

Figure 6.27: Maximum deflection for the 1st three modes (1 Layer Lexan w/large holes).

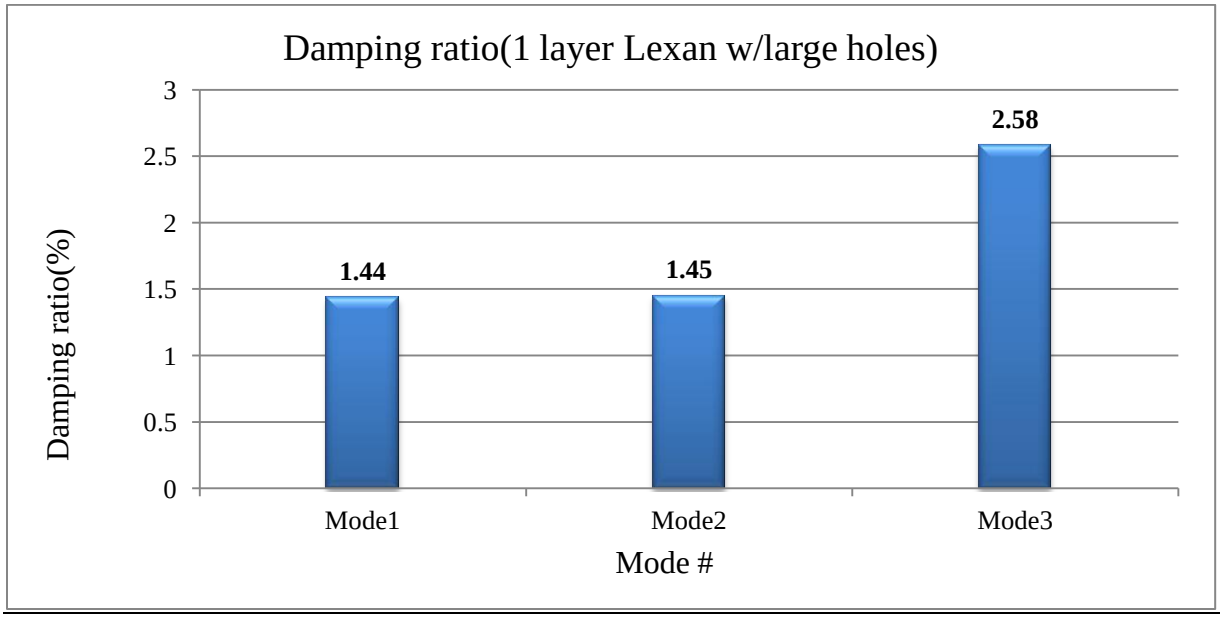

Figure 6.28: Damping ratio for the 1st three modes (1 Layer Lexan w/large holes).

The maximum deflections and the modal damping ratios as it can be seen from figures 6.27 and 6.28 are consistent for each mode in that high values of deflections correspond to low values of modal damping. Mode one manifests the largest maximum deflection as expected.

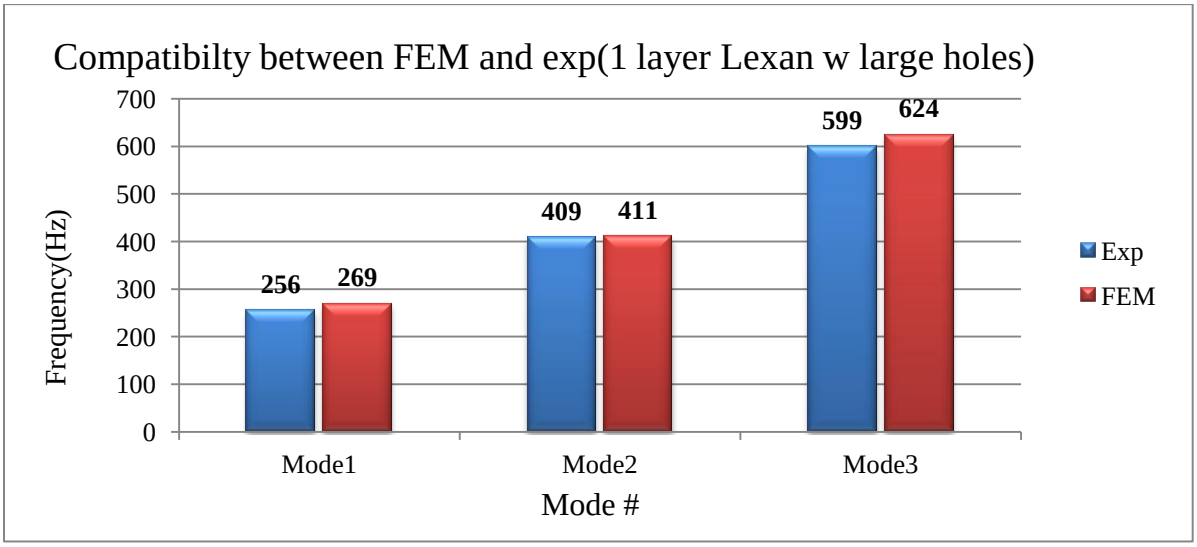

Figure 6.29: Compatibility between experiment and FEM results (1 Layer Lexan w/large holes).

Figure 6.29 shows the very good agreement between experimental and finite element results for each of the first three modes that were considered. This suggests that the experiments were carefully and accurately carried out.

As mentioned before USIL Light was selected to represent the sandwich structures, figures 6.30 to 6.37 shows the following results for USIL Light:

Figure 6.30: The stability diagram which indicates the first three natural frequencies

Figure 6.31: FRF, Coherence and phase

Figure 6.32: FRF results from RADIOSS

Figure 6.33: 1st three mode shapes (displacement contour)

Figure 6.34: 1st three mode shapes using Matlab

Figure 6.35: Maximum deflection for the 1st three modes

Figure 6.36: Damping ratio for the 1st three modes

Figure 6.37: Compatibility between experiment and FEM results

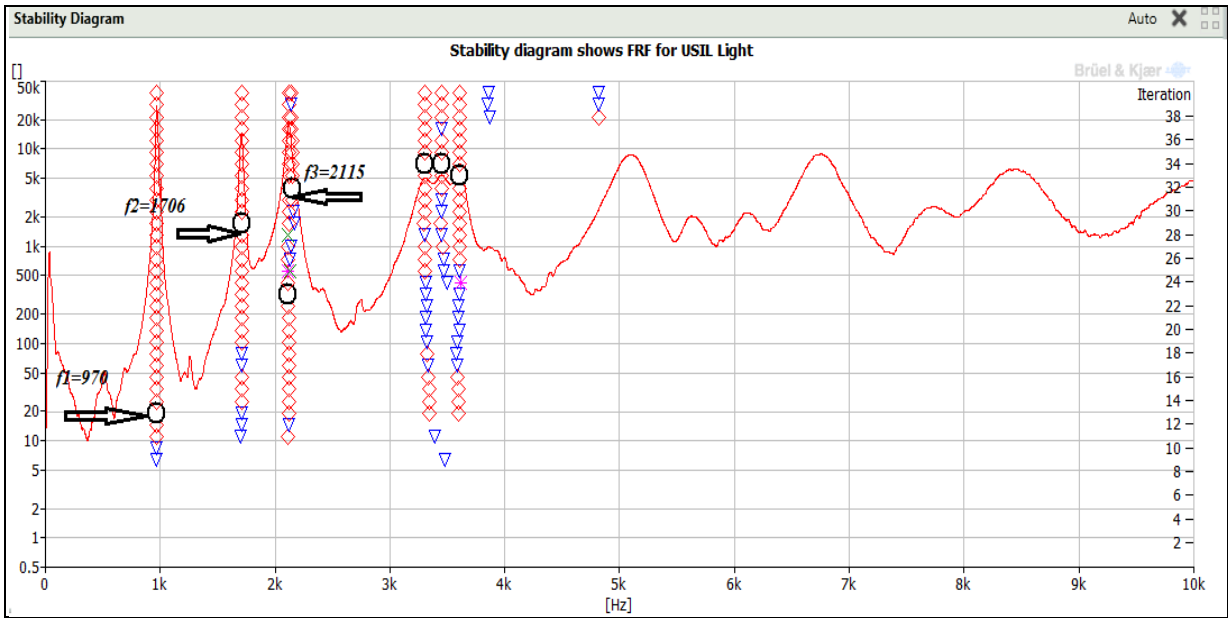

Figure 6.30: The stability diagram which indicates the first three natural frequencies

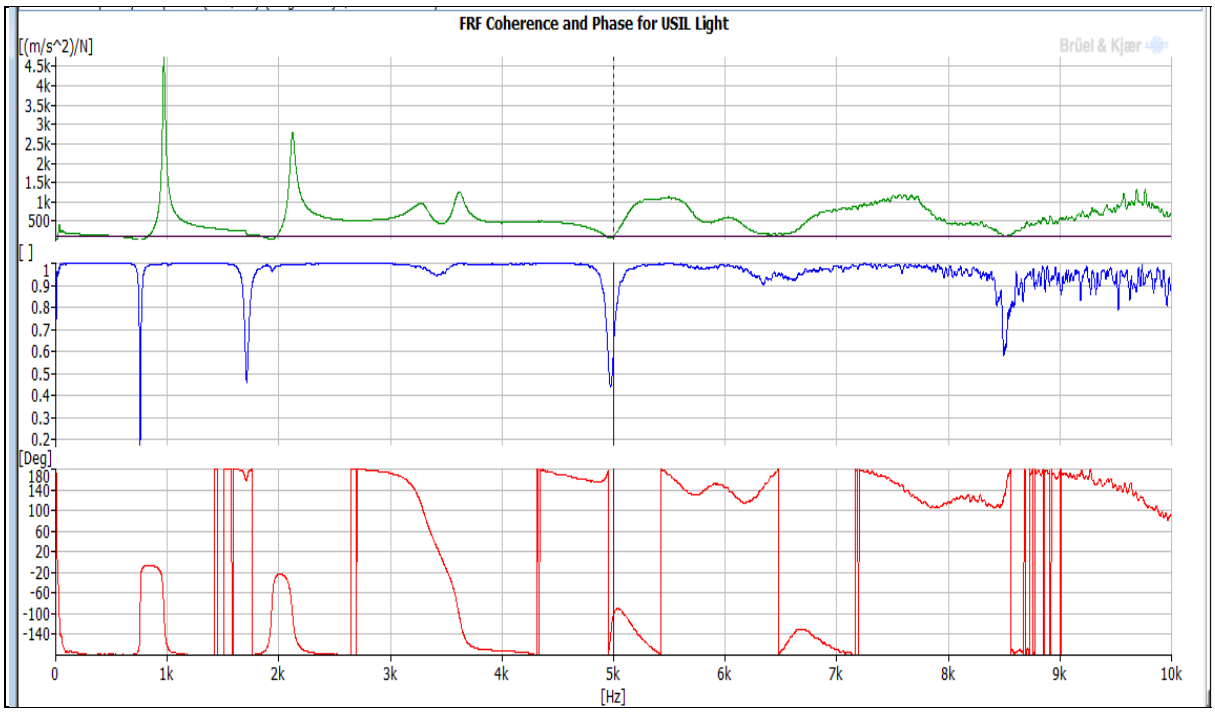

Figure 6.31: FRF, Coherence and phase

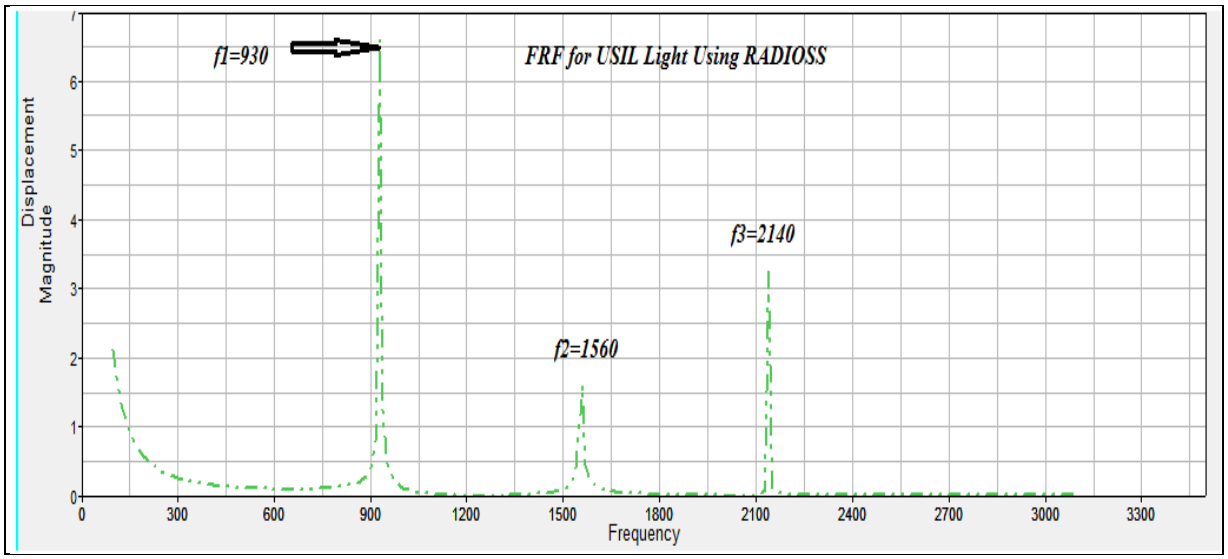

Figure 6.32: FRF results from RADIOSS

The FRF diagram shown in figure 6.30 obtained from PULSE Reflex shows very crisp peaks and well-spaced out resonances suggesting that the material was manufactured with precision. The coherence values (figure 6.31), are virtually at the maximum level and the phase at resonance (about 90^0), the FRF from RADIOSS program (Altair Inc.), which is clear in figure 6.32, shows a very good match with the experiment. It should be noted that the material was treated as a composite within the RADIOSS program, putting in the appropriate set of material properties for the skin and the core separately.

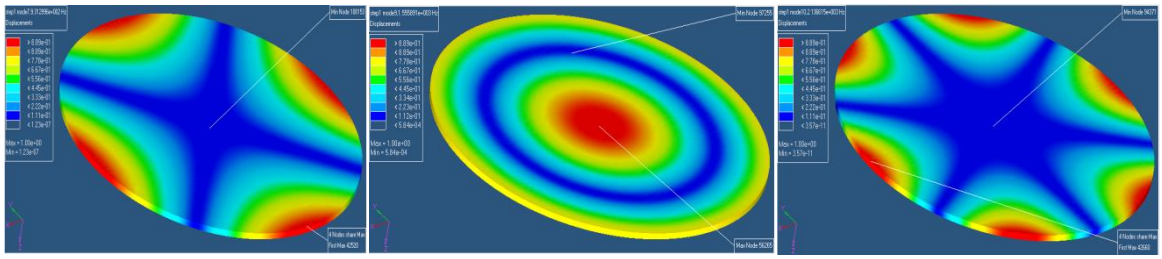

(Displacement Contour) Mode1 Mode2 Mode3

Figure 6.33: 1st three mode shapes (displacement contour)

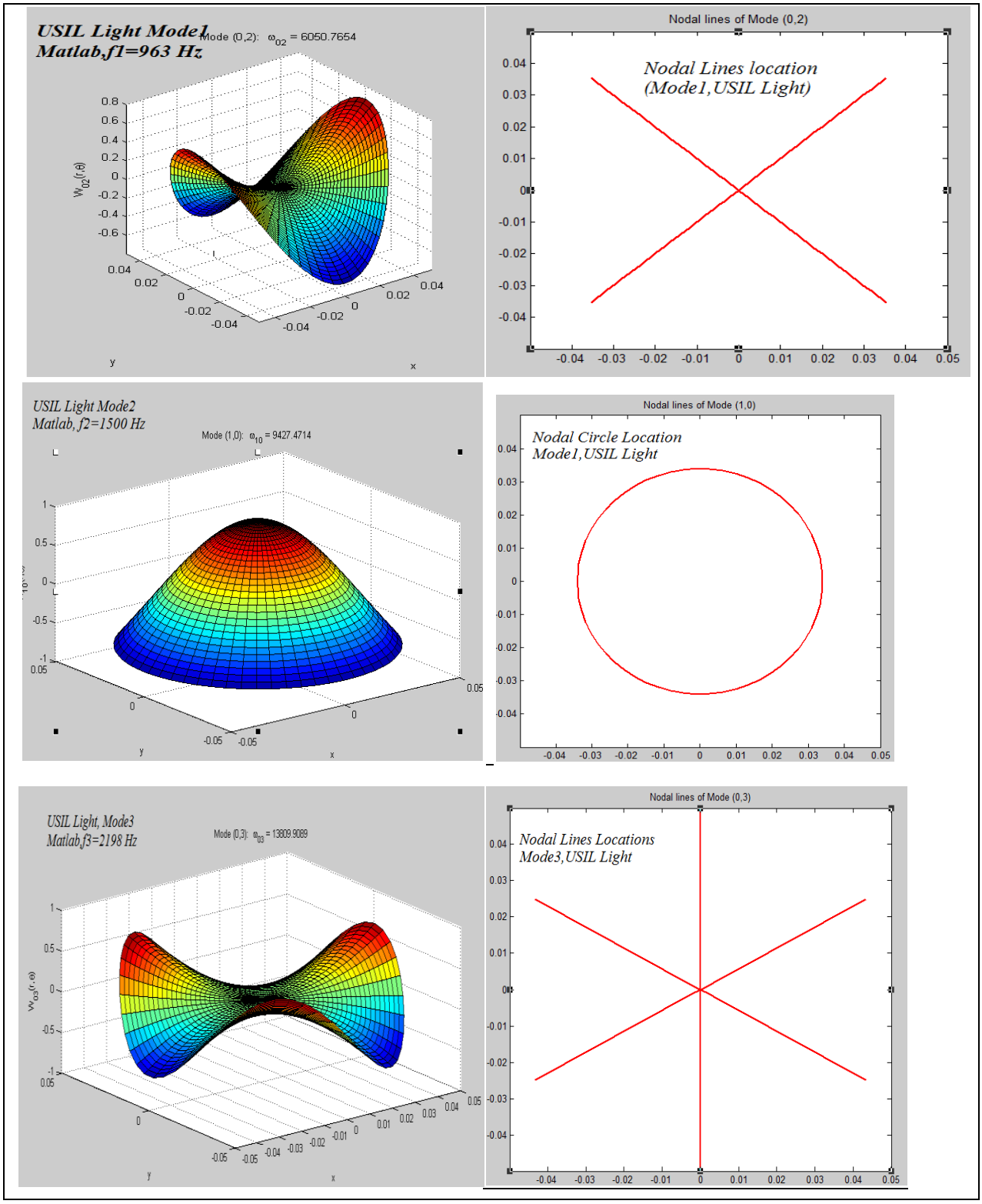

Figure 6.34: 1st three mode shapes using Matlab

As can be seen from figures 6.33 and 6.34, mode shapes obtained by finite element (Abaqus) and Matlab agree completely. The Matlab code allows one to view the locations and patterns of the nodal curves (here lines or circles as the case may be), these also shown in figure 6.34.

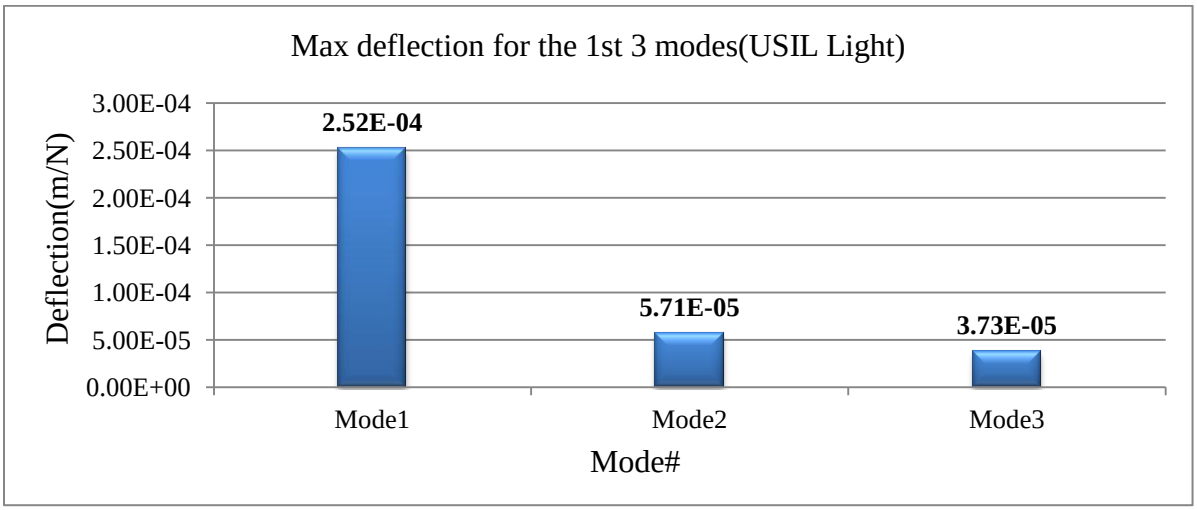

Figure 6.35: Maximum deflection for the 1st three modes

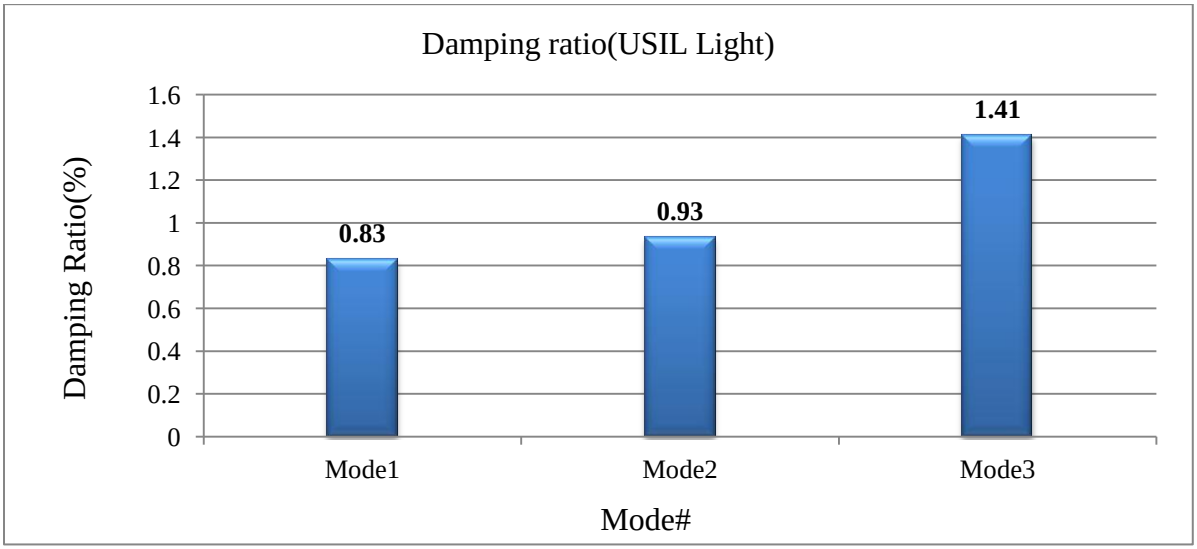

Figure 6.36: Damping ratio for the 1st three modes

Once more it can be seen (figures 6.35, 6.36) that mode1 is dominant with the largest value of maximum displacement among the first three modes. Its modal damping ratio is also the least in this frequency range.

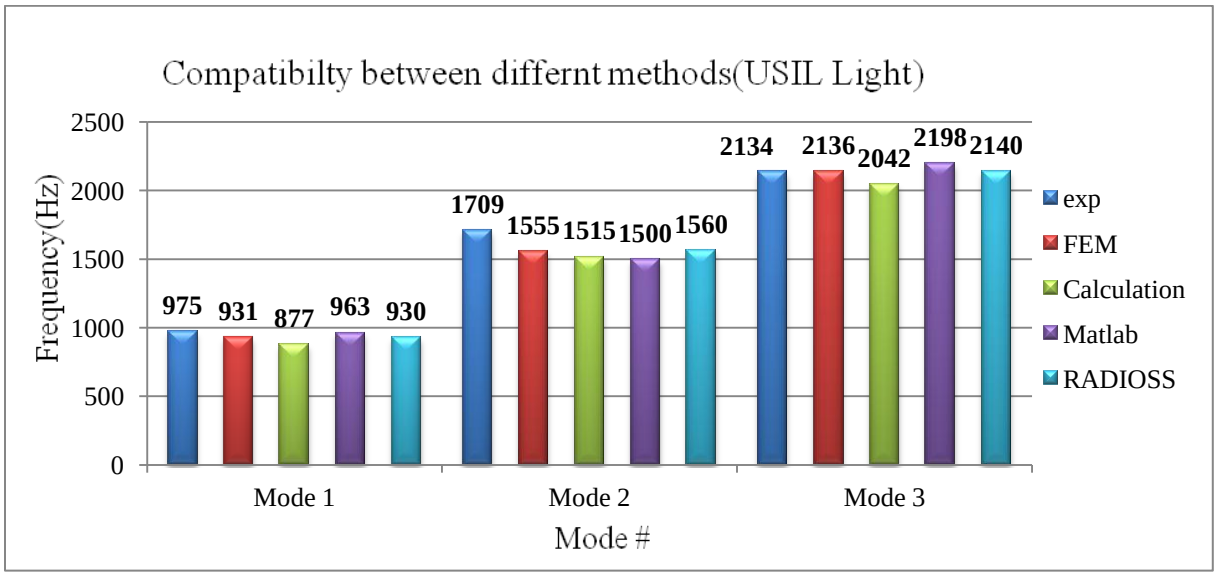

Figure 6.37: Compatibility between experiment and numerical methods results

Figure 6.37 shows very good agreement between experimental and four numerical methods. Excluding the calculation, the maximum deviations of the numerical methods from experimental are 4.6%, 8.7%, 0.2% for modes1to 3 respectively. For the calculations and Matlab method, effective values of Young's modulus E, Poisson's ration ν, and density ρ were utilized. The effective values were based upon the relative thicknesses. Also, the calculation approach employed the Rayleigh energy method to obtain resonance frequencies, while the Matlab solution utilized Bessel functions, which generally give more accurate solutions. Accordingly, the calculation results deviated a little further than the other numerical results. Thus, taking the calculation method into account, the maximum deviations of the numerical methods from experimental are 10%, 9.5%, 4.7% for modes1to 3 respectively.

Table 6.3 below compares the number of elements, number of nodes and element type from finite element simulations for the sandwich and monolithic group; on the other hand the number of peaks from experimental results is shown to indicate modal densities of these samples over a specified frequency range(0-1.6kHz for monolithic and 0-6.4kHz for sandwich).

Table 6.3: Comparison between sandwich and monolithic samples according to number of nodes, elements and element type, with the modal densities

Material		# of nodes	#of elements	Element type	#of peaks(0-1.6kHz monolithic,0-6.4kHz Sandwich)
Sandwich Materials	CRS w/LE 5208	91697	20480	C3D20	4
	USIL Light	70733	15360	C3D20	6
	3Layer Lexan[1]	49098	81876	C3D6	12
	5Layer Lexan[3]	48384	78852	C3D6	14
Monolithic Materials	Single Layer Solid Lexan	7154	3536	C3D20	5
	1 Layer Lexan w/small holes	80156	113784	C3D6	6
	1 Layer Lexan w/membrane	30977	908(membrane) 44232(Lexan)	S3(membrane) C3D6(Lexan)	5
	1 Layer Lexan w/large holes	80156	113784	C3D6	5
	CRS Alone	5931	3848	C3D8I	5

Table 6.4 compares the vibration results for the sandwich and monolithic group, and then these results are shown in a graphical representation in order to give a better understanding about the behavior of these structures.

Table 6.4: Vibration results for Sandwich and Monolithic structures

Material		Mode#	Damping Ratio (%)	Natural Frequency(Hz)		Max deflection(m/N)
				Experiment	Finite Element	
Sandwich Materials	Cold Rolled Steel w/LE5208	1	1.19	3223	3139(2.6%)	0.0000058
		2	1.65	4726	4617(2.3%)	0.00000154
		3	1.95	5289	5354(1.2%)	0.00000161
	USIL Light	1	0.83	970	931(4%)	0.000252
		2	0.93	1706	1555(8.8%)	0.0000571
		3	1.41	2115	2136(0.1%)	0.0000373
	2 layer solid Lexan	1	2.67	598	621(3.8%)	0.00065785
		2	3.51	732	1115(34%)	8.86696E-05
		3	3.38	1042	1432(27%)	0.00012856
	3Layer Lexan[1]	1	1.57	768	838(9%)	0.000162
		2	1.73	1153	1508(23%)	2.92E-05
		3	1.64	1514	1914(21%)	4.47E-05
	5Layer Lexan[2]	1	0.46	1271	1358(6.8%)	7.79E-05
		2	1.54	1955	2420(19%)	2.12E-05
		3	2.41	2784	3004(7.3%)	1.72E-05
Monolithic Materials	1 layer solid Lexan	1	1.32E+00	310	313(0.9%)	1.67E-03
		2	2.70E+00	581	563(3%)	3.87E-04
		3	1.41E+00	715	728(1.8%)	6.19E-04
	1 Layer Lexan w/small holes	1	1.50E+00	303	318(5%)	2.20E-03
		2	3.58E+00	556	559(0.5%)	0.000447
		3	1.65E+00	704	736(4.5%)	0.000538
	1 Layer Lexan w/membrane	1	1.47E+00	290	322(11%)	2.32E-03
		2	2.24E+00	526	574(9%)	2.96E-04
		3	2.05E+00	681	746(9.5%)	5.46E-04
	1 Layer Lexan w/large holes	1	2.58E+00	256	269(5%)	3.56E-03
		2	1.45E+00	409	411(0.5%)	7.78E-04
		3	1.44E+00	599	624(4%)	7.77E-04
	CRS Alone	1	0.76	355	333(6%)	0.00249
		2	0.46	411	553(25%)	0.00184
		3	0.24	863	772(10%)	0.00178

1: Solid-Membrane-Solid 2: Solid-3 Layers w/Small Holes-Solid

It should be mentioned here that, as shown in table 6.4, the percentage error in multi layer Lexan samples was high and this is due to a number of reasons. The gluw ("Supergluw") between the layers did not cure strongly enough, and we had to assemble and disassemble the unit many times to do the experiments of different configurations, hence, air pockets and delaminations could not be ruled out for our Lexan structures.

Figures 6.38 to 6.42show the comparisons between the different samples of the monolithic materials as follows:

Figure 6.38: Comparison between numbers of elements

Figure 6.39: Comparison between natural frequencies for the 1st three modes

Figure 6.40: Comparison between maximum deflections for the 1st three modes

Figure 6.41: Comparison between damping ratios for the 1st three modes

Figure 6.42: Comparison between modal densities

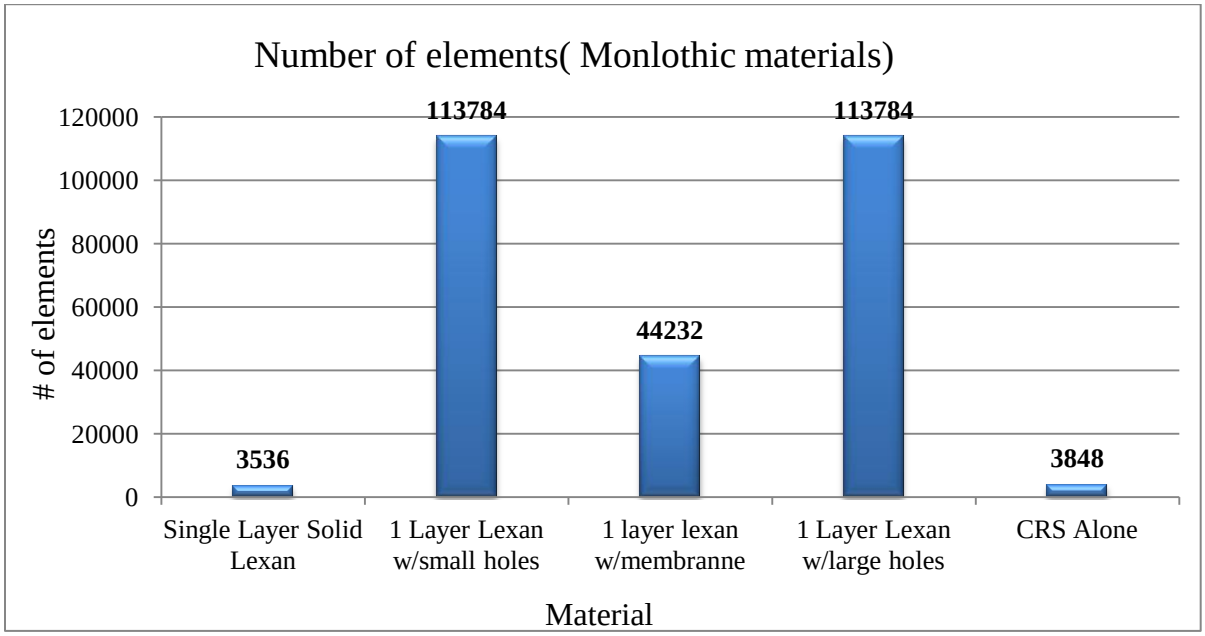

Figure 6.38: number of elements for monolithic materials

The number of elements for monolithic materials(figure 6.38) depend upon the architecture, as can be seen from figure 6.38 the Lexan with holes have more elements than solid Lexan and this is due to the fact that the holes make the structure more complex and therefore it needs more elements to mesh it.

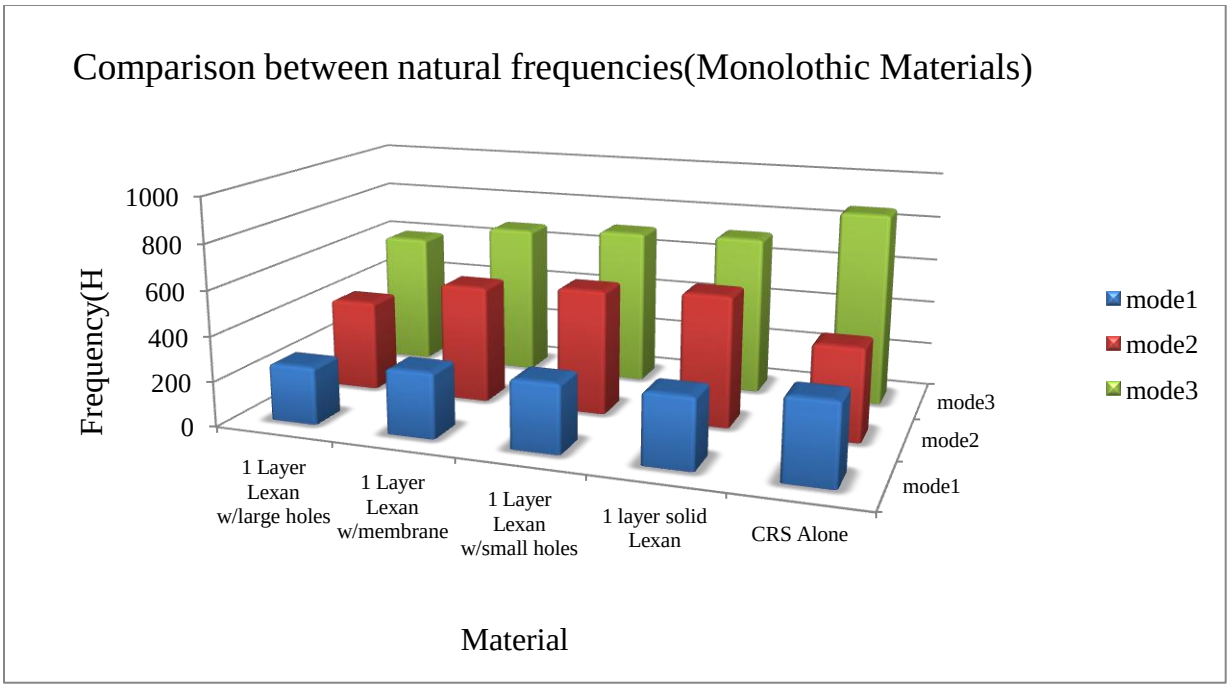

Figure 6.39: Comparison between natural frequencies for the 1st three modes

The modal resonance frequencies experienced in each mode of the Lexan samples as can be seen in figure 6.39 seem to follow the order of the values of overall flexibility as would be expected. The more material is removed from the solid Lexan, the more flexible the sample becomes, and the less the resonance frequencies. No direct comparisons could be drawn between the Lexan and the CRS because of material and thickness differences. It follows that material addition, deletion, or substitution within the sample could be utilized to alter resonance frequencies and deflections.

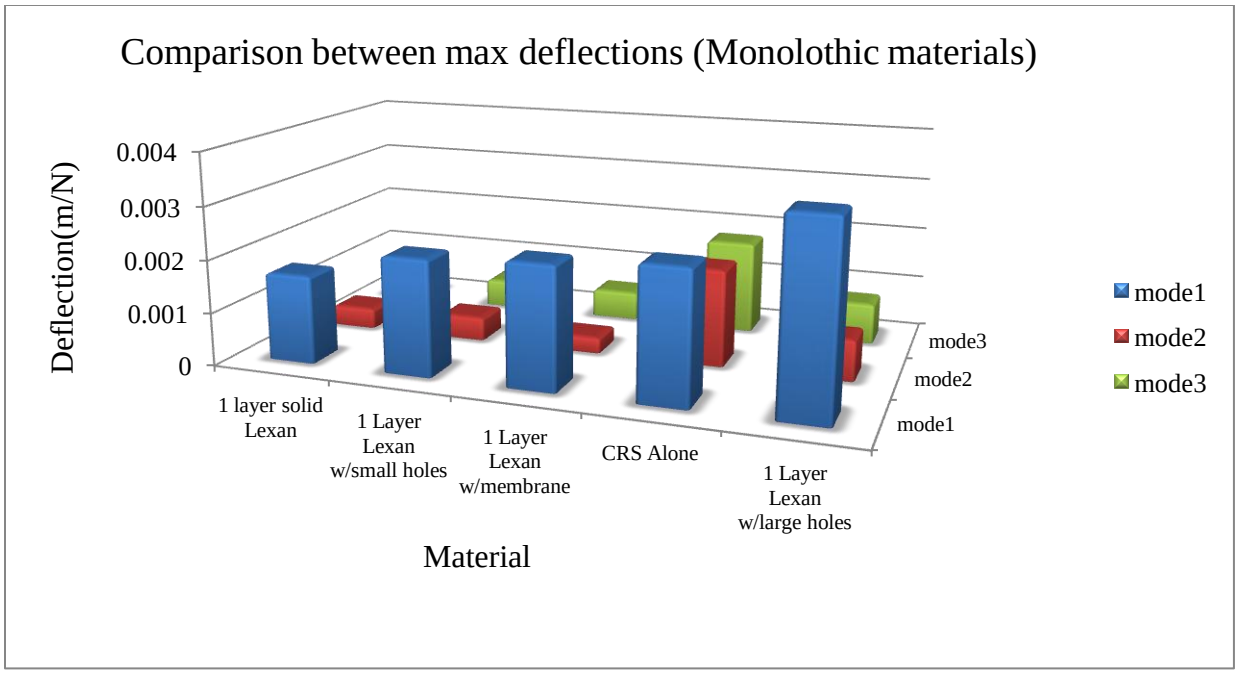

Figure 6.40: Comparison between maximum deflections for the 1st three modes

Figure 6.40 shows the maximum deflection experienced in the first mode by the Lexan samples (all of the same thickness) seems to follow the order of the values of overall flexibility as would be expected. The more material is removed from the solid Lexan, the more flexible the sample becomes. Across materials structural rigidity values (involving elastic modulus, density and geometry) values affect deflections and other variables. With more structural complexity and with the higher modes, the modal deflections distribution may be more complex.

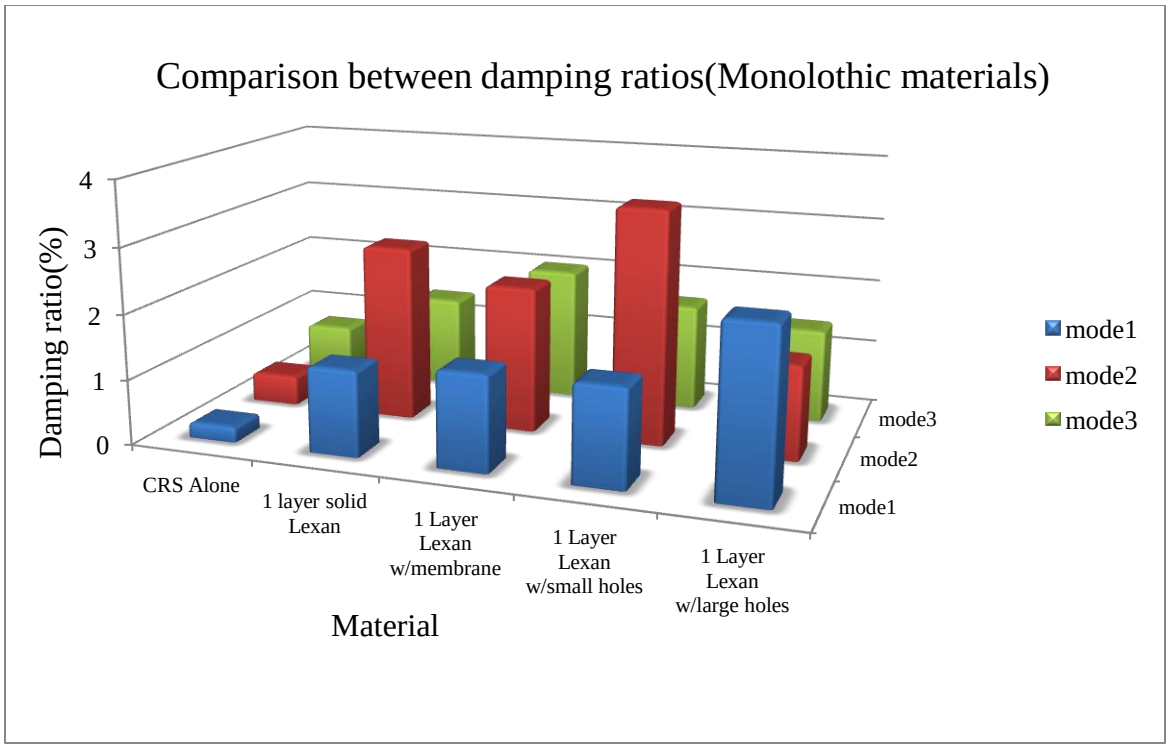

Figure 6.41: Comparison between damping ratios for the 1st three modes

The damping ratio of the metallic CRS is very small as expected of this class of materials. The modal damping ratios (figure6.41) are much higher for the plastic polycarbonate Lexan material than for the CRS. The more solid the material is, it appears that the less the mode-1 damping. For higher modes this may not be guaranteed as the mode shapes vary widely across the modes. Some modes involve predominantly shearing motion and some bending motion.

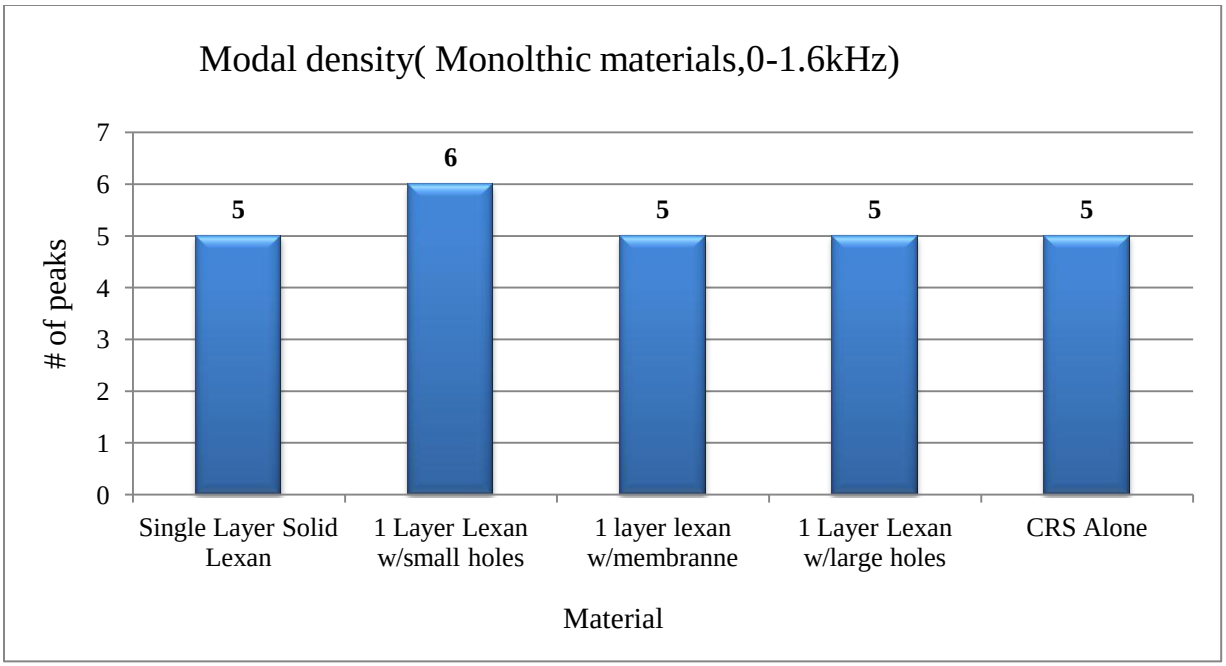

Figure 6.42: Comparison between modal densities

The number of peaks in the (0-1.6 kHz) is practically the same for all the samples. This is believed to be due to the fact that structures are simple disk in each case. Complexity is introduced by the holes drilled into the sample but apparently this does not begin to be significant until the case of Lexan with small holes. In that case we have the largest number of holes (21). This means that from the point of view of manufacturing costs any of these structures could be utilized based on other factors. Figure 6.42shows these facts.

Figures 6.43 to 6.47shows the comparisons between the different samples of the sandwich materials as follows:

Figure 6.43: Comparison between numbers of elements

Figure 6.44: Comparison between natural frequencies for the 1st three modes

Figure 6.45: Comparison between maximum deflections for the 1st three modes

Figure 6.46: Comparison between damping ratios for the 1st three modes

Figure 6.47: Comparison between modal densities

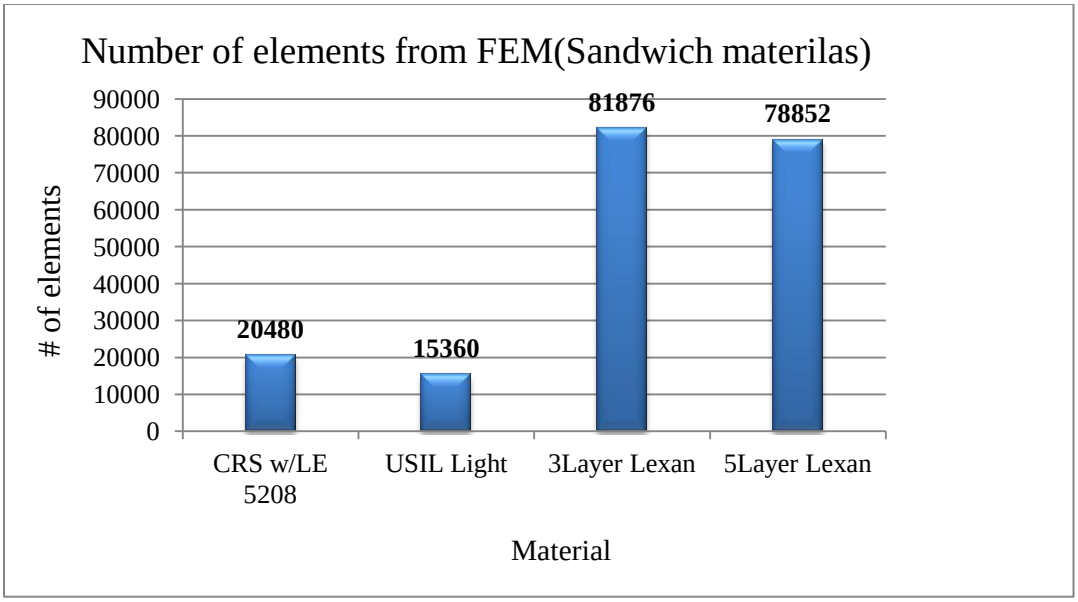

Figure 6.43: Comparison between numbers of elements

From figure 6.43 it may be observed that the Lexan samples shown required a lot more nodes to mesh them than the CRS and USIL light samples. The first reason for these is that the Lexan samples are layered structures. Secondly it is also seen that more nodes were required to mesh the three layer Lexan than the five layer Lexan. This was so because the three layer Lexan had holes and the membrane film which both took more nodes to numerically define them.

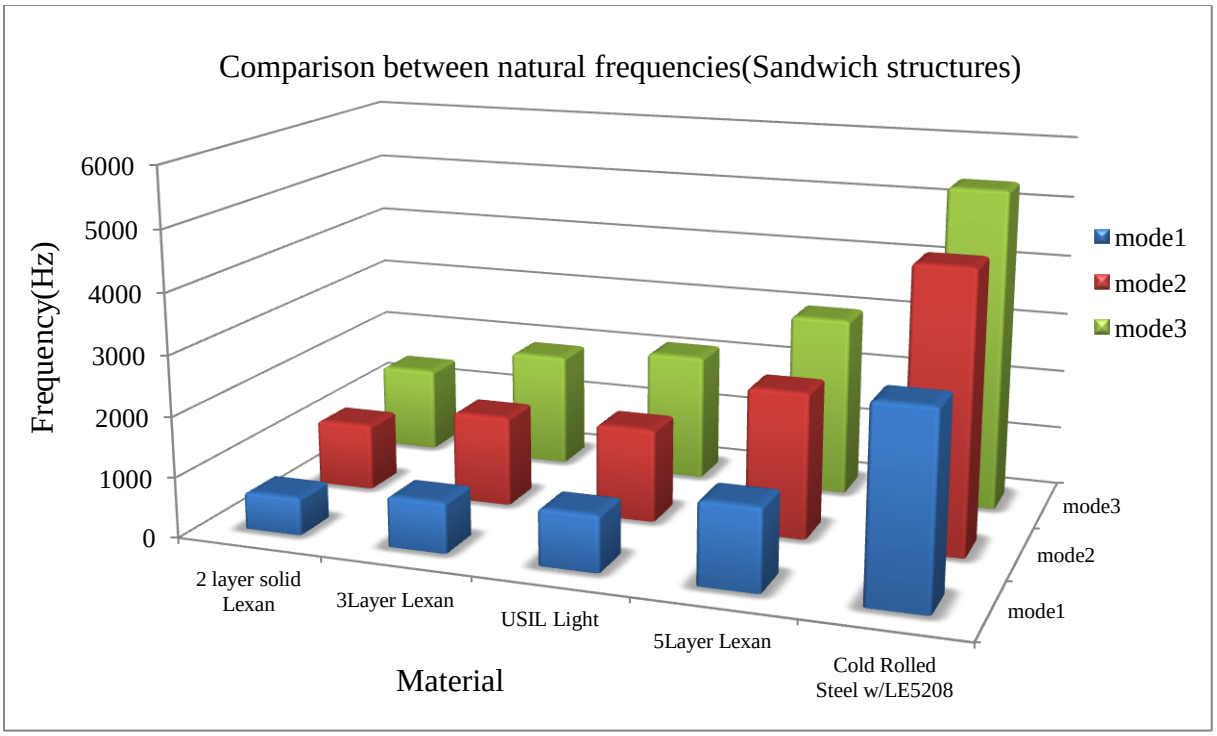

Figure 6.44: Comparison between natural frequencies for the 1st three modes

The distribution of the natural frequencies on as shown in figure 6.44 is very regularly distributed over the first three modes shown, essentially on the basis of stiffness. Thus, since each Lexan layer is of the same 2mm thickness, the natural frequency of the 3 layer structure is higher than that of the 2 layers, etc. It may be recalled that theoretically, the square of natural frequency is proportional to the ratio of the distribution of stiffness to that of mass in the structure.

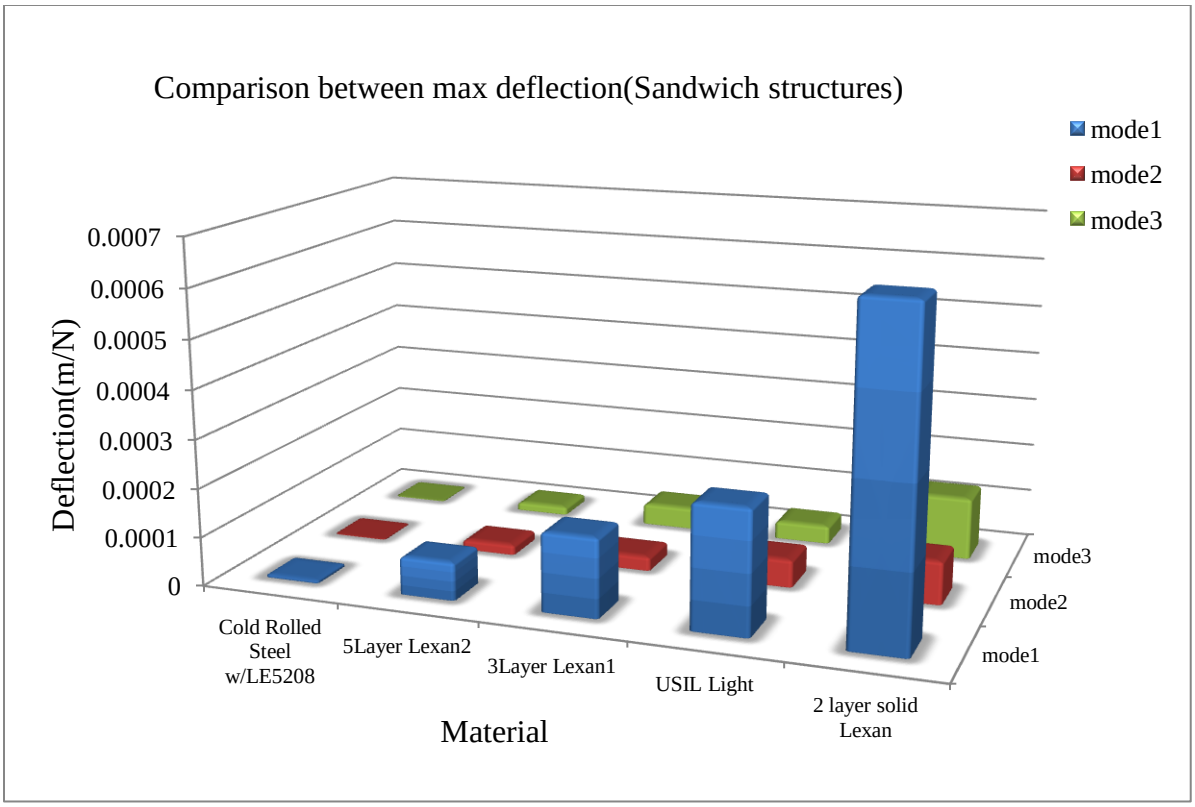

Figure 6.45: Comparison between maximum deflections for the 1st three modes

The maximum deflection values (figure 6.45) seem to show inverse relationship to the rigidity of the specimens, as would be expected from fundamental consideration of vibration principles. The maximum deflection of the CRS is much less than that of any of the Lexan structures because of the significant difference between their elastic moduli.

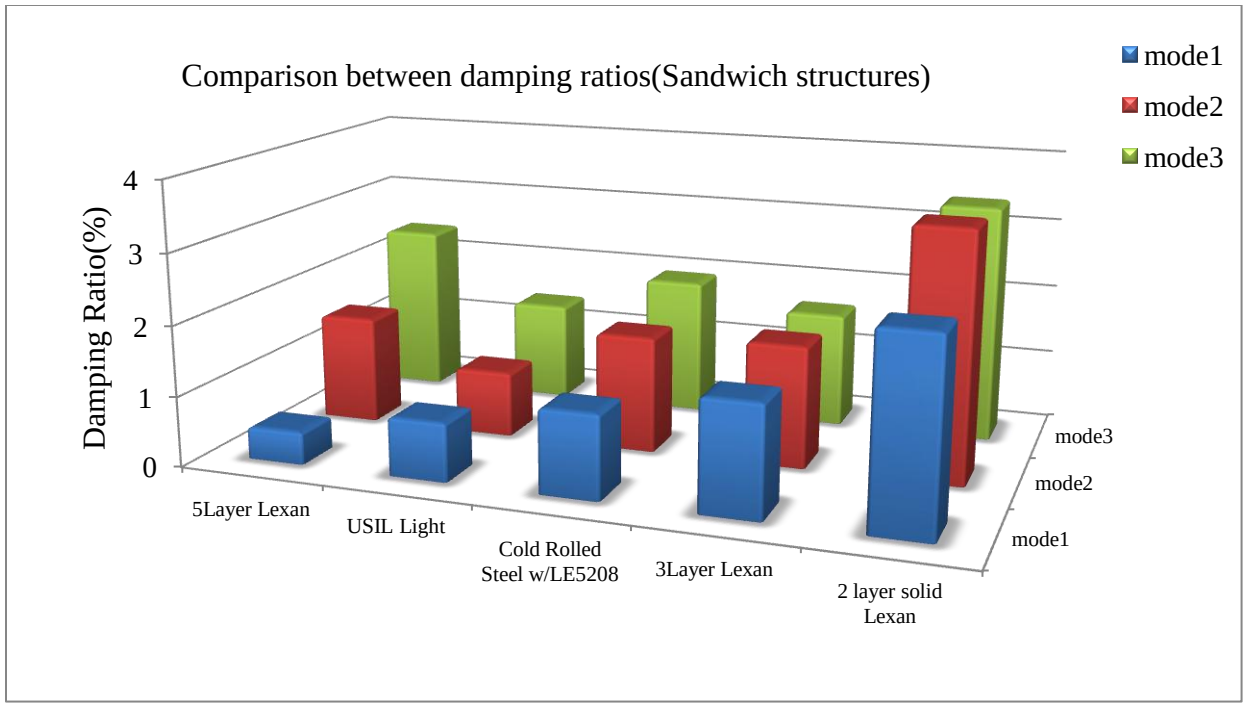

Figure 6.46: Comparison between damping ratios for the 1st three modes

The modal damping ratio values shown in Figure 6.46 indicate for the Lexan, more thickness seems to degrade the damping of the structure. The USIL light and CRS/LE 5208 sandwiches take positions in this arrangement based on their rigidities and the material damping in their make-up

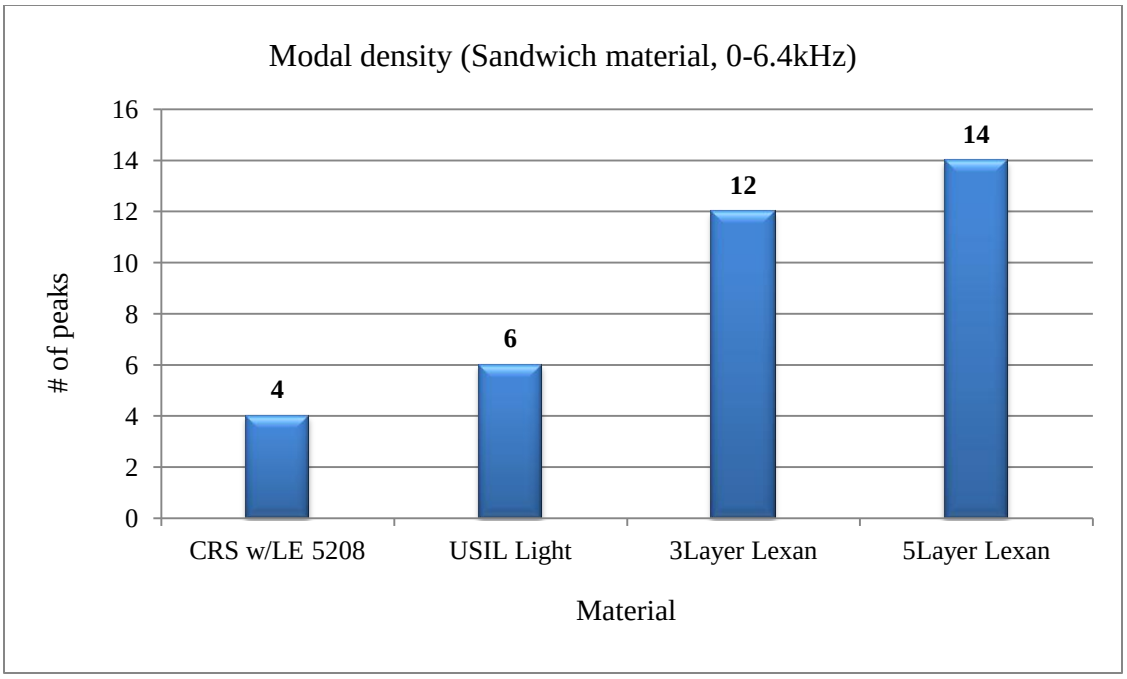

Figure 6.47: Comparison between modal densities

The modal density which is shown in figure 6.47 (0-6.4 kHz) for sandwich structures shows up as four and sex respectively for the CRS and USIL Light structures. This is sparse, showing that the structures are simple and behaved like well-bonded compact disks. On the other hand the multi-layer Lexan samples manifested many more resonances in the same frequency interval. This is due to the presence of several layers and less than perfect adhesive bonding, the presence of holes and membranes as the case may be. Such additional factors usually add more resonance peaks to the vibration response of the structure.

6.3.3 PERIODIC CELLULAR MATERIAL STRUCTURES (PCMS) MATERIALS

The PCMS materials were tested for vibration behavior using PULSE 16.1. To verify the experimental results, finite element simulation was used to get the natural frequencies, and mode

shapes, for each of the samples. The sample selected for PCMS group was Aluminum prismatic Microtruss (circular sample). It should be mentioned here that this sample has been cut from a rectangular sample which we got from the Cellular material Inc (CMI), to fit inside the impedance tube, we noticed that it was very critical to select the coordinates of the cut as it affects the vibration behavior of the material as we will see in the parametric study section later.

Figures 6.48 through 6.54 shows the results for this sample as follows:

Figure 6.48: The stability diagram which indicates the first three natural frequencies

Figure 6.49: FRF, Coherence and phase

Figure 6.50: FRF results from RADIOSS

Figure 6.51: 1st three mode shapes (displacement contour)

Figure 6.52: Maximum deflection for the 1st three modes

Figure 6.53: Damping ratio for the 1st three modes

Figure 6.54: Compatibility between experiment and FEM results

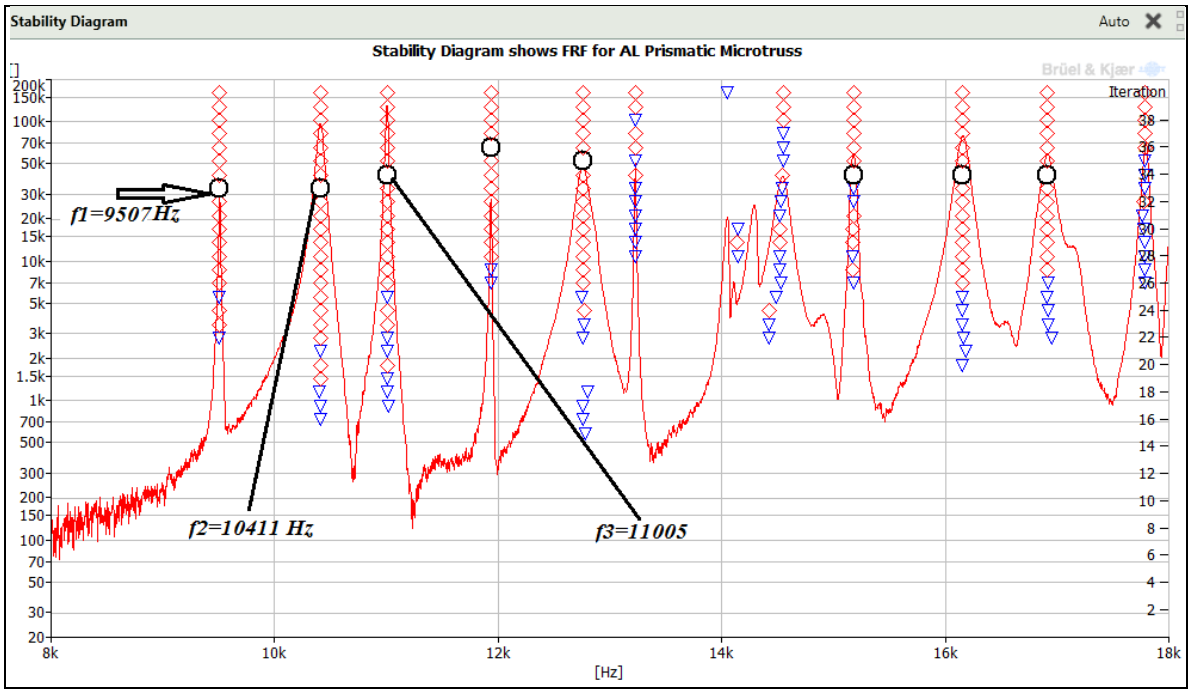

Figure 6.48: The stability diagram which indicates the first three natural frequencies

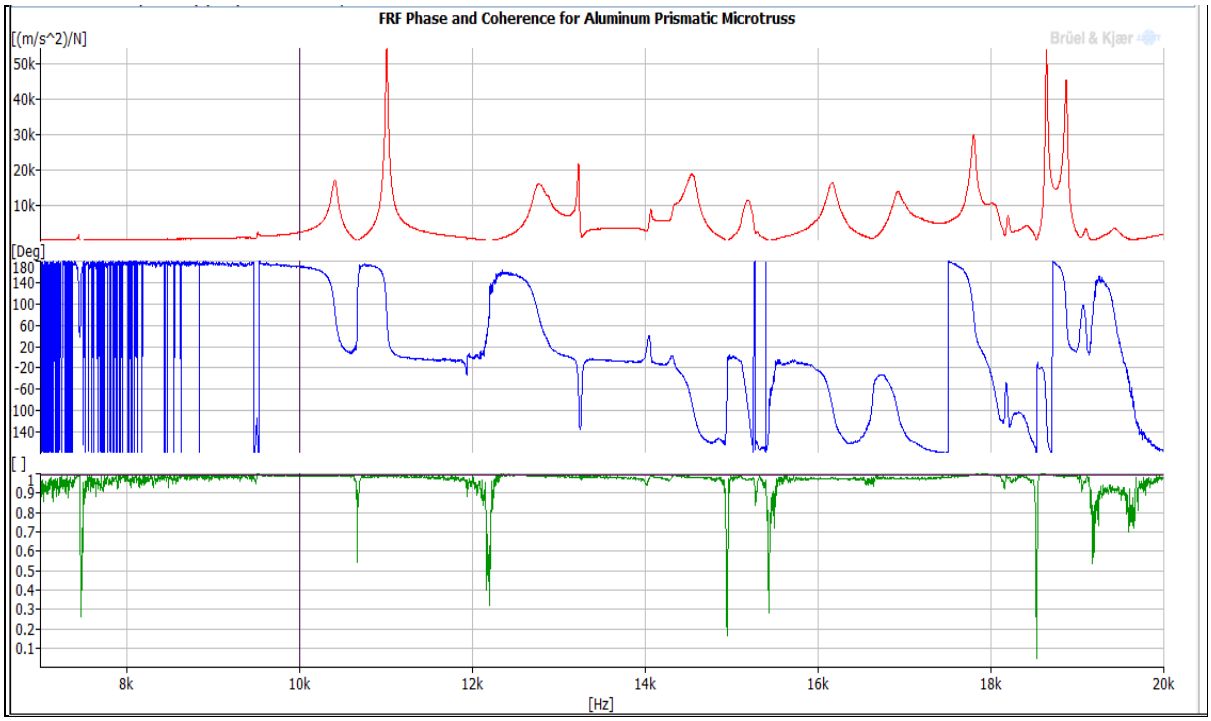

Figure 6.49: FRF, Coherence and phase

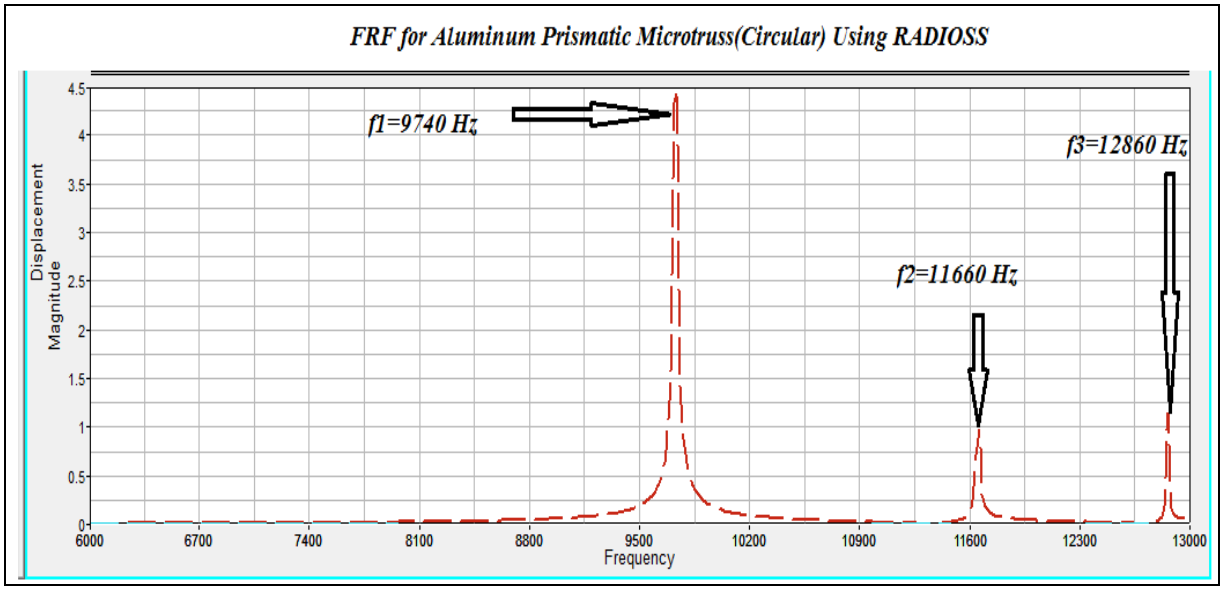

Figure 6.50: FRF results from RADIOSS

Figures 6.48 show the stability diagram, a display of the most accurate rendering of the FRF with different useful annotations. The fact of the structure's complexity is obvious, on account of having many resonances. The resonances are well spaced out and distinct, suggesting that the bending vibration modes are clear and practically free of mixed modes and distortions. From figure 6.49 we observe that the virtually universal unity value of the coherence suggests excellent experimentation, and the phase record is unequivocal in showing the true peaks. Figure 6.50 which was obtained from the RADIOS program of Altair Inc. corroborates the experimental PULSE Bruel & Kjaer experimental results.

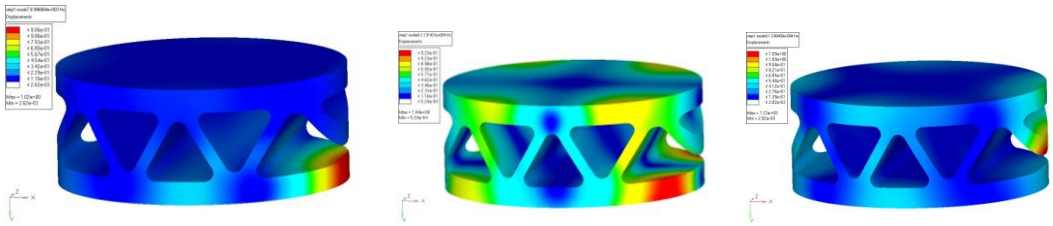

(Displacement contour) Mode1 Mode2 Mode3

Figure 6.51: 1st three mode shapes (displacement contour)

It is obvious from the mode shapes shown in figure 6.51 that the deflections experienced by the upper and lower skins of the structure tend to be quite different. This is due to the disconnection in the core structure joining the skins together. This hanging lip is quite visible in each of the modes. This translates to freedom of motion for the unconnected edge which therefore experiences the maximum displacement, as also shown by the bright colors in the displacement contour legend. It is therefore not surprising that the mode shapes of this structure with a cut are not identical to those of a completely connected structure such as the rectangular sample which shall be mentioned in the section on parametric studies.

This behavior constitutes a very important point with respect to the extraction of parts of different shapes from a block of material that may be available in the engineering store.

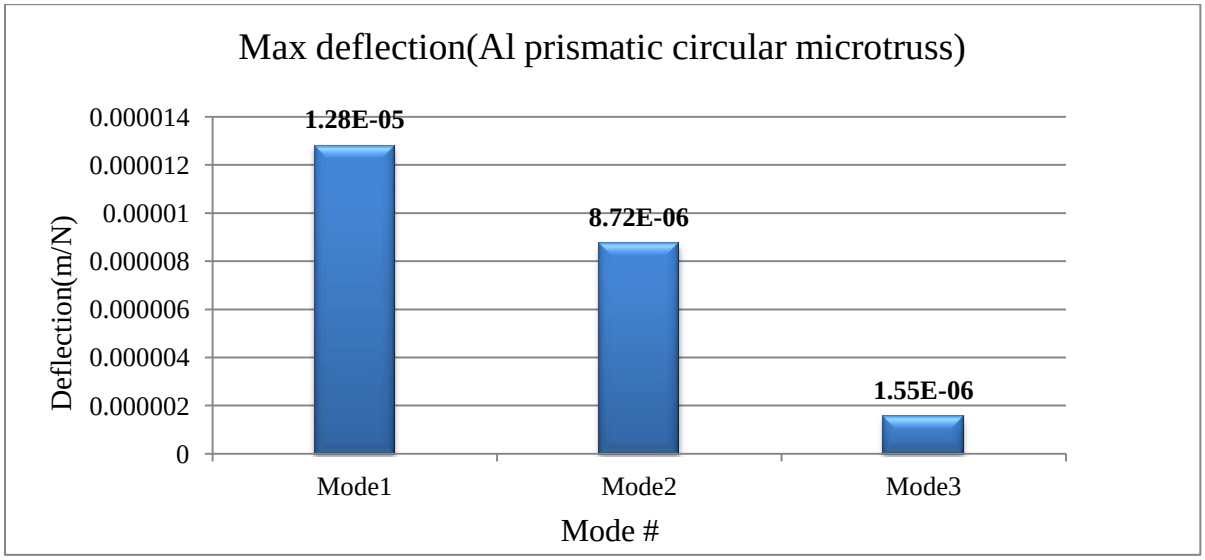

Figure 6.52: Maximum deflection for the 1st three modes

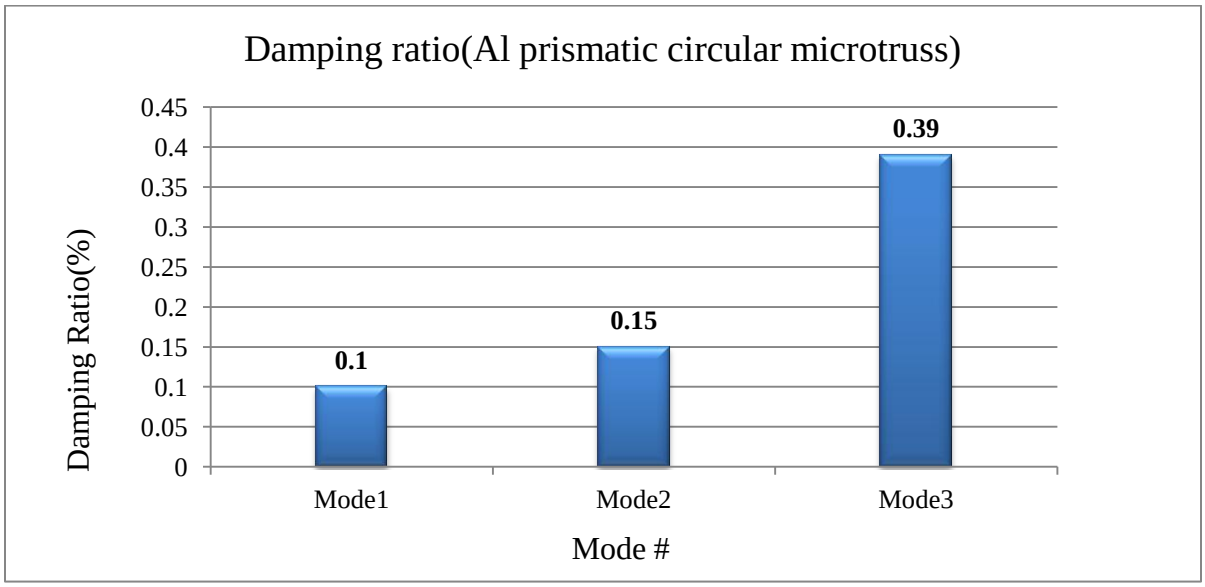

Figure 6.53: Damping ratio for the 1st three modes

Figures 6.52 and 6.53 show that the maximum deflection decrease progressively from mode one to mode three, whereas the modal damping ratio behaves on the opposite way. The damping ratio

values are very reasonable for an aluminum structure, and their sequence shows that the fundamental mode appears to be the most important for the deformation history of this structure. It may be recalled that stress is generally proportional to deflection.

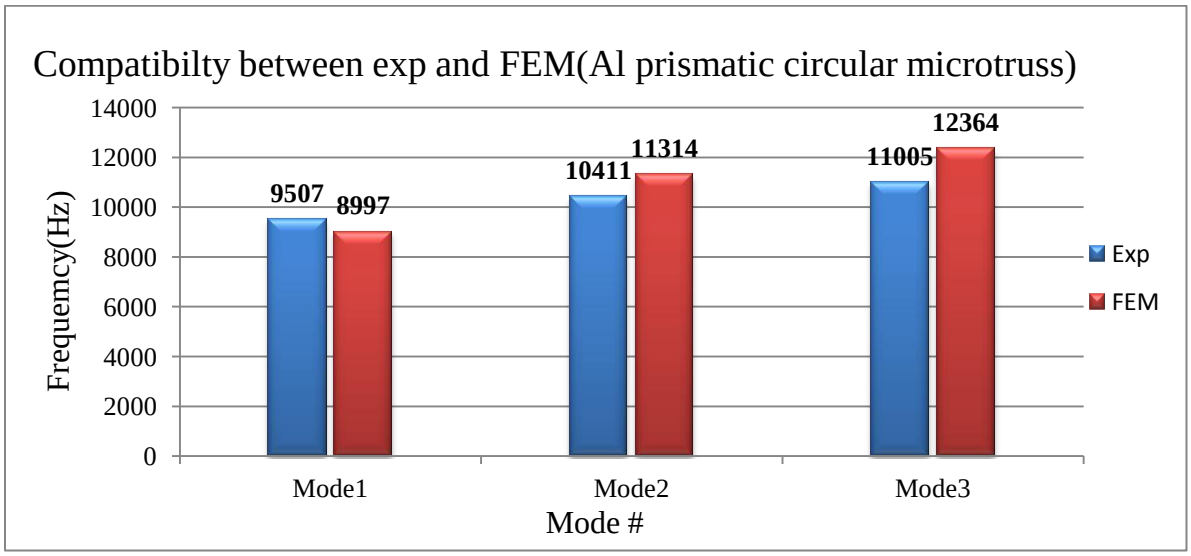

Figure 6.54: Compatibility between experiment and FEM results

Figure 6.54 clearly shows the good agreement between experimental and FEM Abaqus results for natural frequencies. This agreement is considered quit good in light of the fact that it proved impossible to obtain a numerical cut to coincide exactly with the experimental specimen. The percentage deviation from experimental values varied from 5.3% for mode one through 8.6% for mode two to 12% for mode three. The RADIOSS results were not included in this figure because of the limitation on our computing resources restricted us to the use of only one node for the RADIOSS computations.

Table 6.5 compares the number of elements, number of nodes and element type from finite element simulations for the PCMS group; on the other hand the number of peaks from experimental results is shown to indicate modal densities of these samples over a specified frequency range.

Table 6.5: Comparison between PCMS samples according to number of nodes, elements and element type, with the modal densities

Material	# of nodes	#of elements	Element type	#of peaks(0-10kHz)
Aluminum prismatic Microtruss	90015	403255	C3D4	14
Stainless steel triangular honeycomb Microtruss	99938	306280	C3D4	30
Pyramidal aluminum Microtruss	-	-	-	26

Table 6.6 compares the vibration results for the PCMS group, and then these results are shown in a graphical representation in order to give a better understanding about the behavior of these structures.

Table 6.6: Vibration results for PCMS materials

Material	Mode#	Damping ratio(η)%	Natural frequency(Hz)		Max deflection(m/N)
			Experimental	Finite Element	
Alumium prismatic microtruss	1	0.1	9507	8997(5.3%)	0.0000128
	2	0.39	10411	11314(8.6%)	0.00000872
	3	0.15	11005	12364(12%)	0.00000155
Stailess steel triangular honeycomb microtruss	1	0.047	4275	4020(6%)	0.0000125
	2	0.15	4521	4172(7.7%)	0.00000214
	3	0.083	4769	4327(9%)	0.00000322
Pyramidal* aluminum microtruss	1	0.15	2466	-	0.000152
	2	0.32	3181	-	0.000046
	3	0.38	7143	-	0.00000372

*: the sample was not simulated due to its complexity

Figure 6.55 to 6.59 shows the comparisons between the different samples of the PCMS materials as follows:

Figure 6.55: Comparison between numbers of elements

Figure 6.56: Comparison between natural frequencies for the 1st three modes

Figure 6.57: Comparison between maximum deflections for the 1st three modes

Figure 6.58: Comparison between damping ratios for the 1st three modes

Figure 6.59: Comparison between modal densities

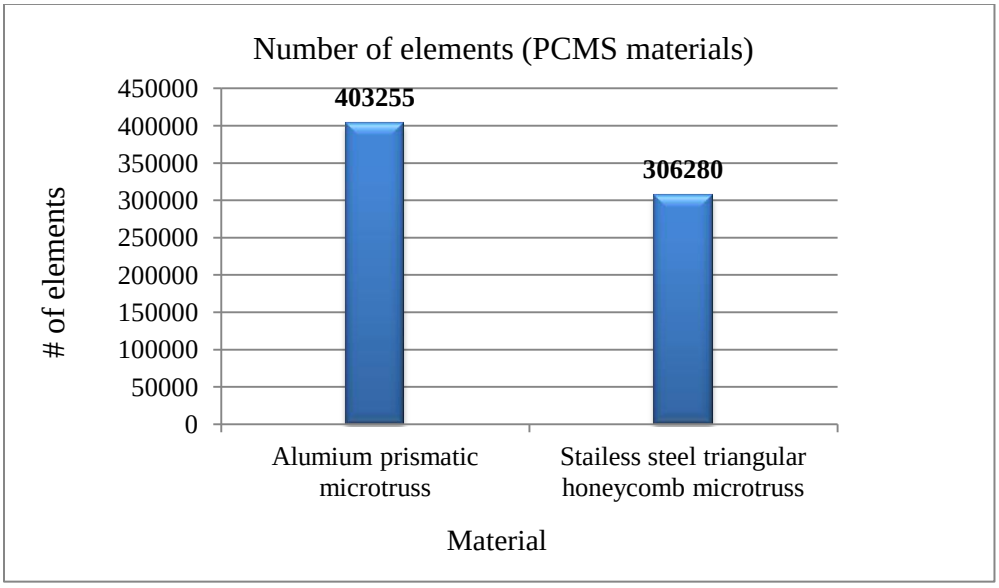

Figure 6.55: Comparison between numbers of elements

As can be seen from figure 6.55, the finite element computations for these structures made very intensive use of computer resources. For instance over 400000 elements and over 300000 elements respectively were used to mesh the aluminum and stainless steel PCMS samples. Wayne State University only holds a student license in Abaqus that does not exceed 100000 nodes. The element numbers are so high because of the intricacy of the designs of these structures. Moreover more elements were required to mesh the aluminum prismatic Microtruss than for the stainless steel honeycomb because the former had more material in it.

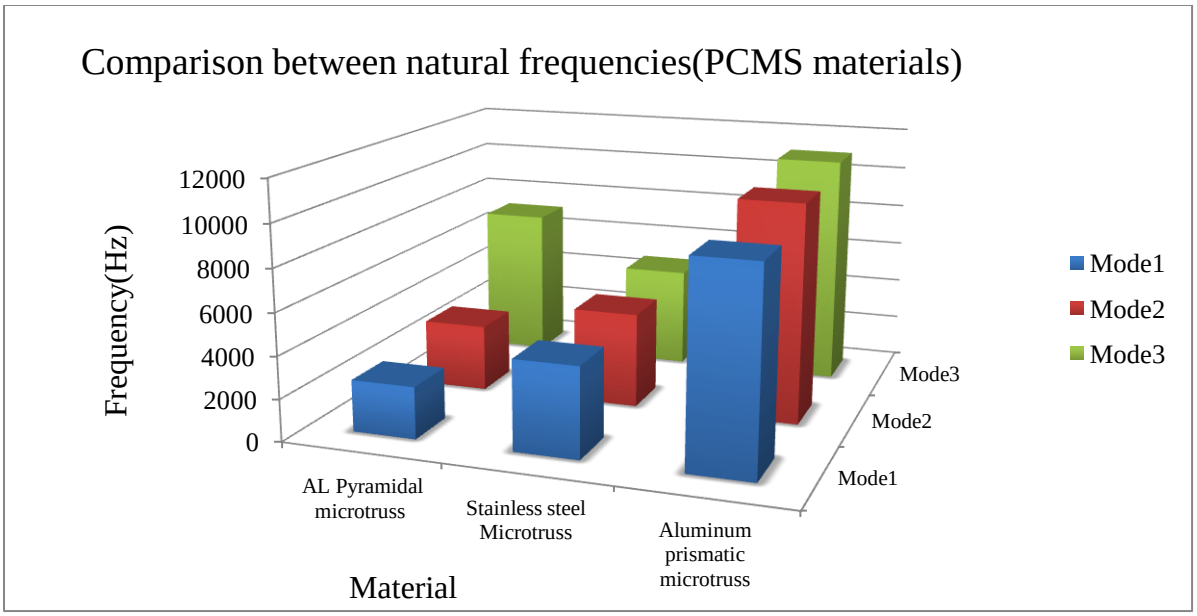

Figure 6.56: Comparison between natural frequencies for the 1st three modes

As can be seen in figure 6.56 for the first two modes the magnitudes of the natural frequency seems to follow the order of stiffness values. Thus, corresponding frequency values for the aluminum prismatic structure are higher than those for stainless steel structure, which are in turn higher than the aluminum pyramidal Microtruss. In the case of mode three it may be recalled that for higher modes and for more complex structures the frequency distribution may be different.

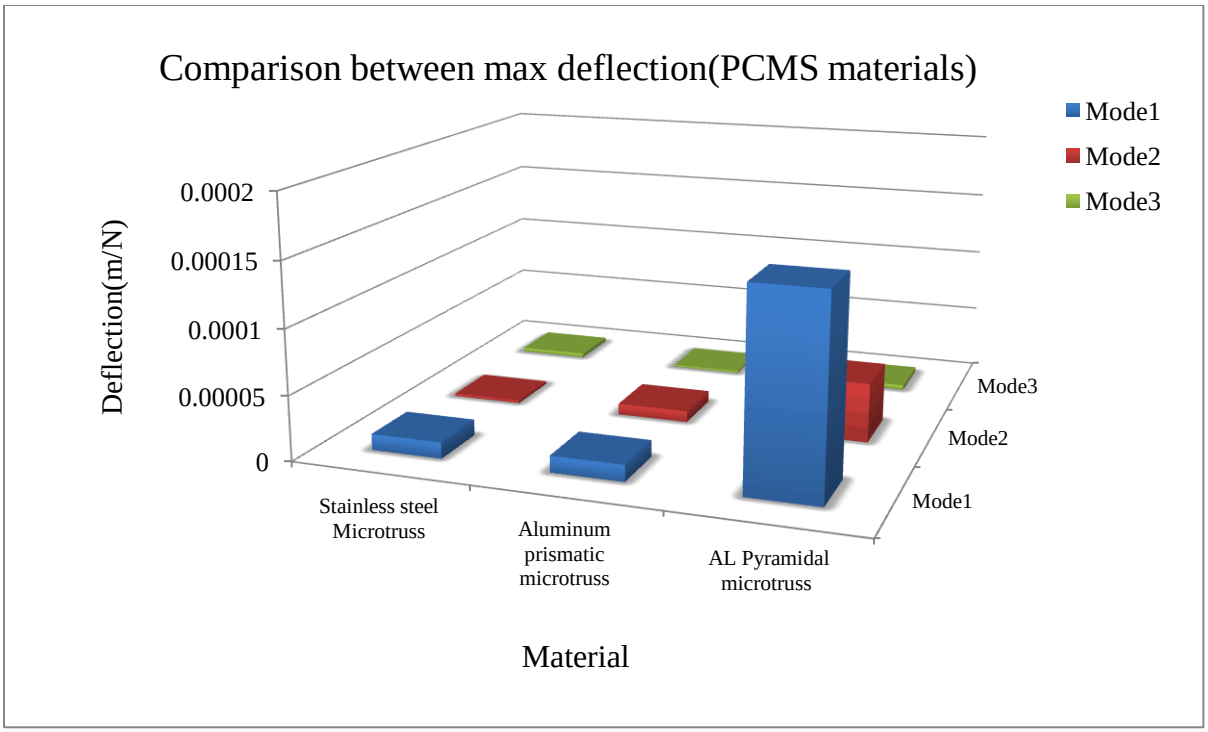

Figure 6.57: Comparison between maximum deflections for the 1st three modes

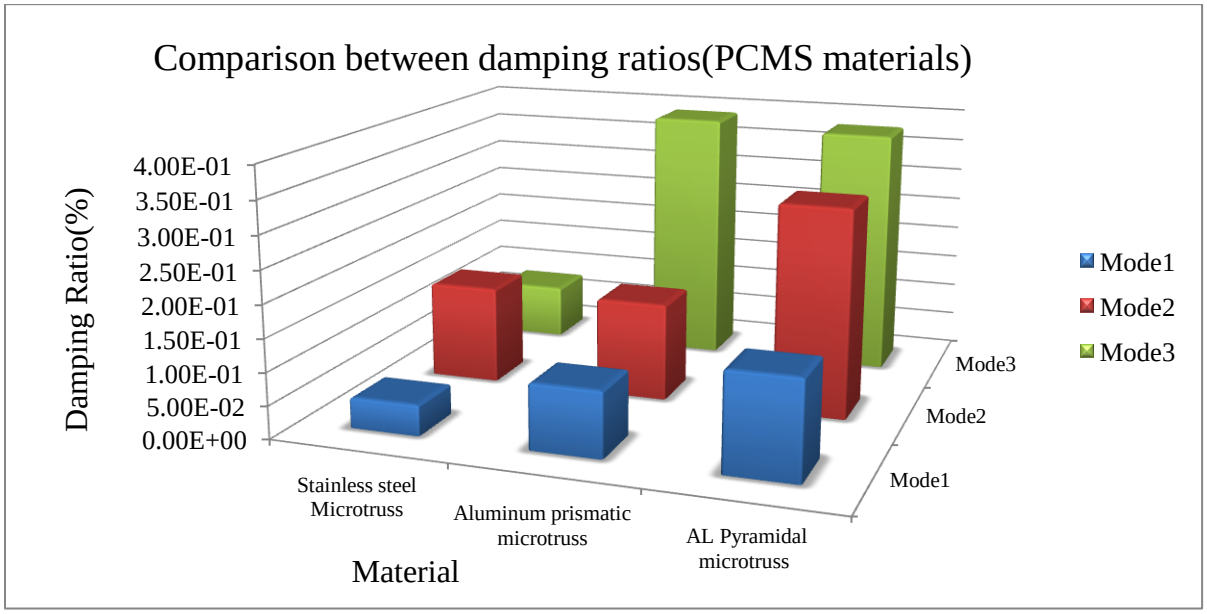

Figure 6.58: Comparison between damping ratios for the 1st three modes

Figures 6.57 and 6.58 show the maximum deflections and the modal damping values for the first three modes of vibration. The first figure reveals that the aluminum pyramidal Microtruss

expediencies significantly more maximum deflection than the other two PCMS materials. This is understandable because the pyramidal structure consists essentially of two relatively thin skins connected by a grid of slender metal bars. This construction makes it far more flexible than the other two. The second figure also shows that the pyramidal Microtruss structure has the highest modal damping ratio. Although one would have expected the damping to be the minimum, in fact the numerous bars in the core structure contribute a lot of damping to the movement of the structure.

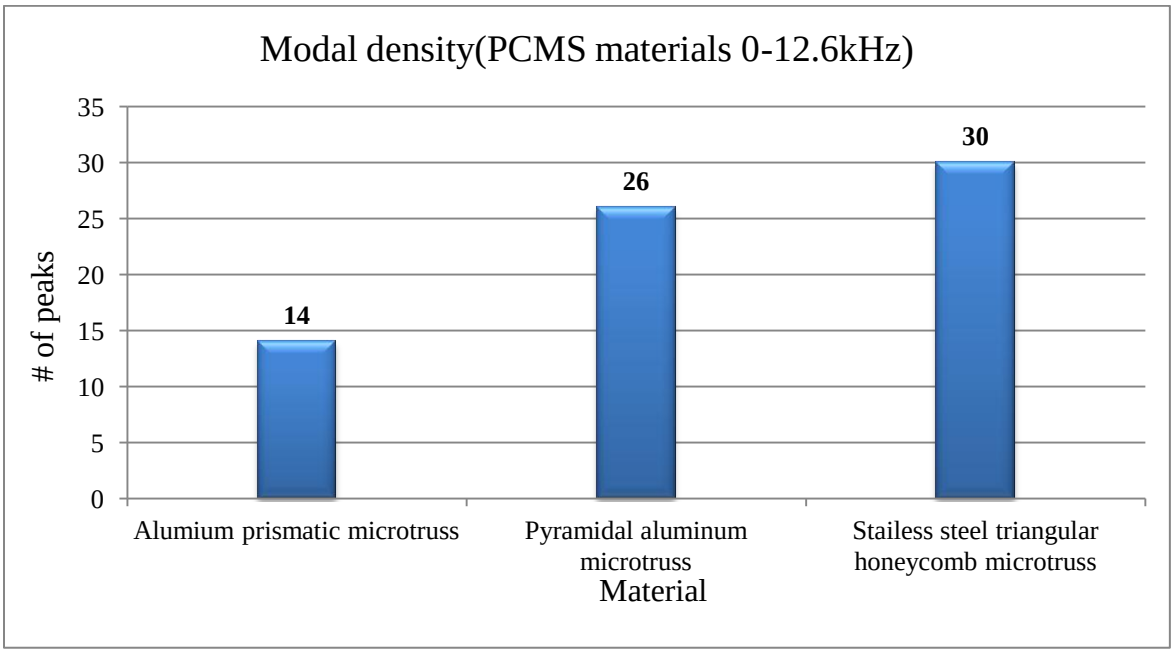

Figure 6.59: Comparison between modal densities

Figure 6.59 shows that the entire group of PCMS materials are complex structures manifesting much higher modal densities than the ones considered earlier. This is a result of their complicated constructions. As mentioned earlier the cost of high modal density comes in terms of amplified material, time and labor costs. It can also be seen from the figure that relatively the construction of the aluminum prismatic Microtruss is about half as complex as the other two.

6.3.4 GENERAL PERIODIC MATERIALS

It was not possible to draw these structures using Unigraphics (WSU Student Version) because of the complexity of these structures; it can be done using other software in the future, so the results for this group are the experimental results only. The Aluminum nuts double staggered micropillars is selected as the sample of this group.

Figure 6.60 to 6.64 shows the results for this sample as follows:

Figure 6.60: The stability diagram which indicates the first three natural frequencies.

Figure 6.61: FRF, Coherence and phase.

Figure 6.62: 1st three mode shapes (displacement contour, experimental results).

Figure 6.63: Maximum deflection for the 1st three modes.

Figure 6.64: Damping ratio for the 1st three modes.

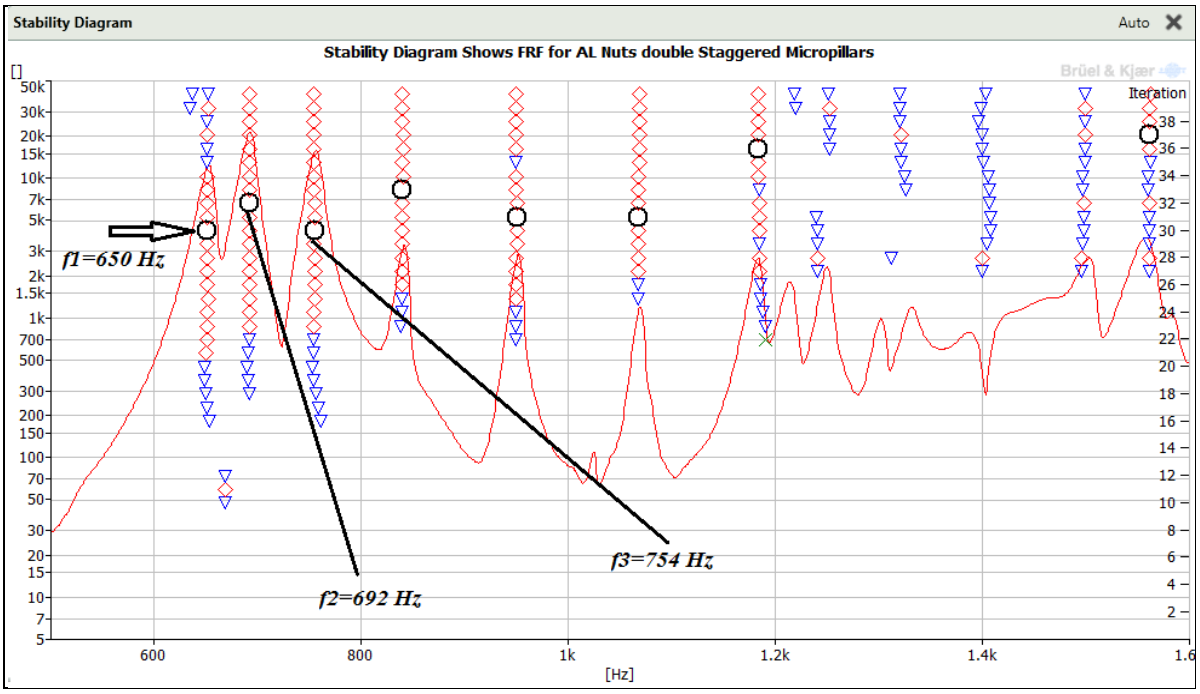

Figure 6.60: The stability diagram which indicates the first three natural frequencies

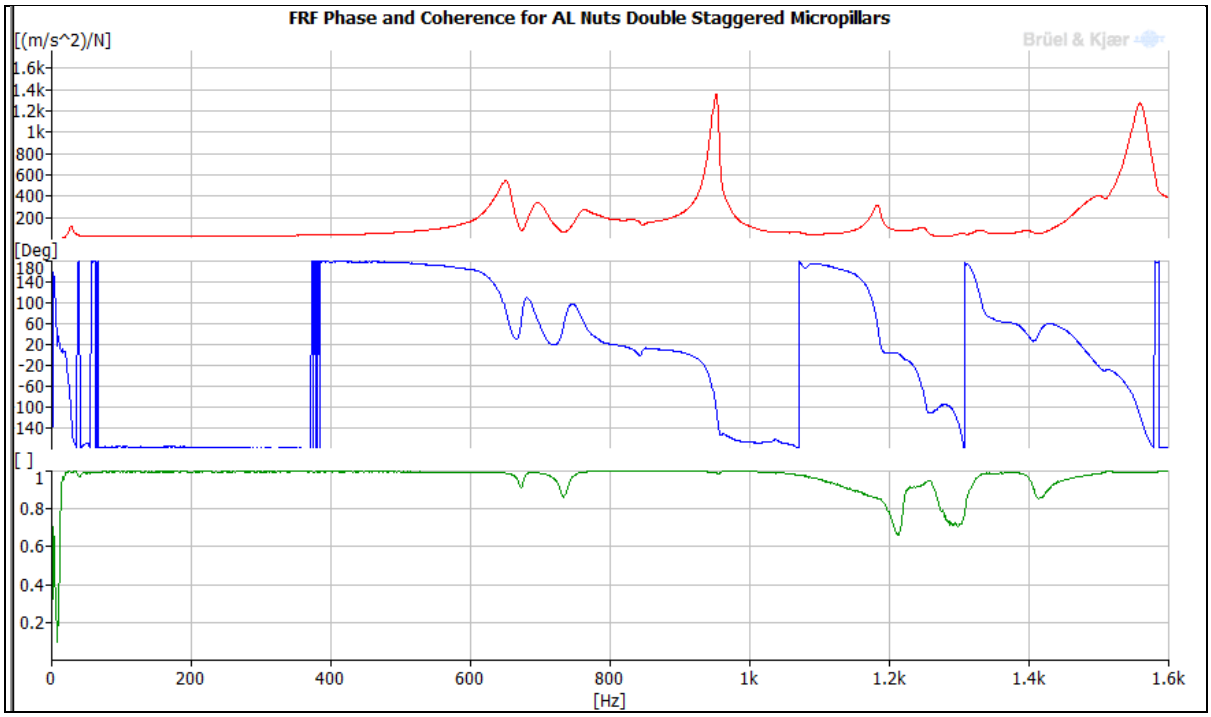

Figure 6.61: FRF, Coherence and phase

Figure 6.60 shows the stability, diagram, a display of the most accurate rendering of the FRF with different useful annotations. The fact of the structure's complexity is obvious, on account of having many resonances. The resonances are well spaced out and distinct, suggesting that the bending vibration modes are clear and practically free of mixed modes and distortions. From figure 6.61 we observe that the virtually universal unity value of the coherence suggests excellent experimentation, and the phase record is unequivocal in showing the true peaks.

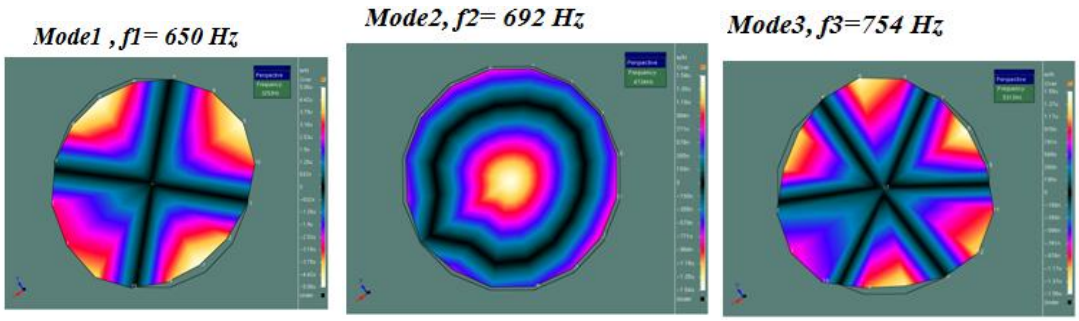

Figure 6.62: 1st three mode shapes (displacement contour)

Figure 6.62 shows the experimental mode shapes. The expected patterns (two diametral nodal lines for the first mode, one circular nodal ring for the second mode and three nodal diameters for the third mode) are evident. However the slight imperfections indicate slight, inevitable experimental errors. It should be noted that the PULSE 16.0, still under development and is unable to import complex geometries.

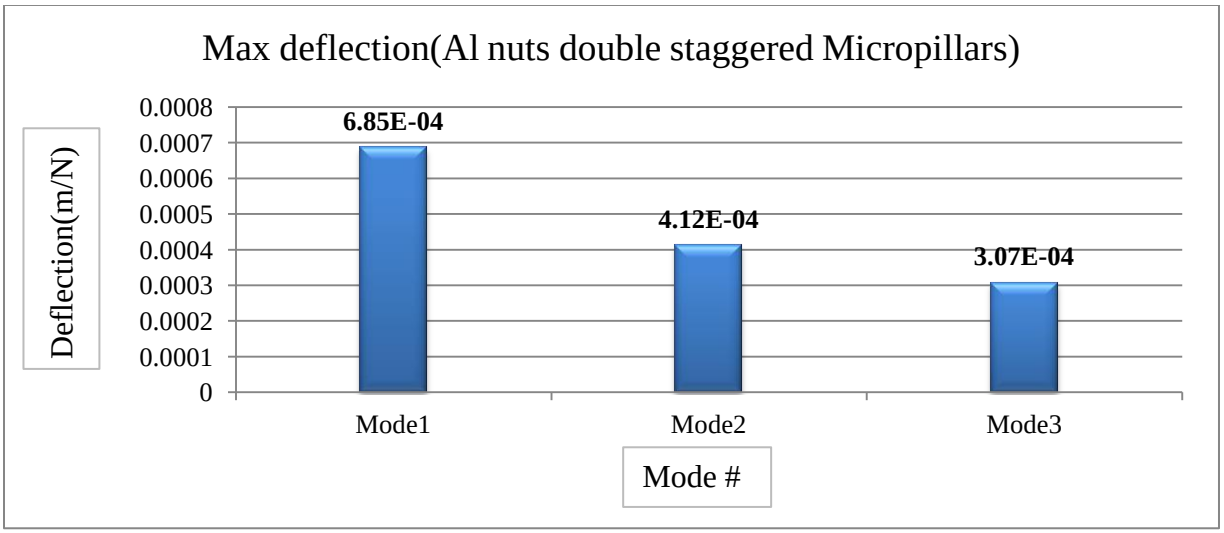

Figure 6.63: Maximum deflection for the 1st three modes

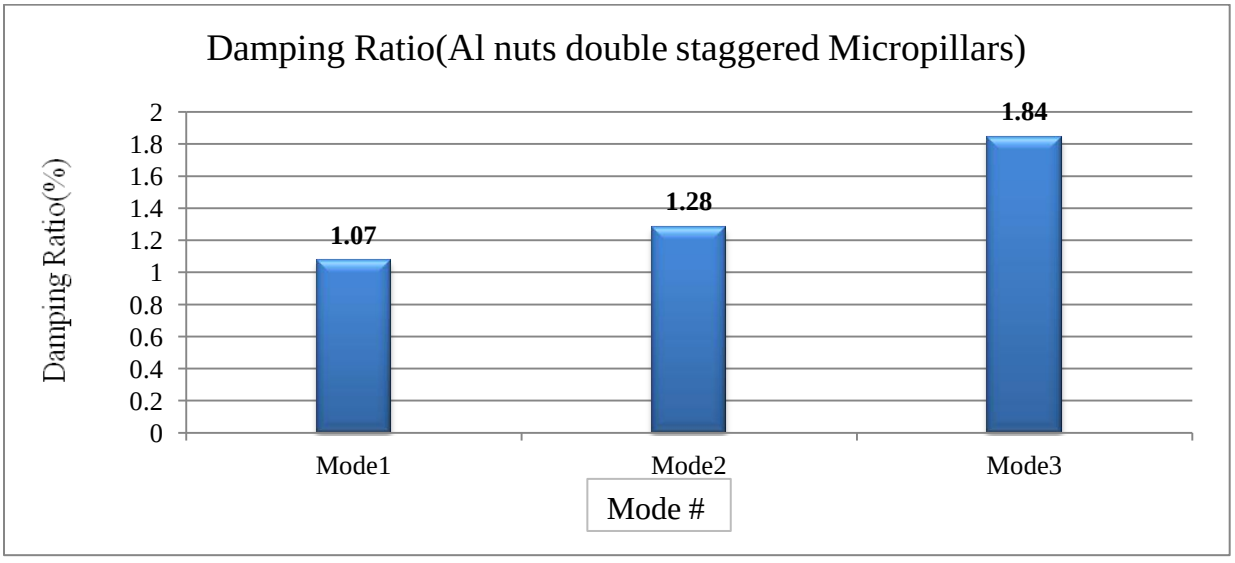

Figure 6.64: Damping ratio for the 1st three modes

Figures 6.63 and 6.64 respectively show the maximum deflections and modal damping ratios for the first three modes. It is obvious that mode one is the dominant mode with the largest maximum deflection and the least modal damping. The maximum deflection decreases with mode while the damping ratio increases with mode.

Table 6.7 compares the vibration results for the general periodic material group, and then these results are shown in a graphical representation in order to give a better understanding about the behavior of these structures. The number of peaks from experimental results is shown to indicate modal densities of these samples over a specified frequency range.

Table 6.7: Vibration results for General periodic materials

Material	Mode#	Damping ratio(η)%	Natural frequency(Hz) Experimental	Max deflection(m/N)	Number of peaks(0-1.6kHz)
Micropillars w/resonators	1	2.31	1095	3.20E-05	6
	2	2.88	1673	9.22E-06	
	3	2.51	2001	1.41E-05	
AL Nut double Staggered MP*	1	1.07	650	6.85E-04	13
	2	1.28	692	4.12E-04	
	3	1.84	754	3.07E-04	
AL Nut double in line MP	1	0.58	572	5.41E-04	10
	2	0.64	683	4.36E-04	
	3	0.72	802	3.56E-04	

*: Micropillars

Figure 6.65 to 6.68 shows the comparisons between the different samples of the PCMS materials as follows:

Figure 6.65: Comparison between natural frequencies for the 1st three modes.

Figure 6.66: Comparison between maximum deflections for the 1st three modes.

Figure 6.67: Comparison between damping ratios for the 1st three modes.

Figure 6.68: Comparison between modal densities.

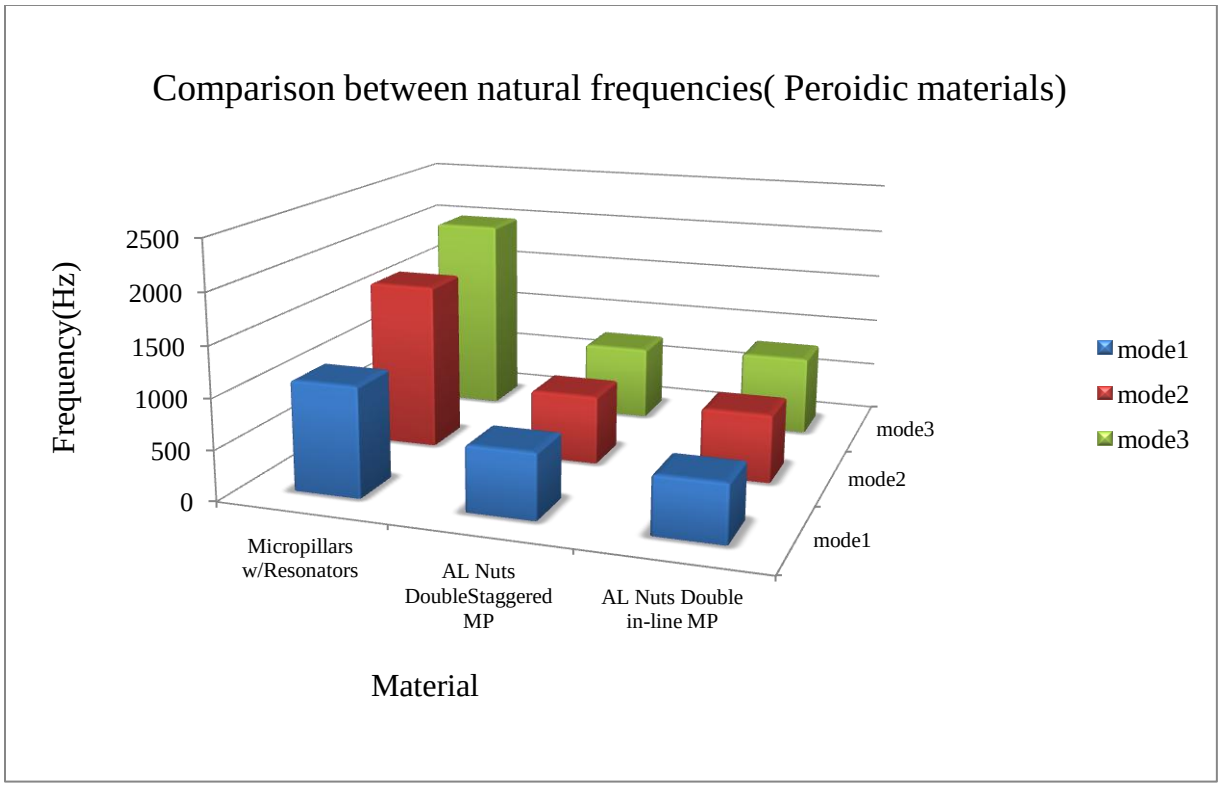

Figure 6.65: Comparison between natural frequencies for the 1st three modes

As it can be seen from figure 6.65 that micropillars with resonators has the maximum natural frequency for the first three modes among the group and this is due to its higher stiffness compared with the other two constructions which look to be approximately the same. The other two samples have much lower frequencies and almost the same because of their similarity of design.

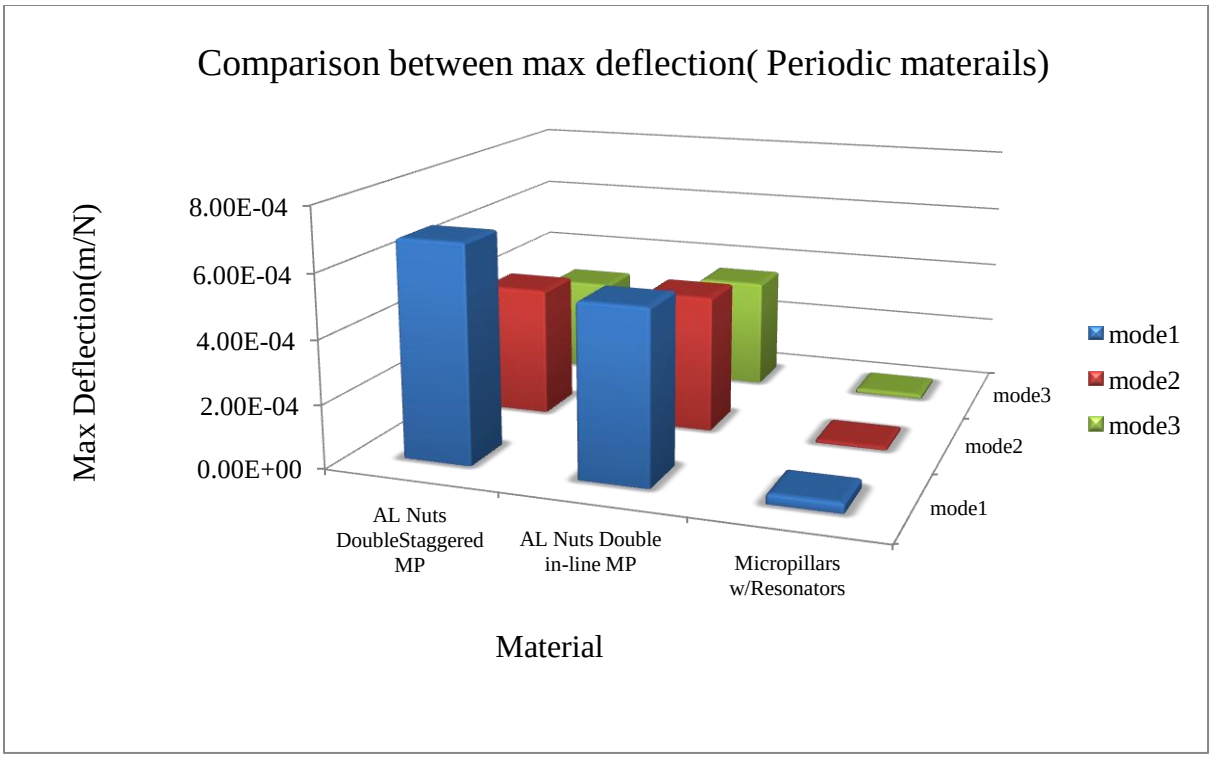

Figure 6.66: Comparison between maximum deflections for the 1st three modes

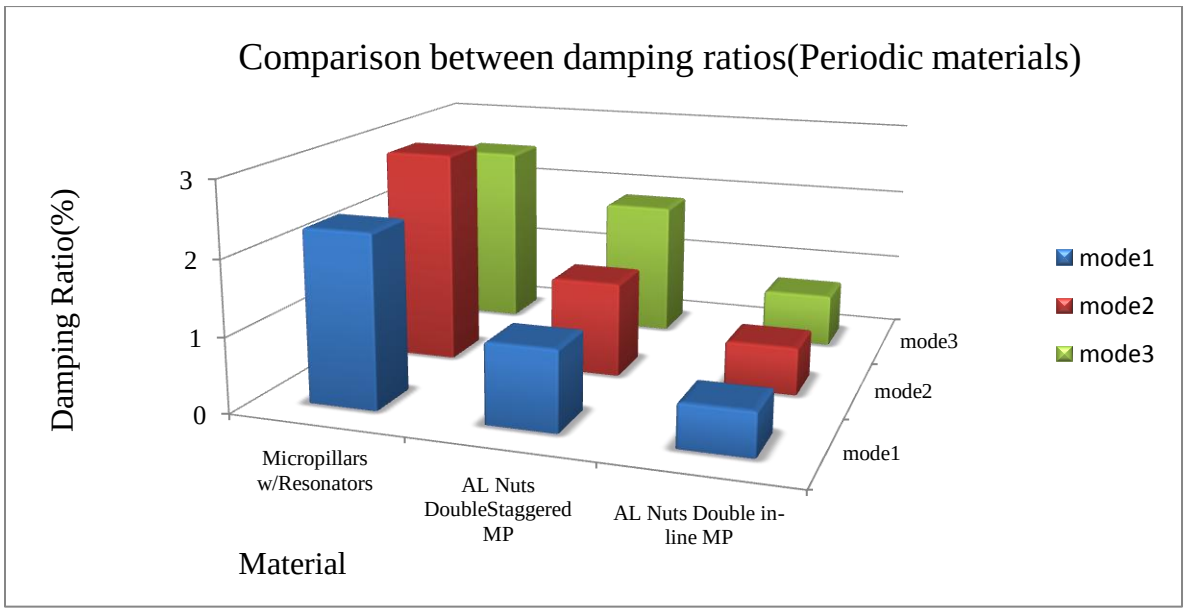

Figure 6.67: Comparison between damping ratios for the 1st three modes

Figures 6.66 and 6.67 respectively shows again that the micropillars with resonator material has the minimum deflection and the maximum damping and this is totally correct as the design of this material which contains these small resonators contribute in absorbing much of the vibration energy which leads to minimum deflection and higher damping. As mentioned before the behavior of this material is of much importance to be studied in the future as a meta material.

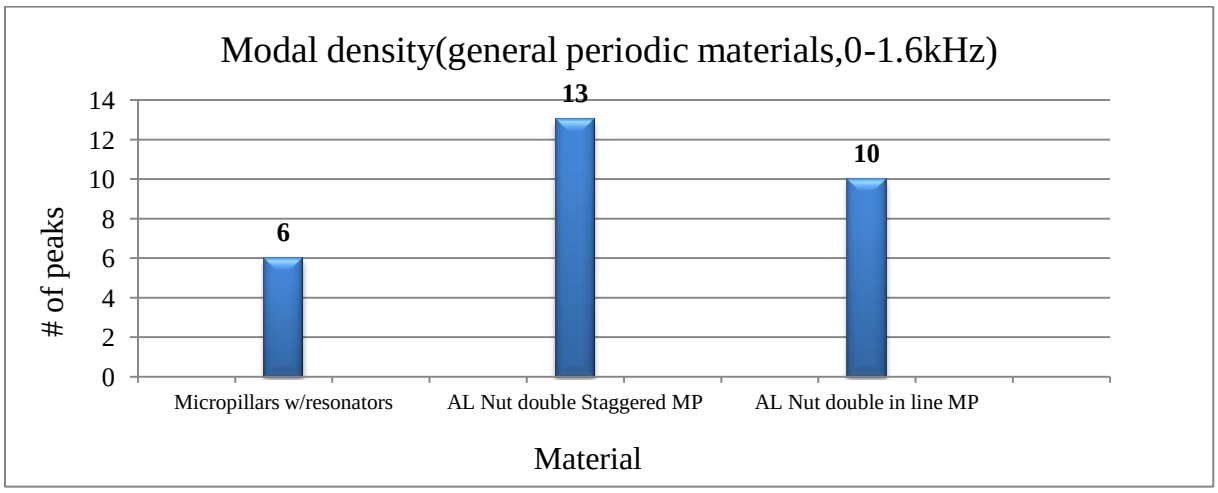

Figure 6.68: Comparison between modal densities

For the modal density (figure 6.68), it can be seen that the structures are complex because we have this number of peaks in a short frequency band, the aluminum nut double staggered micropillars seems to be the most complex among the group.

6.4. PARAMETRIC STUDIES

6.4.1 PARAMETRIC STUDIS FOR SOUND ABSORPTION COEFFICIENT

Parametric studies are normally used to see the effect of changing several parameters on the outcome of any engineering investigation because this will save money and time and give engineers the ability to decide which design should give the optimum results.

In the acoustic area the parametric study was done through writing a Matlab program -which can be found in appendix A at the end of this dissertation -depending on Biot theory discussed earlier in chapter three to calculate the sound absorption coefficient of rigid porous materials to see the effect of different parameters on the absorption coefficient. The material selected was Basalt because it was convenient for us to get its microscopic results from [84] thus saving much time. To verify our computer program, the experimental result was compared with the program result to show compatibility between them. After that the parameters were changed and the results were graphically presented to give an indication of these changes on the sound absorption coefficient.

As mentioned before the material was Basalt with the following properties:

Density: 3000 kg/m^2

Thickness: 1 inch

Structure factor K_s: 3

Porosity: 0.1

Diameter of pore: 0.07 mm

Figure 6.69 shows the compatibility between the experimental and computer program results and it is very good, the slight deviation only underscores the fact that experimental errors inevitable in such an exercise. This benchmark comparison is the logical starting point for a parametric study. This means that we can rely on the results of our parametric exercise since there is closer agreement between the experimental and the computer code results for the same material and conditions. Upon this result we started to change the thickness, porosity and finally structure factor to see the effect of those parameters on the sound absorption.

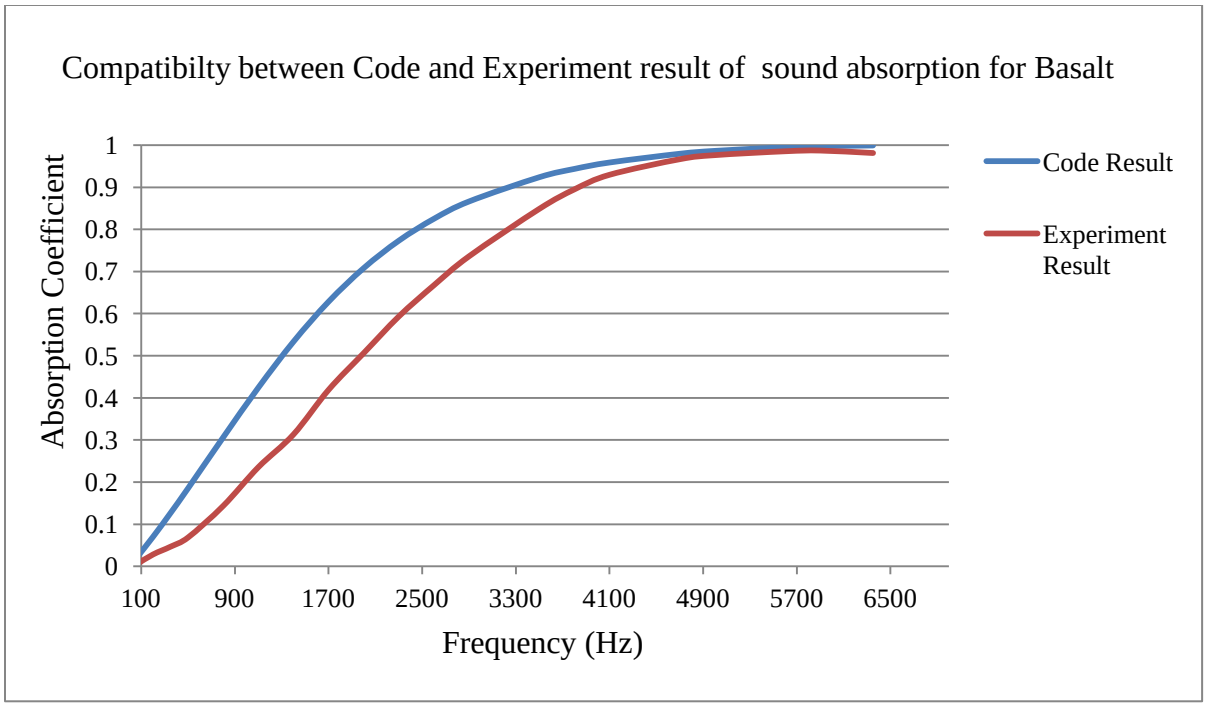

Figure 6.69: Compatibility between experimental and code results for absorption coefficient

Figure 6.70 shows the effect of changing the thickness on the sound absorption. As can be seen, increasing the thickness will increase the sound absorption up to a certain value of thickness beyond which it is no longer possible to increase absorption simply be increasing the thickness, due to the characteristics of acoustic wave motion in the structure. This terminal value of thickness is called the critical thickness [76], and it is a function of frequency, flow resistance, and path length. Decreasing the thickness cause part of the sound wave to skip the material without being absorbed because the wave length of many frequencies exceeds the material thickness. Increasing the thickness is one of the normal solutions in noise control engineering.

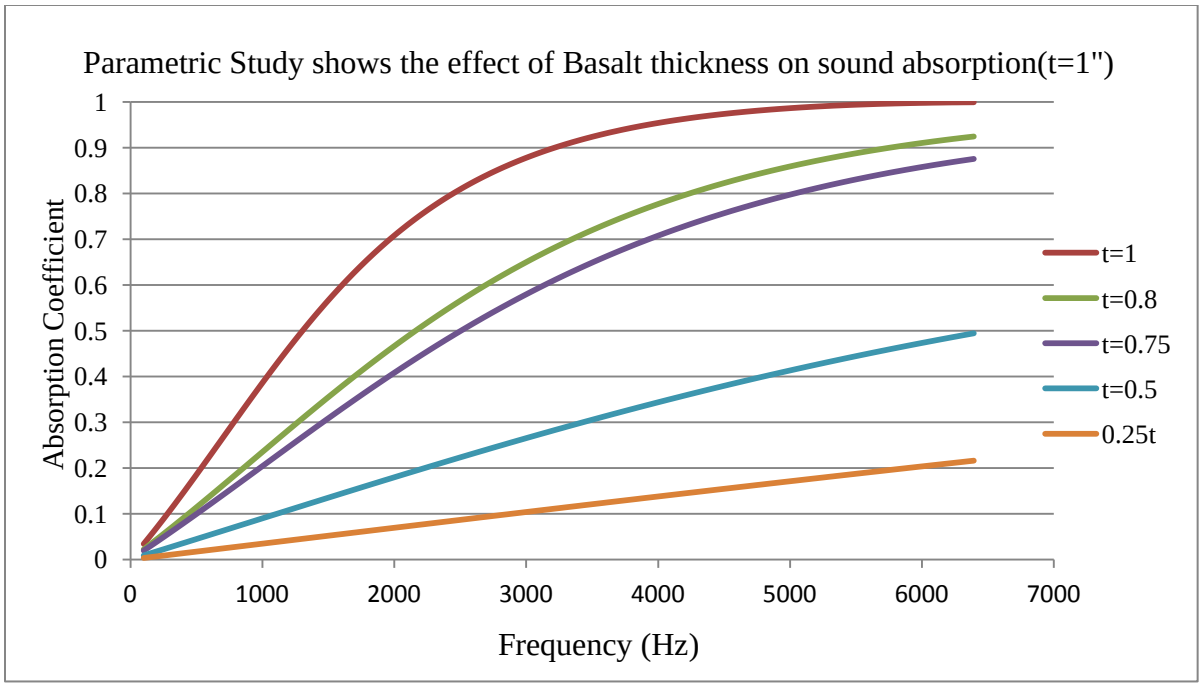

Figure 6.70: Effect of changing thickness on sound absorption

The second parameter which was changed is the porosity which is the volume of air inside the material to the total volume of the material plus air. As can be seen from figure 6.71 that increasing the porosity increases the sound absorption in the low frequency range. For example as the porosity increases from 0.3 to 0.7, the peak of sound absorption is shifted to lower and lower frequencies which is good if the material is to be used to absorb sound in the low frequency area. Sound absorption is mainly due to two factors, viscous friction between the fluid and the solid material and, the thermal effect between the two. In this case the viscous effect in the low frequency range and higher porosity significantly increases. The thermal effect in the same case similarly increases because there is more contact area. However in the high frequency range the sound wave amplitude and wave length are much shorter and at high porosity (meaning less material), both viscous and thermal effects are lower because there is less solid-fluid contact.

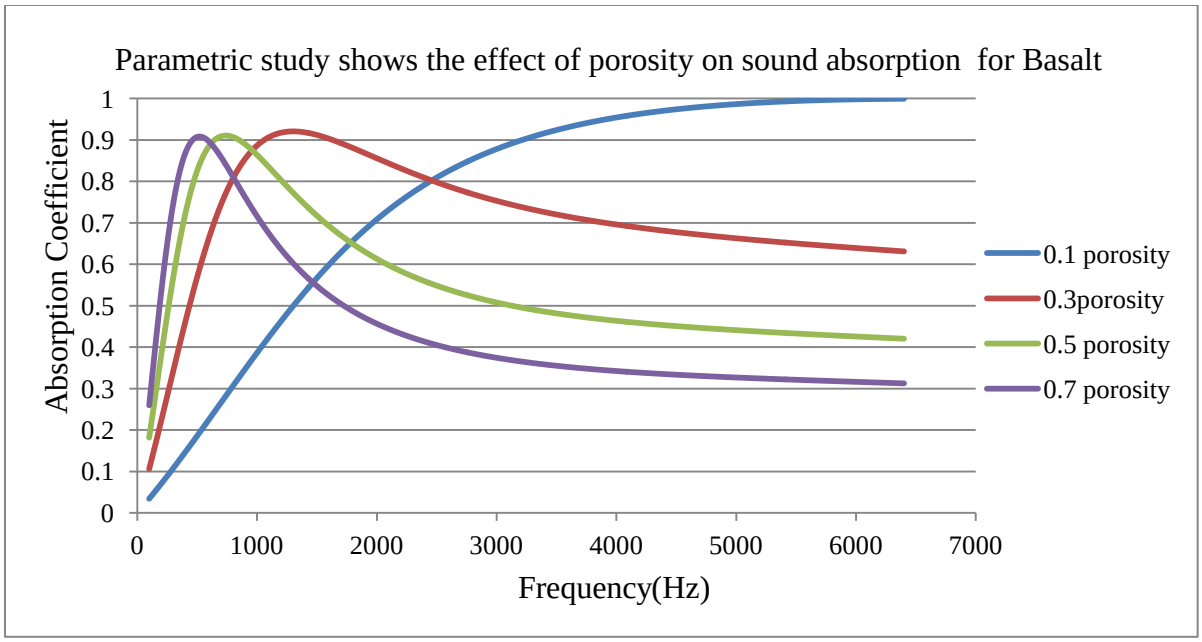

Figure 6.71: the effect of porosity on sound absorption coefficient

Finally the effect of structure factor (figure 6.72) which is the ratio between the length of all pores (the non straight and straight pores) to the length of the straight pores is studied. In this definition straight means parallel to the main flow direction. The value is typically between 3 and 7 in real life [46] situations. The influence of structure factor is straight forward in that this quantity is used to multiply the fluid density in order to obtain an effective density that is used in the flow equations for the sound absorption. The curves shown in the graph indicate how this modification of density affects the calculated acoustic absorption coefficient. It may be observed that at the frequency extremes the effect of increasing structure factor is negligible for a given porosity value. In these zones the absorption coefficient already attains the values of almost zero and almost one (the minimum and maximum possible) respectively. In the middle frequency region the increase in absorption coefficient goes up to 0.25(at about 2000 Hz).

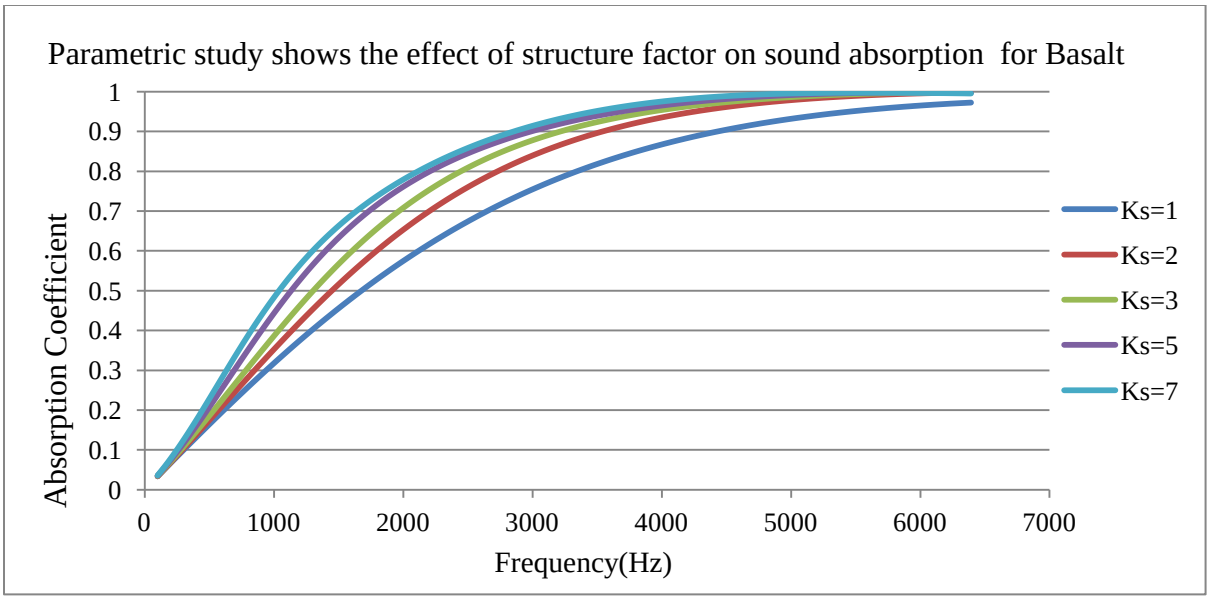

Figure 6.72: the effect of structure factor on sound absorption coefficient

6.4.2 PARAMETRIC STUDIES FOR VIBRATION

The parametric studies for vibration were done to see the effect on natural frequencies, of changing thickness, architecture or layup (Lexan samples), dimensions and finally the origin coordinates of cutting the PCMS circular samples from larger rectangular stock. This last variable was studied to show the importance of choosing very precise coordinates for cutting arbitrary shape samples from usually rectangular stock materials to avoid any variation in the vibration behavior of these structures.

The single layer solid Lexan monolithic sample was selected to see the effect of changing the thickness on the natural frequencies, the simulations were done using Abaqus standard 3D as a solver in the FEM model, the thicknesses selected were (2, 4, 6, 8, and 10 mm). As mentioned in the acoustic parametric study, the first step was to check the compatibility between experimental and finite element results for this sample, the results are shown in figure 6.73 below for the 2mm sample and they show very good agreement.

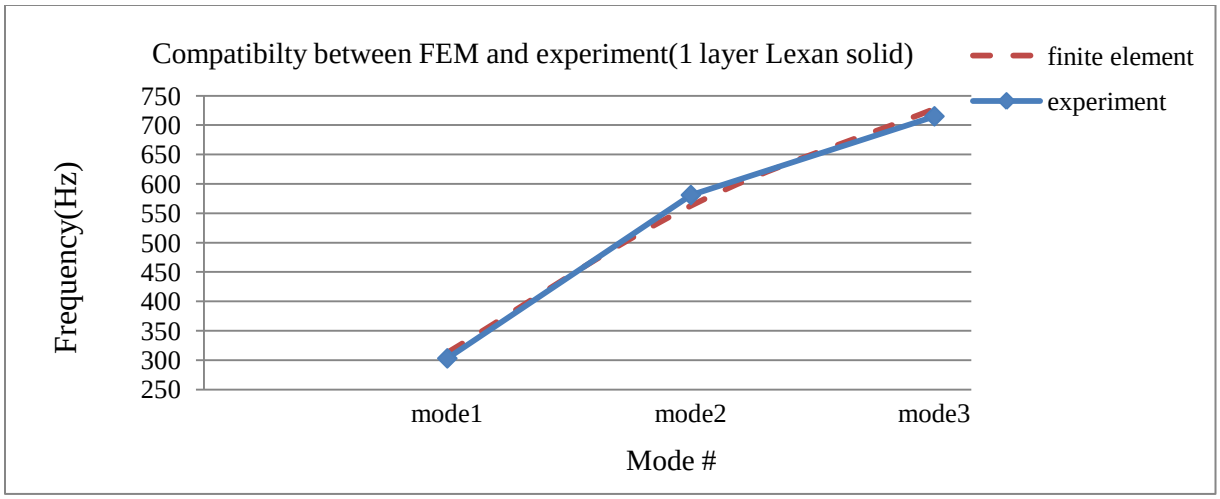

Figure 6.73: Compatibility between experimental and FEM results for natural frequencies

As can be seen from the graph, increasing the thickness increases the natural frequency for each of the first three modes. This is reasonable because increasing the thickness will make the material stiffer, and the effect of this stiffness increase exceeds that of the mass increase, and since frequency is the square root of the ratio of effective stiffness to effective mass, the natural frequency will increase.

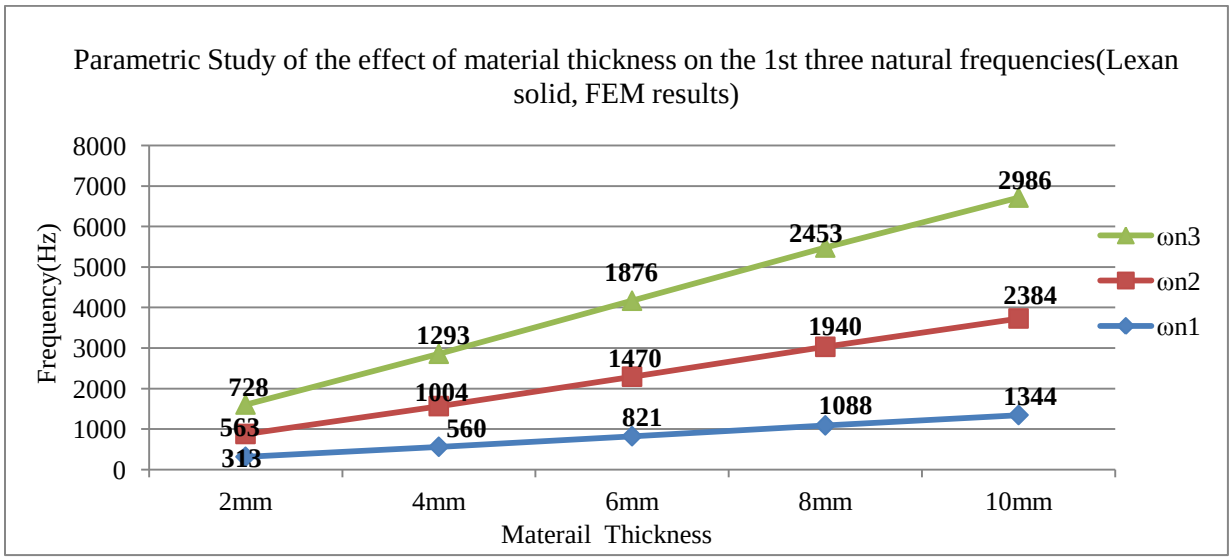

Figure 6.74: effect of thickness on natural frequency

The second parametric study was done to see the effect of changing the architecture of single layer Lexan material on the natural frequency behavior, the samples used were:

1. Single layer solid Lexan
2. Single layer Lexan with small holes
3. Single layer Lexan with large holes
4. Single layer Lexan with membrane

Figure 6.75 shows the results. As can be seen, the natural frequency decreases as more material is removed from the solid Lexan disk. It can also be seen that going from the solid disk to one with small holes(5mm diameter) covered with the silicon membrane and to the one with small holes results in rather small decrements of frequency, but removing large holes (13mm diameter) results in a steep drop in natural frequency. Again, this is reasonable because removing material decreases stiffness, and the effect of this stiffness decrease exceeds that of the mass decrease, and since frequency is the square root of the ratio of effective stiffness to effective mass, the natural frequency will decrease. The observed discrepancy in the frequency decrease over the four structures can be readily attributed to the fact that much more material (2.01e-5 m^3) is removed than for the case of small holes (3.29e-6 m^3). The membrane adds only a little mass (it is 0.2mm thickness).

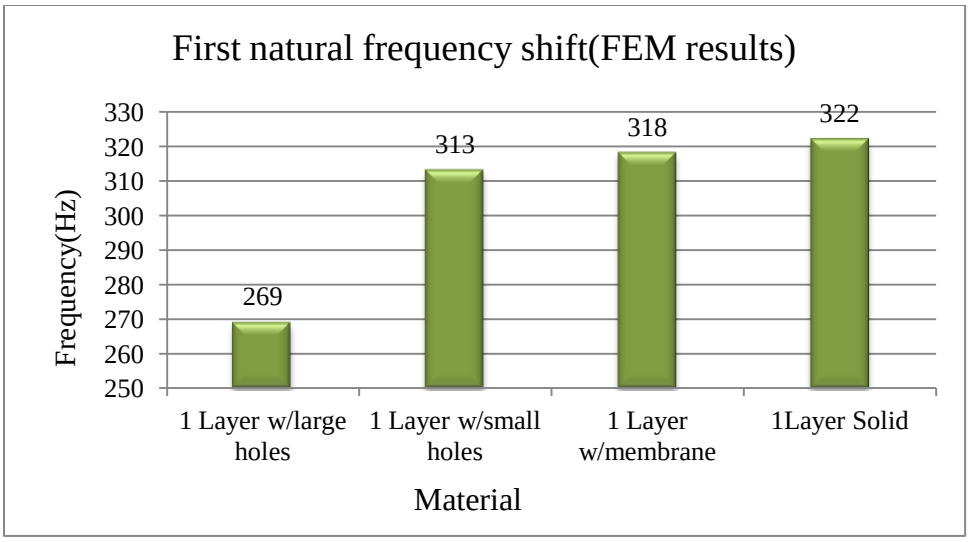

Figure 6.75: Fundamental natural frequency for different architecture

The finite element results were as shown in table 6.8 below.

Table 6.8: the first three resonance frequencies for different Lexan architecture

Material	Mode1	Mode2	Mode3
	f_1	f_2	f_3
1Layer Solid	322	574	746
1 Layer w/small holes	313	559	728
1 Layer w/large holes	269	411	624
1 Layer w/membrane	318	563	736

The effect of sample dimension was studied for PCMS aluminum prismatic rectangular plate, the plate dimensions were as follows:

1. Sample 1, 62.2cm x62.2cm x 4cm, (24.5in. x24.5in. x1.57in.)
2. Sample 2, 15.2 cm. x15.2 cm. x 4cm.,(6in. x6in. x 1.57in.)

Figures 6.76 and 6.77 show the results for the displacement contour for samples 1 and 2 respectively.

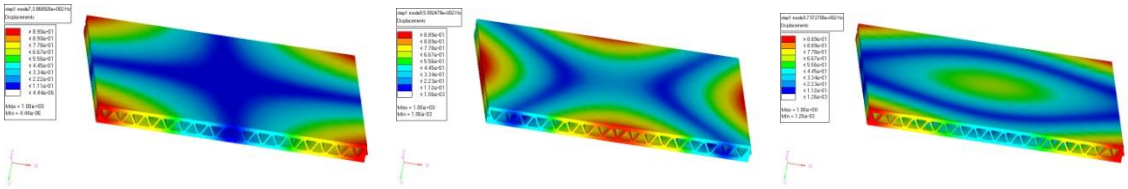

Mode1 Mode2 Mode3

Figure 6.76: displacement contour for sample 1

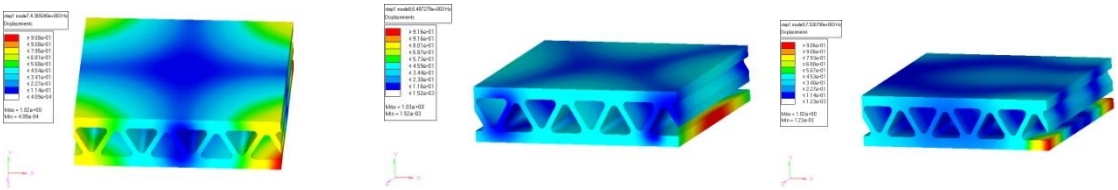

Mode1 Mode2 Mode3

Figure 6.77: displacement contour for sample2

Table 6.9 shows the natural frequencies and VonMises stresses for the first three modes for both samples. It is obvious that the frequencies for sample1 are much lower than those for sample2 , this is due to the fact that as the dimensions increase the structure becomes less stiff and heavier which directly affect the natural frequencies. The maximum deflections are also higher for the larger structure resulting in an increase in VonMises stresses. The mode shapes are clearer for the larger sample (it conforms to the established mode shapes of rectangular plates), and this is due to the fact that there is no mid-structure free edges like those found in the smaller sample. These mid- structure free edges or hanging lips arose from extracting the small sample size from the larger size stock material. Such a hanging lip vibrates wildly on its own and distorts the normal rectangular mode shape.

Table 6.9: natural frequencies and VonMises stress for the CMI samples

Sample number	Dimensions(cm) L*W*H	Mode1		Mode2		Mode3	
		f_1*	σ_1**	f_2	σ_2	f_3	σ_3
1	62.2*62.2*4	386	1.49e5	589	1.81e5	757	1.75e5
2	15.2*15.2*4	4369	405	6487	450	7526	375

*: frequency in hertz **: VonMises Stress in Mpa

The last parametric study was done on different cuts of circular samples (100 mm diameter) from the rectangular aluminum and stainless steel PCMS block materials. The cuts were made digitally using the Unigraphics software. The aluminum samples were classified according to the gap (the distance between the lower extremity of the hanging lip and the top of the lower skin) as shown in figure 6.78 below. Each cut corresponds to a different location of the center of the 100mm circle. The variation between all these centers was no more than 2mm.

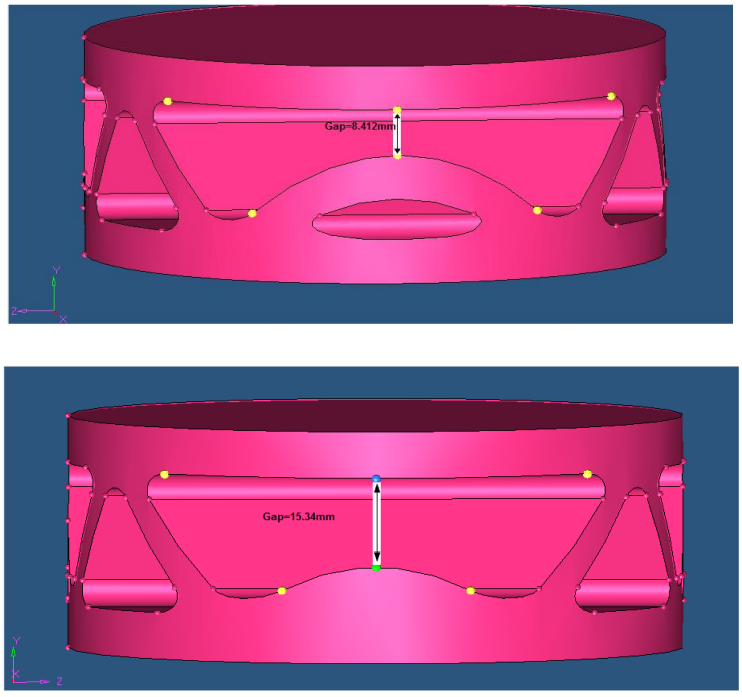

Figure 6.78: Gaps for two different aluminum samples

We have seven different cuts for the aluminum sample. Our sample is part 4 with 3.825mm gap. The center point used to extract this part corresponds to the original location. Each other part was obtained by shifting this center to a different position. In no case was this shift more than 2mm. The results for these samples are shown in table 6.10

Table 6.10: Results for different samples from FEM simulations for aluminum samples

Part #	Gap(mm)	Von Mises Stress(Mpa)			Natural Frequency(Hz)		
		Mode1	Mode2	Mode3	*f1*	*f2*	*f3*
1	8.418	601	2140	1620	9760	11518	12735
2	11.053	624	2120	1280	10244	11602	12814
3	15.34	697	1870	1190	10810	11666	12867
4	3.825	621	2000	941	8997	11314	12364
5	13.608	631	1830	1160	10632	11650	12855
6	12.742	642	1870	1190	10483	11627	12794
7	7.475	626	1400	1060	9570	11478	12680
8	16.249	782	1920	1200	10828	11660	12809

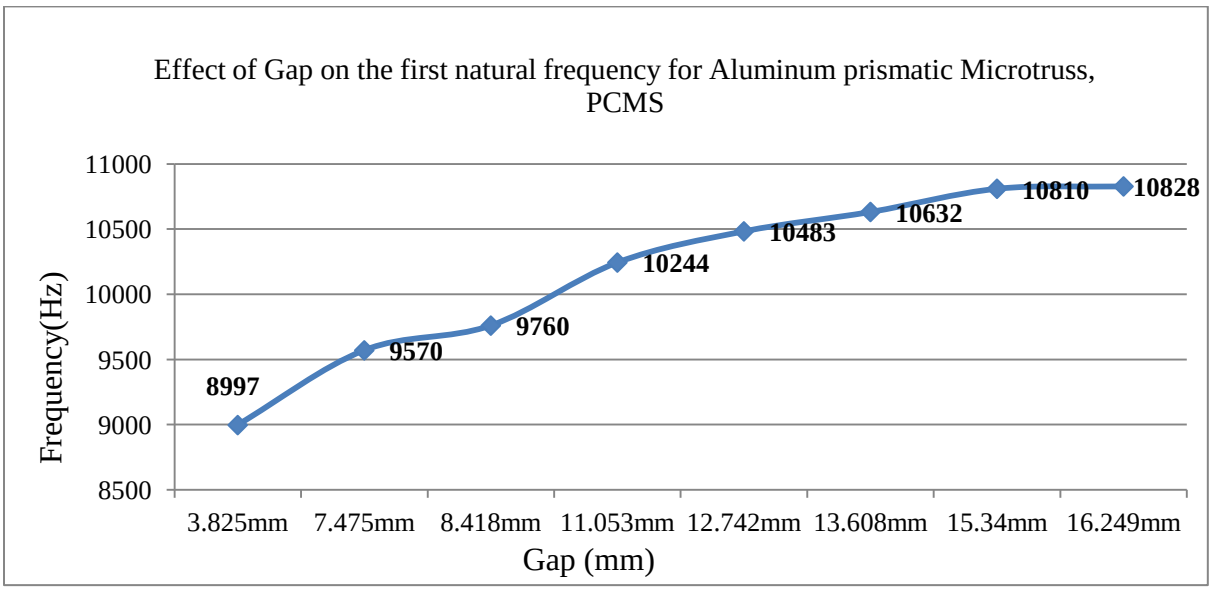

Figure 6.79: The change of frequency with gap

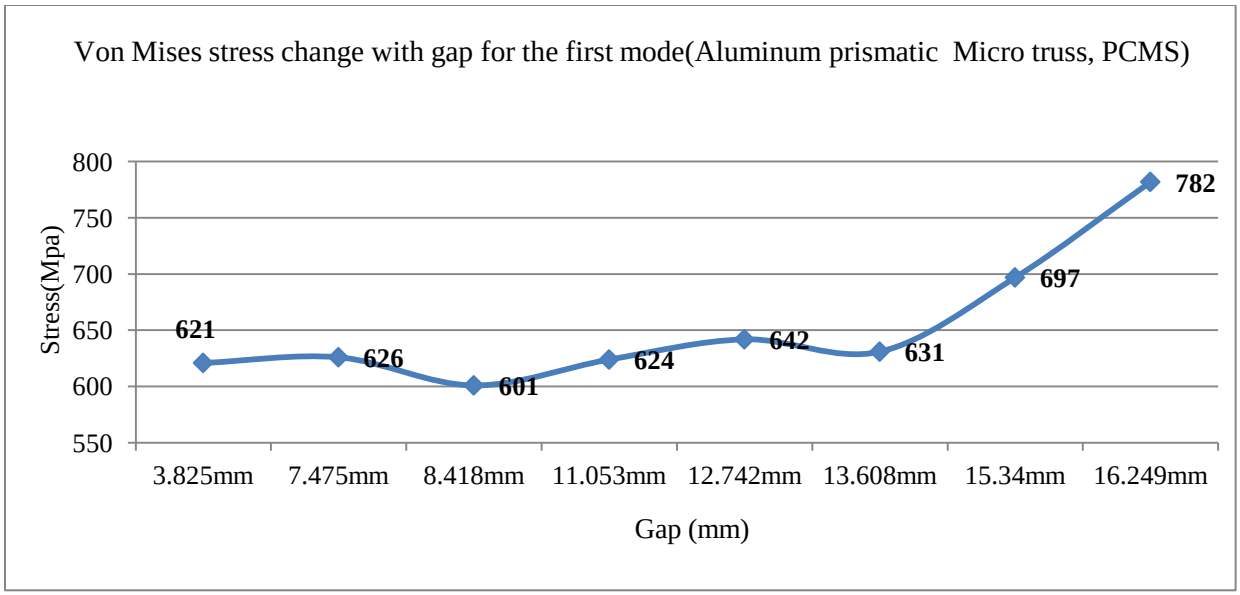

Figure 6.80: Change of VonMises stress with gap

Figure 6.79 and 6.80 show the natural frequencies and VonMises stresses respectively for the differtent cuts. The results are arranged in an acending order of the gap described earilier. Figure 6.79 shows the monotonic increase in natural frequency for increasing gap distance. This is logical because as more materail is progressively removed the remainimg structure becomes more compact and stiffer for relatively little change in mass. This results in frequency increase. On the other hand the VonMises stress which is an indication of the avearge stress shows a somewhat arbitrary behavior. This also understandable because the deflection allover the structure also becomes arbitrarly distributed. The mode shapes for the different samples are shown in figure 6.81 below.

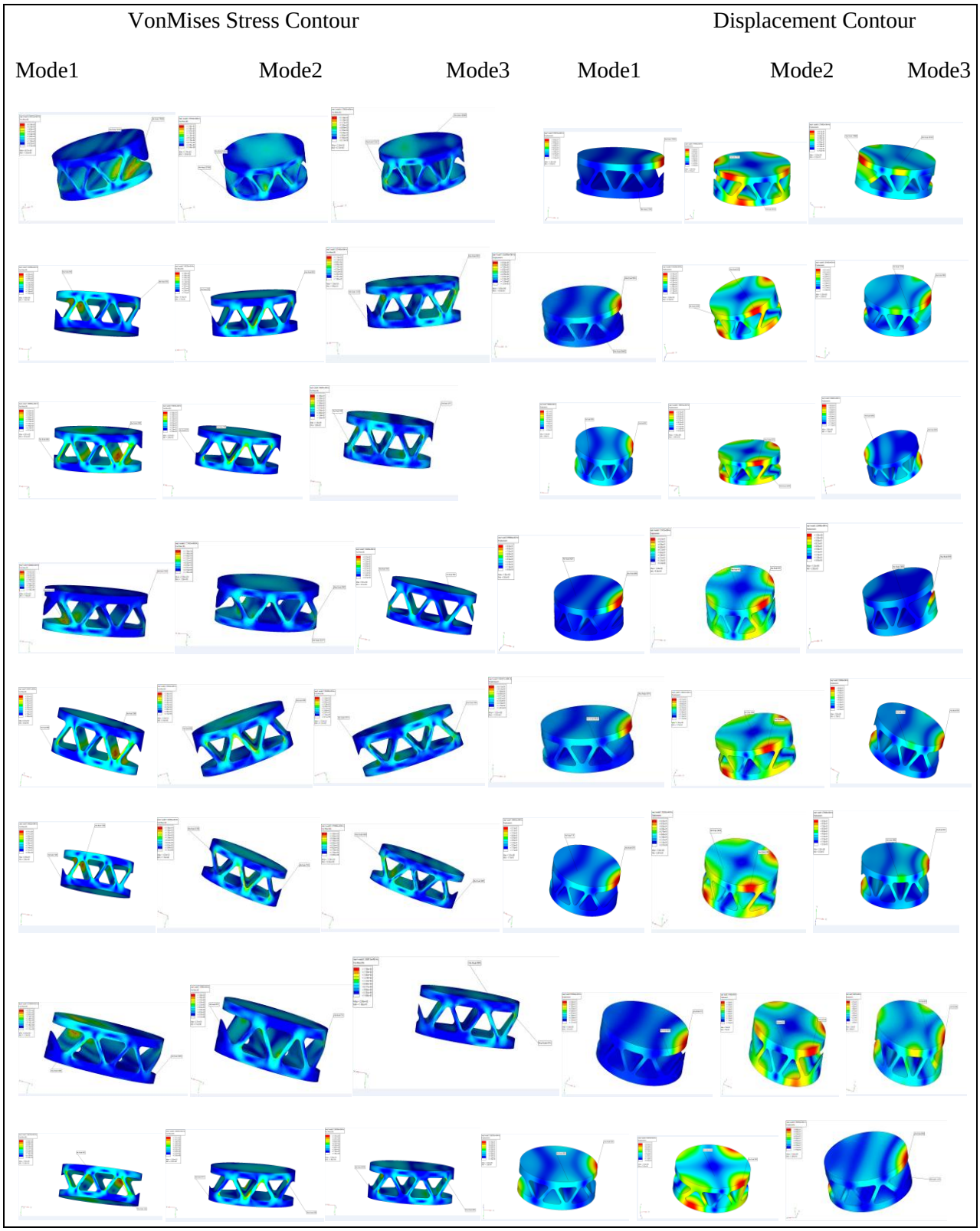

Figure 6.81: VonMises and displacement contours for Aluminum prismatic PCMS cuts arranged according to table 6.10

For the stainless steel we have different cuts as well. However there is no compact criterion (such as the gap used in the first case) to distinguish between the cuts, hence they are named as part 1 to part 9. Our part corresponding to the original center of the 100mm diameter is part5. Figure 6.82 below shows a FEM model for part number 1.

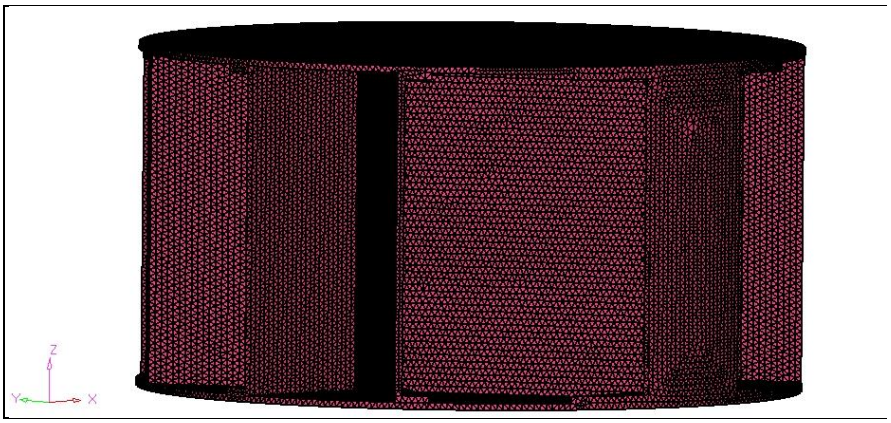

Figure 6.82: Sample number 1 as it appears in FEM model

The results for these samples are shown in table 6.11 below.

Table 6.11: Results for different samples from FEM simulations for stainless steel samples

Part #	Von Mises Stress(Mpa)			Natural Frequency(Hz)		
	Mode1	Mode2	Mode3	*f1*	*f2*	*f3*
part1	698	754	719	3856	4266	4284
part2	765	838	852	3500	3603	3837
part3	780	641	808	3790	4024	4261
part4	796	773	952	3065	3918	4121
part5	860	936	803	4020	4172	4324
part6	865	904	1070	3118	3568	3488
part7	871	631	739	3675	3758	4032
part8	967	563	716	3563	3788	3865
part9	1050	833	744	3496	3643	3786

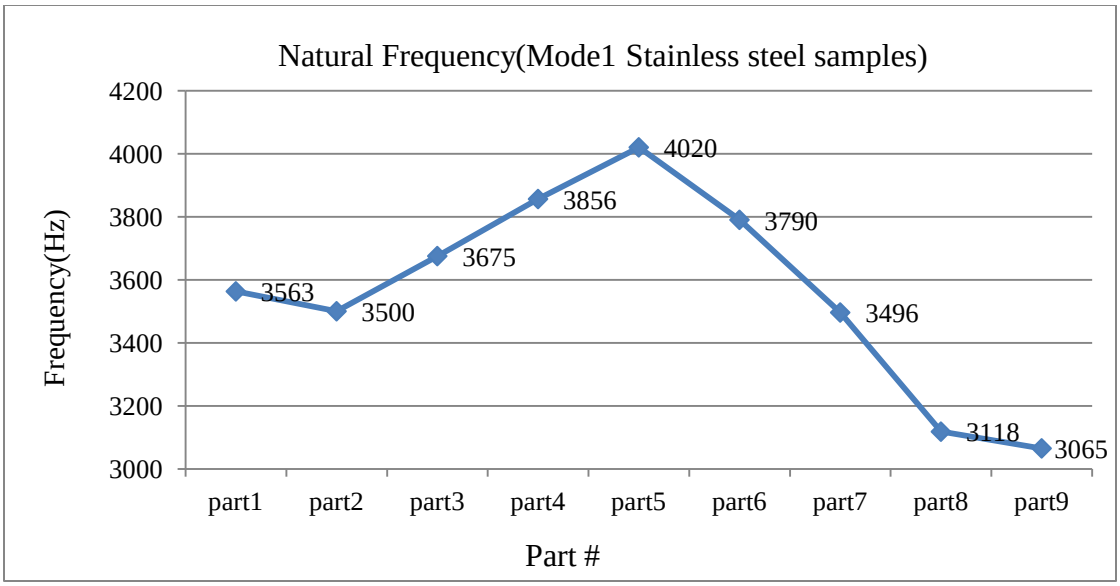

Figure 6.83: The first mode natural frequencies for stainless steel samples

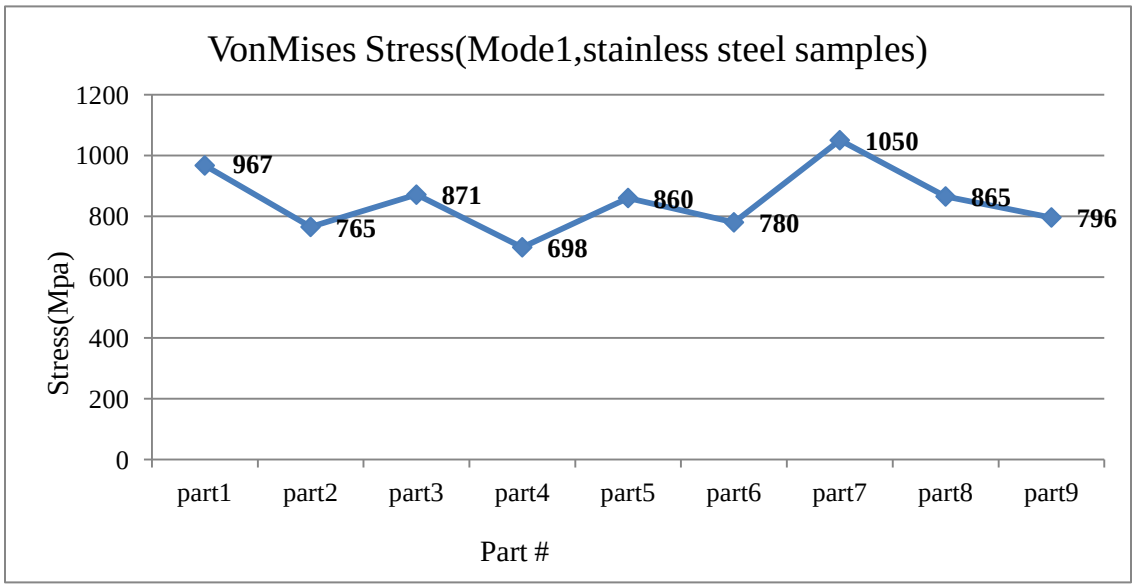

Figure 6.84: The first mode VonMises stress for stainless steel samples

Figure 6.83 and 6.84 show the natural frequencies and VonMises stresses respectively for the differtent cuts. The results are arranged in acenedning order of part number. The natural frequencies don not follow any particular order . This is logical because the stainless steel structure has numorous vertical plates which make up the triangular honeycomb core structure.

Any slight shift in the coordinate of the center of the circular part to the cut makes a big differrence in the vibration behavior because some of these vertical panels may now become loose. The VonMises stress which is an indication of the avearge stress also shows arbitrary behavior. This also understandable because the deflection allover the structure also becomes arbitrarly distributed.

The mode shapes for both dispalcement and VonMises stess contours is shown in figure 6.85 below to give an imperssion about the complexity of these samples.

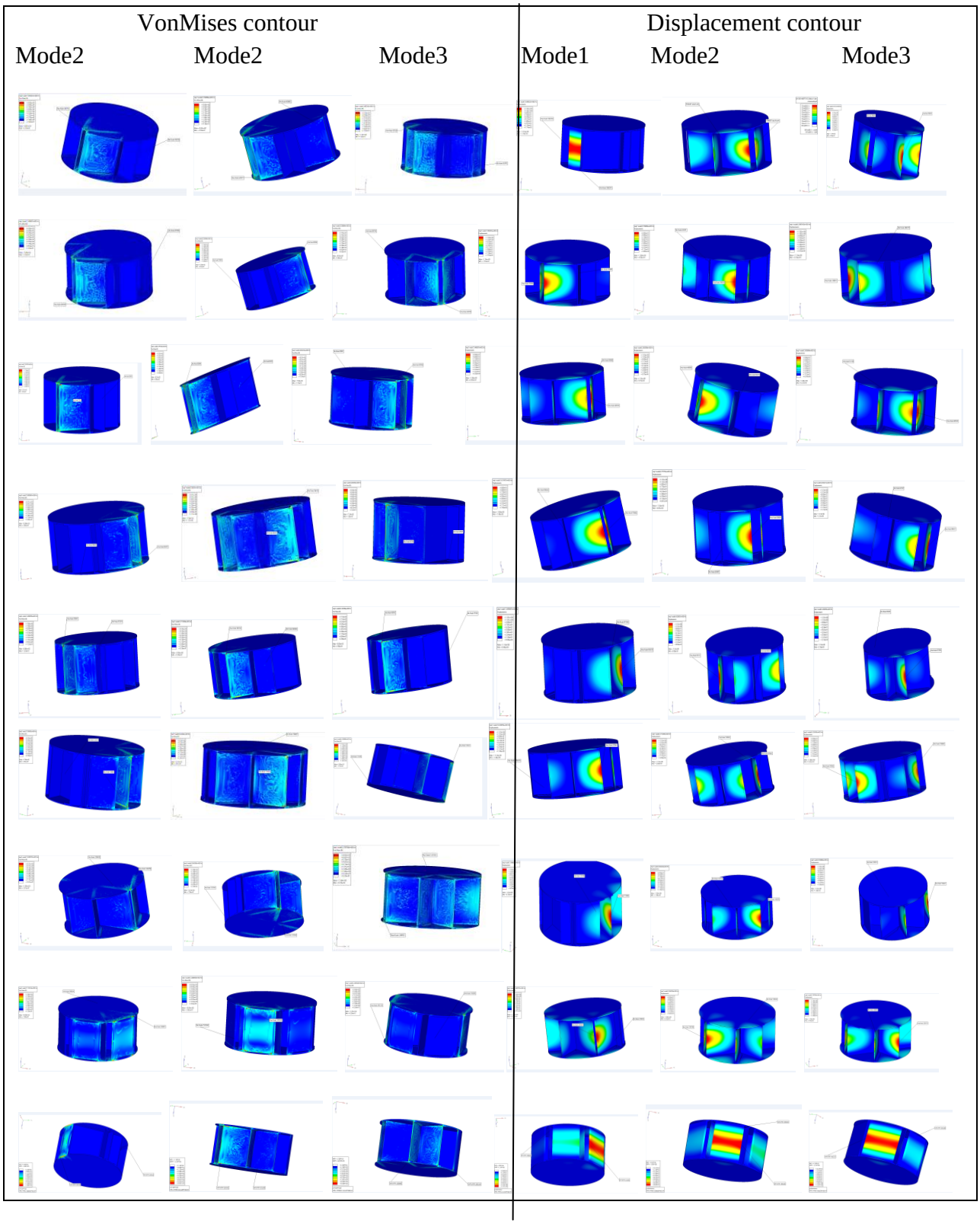

Figure 6.85: VonMises and displacement contours for stainless steel triangular honeycomb PCMS cuts arranged according to table 6.16

The behavior of the cuts from these two periodic materilas brings a very important observation to the forefront. They show that it is crucial to insure that when replictae parts are required, they must be extracted from an exact geometrical location, otherwise it will be impossible to assure consistency in the vibration and stress behaviores of the structures so produced. This has severe production and financial implications.

Inorder to underscore this point, table 6.12 shows a variation of a mere 2mm in the center location of the cut leads to varations of 20% for mode 1 frequency and 29% for mode 1 avearge stress for the aluminum sample and 23% for mode 1 frequency and 41% for mode 1 avearge stress for the stainless steel sample.

Table 6.12: perentage varaitions for the (frequency and strees)from the original sample

Material	Deviation from original location results%					
	Mode1		Mode2		Mode3	
	f	σ*	*f*	σ	*f*	σ
Aluminum prismatic Microtruss	20	29	3	37	4	72
Stainless steel triangular honeycomb Microtruss	23	41	16.7	39	19.3	41

*: VonMises stress

CHAPTER 7

CONCLUSIONS AND FUTURE WORK

7.1 CONCLUSIONS

The work reported in this dissertation has covered six groups of vibro-acoustic containment materials that are presently or potentially useful in the automotive area. These are the fabric, foam, honeycomb, monolithic and sandwich, periodic cellular material structures and general periodic groups. The first two were examined for acoustic containment only, while the remaining four groups were examined for both vibration and acoustic reduction applications.

There are important novel points in the research –

(a) PCMS: Investigation of the vibro-acoustic responses of periodic cellular material structures for possible use in the abatement of noise and vibration. This class of materials had been examined for structural, heat-transfer and multi-functional deployment, but not for the present purposes. From the results, we may conclude that the acoustic performance of this group of materials is unsatisfactory. They will need to be supplemented with good acoustic absorbers. Examples are filling with acoustic foam, or resinated cotton wrapped with very thin plastic to fill the cavities. On the other hand, a honeycomb plate can be attached on one face. It should be remembered that the construction can be modified to improve damping and acoustic absorption, e.g. by including many bars that basically rub against one another when flexed, or including the equivalent of air gaps.

(b) Construction and testing of novel generally periodic structures: Three novel designs of these materials (micro-pillars with resonators, aluminum double staggered micro-pillars, and aluminum double in-line micro-pillars) were made. These materials have the capability of being

utilized as acoustic meta-materials when design tuning is used to proportion their parts to produce negative effective mass and negative effective stiffness with the potential that acoustic and vibration band gaps of frequency could be created.

(c) Lexan vibro-acoustics: although Lexan (GE polycarbonate) is a commercially important industrial material world-wide, investigation of possible different ways of vibro-acoustic applications are sparse. This research has tested Lexan material samples in different formations to elicit behavior in some varying configurations. The results show that, in normal thicknesses, Lexan material is a bad absorber but a good reflector of sound; therefore it will perform well as a sound barrier material and as a suspended acoustic panel which can be set into vibration by incident sound pressure wave. Thick Lexan can be used as sound deadening partitions or enclosures. Because of good impact properties, laminated Lexan can be used as bullet-proof partitions in military cars and security applications.

(d) Programs and codes: A Matlab computer program was written to calculate the acoustic absorption of fibrous materials, and utilized to compute and plot values over the frequency range. Secondly, for some PCMS materials, finite element (RADIOSS) computational programs were completely set up for the calculation of vibration results based on several input parameter sets including geometry variations, etc., but could not be fully calculated owing to computational resources. The numbers of nodes required could not be accommodated in the WSU license available to students. Since the computational infrastructure work is done, all that remains is the acquisition of faster, higher capacity, possibly parallel-architecture computing platform to execute the programs.

(e) Parametric studies: four such studies have been carried out in this work. These were respectively on the acoustic absorption properties of rigid frame porous materials; on Lexan

architectural simulations; on size effect in rectangular PCMS samples; and on effects of tiny variations in the extraction location of smaller samples from general PCMS block-type stock materials for two different PCMS samples.

The major findings of this research are that

1. Fabric materials generally have high absorption coefficients. (Thus useful as filler / addition in synthesized panel materials to improve acoustics).

2. The B&K polyethylene terephthalate (PET) is a good broadband acoustic absorber. Conclusions on the Kathawate Inc. magic foam materials must wait until there is certainty about their manufacturing (oven expansion) methods from raw stock.

3. Acoustic absorption coefficients of honeycomb, periodic materials are high in the mid-frequency range (about 1500 Hz to 4100 Hz). As air contained in the cells is sealed in, and this enables the incident sound to be destructively reflected multiples of times. However, the particular choices of honeycomb to be used or in combination must be carefully made depending on frequencies to be covered.

4. Acoustic absorption coefficients of monolithic and sandwich materials tend to manifest single or only a few peaks, hence limited frequencies are covered, the sandwich materials may not be useful as general absorbers unless some of the component materials are highly absorbent.

5. Replacing some of the absorber material with air (e.g. by drilling holes) or membrane tends to improve flexibility and absorption. It is also confirmed that increasing air gaps in absorber arrangements tends to significantly improve absorption in the low frequency range and slightly deteriorate it at higher frequencies.

6. More rigid materials, such as cold rolled steel and block aluminum, as well as stiff framed structures, even in combination with highly absorbent cores or layers, tend to limit vibration, and should be considered for this purpose in automotives wherever a weight penalty does not work against them.

7. Potential exists for PCMS and generally periodic structures to offer effective vibration control. They may be used in ways mentioned in section (7.1a) and(4.1.6).

7.2 FUTURE WORK

Four areas are seen from this research to merit future work, as they directly grow from the present investigation.

1. Actual panels: It is necessary to next test a few actual automotive panels that are treated with the materials adjudged best from this work. Since the test samples are of the same size, the present findings are totally valid. However, on account of the size effect, such a scale-up is needful.

2. Further analysis and code development: Analytical and computer program development should be performed for other classes of materials in order to foster a wider view of possibilities and how they compare.

3. Computing resources: It is essential to expand the computing resources which are presently available, such that the computation schemes which are already set up may be executed for more parametric studies, and others may also be implemented.

4. Meta-materials: Analysis and computer simulations relating to general periodic materials should be undertaken, as there is great economic benefit in using the band-gap approach to avoid

signal transmission in certain frequency ranges rather than containing them when they are already transmitted.

APPENDEX A

MATLAB CODE TO CALCULATE SOUND ABSORPTION COEFFICIENT FOR POROUS RIGID MATERIALS.

```
%This program is written to calculate sound absorption coefficient for rigid
fram porous materials according to Biot theory using Matlab.
function case1()
%The frequency is changed from 0 to 6.4 kHz with an increment of 2
%FREQ is frequency in Hertz; ω is radial frequency in rad per second
%R_A is the real part of impedance
%R_I is the imaginary part of impedance
%C is the sound velocity (mm/sec)
%RHO is the density of Air (g/mm^3)
%ETHA is the viscosity of Air (g/mm.sec)
%ABSO is the sound absorption coefficient

ETHA=1.8E-5;  C=3.4E5;
RHO=1.21765E-6; l=440;

t = input('Thickness: ');
d= input('Diameter of pores: ');
p=input('Porosity: ');
KS = input('Structure Factor: ');

disp('Thickness= '); disp(t)
disp('Diameter of pores = '); disp(d)
disp('Porosity= '); disp(p)
disp('Structure Factor= '); disp(KS)
FREQ=50;
i=0;
for FREQ=50:FREQ+2:6400
  R=32.0*ETHA/(d*d*t);
  w=2.0*pi*FREQ;
  THETA=atan(-R/(KS*RHO*w));
  K1=sqrt(KS+(R/RHO/w)*(R/RHO/w));
  RHO1=(RHO*C/sqrt(p));
  p1=w/(C*sqrt(p));
  s1=sin(THETA/2.0);
  c1=cos(THETA/2.0);
  A=s1*p1*K1;
  B=c1*p1*K1;
  HTA=tanh(-A);
  TB=tan(B);

  RA=(RHO1*K1*c1*(HTA+HTA*TB*TB)+RHO1*K1*s1*(TB-HTA*HTA*TB))/(HTA*HTA+TB*TB);
  XA=(RHO1*K1*s1*(HTA+HTA*TB*TB)-RHO1*K1*s1*(TB-HTA*HTA*TB))/(HTA*HTA+TB*TB);
  k=C/FREQ;

  RSIMPE=RA/((cos(k*l)+XA*sin(k*l))*(cos(k*l)+XA*sin(k*l))+
RA*sin(k*l)*RA*sin(k*l));
  ISIMPE=((sin(k*l)-XA*cos(k*l))*(cos(k*l)+XA*sin(k*l))-
RA*RA*cos(k*l)*sin(k*l))/((cos(k*l)+XA*sin(k*l))*(cos(k*l)+XA*sin(k*l))+RA*si
n(k*l)*RA*sin(k*l));
```

```
  ABSO=4.0*RSIMPE/((1.0+RSIMPE)*(1.0+RSIMPE)+ISIMPE*ISIMPE);
  i=i+1;
    FREQarray(i) = FREQ;
    ABSOarray(i) = ABSO;
  disp('FREQ = ');disp(FREQ); disp('           ');disp('ABSO= ');disp(ABSO)
end

plot(FREQarray,ABSOarray,'-
gd','LineWidth',2,'MarkerEdgeColor','k','MarkerFaceColor','y','MarkerSize',2)
title('FREG vs ABSO')
xlabel('FREQ','FontSize',12);
ylabel('ABSO','FontSize',12)
grid on
```

APPENDIX B
MATLAB CODE TO CALCULATE NATURAL FREQUENCIES AND MODE SHAPES FOR LEXAN

The following is a program written in Matlab using vibration toolbox [Reference 71] to calculate the natural frequencies and mode shapes for single layer solid Lexan.

```
>> rou= 2.64; E=2350e6; mu=0.375;
>> a=50e-3; h=2.2e-3;
>> Plate_Pars=[rou E mu a h];
>> cirplate(Plate_Pars,0)

 System Information
 ------------------
 Material Properties:
    Mass density (mass/area) rou = 2.64
    Young's modulus E = 2350000000
    Poisson's ratio mu = 0.375

 Geometric Properties:
    Radius a = 0.05
    Thickness h = 0.0022

 Bending stiffness D = E*h^3/(1-mu^2)/12 = 2.4265
 c = sqrt(D/rou) = 0.9587

 Boundary Conditions:
   Free edge at r = a: Mr = 0, Vr = Qr + 1/r*(Mrs,s), where s = theta
Natural Frequencies:
 -------------------

    w_mn      n = 0        1        2         3         4
 ------------------------------------------------------------
  m =
  1.0e+005 *

         0         0         0    0.0208    0.0478    0.0836
    0.0000    0.0351    0.0789    0.1351    0.2025    0.2805
    0.0000    0.1480    0.2298    0.3236    0.4289    0.5452
    0.0000    0.3371    0.4567    0.5881    0.7311    0.8853
    0.0000    0.6020    0.7593    0.9285    1.1091    1.3012

 Here  w_mn = natural frequency in rad/s
       m = number of nodal circles
       n = number of nodal diameters

 * Note:  The membrane has rigid-body modes (zero eigenvalues)

 Mode Shapes
```

```
 -----------

    Wmn(r, theta) = [Jn(g_mn*r) + d_mn*In(g_mn*r)]*cos(n*theta),  0<=r<=a,
0<=theta<=2*pi

  Here Jn = Bessel function of the first kind
       In = Bessel function of the second kind
       g_mn = frequency parameters, w_mn = g_mn^2* sqrt(D/rou)
       d_mn = constants of mode shapes

    g_mn      n = 0        1        2         3         4
 ------------------------------------------------------------
  m =
         0         0         0   46.5482   70.6291   93.3573
    1.0000   60.5463   90.7083  118.6883  145.3275  171.0621
    2.0000  124.2600  154.8284  183.7288  211.5117  238.4783
    3.0000  187.5161  218.2518  247.6797  276.1513  303.8847
    4.0000  250.5772  281.4279  311.1992  340.1361  368.4035

    d_mn      n = 0        1        2         3         4
 ------------------------------------------------------------
  m =
         0         0         0    0.2306    0.1009    0.0483
    1.0000   -0.0811   -0.0187   -0.0055   -0.0019   -0.0007
    2.0000    0.0031    0.0007    0.0002    0.0001    0.0000
    3.0000   -0.0001   -0.0000   -0.0000   -0.0000   -0.0000
    4.0000    0.0000    0.0000    0.0000    0.0000    0.0000

 Non-dimensional Frequency Parameters, z_mn = g_mn*a
 ---------------------------------------------------

    z_mn      n = 0        1        2         3         4
 ------------------------------------------------------------
  m =
         0         0         0    2.3274    3.5315    4.6679
    1.0000    3.0273    4.5354    5.9344    7.2664    8.5531
    2.0000    6.2130    7.7414    9.1864   10.5756   11.9239
    3.0000    9.3758   10.9126   12.3840   13.8076   15.1942
    4.0000   12.5289   14.0714   15.5600   17.0068   18.4202


   To plot mode shape W_mn, use function PLOTMSH4(m,n)
   To animade mode (m,n), use function ANIMODE4(m,n)
PLOTMSH4(0,2), Mode 1

 Spatial Distribution of Mode (0,2)
 ----------------------------------
  Number of nodal circles m = 0
  Number of nodal diameters n = 2
```

```
  Natural frequency = 2077.2545
  Modeshape:
        Wmn(r,theta) = Fmn(r)*cos(n*theta)
    where
        Fmn(r) = [Jn(g_mn*r) + d_mn*In(g_mn*r)]
        Jn and In = Bessel functions of the first and second kind
        g_mn = 46.5482, d_mn = 0.23065


>> PLOTMSH4(1,0),Mode2

 Spatial Distribution of Mode (1,0)
 ----------------------------------
  Number of nodal circles m = 1
  Number of nodal diameters n = 0

  Natural frequency = 3514.4624
  Modeshape:
        Wmn(r,theta) = Fmn(r)*cos(n*theta)
    where
        Fmn(r) = [Jn(g_mn*r) + d_mn*In(g_mn*r)]
        Jn and In = Bessel functions of the first and second kind
        g_mn = 60.5463, d_mn = -0.081148

  Locations of nodal circles:
    r =
    0.0340

 This is the end of the code
```

APPENDIX C
EGIN VALUE OUTPUT FOR ONE LAYER LEXAN WITH LARGE HOLES

```
   Abaqus 6.9-2                                  Date 06-Feb-2012   Time 21:58:54
   For use at Wayne State University under license from Dassault Systemes or its
subsidiary.


                The Abaqus Software is a product of:

                  Dassault Systemes Simulia Corp.
                        Rising Sun Mills
                        166 Valley Street
                  Providence, RI 02909-2499, USA


               Available for internal use at Wayne State University.
               The Abaqus Online Support System is accessible
               through the "My Support" section of the SIMULIA
               Home Page at http://www.simulia.com.

               Support policies for academic licenses are described
               on the SIMULIA web site at
               http://www.simulia.com/academics/academic_support.html.

                       On machine lan1.grid.wayne.edu
                       you are authorized to run
                       Abaqus/Standard until 04-Oct-2012

                       Your site id is: 08WAYNEUA


                For assistance or any other information you may
                obtain contact information for your local office
                from the world wide web at:

                  http://www.simulia.com/about/locations.html

* * * * * * * * * * * * * * * * * * * * * * * * * * * * * * * * * * * * * * *
*                                                                             *
*                        ****************                                     *
*                        *  N O T I C E  *                                     *
*                        ****************                                     *
*                                                                             *
*                                                                             *
*                         Abaqus 6.9-2                                        *
*                                                                             *
*                BUILD ID: 2009_07_10-10.30.58 92676                          *
*                                                                             *
*                                                                             *
*  Please make sure you are using release 6.9 manuals                         *
*  plus the notes accompanying this release.                                  *
*                                                                             *
*                                                                             *
*                                                                             *
*                                                                             *
*                                                                             *
```

PROCESSING PART, INSTANCE, AND ASSEMBLY INFORMATION
****

END PROCESSING PART, INSTANCE, AND ASSEMBLY INFORMATION
****

OPTIONS BEING PROCESSED
****

```
*NODE
*ELEMENT,TYPE=STRI65,ELSET=lexan
*MATERIAL, NAME=lexan
*DENSITY
*ELASTIC, TYPE = ISOTROPIC
*SHELL SECTION, ELSET=lexan, MATERIAL=lexan
*SHELL SECTION, ELSET=lexan, MATERIAL=lexan
*STEP, INC =         1000, NLGEOM = YES, PERTURBATION
*FREQUENCY, EIGENSOLVER = LANCZOS, NORMALIZATION = DISPLACEMENT
*STEP, INC =         1000, NLGEOM = YES, PERTURBATION
*STEP, INC =         1000, NLGEOM = YES, PERTURBATION
*FREQUENCY, EIGENSOLVER = LANCZOS, NORMALIZATION = DISPLACEMENT
*FREQUENCY, EIGENSOLVER = LANCZOS, NORMALIZATION = DISPLACEMENT
*EL FILE, POSITION = AVERAGED AT NODES
*END STEP

***WARNING: THE NLGEOM FLAG WILL BE DE-ACTIVATED BECAUSE IT WAS NOT ACTIVE IN
            THE BASE STATE.
*STEP, INC =         1000, NLGEOM = YES, PERTURBATION
*FREQUENCY, EIGENSOLVER = LANCZOS, NORMALIZATION = DISPLACEMENT
*FREQUENCY, EIGENSOLVER = LANCZOS, NORMALIZATION = DISPLACEMENT
*NODE FILE
*END STEP
```

P R O B L E M S I Z E

NUMBER OF ELEMENTS IS	14990
NUMBER OF NODES IS	31292
NUMBER OF NODES DEFINED BY THE USER	31292
TOTAL NUMBER OF VARIABLES IN THE MODEL	187752

(DEGREES OF FREEDOM PLUS ANY LAGRANGE MULTIPLIER VARIABLES)

ESTIMATES ASSUME MAXIMUM OF 6 ACTIVE DEGREES OF FREEDOM PER NODE FOR 5 DOF ELEMENTS

END OF USER INPUT PROCESSING

JOB TIME SUMMARY
USER TIME (SEC) = 2.6100
SYSTEM TIME (SEC) = 0.42000
TOTAL CPU TIME (SEC) = 3.0300
WALLCLOCK TIME (SEC) = 4
1

Abaqus 6.9-2 Date 06-Feb-2012 Time 21:59:01
For use at Wayne State University under license from Dassault Systemes or its subsidiary.

STEP 1 INCREMENT 1

TIME COMPLETED IN THIS STEP 0.00

S T E P 1 C A L C U L A T I O N O F E I G E N V A L U E S

F O R N A T U R A L F R E Q U E N C I E S

THE LANCZOS EIGENSOLVER IS USED FOR THIS ANALYSIS
Abaqus WILL COMPUTE UNCOUPLED
STRUCTURAL AND ACOUSTIC MODES
NUMBER OF EIGENVALUES 15
HIGHEST FREQUENCY OF INTEREST 1.00000E+18
MAXIMUM NUMBER OF STEPS WITHIN RUN 35
BLOCK SIZE FOR LANCZOS PROCEDURE 7
THE EIGENVECTORS ARE SCALED SO THAT
THE LARGEST DISPLACEMENT ENTRY IN EACH VECTOR
IS UNITY

THIS IS A LINEAR PERTURBATION STEP.
ALL LOADS ARE DEFINED AS CHANGE IN LOAD TO THE REFERENCE STATE

TOTAL MASS OF MODEL

1.4737189E-05

LOCATION OF THE CENTER OF MASS OF THE MODEL

-5.0217554E-04 -3.5795413E-09 0.000000

MOMENTS OF INERTIA ABOUT THE ORIGIN

I(XX)	I(YY)	I(ZZ)
9.5235437E-03	1.0316722E-02	1.9833769E-02

PRODUCTS OF INERTIA ABOUT THE ORIGIN

I(XY)	I(XZ)	I(YZ)
-3.4137204E-13	0.000000	0.000000

MOMENTS OF INERTIA ABOUT THE CENTER OF MASS

I(XX)	I(YY)	I(ZZ)
9.5235437E-03	1.0316722E-02	1.9833769E-02

PRODUCTS OF INERTIA ABOUT THE CENTER OF MASS

I(XY)	I(XZ)	I(YZ)
-3.4134555E-13	0.000000	0.000000

M E M O R Y E S T I M A T E

PROCESS	FLOATING PT OPERATIONS PER ITERATION	MINIMUM MEMORY REQUIRED (MBYTES)	MEMORY TO MINIMIZE I/O (MBYTES)
1	4.46E+09	100	1319

E I G E N V A L U E O U T P U T

MODE NO	EIGENVALUE	FREQUENCY (RAD/TIME)	FREQUENCY (CYCLES/TIME)	GENERALIZED MASS	COMPOSITE MODAL DAMPING
1	-3.62916E-05	0.0000	0.0000	4.00201E-06	0.0000
2	-1.83950E-05	0.0000	0.0000	1.19590E-05	0.0000
3	-5.47595E-06	0.0000	0.0000	1.08393E-05	0.0000
4	3.28435E-05	5.73093E-03	9.12106E-04	3.54520E-06	0.0000
5	3.60072E-05	6.00060E-03	9.55025E-04	6.73178E-06	0.0000
6	8.38131E-05	9.15495E-03	1.45706E-03	1.04820E-05	0.0000
7	2.90498E+06	1704.4	271.26	3.20951E-06	0.0000
8	3.08678E+06	1756.9	279.62	2.84219E-06	0.0000
9	6.97361E+06	2640.8	420.29	3.61025E-06	0.0000
10	1.61425E+07	4017.8	639.45	2.57056E-06	0.0000
11	1.68599E+07	4106.1	653.50	2.11985E-06	0.0000
12	3.63335E+07	6027.7	959.34	2.51842E-06	0.0000
13	3.67619E+07	6063.2	964.98	2.98243E-06	0.0000
14	5.03890E+07	7098.5	1129.8	1.83132E-06	0.0000
15	5.18386E+07	7199.9	1145.9	2.24029E-06	0.0000

THE ANALYSIS HAS BEEN COMPLETED

ANALYSIS COMPLETE
WITH 1 WARNING MESSAGES ON THE DAT FILE

```
JOB TIME SUMMARY
  USER TIME (SEC)      =   68.370
  SYSTEM TIME (SEC)    =   19.550
  TOTAL CPU TIME (SEC) =   87.920
  WALLCLOCK TIME (SEC) =         97
```

APPENDIX D
VIBRATION RESULTS FOR ONE MORE SAMPLE FROM EACH GROUP DESCRIBED IN THE DISSERTATION WITH SAME SEQUENCE

1. Aluminum honeycomb

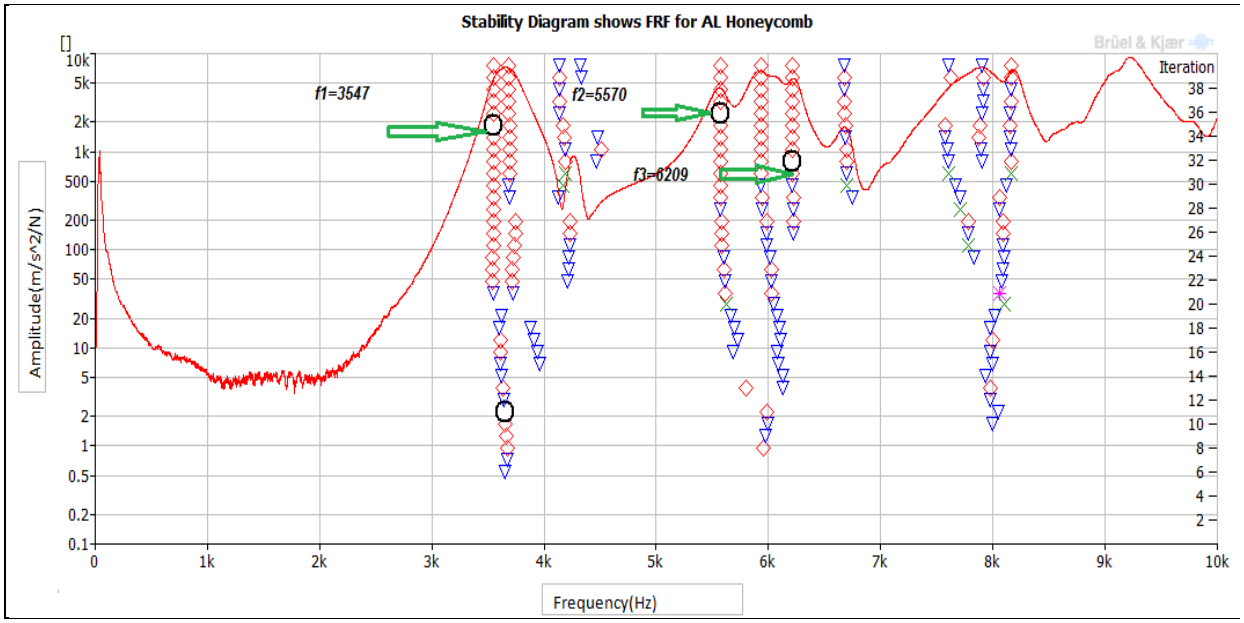

Figure D1: The stability diagram which indicates the first three natural frequencies

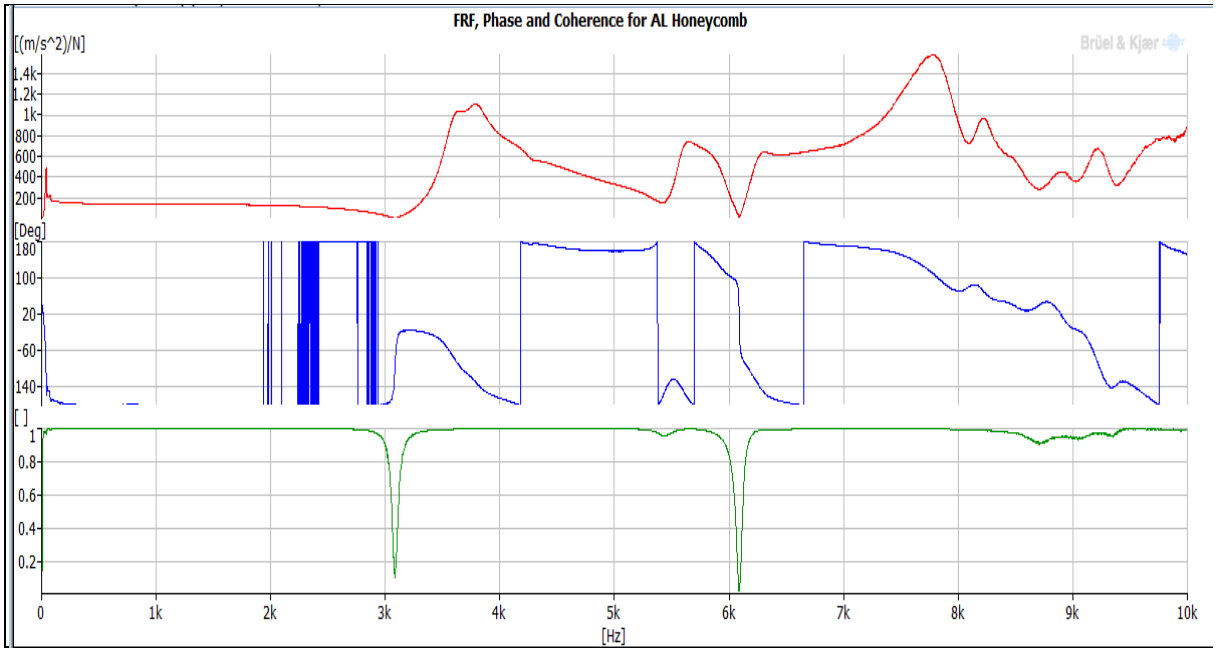

Figure D2: FRF, Coherence and phase

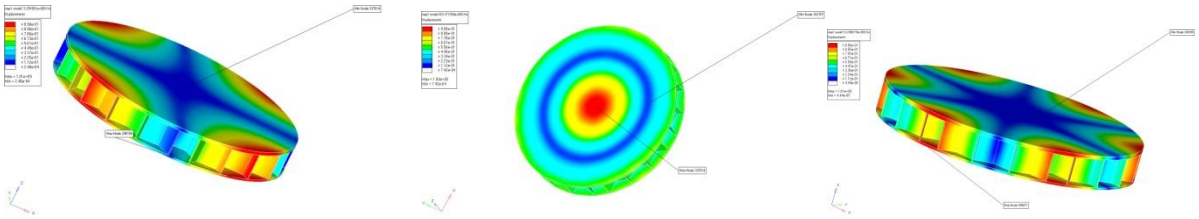

Figure D3: 1st three mode shapes (displacement contour)

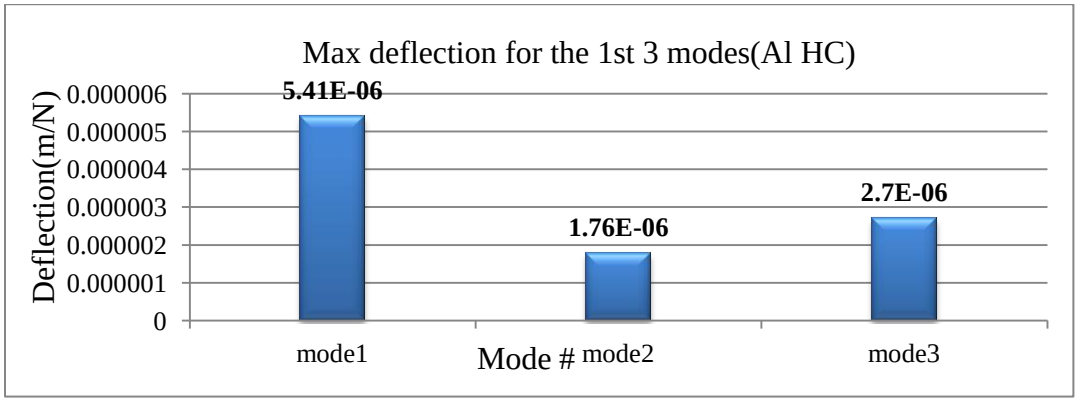

Figure D4: Maximum deflection for the 1st three modes

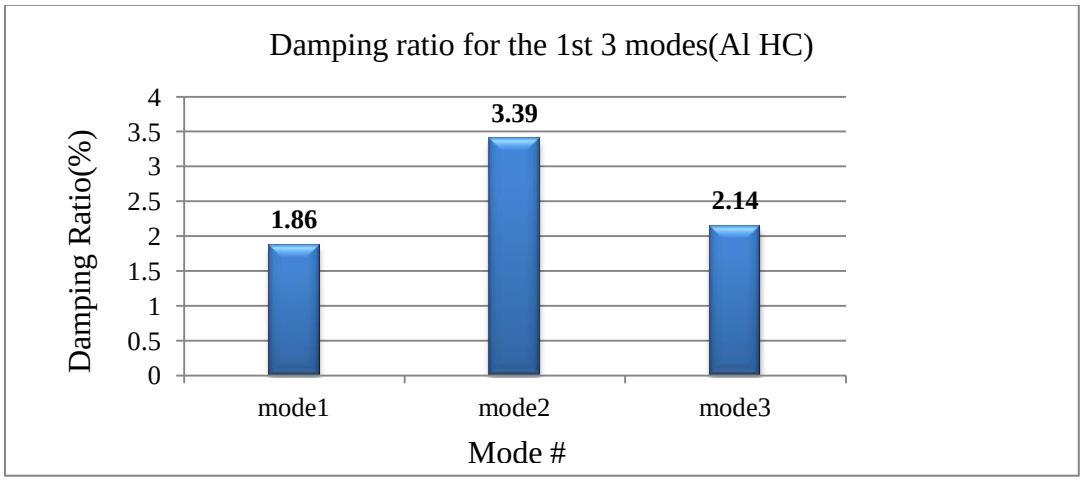

Figure D5: Damping ratio for the 1st three modes

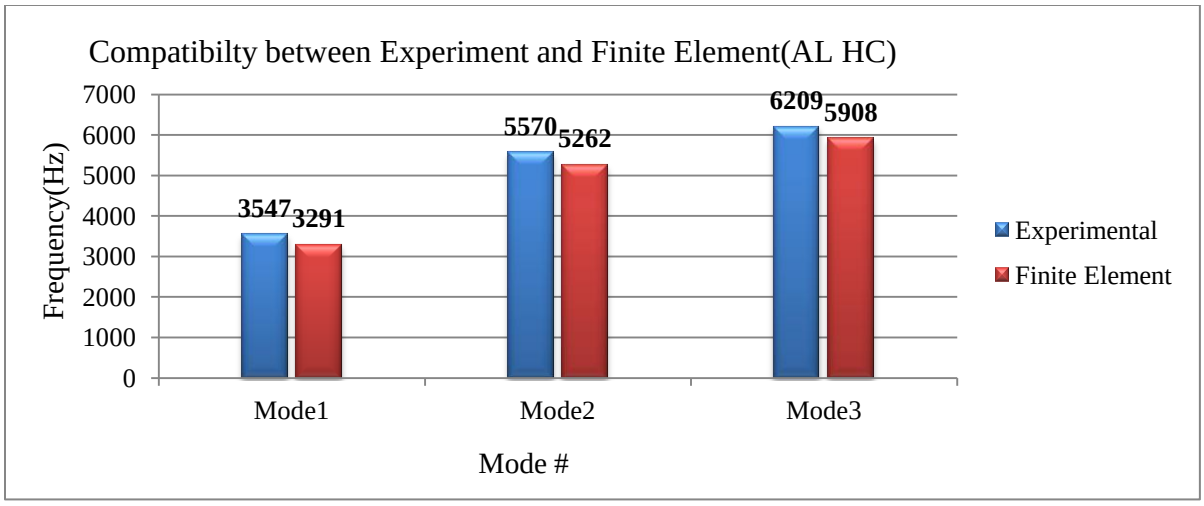

Figure D6: Compatibility between experiment and FEM results

2. 1 layer solid Lexan

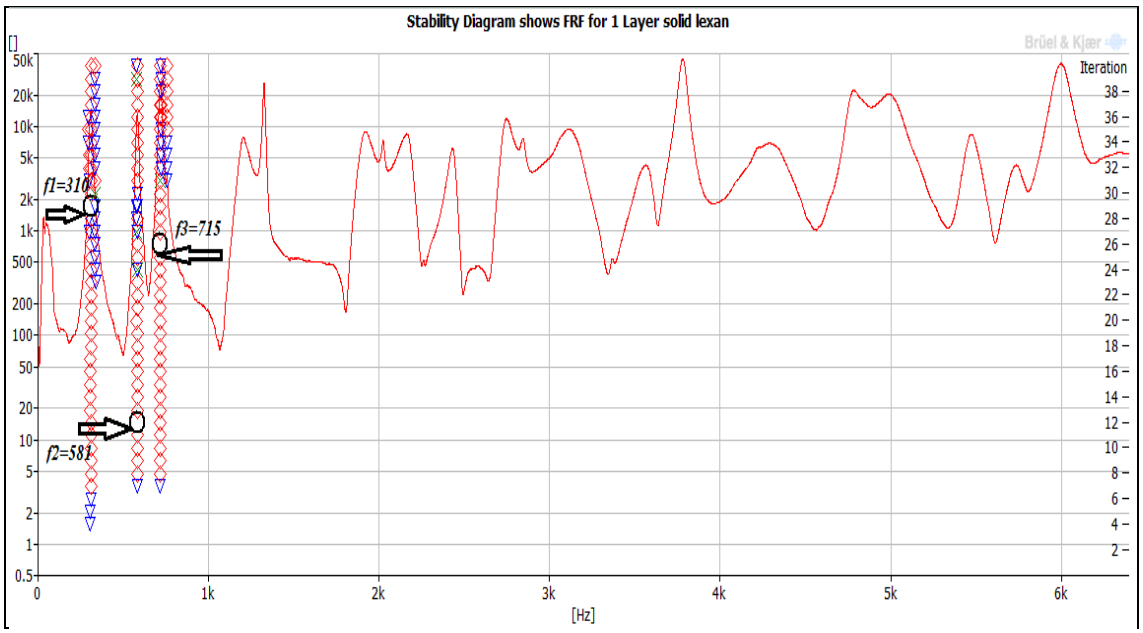

Figure D7: The stability diagram which indicates the first three natural frequencies

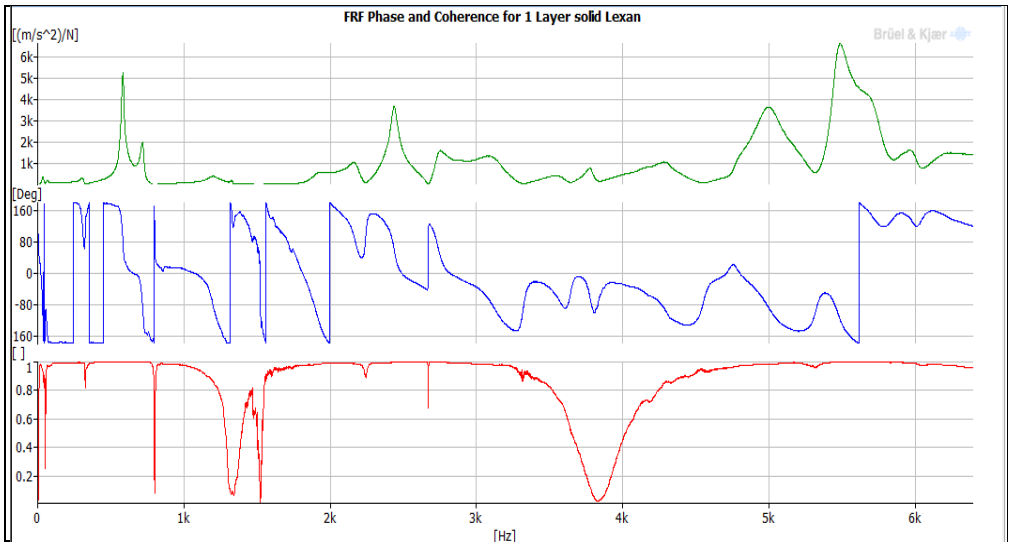

Figure D8: FRF, Coherence and phase

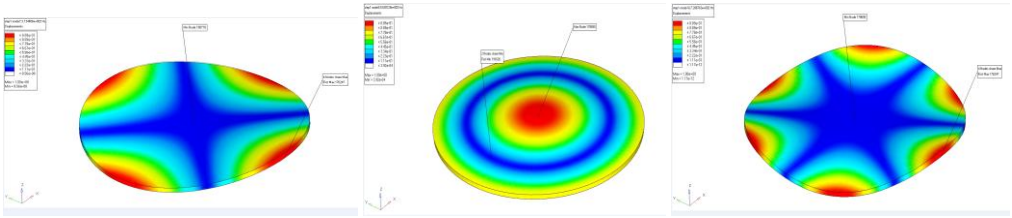

Figure D9: 1st three mode shapes (displacement contour)

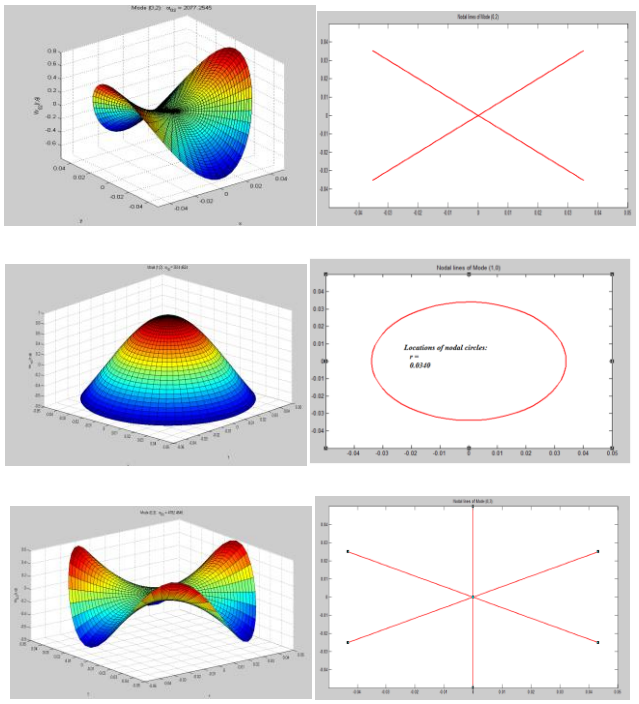

Figure D10: 1st three mode shapes (displacement contour, Matlab)

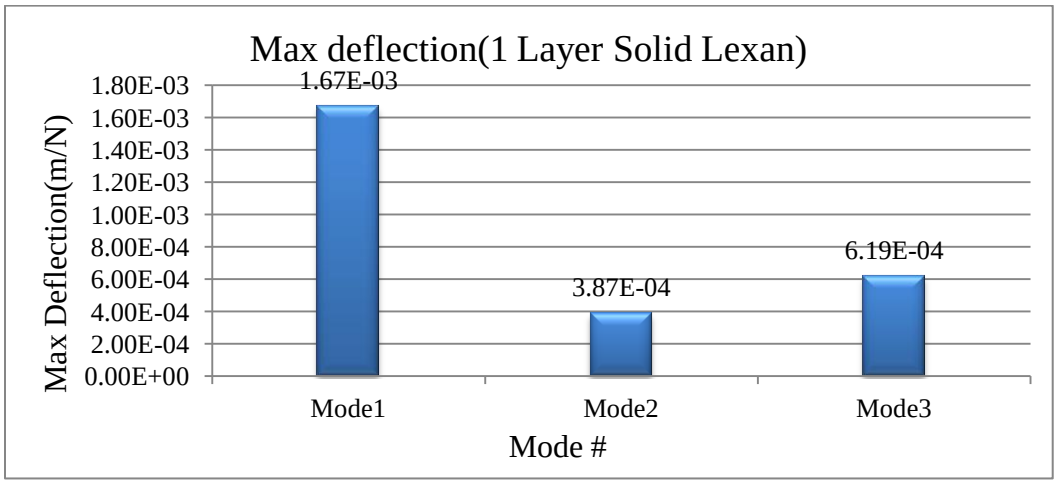

Figure D11: Maximum deflection for the 1st three modes

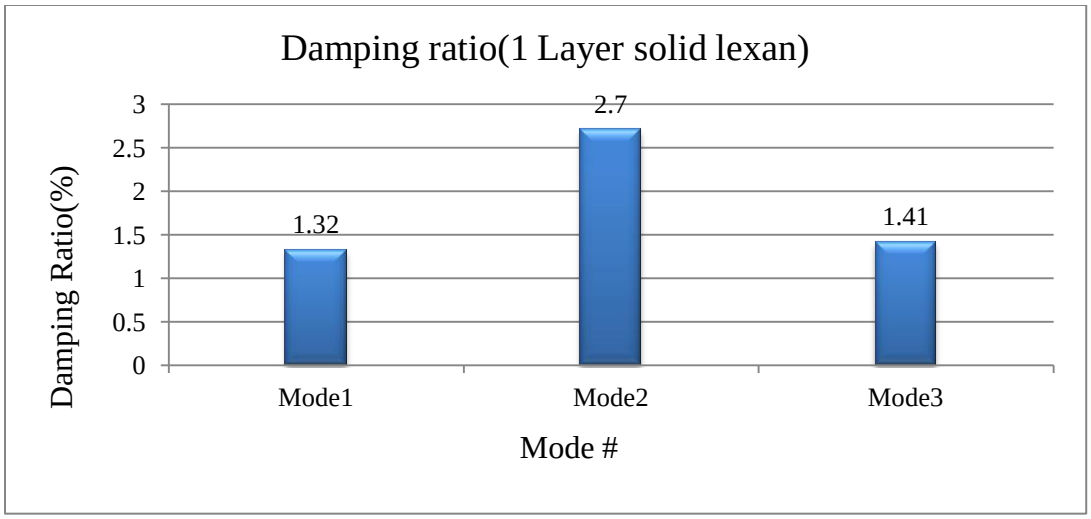

Figure D12: Damping ratio for the 1st three modes

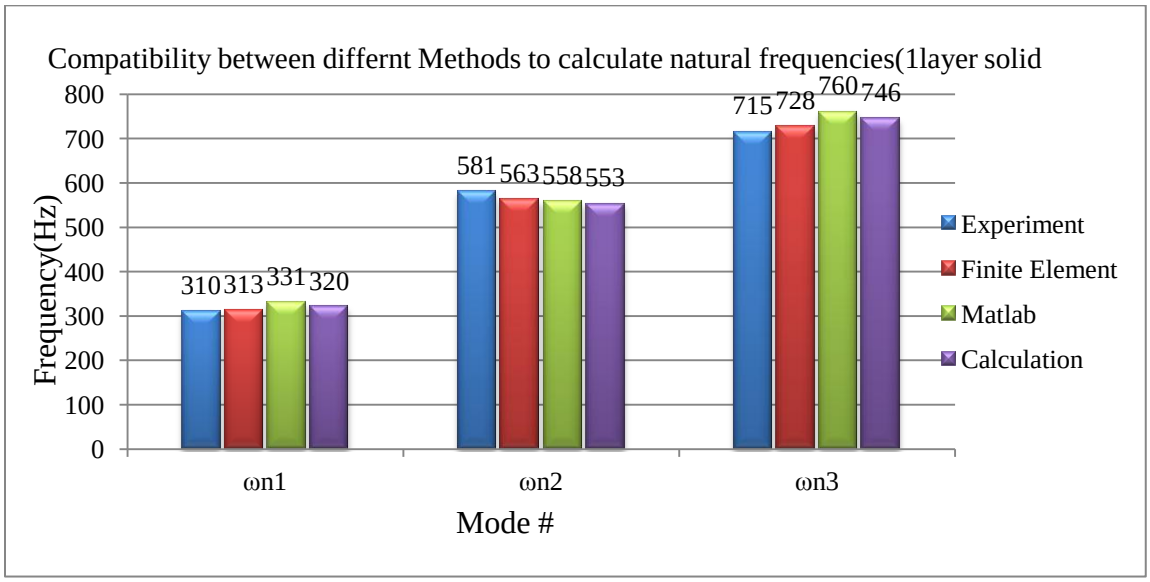

Figure D13: Compatibility between experiment and FEM results

3. Stainless steel triangular honeycomb Microtruss

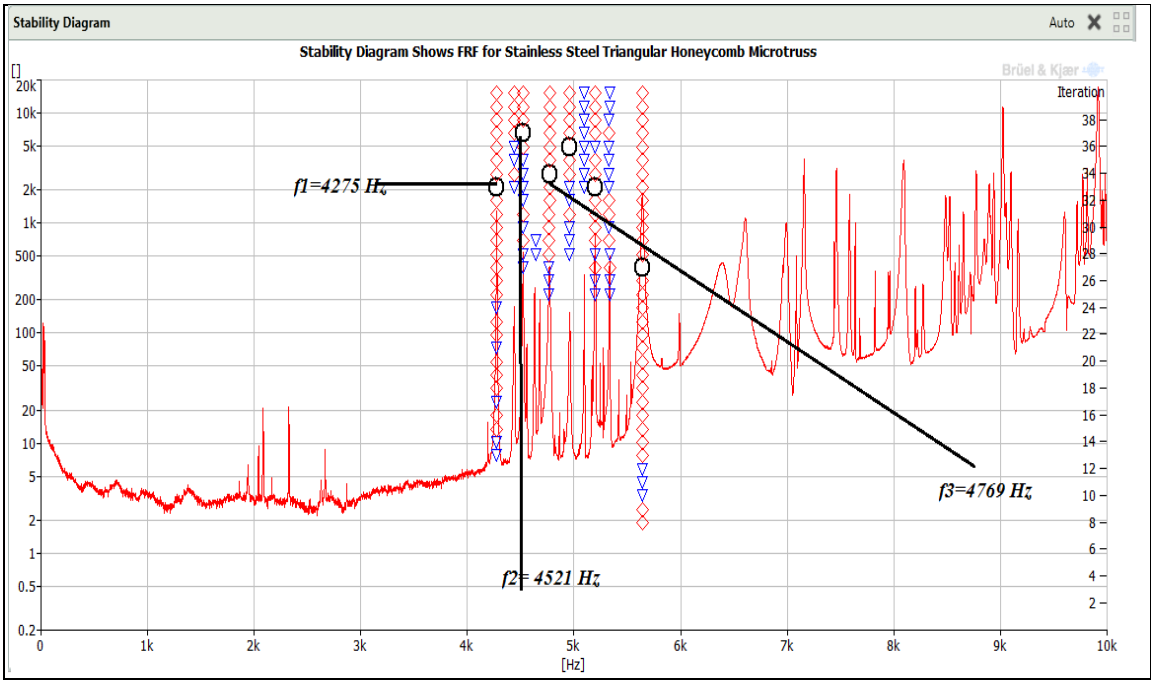

Figure D14: The stability diagram which indicates the first three natural frequencies

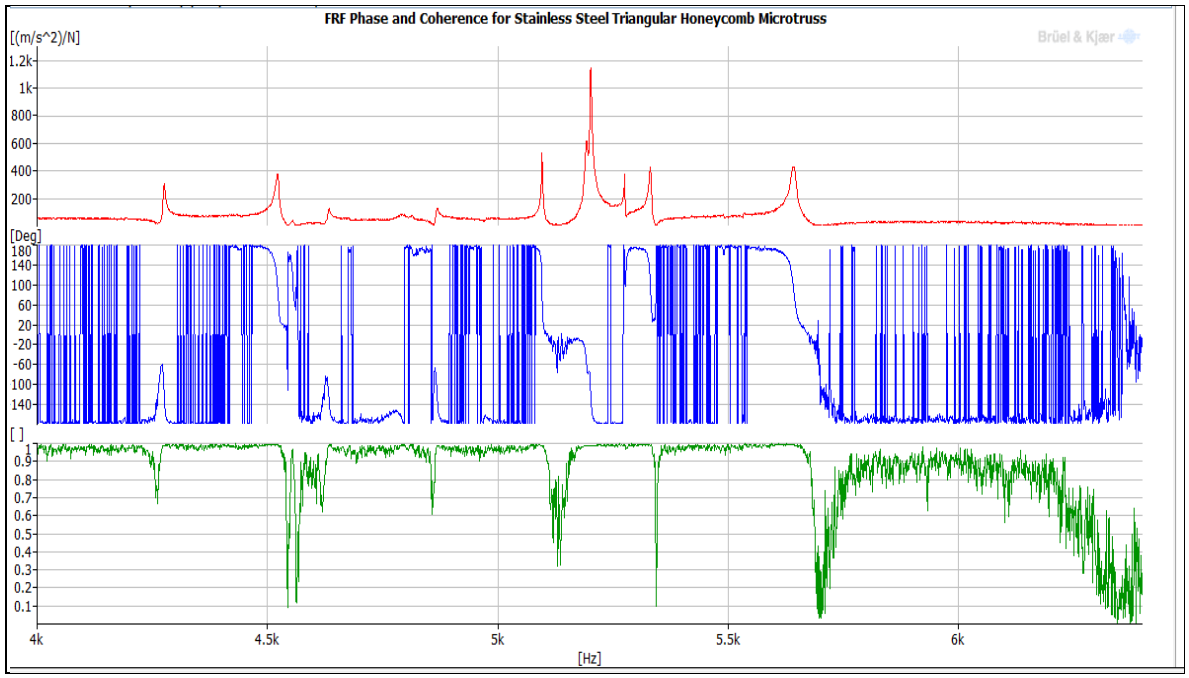

Figure D15: FRF, Coherence and phase

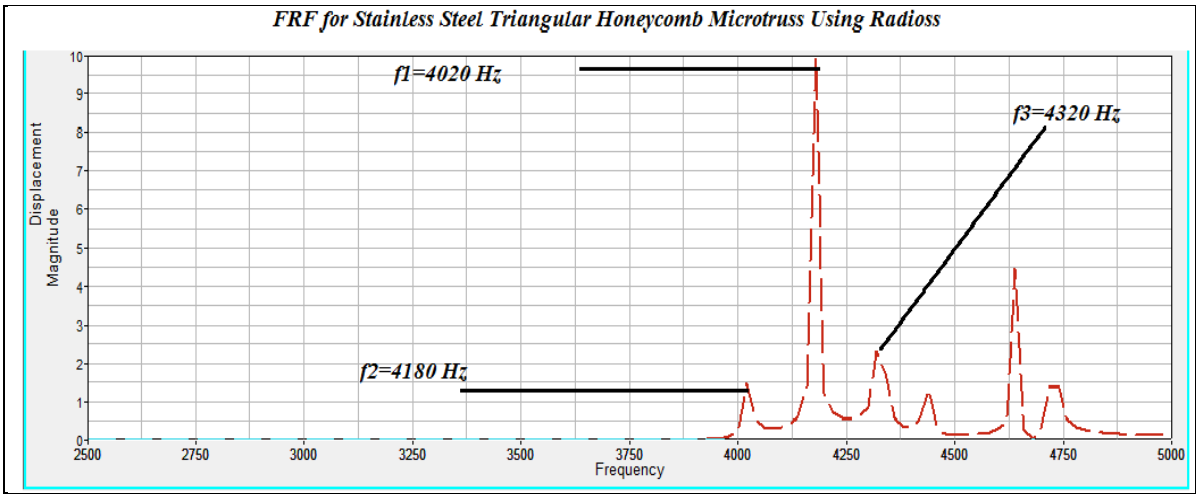

Figure D16: FRF results from RADIOSS

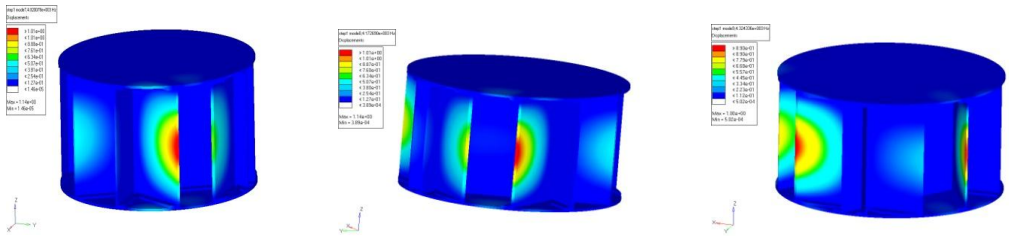

(Displacement contour)Mode1 Mode2 Mode3

Figure D17: 1st three mode shapes (displacement contour)

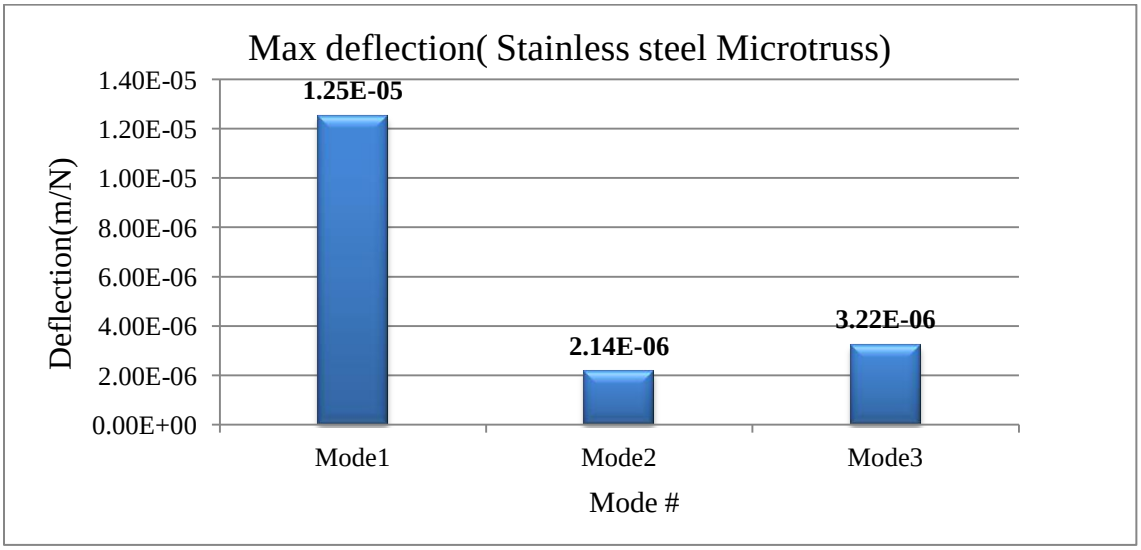

Figure D18: Maximum deflection for the 1st three modes

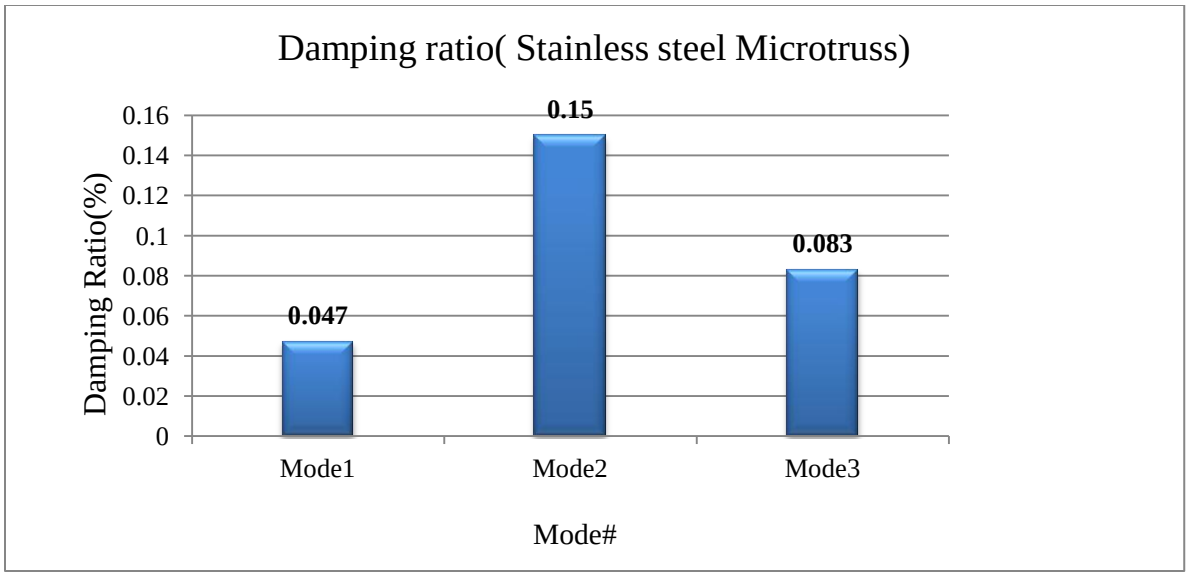

Figure D19: Damping ratio for the 1st three modes

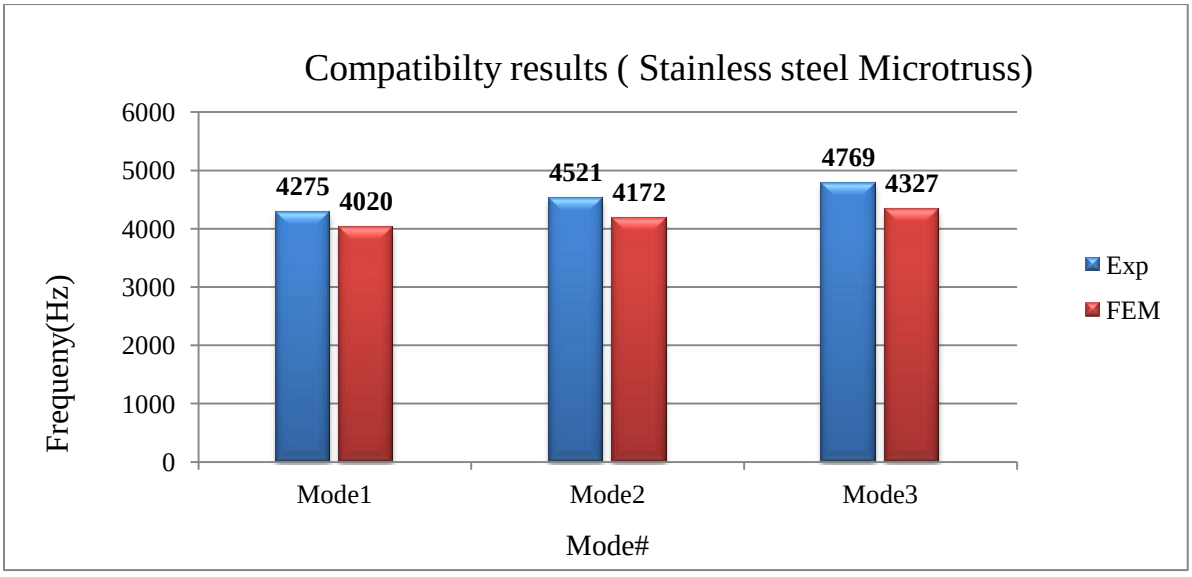

Figure D20: Compatibility between experiment and FEM results

4. Aluminum nuts double in-line Micropillars

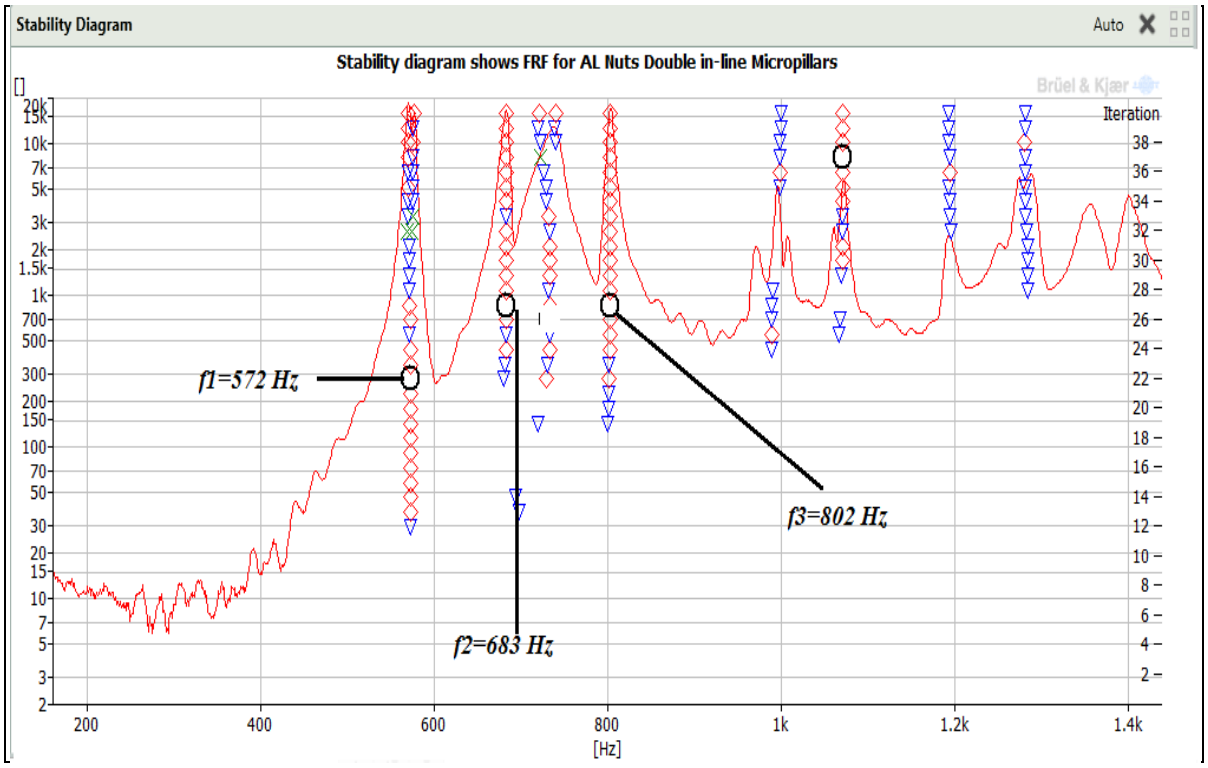

Figure D21: The stability diagram which indicates the first three natural frequencies

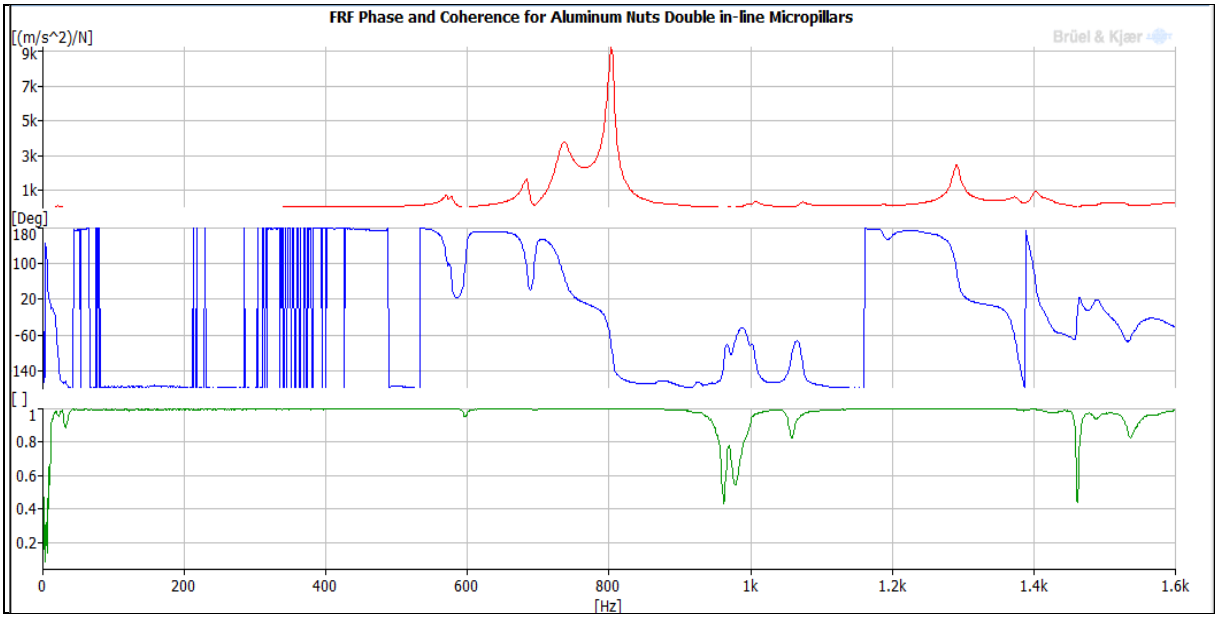

Figure D22: FRF, Coherence and phase

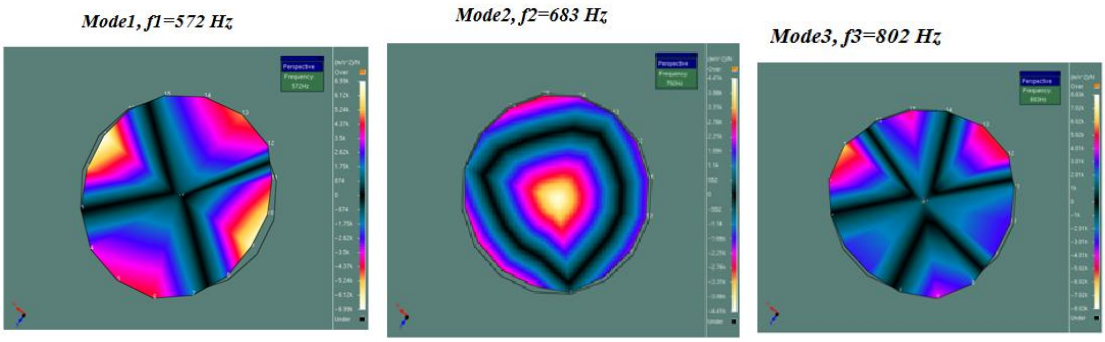

Figure D23: 1st three mode shapes (displacement contour)

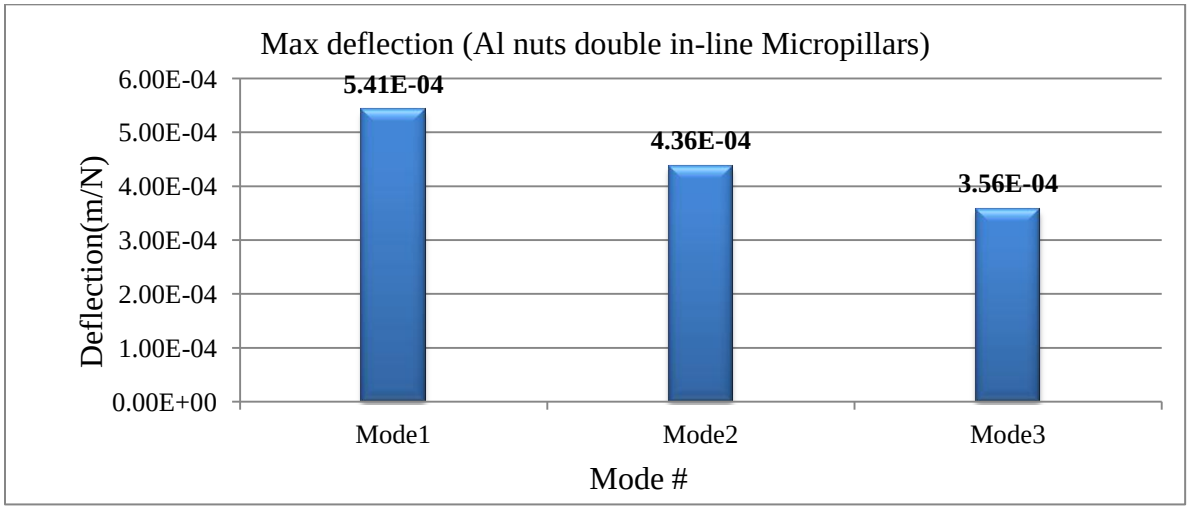

Figure D24: Maximum deflection for the 1st three modes

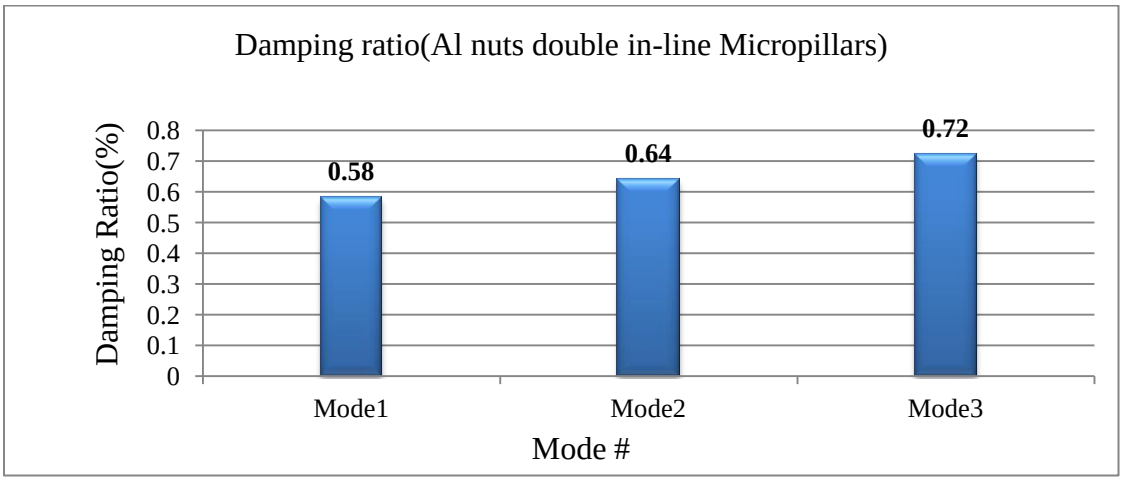

Figure D25: Damping ratio for the 1st three modes

REFERENCES

[1] Anon.,"Vibro-acoustics now key to automotive competition," Noise and Vibration Worldwide, June 2003, 13-15.

[2] Englehardt, K. J., and Toon, J., 2008, "Reducing Noise: Micro Honeycomb materials enable a new physics of sound reduction," Georgia Tech Research News, September 30, 2008.

[3] O'Boy, D.J., and Krylov, V. V., 2011, "Damping of flexural vibrations in circular plates with tapered central holes," Journal of sound and Vibration, 330, 2220-2236.

[4] J. C. Whitney, Inc., 2011, "Everything Automotive Catalogue".

[5] Rao, S.S, "Mechanical Vibrations," Prentice-Hall, London, 2003.

[6] Cerrato J. G et al. Automatic detection of buzz, squeak and rattle events, SAE Paper 2001-01-1479; 2001

[7] Shin, S-H and Cheong, C.,"Experimental characterization of instrument panel buzz, squeak and rattle (BSR) in a vehicle," Applied Acoustics, (71) 2010 1162-1168.

[8] Karavarana F, Reiders B. Squeak and rattle – state of the art and beyond, SAE Paper 1999-01-1728, SAE noise & vibration conference & exposition. Traverse City, Michigan; May 17–20, 1999.

[9] Gosavi, SS, Automotive buzz, squeak and rattle (bsr) detection and prevention, SAE Paper, 2005, 26-56.

[10] Kreppold EM. A modern development process to bring silence into interior components. SAE Paper 2007-01-1219, World Congress, Detroit, Michigan; April 16–19, 2007.

[11] Jay M, Gu Y. Excitation and measurement of bsr in vehicle seats. SAE Paper No. 2001-01-1552; 2001.

[12] Poisson, S. D., “Memoir sur l’equibre et le movement des corp elastique,” M ‘em acad Vol. 8, 1829.

[13] Kirchhoff, G., “ llber das Gleichgewicht und die Bewegung einer elastischer. Scheibe,” Journal filr Math. (Crelle), Vol. 40, 1850.

[14] Rayleigh, L., (John W. Strutt) “The theory of sound,” Macmillan, London, 1894.

[15] Lamb, H. “Statics,” (Cambridge University Press, 1960; reprint of the third edition of 1928 of the textbook first published in 1912).

[16] Airey, J.R., “The vibrations of circular plates and their relation to Bessel functions, Proceedings of the Physical Society of London Volume 23 ,p. 225, 1910.

[17] Timoshenko, S.P., “Vibration Problems in Engineering,” D. Van Nostrand Company, 1st Ed. 1928, 2nd Ed. 1937, 3rd Ed. 1955 (with D. H. Young).

[18] Wood, A.B., “An experimental determination of the frequencies of free circular plates. Authors: Wood, A. B.,” Proceedings of the Physical Society, Volume 47, Issue 5, pp. 794-799 (1935).

[19] Iguchi, S, 1937, “Allgemeine Lösung der Knickungsaufgabe für rechteckige Platten”. Ingenieur-Archiv,vol.7,pp207-215

[20] Iguchi, S, 1953, “Die Eigenschwingungen und Klangfiguren der vierseiting freien rechteckigen Platte durch Schubkrafte.Ingenieur-Archiv,vol.9,pp 1-12.

[21] Warburton, G.B., “The vibration of rectangular plates,” Proceedings of The Institution of Mechanical Engineers. 168, 371-384 (1954).

[22] Lekhnitskii, S.G., Tsai, S.W., T. Cheron, T., “Anisotropic Plates,” (1947).

[23] Leissa, A.W., “Vibration of Plates,” NASA SP-160, U.S Gov’t Printing Office. 10-13 (1969).

[24] Zelenev, Yu V., Electrova,L. M., Determination of the dynamic parameters of polymer plates, Soviet Physical Acoustics 18 (1973) 339–341.

[25] Gorman, D.J. Free vibration analysis of cantilever plates by the method of superposition Journal of Sound and Vibration, v 49, n 4, p 453-67, 22 Dec. 1976

[26] Gorman, D.J. ,"Free vibration analysis of rectangular plates with inelastic lateral support on the diagonals,"Journal of the Acoustical Society of America, v 64, n 3, p 823-6, Sept. 1978.

[27] Gorman, D.J , "Highly accurate analytical solution for free vibration analysis of simply supported right triangular plates,"..Journal of Sound and Vibration, v 89, n 1, p 107-118, Jul 8 1983.

[28] Dickinson, S.M., "The bucking and frequency of flexural vibration of rectangular isotropic and orthotropic plates using Rayleigh's method," J. Sound and Vibration. 61(1), 1-8 (1978).

[29] Dinis, L. M. S. and Owen, D. R. J., "Elastic viscoplastic analysis of plates by the finite element method." Compui. Struct. 8, 207215 (1977). 20.

[30] Blevins, R.D., "Formulas for Natural Frequency and Mode Shape," (1979).

[31] D.J. O'Connor, A finite element package for the analysis of sandwich construction, Compos. Struct. 8 (1987), pp. 143–161.

[32] Ewins, D.J., "Modal Testing: Theory and Practice," (1984).

[33] Deobald, L. R., Gibson. F., Determination of elastic constants of orthotropic plates by a modal analysis/ Rayleigh–Ritz technique, Journal of Sound and Vibration 124 (1988) 269–283.

[34] Bardell, N.S.,"Free vibration analysis of a flat plate using the hierarchical finite element method," Journal of Sound and Vibration, v 151, n 2, p 263-89, 8 Dec. 1991.

[35] Lai, T.C, Lau, T.C.,"Determination of elastic constants of a generally orthotropic plate by modal analysis, Modal analysis," v 8, n 1, p 15-33, Jan 1993.

[36] L.J. Lee, Y.J. Fan., "Bending and vibration analysis of composite sandwich plates," Computers and Structures, v 60, n 1, p 103-12, 3 July 1995.

[37] Zhang, Q.J.; Sainsbury, M.G.,"Galerkin element method applied to the vibration of rectangular damped sandwich plates, "Computers and Structures, v 74, n 6, p 717-730, Febrary 1, 2000.

[38] Klosowski, K. Woźnica and D. Weichert " Dynamics of elasto-viscoplastic plates and shells "Archive of Applied Mechanics, Volume 65, Number 5 (1995), 326-345.

[39] Klosowski, P (1999). "Different types of constitutive equations in dynamic response of an elasto-viscoplastic circular plate and cylindrical panel Arch". Civil engineering (Johannesburg, South Africa)(1021-2000), 45(2), p.231.

[40] Hoshino, Hiroaki , Sakurai, Toshiaki; Takahashi, Kunihiro,"Vibration reduction in the cabins of heavy-duty trucks using the theory of load transfer paths," JSAE Review, v 24, n 2, p 165-171, April 2003

[41] Sun, Liping,; Ai, Shangmao; Chen, Hailong,, "Vibro-acoustic statistical energy analysis of a classic submarine structure, "Harbin Gongcheng Daxue Xuebao/Journal of Harbin Engineering University, v 27, p 507-512, December 2006.

[42] Pappada`, S.; Gren, P.; Tatar, K.; Gustafson, T.; Rametta, R.; Rossini, E.;Maffezzoli, A, ".Mechanical and Vibration Characteristics of Laminated Composite Plates Embedding

Shape Memory Alloy Superelastic Wires," Journal of Materials Engineering and Performance, v 18, n 5-6, p 531-7, Aug. 2009

[43] Shin, S-H and Cheong, C.,"Experimental characterization of instrument panel buzz, squeak and rattle (BSR) in a vehicle," Applied Acoustics, (71) 2010 1162-1168.

[44] Cremer, L.L., "Theorie der schalldammung dummer wande bei schragen eingall," Acustica. 81 (1942).

[45] London, "Transmission of reverberant sound through double walls," J. Acoust. Soc. Am. 22(2): 270 (1950).

[46] Zwikker, C., Kosten, C.W., "Sound Absorbing Materials," Elsevier Publishing Company, Inc. (1949).

[47] Vogel, T., "Sur les vibrations de certains systems elstiques damns un champ sonore," Ph. D. Thesis, Marseille (1947).

[48] Hickman, H.S.; Risty, D.E.; Stewart, E.S.,"Properties of sandwich-type structures as acoustic windows" Acoustical Society of America -- Journal, v 29, n 7, p 858-864, July, 1957.

[49] Kurtze, G, "Bending wave propagation in multilayer plates," Acoustical Society of America -- Journal, v 31, n 9, p 1183-1201, Sept, 1959.

[50] Watters 1959 G. Kurtze and B.G. Watters, "New wall design for high transmission loss or high damping," Journal of the Acoustical Society of America, 31(6), 739-748 (1959).

[51] Maidanik, G., "Response of ribbed panels to reverberant acoustic field," J. Acoust. Soc. Am. 34, 809-826 (1962).

[52] Ford, R.D.; Lord, P.; Walker, A.W., Sound transmission through sandwich constructions Journal of Sound and Vibration, v 5, n 1, p 9-21, Jan, 1967.

[53] Sharp, B.H.S.; Beauchamp, J.W., “Transmission loss of multilayer structures, “Journal of Sound and Vibration, v 9, n 3, p 383-392, May, 1969.

[54] Spronck, F, “Transparency to sound of thin plates,” Proceedings of the 7th international congress on acoustics, p 301-4, 1971.

[55] Sewell, E. C. (1970). Transmission of Reverberant Sound through a Single-Leaf Partition Surrounded by an Infinite Rigid Baffle. J. Sound Vib. Vol 12 , 21-32.

[56] Smolenski, C.P., Krokosky, E.M. Dilational-mode sound transmission in sandwich panels Journal of the Acoustical Society of America, v 54, n 6, p 1449-57, 1973

[57] Dym, C.L., Lang, M.A.,”Transmission of sound through sandwich panels,” Journal of the Acoustical Society of America, v 56, n 5, p 1523-32, Nov. 1974.

[58] Guyader, J.L., and Lesueur, C., ”Acoustic transmission through orthotropic multilayered plates, Part II: Transmission Loss, ” J. Sound and Vibration. 58(1), 69-86 (1978).

[59] Woodcock, R., Nicolas, J., “A generalized model for predicting the sound transmission properties of generally orthotropic plates with arbitrary boundary conditions,” J. Acoust. Soc. Am. 97(2), (1995).

[60] Pates, Carl S., Mei, Chuh; Shirahatti, Uday.”Analysis of coupled structural-acoustic problems using the boundary and finite element methods,” Collection of Technical Papers - AIAA/ASME/ASCE/AHS/ASC Structures, Structural Dynamics and Materials Conference, v 4, p 1835-1843, 1994.

[61] Fringuellino, M., Guglielmone, C., “Progressive impedance method for the classical analysis of acoustic transmission loss in multilayered walls,” Applied Acoustics. 59 (2000).

[62] Lim, T.C ,"Automotive panel noise contribution modeling based on finite element and measured structural-acoustic spectra,". Applied Acoustics, v 60, n 4, p 505-19, Aug. 2000.

[63] Hills, E. , Mace, B.R.; Ferguson, N.S.,Acoustic response variability in automotive vehicles Journal of Sound and Vibration, v 321, n 1-2, p 286-304, 20 March 2009.

[64] Wang binxing,; Zheng sifa; Zhoul lin; Liu shengqiang; Lian xiaomin; Li keqiang,,"Acoustic modelling and analysis of vehicle interior noise based on numerical calculation," Proceedings of the 2010 International Conference on Intelligent Computation Technology and Automation (ICICTA 2010), p 404-7, 2010.

[65] Dhaval Jain, "Modeling the characteristics of new-generation Ford vehicle panels for efficient noise, vibration and harshness performance" .Master Thesis,Wayne State University,2002.

[66] Lagrange, J. L., Volume XI: Mecanique Analytique (reprinted from second edition, 1811-1815). Gauthier-Villars et fils, Paris:1888–89).

[67] Biot, M. A., Theory of propagation of elastic waves in a fluid-saturated porous solid. 1. Low-frequency range", Journal of the acoustical society of America, vol. 28, March, 1956, pp. 168-178.

[68] Allard, Jean F., Depollier, Claude, Guignouard, Philippe, and Rebillard, Pascal, '"Effect of A resonance of the frame on the surface impedance of glass wool of high density and Stiffness", the Journal of the Acoustical Society of America, Vol. 89(3}, March, 1991, pp. 999-1001.

[69] Wadley, H.N.G., (2002), "Cellular metals manufacturing," Advanced Engineering Materials, 4(10), pp. 726 -733.

[70] Wadley,H.N.G., Fleck, N. A., Evans, A.G., (2003),"Fabrication and structural performance of periodic cellular metal sandwich structures," Composites Science and Technology 63, 2331–2343.

[71] Bruel and Kjaer,"PULSE multi-analyzer system type 3560, installation hardeware"2009.

[72] Bruel and Kjaer., "Two Microphone Impedance Tube Theoretical Manual," (1992).

[73] Dossing, O., Bruel and Kjaer., "Structural Testing (Part I, II) User Manual," (1988).

[74] Bruel and Kjaer," Hammer demo guide, modal analysis using PULSE", 2009.

[75] Bruel and Kjaer,"Pulse Reflex modal analysis, version 16.1" 2011.

[76] Peter Wides,"Introduction to finite element analysis", Virginia Tech, 1997.

[77] Abaqus Analysis User's Manual, Dassault Systems, 2009.

[78] Altair Engineering Inc. "RADIOSS theory manual ",version 10,2009.

[79] Yang, "Stress, Strain and Structural Dynamics", Book, 2005, Elsevier.

[80] Huoy-Shyi Tsay, Fung-Huei Yeh," The influence of circumferential edge constraint on the acoustical properties of open-cell polyurethane foam samples", Journal of Acoustical society of America,pp 2804-2814,2006.

[81] J.Pfretzschner,F.Simon,R.M Rodriguez,and C. de la Colina," Simplified calculus to estimate the acoustical absorption of non-planar materials", Institute de Acustica (CSIC),1999.

[82] J. Pfretzschner, R. Mª. Rodríguez," Acoustical absorption and critical thickness" Instituto de Acústica-CSIC. C/ Serrano, 144. 28006 Madrid-Spain,2001.

[83] Everst. F.A,"The master handbook of acoustics",2nd edition, tab books,1989.

[84] Jaesuk Lee, " Low velocity impact and sound absorption of composite sandwiches" ,Dissertation, Wayne State University, 1999.

ABSTRACT

INVESTIGATION AND IMPROVEMENT OF NOISE, VIBRATION AND HARSHNESS (NVH) PROPERTIES OF AUTOMOTIVE PANELS

by

MOHAMMAD AL-ZUBI

August 2012

Advisor: Dr. Emmanuel Ayorinde

Major: Mechanical Engineering

Degree: Doctor of Philosophy

The reduction of noise and vibration in and across several components and modules of the automotive, such as the panels, doors, engine covers, seats, and others, is of primary importance. The NVH performance may be a crucial factor in the purchase decisions of numerous buyers. This work investigates through experimental, analytical and computational methods, six groups of sample materials - fabric, foam, honeycomb, monolithic and sandwich, periodic cellular material structures (PCMS), and generally periodic materials, to assess their suitability for maximum containment of noise and vibration. Various architectural forms have also been considered. State-of-the art instrumentation and adequate analytical and computational methods have been utilized. Five major novel accomplishments have been logged in the work. Vibro-acoustic responses of PCMS materials and newly-constructed generally periodic materials are explored, and some computer procedures are generated. The results give some suggestions for design directions to follow in order to achieve better performances.

AUTOBIOGRAAPHICAL STATEMENT

MOHAMMAD AL- ZUBI

Mohammad Ahmed AL Zubi was born on October 18, 1972 in Jordan. He received his bachelor degree in Mechanical Engineering from the Mu'tah University in Jordan, 1994. Upon graduation, he started working as a maintenance engineer in the Royal Jordanian Air Force until 2008; during his service he got his Master degree in Industrial Automation Engineering in 2006. Mohammad got a scholarship from his government in 2009, then he joined Wayne State University as a PhD student in September 2009, he was a graduate teaching assistance from 2010 to 2012. Mohammad has published several papers in ASME conferences; also he submitted two Journal papers before his defense. Upon receiving his doctoral degree Mohammad will go back to his country Jordan to continue his academic life as a professor at Tafila Technical University. He hopes to continue his research in the areas of automotive NVH.